Chiral properties of dynamical Wilson fermions

DISSERTATION

zur Erlangung des akademischen Grades
doctor rerum naturalium
(Dr. rer. nat.)
im Fach Physik

eingereicht an der
Mathematisch-Naturwissenschaftlichen Fakultät I
der Humboldt-Universität zu Berlin

von
Herr Dipl.-Phys. Roland Hoffmann
geboren am 06.06.1977 in München

Präsident der Humboldt-Universität zu Berlin:
Prof. Dr. Jürgen Mlynek

Dekan der Mathematisch-Naturwissenschaftlichen Fakultät I:
Prof. Thomas Buckhout, PhD

Gutachter:

1. Prof. Dr. Ulrich Wolff
2. Dr. Rainer Sommer
3. Prof. Dr. Sinya Aoki

eingereicht am: 18. Mai 2005
Tag der mündlichen Prüfung: 12. August 2005

Abstract

Quantum Chromodynamics with two light quark flavors is considered in the lattice regularization with improved Wilson fermions. In this formulation chiral symmetry is explicitly broken by cutoff effects linear in the lattice spacing a. As a consequence the isovector axial currents require improvement (in the Symanzik sense) as well as a finite renormalization if they are to satisfy the continuum Ward–Takahashi identities associated with the isovector chiral symmetries up to small lattice corrections of $\mathrm{O}(a^2)$.

In exploratory numerical simulations of the lattice theory algorithmic difficulties were encountered at coarse lattice spacings. There the hybrid Monte Carlo algorithm used suffers from a distorted Dirac spectrum in the form of unphysically small eigenvalues. This is shown to be a cutoff effect, which disappears rapidly as the lattice spacing is decreased. An alternative algorithm, the polynomial hybrid Monte Carlo algorithm, is found to perform significantly better in the presence of exceptionally small eigenvalues.

Extending previously used methods both the improvement and the renormalization of the axial current are implemented non–perturbatively in terms of correlation functions formulated in the framework of the Schrödinger functional. In both cases this is achieved by enforcing continuum Ward identities at finite lattice spacing. Together, this restores the isovector chiral symmetry to quadratic order in the lattice spacing. With little additional effort the normalization factor of the local vector current is also obtained.

The methods developed and implemented here can easily be applied to other actions formulated in the Schrödinger functional framework. This includes improved gauge actions as well as theories with more than two dynamical quark flavors.

Keywords:
Lattice QCD, chiral symmetry, renormalization, improvement

Zusammenfassung

Quantenchromodynamik mit zwei leichten Quarks wird in der Gitterregularisierung mit verbesserten Wilson Fermionen betrachtet. Die chirale Symmetrie in dieser Formulierung wird von Gitterartefakten, die linear im Gitterabstand a sind, explizit gebrochen. Daher erfordern die axialen Isospin Ströme Verbesserung (im Symanzik Sinn), sowie eine endliche Renormierung, wenn sie die Ward–Takahashi Identitäten des Kontinuums bis auf kleine Gitterkorrekturen proportional zu a^2 erfüllen sollen.

Algorithmische Probleme bei großen Gitterabständen machen die numerischen Simulationen der Gittertheorie schwierig. Der Hybrid Monte Carlo Algorithmus leidet unter einem verformten Dirac Spektrum in Form unphysikalisch kleiner Eigenwerte. Es wird gezeigt, daß dies ein Gitterartefakt ist, welches schnell verschwindet, wenn der Gitterabstand verringert wird. Ein alternativer Algorithmus, der polynomische Hybrid Monte Carlo Algorithmus, zeigt erheblich bessere Eigenschaften im Umgang mit den außergewöhnlich kleinen Eigenwerten.

Durch Erweiterung und Verbesserung vorher verwendeter Methoden wird die nicht–perturbative Verbesserung und Renormierung des Axialstroms durch Korrelationsfunktionen im Schrödinger Funktional implementiert. In beiden Fällen wird dies erzielt, indem man Ward Identitäten des Kontinuums bei endlichem Gitterabstand erzwingt. Zusammen stellt dies die chirale Symmetrie bis zur quadratischen Ordnung im Gitterabstand wieder her. Mit wenig zusätzlichem Aufwand wird auch der Normierungsfaktor des lokalen Vektorstroms berechnet.

Die Methoden, die hier entwickelt und implementiert wurden, können leicht auch für andere Wirkungen verwendet werden, die im Schrödinger Funktional formuliert werden können. Dies umfaßt verbesserte Eichwirkungen sowie Theorien mit mehr als zwei dynamischen Quarks.

Schlagwörter:
Gitter QCD, Chirale Symmetrie, Renormierung, Verbesserung

Contents

Chapter 1

Introduction

Compared to the electroweak sector of the standard model of particle physics, quantum chromodynamics (QCD) with its few parameters and extensive symmetries seems to be a rather simple theory. Still, it is expected to describe the whole spectrum of strong interaction phenomena from high–energy hadron collisions to the decays of heavy–quark bound states and of course the hadron masses themselves. Since its birth in the 1960s QCD has been confronted with experiment in innumerable cases and is now a well–established part of the standard model.

At high energies the relevant degrees of freedom (quarks and gluons) are found to be only weakly coupled and the non–interacting theory can serve as a starting point for a perturbative treatment. The breaking of Bjorken scaling [1] in deep inelastic lepton–hadron scattering, which is the original and still one of the most powerful quantitative tests of (perturbative) QCD, is associated with these energy scales.

At low energies the strong interactions show a very different behavior. The coupling becomes strong such that a description in terms of weakly interacting quarks and gluons is no longer appropriate. Instead, the relevant degrees of freedom seem to be the light mesons (pions). Also here precise experimental data are available, in particular for the masses and other properties of the light hadrons. If one wants to establish that the same Lagrangian describes both regimes, vast energy differences need to be bridged [2].

As an additional complication, the transition in the effective degrees of freedom makes it much more difficult to work out the QCD predictions at low energies, because perturbation theory, the "standard tool" of particle physics, fails here. While effective theories are useful at this point, they do not constitute a first–principle method. Also, some non–perturbative predictions can be made on the basis of symmetry considerations or QCD sum rules, but these can not be applied to all problems one might be interested in and often also require additional assumptions.

With the lattice regularization Wilson [3] proposed a radically different approach. Lattice QCD allows for first–principle predictions without any additional assumptions and can be applied to a variety of problems, from the hadron spectrum to meson decay constants and the running of the coupling or even the topological structure of the QCD vacuum.

In this formulation one discretizes the fields and the action using a Euclidean space–time lattice. Thus, before any computation is made, the high frequencies are removed from the theory, rendering the latter ultraviolet finite. The infrared divergencies related to zero modes can also be be cured by either considering a non–zero quark mass or a finite volume with fixed boundary conditions in at least one direction (see Chapter 5). At this point the theory is mathematically well–defined without reference to perturbation theory.

Moreover, if the lattice is small enough, a numerical evaluation on the computer becomes feasible. In this way the lattice serves two purposes: it regularizes the theory with a momentum cutoff proportional to the inverse lattice spacing and at the same time it is a tool to evaluate observables non–perturbatively. While today the main aspect of lattice QCD is clearly in numerically obtaining phenomenological predictions from Monte Carlo simulations, one should not forget that in many cases the lattice is the only way to define a quantum field theory beyond perturbation theory.

As with any other regularization, the regulator has to be removed before results can be compared to experiment. On the lattice this means that the *continuum limit* has to be taken by making the lattice spacing a smaller and smaller. Here one encounters the usual ultraviolet divergencies, which require renormalization of the bare parameters and operators.

In numerical simulations the accessible lattice spacings are strongly constrained by the computer resources and the scaling behavior of the available algorithms. In fact, for a long time after the invention of lattice QCD, simulations were only possible in the *quenched approximation*. Here the observables are evaluated on a gauge background generated with the gauge action *only*, which in terms of Feynman diagrams amounts to removing all virtual quark lines. While this makes the simulations significantly easier, it does not represent a controlled approximation and thus (in principle) calls into question all physical predictions obtained in this way. Still, impressive results were obtained from quenched simulations and in particular the hadron spectrum is in rather good agreement with experiment [4].

With new computer generations and algorithmic improvements unquenched (or "dynamical") simulations are now possible at reasonable lattice spacings and volumes. However, these algorithms typically slow down proportional to a^7 (see e.g. [5]) or even worse, such that a factor two in lattice spacing can change the computational effort by more than two orders of magnitude. As a result a is usually varied only in a very limited range, say from $0.1\,\mathrm{fm}$ to $0.05\,\mathrm{fm}$ and hence close attention should be paid to how the observables of interest approach the continuum. Naturally, this is strongly influenced by the details of how the continuum theory was discretized.

Today there exists a large variety of discretizations of lattice QCD in addition to Wilson's original formulation, on which this work is based. These differ in both the discretization of the gauge and – more importantly – the fermionic action. A brief overview with emphasis on their different properties concerning chirality will be given in Chapter 4.

A systematic description of the approach to the continuum limit of a lattice theory was found by Symanzik [6, 7, 8]. The symmetries of the lattice action define a set of operators, which, if inserted in correlation functions of the continuum theory, asymptotically reproduce the discretization errors of the lattice theory. In other words, the lattice theory is described in terms of an effective low–energy ($\ll a^{-1}$) continuum theory, whose Lagrangian contains $(4+k)$–dimensional interaction terms with couplings proportional to a^k. On this basis one exploits the freedom to change the lattice discretization by irrelevant operators to remove the cutoff effects, i.e. the lattice artifacts, order by order in the lattice spacing.

This procedure is known as the Symanzik *improvement* programme and concerns both the action and the composite fields, i.e. for QCD in particular the quark bilinears. In this way the continuum limit can be "accelerated" and a smaller range of lattice spacings might be sufficient for a reliable extrapolation. The application of the improvement programme to Wilson fermions is a central part of this work and a first (general) discussion will be given in Chapter 3.

Renormalization is commonly discussed in the framework of perturbation theory, where divergencies in Feynman diagrams are removed e.g. through a subtraction prescription based on dimensional regularization. Due to the non–perturbative nature of the low–energy sector of QCD this approach is no longer sufficient in this case. As will be detailed in Chapter 8, a perturbative calculation of renormalization factors does not result in a controlled estimate of systematic errors of renormalized correlation functions at low energies.

When approaching the continuum, the bare parameters in the action have to be tuned such that a set of renormalized quantities is kept fixed. These can be mass ratios or otherwise defined renormalized couplings and their specific choice defines the renormalization scheme. In this context as well as for the additional renormalizations required for the composite fields we employ a finite volume scheme based on the Schrödinger functional first discussed in [9, 10]. Chapter 5 will provide the reader with the necessary background.

Despite its rich structure, some of the phenomenologically most relevant questions are not concerned with effects within QCD alone. In particular, one often considers QCD observables, which can be interpreted as matrix elements of the effective weak Hamiltonian between QCD bound states. A prominent example is the pion decay constant F_π, defined through the matrix element

$$\langle 0|A_\mu(0)|\pi\rangle = ip_\mu F_\pi \tag{1.1}$$

of the axial current between the vacuum and a pion state with momentum p. Regarded as an insertion of the effective weak Hamiltonian, it parameterizes the amplitude for a pion to decay into a lepton anti–neutrino pair through a virtual W boson. Here it is most evident how the renormalization and improvement of the axial current directly affect the physical result of a lattice estimate of F_π.

For quenched lattice QCD with Wilson fermions the renormalization factor [11] and improvement constant [12] of the axial current are known non–perturbatively. Both are obtained by enforcing the chiral symmetry of the underlying continuum theory at finite lattice spacing. The non–perturbative implementation for the case of lattice QCD with two degenerate flavors of Wilson quarks is the central part and the resulting renormalization factor and improvement coefficient are the main result of this work.

Another important application of the renormalized improved axial current is in the context of a programme to calculate the fundamental parameters of QCD from hadronic input parameters. In fact, the work presented here is an integral part of an effort to calculate renormalized quark masses from first principles. The former also constitute an essential ingredient in tests of the standard model.

With the same method as in the quenched case [13], the starting point for such a calculation is the current quark mass derived from the non–conservation of the axial current (PCAC relation). The renormalization of the pseudo–scalar density, which is also required in this context, has already been performed [14, 15] such that together with the results from this work all necessary tools are available.

Starting from a review of the most important properties of QCD (Chapter 2), which includes a derivation of the Ward–Takahashi identities associated with the chiral symmetry, we will turn to the peculiarities of the lattice formulation (Chapter 3) and discuss the continuum limit, renormalization and Symanzik improvement. This is followed by a chapter concerned with the status of chiral symmetry in different lattice discretizations (Chapter 4) with particular emphasis on Wilson fermions. The introductory part concludes with a presentation of the Schrödinger functional (SF) as a renormalization scheme and our chosen method to compute renormalization factors and improvement constants (Chapter 5). The necessary correlation functions and notation to be used are also introduced there.

The first chapter of the main part (Chapter 6) discusses Monte Carlo algorithms, data analysis and other technical aspects of our simulations. Algorithmic issues, which we faced in the numerical evaluation of the axial current normalization condition, are also reported. These problems are traced back to a distortion of the spectrum of the Wilson–Dirac operator, which in turn can be interpreted as a cutoff effect.

The remaining chapters are devoted to the non–perturbative axial current improvement (Chapter 7) and renormalization (Chapter 8). The former is implemented by requiring a current quark mass derived from a Ward identity to be independent of the external states, which are varied using projection techniques. The integrated axial Ward identity with operator insertions is used to formulate a normalization condition for the axial current on the lattice. Numerical results of our implementation are presented and summarized in interpolating formulae for future use.

Finally, the last chapter summarizes all results and discusses their possible application. In abbreviated form the findings of the present work have been published in [16, 17, 18, 19, 20].

Chapter 2

Continuum QCD

2.1 History and properties

Already in the 1960s it was conjectured that the observed large number of strongly interacting particles, the hadrons, are composite objects made from supposedly fundamental building blocks called *partons*. In the spirit of Rutherford's scattering experiments, which revealed the structure of the atom, hadrons were probed with beams of highly energetic leptons in order to learn about the underlying dynamics that govern the formation of partons into hadrons.

The most interesting experimental results came from the kinematic region of deep inelastic scattering, where both the momentum transfer q^2 and the energy transfer ν from the leptons are very large with the ratio q^2/ν fixed. As proposed by Bjorken in 1969 [1], in this region the structure functions, which parameterize the momentum distribution within the hadron, were found to depend only on the ratio q^2/ν (Bjorken scaling).

The easiest way to understand this behavior is to assume that the leptons scatter off almost-free pointlike particles, the constituents of the hadrons. To accommodate Bjorken scaling, the theory describing the dynamics of the partons should therefore have the feature that the interaction becomes weak at high energies (or small distances). The only known quantum field theories[1] with this property, which is now called *asymptotic freedom*, are the non–Abelian gauge theories introduced by Yang and Mills [21].

The working hypothesis is now that the interaction of the fundamental degrees of freedom – at this point renamed *quarks* by Gell-Mann – is described by a non–Abelian gauge theory.

At the same time experimental observations required the quarks to have an additional unobserved quantum number ("color") in order to avoid conflict with the Pauli exclusion principle. Most of the difficulties could be resolved by identifying the symmetry corresponding to the new quantum numbers with the non–

[1]More precisely: the only renormalizable quantum field theories in four dimension.

Abelian gauge symmetry. Further experimental input and theoretical arguments uniquely fixed the gauge group to be $SU(3)$. This theory was named quantum chromodynamics, QCD, and its gauge quanta are called gluons.

At this point one should note that it is the property of being asymptotically free that ensures the applicability of perturbation theory at high energies. One of the successes of perturbative QCD is the correct prediction of the (logarithmic) corrections to Bjorken scaling, which is now known to be strictly valid only in the limit of infinite energy.

In contrast to Abelian gauge theories like quantum electrodynamics, QED, the field quanta of non–Abelian theories also carry charge and thus interact among themselves. Indeed, perturbation theory shows that it is precisely this self–interaction, which is responsible for asymptotic freedom. The situation is opposite to the one found in QED, where perturbation theory predicts the effective charge of the electron to *increase* with energy.

We can now write down the Lagrangian density for the gluonic ($\mathcal{L}_g$) and fermionic ($\mathcal{L}_f$) part of QCD with $N_{\rm f}$ flavors of quarks.

$$\begin{aligned} \mathcal{L}_g &= -\tfrac{1}{2}\,\mathrm{Tr}\,F_{\mu\nu}F^{\mu\nu}\ , \\ \text{with the field strength}\ \ F_{\mu\nu} &= \partial_\mu A_\nu - \partial_\nu A_\mu + g_0[A_\mu, A_\nu]\ . \end{aligned} \tag{2.1}$$

Here g_0 is the bare gauge coupling and A_μ the Lie–algebra valued anti–Hermitian $SU(3)$ gauge field. For the fermionic part we have

$$\mathcal{L}_f = \sum_{f=1}^{N_{\rm f}} \bar\psi_f(i\not{D} - m_f)\psi_f\ , \tag{2.2}$$

with the gauge covariant derivative $\not{D} = \gamma_\mu(\partial_\mu + g_0 A_\mu)$ and the bare quark masses m_f. The two color indices of A_μ as well as the color and Dirac indices of $\bar\psi$ and ψ have been suppressed.

To account for the observed particle spectrum, hadron states and in general all physical observables are postulated to be color singlets. In this way an unobserved proliferation of states due to the color symmetry is prevented. This non–perturbative phenomenon (known as *confinement* of color) is ascribed to an increase of the force between color sources at long distances ($\simeq 1\,\mathrm{fm}$). Since, as a consequence, even at high interaction energies the initial and final states are subject to confinement, also perturbation theory is affected and hadronic matrix elements cannot be obtained using a purely perturbative treatment. This problem is usually addressed by factorizing them into a "hard" (perturbative) and a "soft" (non–perturbative) part using e.g. the operator product expansion (OPE). The soft part is then parameterized by effective couplings.

Lattice simulations of pure non–Abelian gauge theories show that for large distances the energy of two static color sources grows linearly with the so–called string tension $\sigma \simeq 1\,\mathrm{GeV/\,fm}$ (see e.g. [22]). Hence there is strong numerical evidence in support of the confinement hypothesis. However, an analytical first–principle explanation from the underlying dynamics is still missing although many attempts have been made, e.g. in terms of condensation of topological excitations [23].

Finally, the most important ingredient to understanding the strong interactions at low energies is *chiral symmetry.* For degenerate quarks the QCD Lagrangian (2.2) is flavor–blind and hence invariant under (global, i.e. space–time independent) unitary transformations of the $N_{\rm f}$–component fermion fields. In addition, for massless quarks there is also no coupling between the left– and right–handed field components

$$\psi_L = \tfrac{1}{2}(1-\gamma_5)\psi \quad \text{and} \quad \psi_R = \tfrac{1}{2}(1+\gamma_5)\psi \; . \tag{2.3}$$

Therefore separate $U(N_{\rm f})$ transformations of these fields according to

$$\left.\begin{array}{l}\psi_L \to U_L\psi_L \\ \psi_R \to U_R\psi_R\end{array}\right\} \quad \Rightarrow \quad \psi \to U_R\psi_R + U_L\psi_L \tag{2.4}$$

are also a symmetry of the massless QCD Lagrangian. These are usually written in terms of the vector and axial vector transformations

$$\begin{array}{lllll} U_R = U_L = U & \Rightarrow & \psi \to U\psi = \mathrm{e}^{i\omega^a\lambda^a}\psi & & \text{(vector)} \\ U_R = U_L^\dagger = U & \Rightarrow & \psi \to U_5\psi = \mathrm{e}^{i\omega^a\lambda^a\gamma_5}\psi & & \text{(axial)} \; . \end{array} \tag{2.5}$$

At the classical level this $U(N_{\rm f})_{\rm V}\times U(N_{\rm f})_{\rm A}$ symmetry gives rise to two conserved currents (the vector and the axial current) for each generator λ^a of $U(N_{\rm f})$,

$$\begin{array}{rcl} A^a_\mu & = & \bar\psi\gamma_\mu\gamma_5\lambda^a\psi \; , \\ V^a_\mu & = & \bar\psi\gamma_\mu\lambda^a\psi \; , \end{array} \tag{2.6}$$

where the λ^a act on the flavor indices of the fermion fields. To summarize, the concrete requirements for the $U(N_{\rm f})_{\rm V} \times U(N_{\rm f})_{\rm A}$ flavor chiral symmetry are that the Dirac operator is diagonal in flavor space and that it anti–commutes with γ_5.

Since the masses of the up and down quarks are much below typical hadronic energy scales, massless QCD with $N_{\rm f}=2$ seems to be a reasonable approximation of nature. In this case, the vector symmetry $SU(2)_{\rm V} \times U(1)_{\rm V}$ implies isospin symmetry and quark number conservation, which are indeed experimentally confirmed to a high precision.

The fact that the corresponding axial symmetries are not found in the strong interactions is believed to be due to a condensation of quark–antiquark pairs, such that these symmetries are spontaneously broken by the QCD vacuum. In this picture the isospin triplet of light pseudo–scalar mesons, the pions, become the quasi–Goldstone bosons of the spontaneously broken axial symmetry.[2] Their

[2] A direct proof of the Goldstone theorem for this case will be given in Section 8.1.

non–vanishing mass is explained by the fact that for small but non–zero quark mass the $SU(2)_{\mathrm{A}}$ is only an approximate symmetry and the pions are hence not true Goldstone bosons.

The identification of the pions as the Goldstone bosons of spontaneous chiral symmetry breaking leads to various relations between matrix elements, whose experimental verification helped in establishing this picture. A systematic study of the low–energy limit of QCD can be performed in the framework of *chiral perturbation theory* [24]. This is a low–energy effective theory of the strong interactions, where pions are introduced as fundamental degrees of freedom. The quark masses are treated as a perturbation to the chirally invariant Lagrangian.

In a somewhat worse approximation of nature this picture can be extended to three flavors if the strange quark mass is also neglected. The Ward–Takahashi identities resulting from the $SU(2)_{\mathrm{V}} \times SU(2)_{\mathrm{A}}$ symmetry of massless two–flavor QCD are derived in Section 2.3.

The conservation of the singlet axial current corresponding to the remaining $U(1)_{\mathrm{A}}$ symmetry is violated by quantum corrections, which are related to the topological structure of the QCD vacuum. This is known as the axial (or chiral) anomaly and is crucial in explaining the absence of an isosinglet pseudo–scalar meson with mass comparable to that of the pions. In the path integral formulation (see below) the anomaly can be understood from the fact that the $U(1)_{\mathrm{A}}$ transformation does not leave the integral measure invariant [25]. This is particularly transparent [26] in a lattice regularization using Ginsparg–Wilson fermions, which are invariant under a chiral symmetry, differing from (2.5) only at finite lattice spacing.

2.2 Euclidean path integral

While scalar field theories can be quantized efficiently in the operator language, for gauge theories it is more convenient to employ the functional integral (or path integral) formalism. In this approach the fundamental quantity is the generating functional

$$\mathcal{Z}[J] = \int_{\text{fields}} \exp\left\{ i \int \mathrm{d}^4x (\mathcal{L} + J \cdot \text{fields}) \right\} \,. \tag{2.7}$$

Correlation functions are generated by taking functional derivatives with respect to the sources $J(x)$ and perturbation theory is set up by expanding the (gauge fixed) action $S = \int \mathrm{d}x^4 \mathcal{L}$ around a saddle point. Feynman rules can essentially be read directly from the Lagrangian.

However, the functional integral is also the starting point for the so far most successful non–perturbative treatment of QCD, the lattice regularization. There the partition function $\mathcal{Z} = \mathcal{Z}[0]$ is evaluated directly using Monte Carlo methods. This approach requires a statistical interpretation of the path integral (2.7), where the phase factor $\exp(iS)$ becomes a Boltzmann weight. To achieve this the theory is transcribed from Minkowski to Euclidean space by introducing an imaginary time coordinate ("Wick rotation"). This formulation also reveals the deep connection between quantum field theories and statistical systems.

With a purely imaginary time coordinate the space–time metric becomes Euclidean. Under certain condition the Minkowskian correlation functions (the so–called Wightman functions) can be analytically continued into this region to obtain Euclidean correlation functions (Schwinger functions). From the more accessible Schwinger functions the physical Wightman functions in Minkowski space and thus the quantum field theory generated by (2.7) can be reconstructed.

In the path integral formulation the fermionic anti–commutation properties are accommodated through a representation of the fields ψ and $\bar{\psi}$ as Grassmann variables. The integral over the fields is therefore a Grassmann integral for the fermionic part. On the lattice the gauge fields are represented by compact link variables (see Chapter 3) such that the path integral is then defined in terms of the Haar measure on the gauge group.

The QCD fermion action for one quark flavor in its Euclidean form is given by

$$\begin{aligned} S &= \int \mathrm{d}^4x\, \bar{\psi}(\gamma_\mu D_\mu + m_0)\psi, \;, && (2.8)\\ \text{where} \quad D_\mu &= \partial_\mu + g_0 A_\mu \;. && (2.9) \end{aligned}$$

Before the properties of the Euclidean lattice formulation as a non–perturbative regulator are discussed in Chapter 3, where for simplicity the case of a pure gauge theory is considered, we will derive the Ward identities associated with the *local* versions of the transformations (2.5).

2.3 Current algebra and continuum Ward identities

For the two–flavor case ($\lambda^a = \tau^a/2$ with the Pauli matrices τ^a) the infinitesimal chiral transformations are written as

$$\text{vector} \quad \begin{cases} \psi & \rightarrow \quad \psi + i\omega^a \cdot \frac{1}{2}\tau^a\psi \\ \bar{\psi} & \rightarrow \quad \bar{\psi} - i\omega^a \cdot \bar{\psi}\frac{1}{2}\tau^a \;, \end{cases} \qquad (2.10)$$

$$\text{axial} \quad \begin{cases} \psi & \rightarrow \quad \psi + i\omega^a \cdot \frac{1}{2}\tau^a\gamma_5\psi \\ \bar{\psi} & \rightarrow \quad \bar{\psi} + i\omega^a \cdot \bar{\psi}\gamma_5\frac{1}{2}\tau^a \;. \end{cases} \qquad (2.11)$$

We define the vector and axial variations of (composite) fields $\mathcal{O}$ through $\mathcal{O} \rightarrow \mathcal{O} + i\delta\mathcal{O}$, with

$$\delta_V\mathcal{O} = \omega^a\delta_V^a\mathcal{O} \quad \text{and} \quad \delta_A\mathcal{O} = \omega^a\delta_A^a\mathcal{O} \;, \qquad (2.12)$$

where (in case of a local transformation) ω^a is evaluated at the space–time point where $\mathcal{O}$ lives. For the quark fields we obtain

$$\delta_V^a \psi(x) = \tfrac{1}{2}\tau^a \psi(x), \quad \delta_V^a \bar{\psi}(x) = -\bar{\psi}(x)\tfrac{1}{2}\tau^a \,, \tag{2.13}$$

$$\delta_A^a \psi(x) = \tfrac{1}{2}\tau^a \gamma_5 \psi(x), \quad \delta_A^a \bar{\psi}(x) = \bar{\psi}(x)\gamma_5 \tfrac{1}{2}\tau^a \,. \tag{2.14}$$

These can be used to calculate the variation of arbitrary expressions $\mathcal{O}$ built from the basic fields by treating δ_V^a and δ_A^a as first order differential operators. In particular, for the variations of the isospin vector and axial vector currents,

$$V_\mu^a(x) = \bar{\psi}(x)\gamma_\mu \tfrac{1}{2}\tau^a \psi(x), \qquad A_\mu^a(x) = \bar{\psi}(x)\gamma_\mu\gamma_5 \tfrac{1}{2}\tau^a \psi(x), \tag{2.15}$$

one obtains for example

$$\begin{aligned}
\delta_A^a V_\mu^b &= \frac{\partial V_\mu^b}{\partial \psi}\delta_A^a \psi + \delta_A^a \bar{\psi}\,\frac{\partial V_\mu^b}{\partial \bar{\psi}} \\
&\overset{(2.15)}{=} \bar{\psi}\gamma_\mu \tfrac{1}{2}\tau^b \delta_A^a \psi + \delta_A^a \bar{\psi}\gamma_\mu \tfrac{1}{2}\tau^b \psi \\
&\overset{(2.14)}{=} \bar{\psi}\gamma_\mu \tfrac{1}{2}\tau^b \tfrac{1}{2}\tau^a \gamma_5 \psi + \bar{\psi}\gamma_5 \tfrac{1}{2}\tau^a \gamma_\mu \tfrac{1}{2}\tau^b \psi \\
&= \bar{\psi}\gamma_\mu [\tfrac{\tau^b}{2}, \tfrac{\tau^a}{2}]\gamma_5 \psi = -i\epsilon^{abc} A_\mu^c \,,
\end{aligned}$$

since the generators of $SU(2)$ satisfy the algebra

$$[\tfrac{\tau^a}{2}, \tfrac{\tau^b}{2}] = \tfrac{\tau^a}{2}\tfrac{\tau^b}{2} - \tfrac{\tau^b}{2}\tfrac{\tau^a}{2} = i\epsilon^{abc}\tfrac{\tau^c}{2} \,.$$

Calculating all variations using $\{\gamma_\mu, \gamma_5\} = 0$ it is easily verified that the currents form a closed algebra

$$\delta_V^a V_\mu^b(x) = -i\epsilon^{abc} V_\mu^c(x), \qquad \delta_A^a V_\mu^b(x) = -i\epsilon^{abc} A_\mu^c(x) \,, \tag{2.16}$$

$$\delta_V^a A_\mu^b(x) = -i\epsilon^{abc} A_\mu^c(x), \qquad \delta_A^a A_\mu^b(x) = -i\epsilon^{abc} V_\mu^c(x) \,. \tag{2.17}$$

The Ward identities associated with the chiral symmetry of the action are now derived by performing local infinitesimal transformations of the quark and anti-quark fields in the Euclidean functional integral.

2.3.1 Variation of the action

The starting point is the Euclidean fermion action (2.8) for two quark flavors, where now m_0 is a diagonal 2×2 matrix in isospin space. We perform *local* infinitesimal variations of the fermionic fields and study their effect on the classical QCD action. These variations are parameterized by $\omega^a(x)$ with support in a space-time region $\mathcal{R}$. The isospin vector variation of the fermionic action is

$$\begin{aligned}
\delta_V S &= \int_{\mathcal{R}} \mathrm{d}^4 x \left[(\delta_V \bar{\psi})(\gamma_\mu D_\mu + m_0)\psi + \bar{\psi}(\gamma_\mu D_\mu + m_0)\delta_V \psi \right] \\
&\overset{(2.13)}{=} \int_{\mathcal{R}} \mathrm{d}^4 x \left[-\omega^a \bar{\psi}\tfrac{1}{2}\tau^a(\gamma_\mu \partial_\mu + m_0)\psi + \bar{\psi}(\gamma_\mu \partial_\mu + m_0)\omega^a \tfrac{1}{2}\tau^a \psi \right] ,
\end{aligned}$$

where the terms containing the gauge fields A_μ canceled. Performing a partial integration of the second expression, which does not give boundary terms since the variation vanishes outside the region $\mathcal{R}$, yields

$$\begin{aligned}
\delta_V S &= \int_{\mathcal{R}} \mathrm{d}^4x\, \omega^a \Big[-\bar\psi \tfrac{1}{2}\tau^a[\gamma_\mu\partial_\mu + m_0]\psi - \Big[\gamma_\mu(\partial_\mu\bar\psi) - m_0\Big]\tfrac{1}{2}\tau^a\psi\Big] \\
&= \int_{\mathcal{R}} \mathrm{d}^4x\, \omega^a \Big[-\partial_\mu\left(\bar\psi\tfrac{1}{2}\tau^a\gamma_\mu\psi\right) - \bar\psi\,[\tfrac{1}{2}\tau^a, m_0]\,\psi\Big] \\
&\overset{(2.15)}{=} \int_{\mathcal{R}} \mathrm{d}^4x\, \omega^a(x) \Big[-\partial_\mu V^a_\mu(x) - \bar\psi(x)\,[\tfrac{1}{2}\tau^a, m_0]\,\psi(x)\Big] . \qquad (2.18)
\end{aligned}$$

In the case of degenerate quarks m_0 is proportional to the unit matrix and hence the commutator with τ^a vanishes.

In the same way the isospin axial vector variation of the action can be computed using the anti-commutator $\{\gamma_\mu, \gamma_5\} = 0$. Since in (2.14) the variations of ψ and $\bar\psi$ appear with the same sign, the mass now results in an anti–commutator term. Again performing a partial integration of the second term results in

$$\begin{aligned}
\delta_A S &\overset{(2.14)}{=} \int_{\mathcal{R}} \mathrm{d}^4x \left[\omega^a\bar\psi\gamma_5\tfrac{1}{2}\tau^a\left(\gamma_\mu\partial_\mu + m_0\right)\psi + \bar\psi\left(\gamma_\mu\partial_\mu + m_0\right)\omega^a\tfrac{1}{2}\tau^a\gamma_5\psi\right] \\
&= \int_{\mathcal{R}} \mathrm{d}^4x\, \omega^a(x) \Big[-\partial_\mu A^a_\mu(x) + \bar\psi(x)\gamma_5\{\tfrac{1}{2}\tau^a, m_0\}\psi(x)\Big] .
\end{aligned}$$

For two degenerate quarks this expression becomes

$$\delta_A S = \int_{\mathcal{R}} \mathrm{d}^4x\, \omega^a(x)\Big[-\partial_\mu A^a_\mu(x) + 2m_0 P(x)\Big] , \qquad (2.19)$$

with the pseudo-scalar density

$$P^a(x) = \bar\psi(x)\gamma_5\tfrac{1}{2}\tau^a\psi(x) . \qquad (2.20)$$

2.3.2 Ward identities

Through a formal manipulation of the functional integral the expectation value of the variation of an operator can be related to that of the action. Later we will discuss how such relations are realized in the regularized quantum theory. If the fermion integration measure is denoted by $\mathcal{D}\psi$, we have for a linear transformation of the Grassmann fields [3]

$$\begin{aligned}
&\psi' = A\psi \qquad \bar\psi' = \bar\psi\bar A \\
\Rightarrow \quad &[\mathcal{D}\bar\psi\mathcal{D}\psi] = \det\bar A\det A[\mathcal{D}\bar\psi'\mathcal{D}\psi'] = J^{-1}[\mathcal{D}\bar\psi'\mathcal{D}\psi'] . \qquad (2.21)
\end{aligned}$$

[3] The rules of Grassmann integration imply that the Jacobian is the *inverse* of what one would expect from bosonic integrals, hence the appearance of J^{-1} in (2.21).

Using $\det(1+\omega X) = 1+\omega\mathrm{Tr}\,X+\mathrm{O}(\omega^2)$, one obtains for the infinitesimal versions of the isovector transformations (2.10) and (2.11)

$$\begin{aligned} \text{vector} \qquad J &= 1 + \mathrm{O}(\omega^2) && (2.22)\\ \text{axial} \qquad J &= 1 + i\omega^a \mathrm{Tr}\,(\tau^a\gamma_5) + \mathrm{O}(\omega^2)\ . && (2.23) \end{aligned}$$

Since the Pauli matrices are traceless, the Jacobian is unchanged for both isovector transformations and one can perform the infinitesimal variable transformation in the path integral according to

$$\begin{aligned} \mathcal{Z} = \int_{\text{fields}} e^{-S} \quad \Rightarrow \quad \langle\mathcal{O}\rangle &= \mathcal{Z}^{-1}\int_{\text{fields}} \mathcal{O}\, e^{-S} = \mathcal{Z}^{-1}\int_{\text{fields}} (\mathcal{O}+\delta\mathcal{O})\, e^{-S}(1-\delta S)\\ &= \langle\mathcal{O}\rangle + \langle\delta\mathcal{O}\rangle - \langle\mathcal{O}\delta S\rangle\\ \Rightarrow \quad \langle\delta\mathcal{O}\rangle &= \langle\mathcal{O}\delta S\rangle\ . \end{aligned} \tag{2.24}$$

We can now derive the integrated Ward identities associated with the flavor chiral symmetry of the theory with two degenerate quarks. To this end we insert the vector (2.18) and axial (2.19) variations into (2.24). Choosing there an operator $\mathcal{O}_{\text{ext}}$ (for *ext*ernal) with support only outside the region $\mathcal{R}$, where we perform the transformations, the left–hand side of eq. (2.24) vanishes and we have

$$\begin{aligned} 0 &= \int_{\mathcal{R}} \mathrm{d}^4x\, \omega^a(x)\Big\langle -\partial_\mu V^a_\mu(x)\,\mathcal{O}_{\text{ext}}\Big\rangle && (2.25)\\ \text{and}\quad 0 &= \int_{\mathcal{R}} \mathrm{d}^4x\, \omega^a(x)\Big\langle [-\partial_\mu A^a_\mu(x) + 2m_0 P(x)]\,\mathcal{O}_{\text{ext}}\Big\rangle\ . && (2.26) \end{aligned}$$

These hold for any variation $\omega^a(x)$ and one can thus conclude that the expectation value multiplying it vanishes. This gives the vector current conservation in the form

$$\langle\partial_\mu V^a_\mu(x)\mathcal{O}_{\text{ext}}\rangle = 0\ , \tag{2.27}$$

and for the isovector axial current one has the PCAC (*p*artial *c*onservation of the *a*xial *c*urrents) relation

$$\langle\partial_\mu A^a_\mu(x)\mathcal{O}_{\text{ext}}\rangle = 2m_0\langle P^a(x)\mathcal{O}_{\text{ext}}\rangle\ . \tag{2.28}$$

Both are valid for operators $\mathcal{O}_{\text{ext}}$ not located at the point x. Integrated Ward identities with non–trivial operator insertions will be derived in Section 8.1 to be used in the normalization conditions for the vector and axial currents in the lattice regularization with Wilson fermions.

2.3.3 Anomalous symmetries

Since the quantized theory requires a regularization, it is not immediately obvious how e.g. the above relations have to be interpreted. If a symmetry is preserved in the quantum theory, this implies that it is either unbroken by the regulator or is recovered in the limit where the latter is removed. Perturbation theory shows that this is the case for the isovector symmetries discussed above. In Chapter 8 we will see that in a specific lattice formulation of the theory the above relations can be made to hold up to (small) lattice corrections. This can be interpreted as showing that even beyond perturbation theory the isovector symmetries are preserved in the quantized theory.

A transformation is called *anomalous* if it is a symmetry of the classical theory (i.e. the unregulated action), but not of the quantum theory. Depending on the chosen regularization, an anomaly can arise in different ways. One possibility is that the integration measure of the functional integral is not invariant under the transformation. If such a transformation is parameterized by an infinitesimal ω, we can write the Jacobian as $J = 1 + i\omega\delta J$ and instead of (2.24) one then has

$$\langle \delta\mathcal{O} \rangle = \langle \mathcal{O}\delta S \rangle + \langle \mathcal{O}\delta J \rangle \; . \tag{2.29}$$

It can also happen that a symmetry is broken by the regulator in such a way that it is not recovered in the renormalized theory. To illustrate these points we consider the iso*singlet* transformations

$$\begin{array}{lll} \text{vector} & \delta_V\psi = \psi \; , & \delta_V\bar{\psi} = -\bar{\psi} \; , \\ \text{axial} & \delta_A\psi = \gamma_5\psi \; , & \delta_A\bar{\psi} = \bar{\psi}\gamma_5 \; . \end{array} \tag{2.30}$$

For those eq. (2.22) is still true and in fact the $U(1)_{\mathrm{V}}$ (quark number conservation) is preserved in the quantized theory. For the axial transformation, instead of (2.23) we obtain for the Jacobian $\delta J = 2\mathrm{Tr}\,\gamma_5$.

The axial anomaly mentioned in the introduction has the non–conservation of the isosinglet axial current $A_\mu = \bar{\psi}\gamma_\mu\gamma_5\psi$ even at vanishing quark mass as a *physical* consequence. Therefore any admissible regularization of QCD needs to be able to reproduce it correctly. This can happen through a non–trivial redefinition of γ_5, i.e. for (2.30) to be a symmetry of the regularized action one has to replace γ_5 with some $\hat{\gamma}_5$. This is the case for dimensional regularization or Ginsparg–Wilson fermions (see Section 4.1), where the anomaly comes from δJ in (2.29) according to ($m = 0$)

$$\langle \partial_\mu A_\mu(x)\mathcal{O}_{\mathrm{ext}} \rangle = 2\langle \mathcal{O}_{\mathrm{ext}}\mathrm{Tr}\,\hat{\gamma}_5 \rangle \; . \tag{2.31}$$

Alternatively, the anomaly can arise from an explicit chiral symmetry breaking by the regulator, such that the iso*vector* axial symmetry is recovered in the renormalized theory, but the $U(1)_{\mathrm{A}}$ is not. This the case in a lattice regularization with Wilson fermions, where the anomaly can be understood as coming from the chiral variation of the Wilson term (see Section 4.2).

Chapter 3

Gauge theories on the lattice

Consider a field theory with a matter field $\psi^i(x)$, where x is the space–time coordinate and i refers to some internal degree of freedom. The requirement that one should be able to choose the basis to describe this internal degree of freedom independently on every space–time point results in the principle of *local gauge invariance*. To achieve this, the matter fields need to be coupled to a *gauge field* $A^{ij}_\mu(x)$, which takes care of the basis transformation between different (but infinitesimally close) space–time points ("parallel transporter"). This is done via the "minimal coupling prescription", which replaces the derivative ∂_μ with the covariant derivative $D_\mu = (\partial_\mu + g_0 A_\mu)$ such that $D_\mu\psi$ has the same properties under local basis transformations (*gauge transformations*) as ψ itself. For the case of QCD the internal degree of freedom of the quark fields ψ is that of "color" and i is the index of the fundamental (3) representation of $SU(3)$ ($\bar{\psi}$ is in the $\bar{3}$ representation). The anti–Hermitian gauge fields are conventionally parameterized as

$$A^{ij}_\mu = \sum_a i\mathrm{A}^a_\mu(\lambda_a)_{ij} \ , \tag{3.1}$$

where λ_a are the eight generators of $SU(3)$ (Gell-Mann matrices). The trace of the square of the local field strength (2.1) is the only term that can be made from the gauge fields that is gauge–invariant, has mass–dimension four or less and is compatible with time–reversal, charge–conjugation and parity. The geometric interpretation of the field strength tensor $F_{\mu\nu}$ is the local curvature in color space as obtained by connecting color bases around an infinitesimal square in the μ–ν–plane.

In the discrete theory the matter fields are defined on the sites of the lattice and to gauge connect those we always need parallel transporters for *finite* distances. It is therefore more natural to describe the gauge degrees of freedom in terms of *link variables* $U_\mu(x) \in SU(3)$. These are the path–ordered exponentials of the integral of (3.1) from x along the link of length a to the next lattice site in the μ direction. The variable $U_\mu(x)$ is thus associated with this link and by definition the link in the opposite direction is its inverse $U_{-\mu}(x+\hat{\mu}) = U^\dagger_\mu(x)$, where

$\hat{\mu}$ is a vector of length a in the μ direction. Under a local gauge transformation $\Lambda(x) \in SU(3)$ the links and quark fields transform as

$$\begin{aligned} U_\mu(x) &\xrightarrow{\Lambda} \Lambda(x)U_\mu(x)\Lambda(x+\hat{\mu})^\dagger \\ \psi(x) &\xrightarrow{\Lambda} \Lambda(x)\psi(x) \\ \bar{\psi}(x) &\xrightarrow{\Lambda} \bar{\psi}(x)\Lambda(x)^\dagger , \end{aligned} \tag{3.2}$$

such that

$$\begin{aligned} \nabla_\mu\psi(x) &= \tfrac{1}{a}[U_\mu(x)\psi(x+\hat{\mu}) - \psi(x)] \\ \nabla^\star_\mu\psi(x) &= \tfrac{1}{a}[\psi(x) - U^\dagger_\mu(x-\hat{\mu})\psi(x-\hat{\mu})] \\ \widetilde{\nabla}_\mu\psi(x) &= \tfrac{1}{2}(\nabla_\mu+\nabla^\star_\mu)\psi(x) \end{aligned} \tag{3.3}$$

define covariant derivatives on the lattice. Normal lattice derivatives ∂_μ, $\partial^\star_\mu$ and $\tilde{\partial}_\mu$ are defined by setting $U_\mu \equiv 1$ in eqs. (3.3).

On the lattice the field strength is measured by tracing the gauge links around closed loops and hence the simplest admissible lattice gauge action is Wilson's plaquette action

$$S_g[U] = \frac{1}{g_0^2}\sum_p \mathrm{Tr}\ \{1 - U_p\} , \tag{3.4}$$

where p runs over all oriented elementary plaquettes (1×1 loops) and U_p is the product of the gauge links around a plaquette

$$U_p(x) = U_{x;\mu,\nu} = U_\mu(x)\cdot U_\nu(x+\hat{\mu})\cdot U^\dagger_\mu(x+\hat{\nu})\cdot U_\nu(x)^\dagger , \tag{3.5}$$

$$U_p(x) \xrightarrow{\Lambda} \Lambda(x)U_p(x)\Lambda(x)^\dagger . \tag{3.6}$$

For gauge group $SU(N)$ the bare gauge coupling is commonly expressed through $\beta = 2N/g_0^2$. A small a expansion of the gauge links in terms of the gauge fields gives

$$U_{x;\mu,\nu} = 1 + a^2 F_{\mu\nu} + \frac{a^4}{2}F^2_{\mu\nu} + \ldots \tag{3.7}$$

such that the sum over oriented plaquettes in (3.4) reduces to the Yang–Mills action (2.1). In fact this is true for any lattice action of the form (3.4) composed of closed loops of gauge links. Improved gauge actions (see Section 3.3) can thus be defined by adding more extended loops with suitably chosen coefficients [27, 28] to (3.4).

3.1 Monte Carlo integration

To obtain the expectation value of a gauge–invariant observable $F[U]$ in the quantum field theory described by (3.4) we need to evaluate the integral

$$\langle F\rangle = \frac{1}{\mathcal{Z}}\int\mathcal{D}U\ F[U]\mathrm{e}^{-S[U]} \quad \text{with} \quad \mathcal{Z} = \int\mathcal{D}U\ \mathrm{e}^{-S[U]} , \tag{3.8}$$

where $\mathcal{D}U$ denotes the product of the $SU(3)$ Haar measures for all links on the lattice. For a 4–dimensional lattice of linear extension L there are $4{\cdot}(L/a)^4$ links, which in typical simulations is of order 10^5 or larger. The only way to evaluate such high–dimensional integrals is using Monte Carlo techniques.

To this end one generates gauge link configurations U_i that are distributed with a probability $P_i \propto \mathcal{D}U_i \mathrm{e}^{-S[U_i]}$ (importance sampling). The integral (3.8) is then statistically approximated by

$$\langle F \rangle = \frac{1}{N} \sum_{i=1}^{N} F[U_i] + \mathrm{O}\Big(\frac{1}{\sqrt{N}}\Big) \ . \tag{3.9}$$

Unless a *global* heatbath algorithm is available for the system one wants to simulate, configurations are produced by an algorithm that updates a given configuration to obtain the next one (Markov chain). Configurations generated in this way are not statistically independent and therefore *autocorrelation* effects need to be taken into account in the data analysis.

For the case of pure gauge actions (or equivalently in quenched QCD) the local heatbath [29, 30] is an efficient algorithm to generate correctly distributed ensembles of gauge configurations and lattice sizes up to $L/a = \mathrm{O}(10^2)$ are possible today. When the correlation lengths in the system become large, autocorrelation along the Markov chain increases and the algorithm rapidly becomes inefficient (critical slowing down). This can be countered by adding (microcanonical) overrelaxation updates [31] to the heatbath algorithm.

If we want to consider full QCD, the fermionic part needs to be treated analytically because the Grassmann–valued quark fields cannot be handled in a computer simulation. Since the fermion action is bilinear in the quark fields, the Grassmann integral can be performed and for the partition function one gets ($M = D + m$)

$$\begin{aligned} \mathcal{Z} &= \int \mathcal{D}U \mathcal{D}\bar{\psi} \mathcal{D}\psi \, \mathrm{e}^{-S_g[U] - \bar{\psi} M[U] \psi} && (3.10) \\ &\propto \int \mathcal{D}U \ \det M[U] \mathrm{e}^{-S_g[U]} \ . && (3.11) \end{aligned}$$

In the path integral for an observable $O(U, \psi, \bar{\psi})$ this integration of the fermionic fields results in a new observable $\widetilde{O}(U)$, which depends only on the gauge field (Wick contraction). Instead of the fermion fields $\widetilde{O}$ contains matrix elements of the fermion propagator $S = M^{-1}$ and as a consequence it can be a very complicated and non–local function of U. For the "pion–pion" correlator $(\bar{\psi}\gamma_5\psi)_x(\bar{\psi}\gamma_5\psi)_y$ one obtains e.g.

$$\begin{aligned} &\langle (\bar{\psi}\gamma_5\psi)_x(\bar{\psi}\gamma_5\psi)_y \rangle = \\ &\frac{1}{\mathcal{Z}} \int \mathcal{D}U \Big(\mathrm{Tr}\,\{S_{xx}[U]\gamma_5\} \mathrm{Tr}\,\{S_{yy}[U]\gamma_5\} \\ &\qquad - \mathrm{Tr}\,\{S_{xy}[U]\gamma_5 S_{yx}[U]\gamma_5\} \Big) \det M[U] \mathrm{e}^{-S_g[U]} \ , \end{aligned} \tag{3.12}$$

where the trace is taken over Dirac indices. Algorithms for simulating full QCD, i.e. the generation of a gauge ensemble according to $\mathcal{D}U\,\det M[U]\mathrm{e}^{-S_g[U]}$, will be discussed in detail in Chapter 6.

3.2 Continuum limit and renormalization

As already mentioned, the regulator has to be removed before physical predictions can be made. In the statistical analogy the mass (in lattice units) $a\cdot m$ of the lowest–lying state (e.g. the 0^{++} glueball for a pure gauge theory) corresponds to the inverse correlation length of the statistical system. Usually masses are obtained from the exponential decay of suitable correlation functions.

If a continuum limit with a finite physical mass exists, it means that by tuning the bare parameters (β in pure gauge theory) we can find a limit, where $a{\cdot}m$ goes to zero, while a physical quantity like a mass ratio am_1/am_2 remains finite. Thus the continuum limit of the lattice field theory corresponds to a critical point (second order phase transition) of a statistical system. When approaching the continuum, one has to increase L/a such that the correlators are not affected by finite–size effects. If one is interested in the continuum limit of explicit finite–volume quantities, $L{\cdot}m$ has to be kept fix as a goes to zero.

In practice one picks one observable with small variance to *set the scale*, i.e. other observables are expressed in units of this one. For $SU(3)$ gauge theory and also QCD the most commonly used quantity is the hadronic length scale r_0 [32], defined through the force $F(r)$ between two static color sources. More precisely, r_0 is the distance where

$$1.65 = r^2 F(r)\Big|_{r=r_0} \,. \tag{3.13}$$

The choice of the constant 1.65 is based on phenomenological quark potential models, where the distance r_0 defined in this way corresponds to approximately 0.5 fm. Assigning physical units to lattice results in this way introduces large systematic errors due to uncertainty in the physical value of r_0, but as long as results are expressed in terms of r_0 this provides a well–defined way to compare lattice results from different actions and/or lattice spacings. For the simple plaquette gauge action the value of r_0/a is known quite precisely for the relevant range of β values [33].

While this amounts to a non–perturbative determination of $a(\beta)$, the evolution $a\cdot\partial g_0/\partial a$ can also be calculated in perturbation theory. The result is valid for g_0 going to zero and predicts an exponential decrease of the lattice spacing as g_0 vanishes (*asymptotic scaling*). Thus the continuum limit is obtained by sending g_0 to zero, or equivalently β to infinity. As will be detailed in the next section, physical observables approach their continuum values with powers of the lattice spacing a such that in practice a small range of β values is generally sufficient for a reliable continuum extrapolation.

The situation in full QCD is more complicated since additional dimensionful parameters are present in the form of the quark masses. These have to be tuned such that in the $\beta \to \infty$ limit a corresponding number of renormalized quantities is kept constant. If a lattice regularization with (at least remnant) chiral symmetry is employed, a massless continuum limit is obtained by simply setting the bare quark masses to zero at each value of β. In other cases (e.g. Wilson fermions, see Section 4.2) additive mass renormalization requires that one finds a line in bare parameter space, where a suitable defined quark mass (i.e. through the PCAC relation) vanishes.

3.3 Symanzik improvement

A very insightful way of looking at the continuum limit of a lattice field theory is due to Symanzik [6, 7, 8]. Instead of taking the lattice as something that approximates a continuum theory, he turns the tables and declares the discretized theory *at finite cutoff* to be the main object of interest. One can then construct a new theory in the continuum that asymptotically describes the lattice theory.

More precisely, the discretization effects are modeled [34] by adding higher–dimensional interaction terms (accompanied by powers of the lattice spacing) to the original continuum action

$$S_{\mathrm{eff}} = \int \mathrm{d}^4 x \Big\{ \mathcal{L}_0(x) + a\mathcal{L}_1(x) + a^2\mathcal{L}_2(x) + \dots \Big\} . \tag{3.14}$$

Here $\mathcal{L}_0$ is the continuum QCD Lagrangian and the terms $\mathcal{L}_1, \mathcal{L}_2, \dots$ are linear combinations of those local operators, which The coefficients a, a^2, …are additional couplings with negative mass dimension, which renders the theory described by (3.14) non–renormalizable by power–counting. However, we are not interested in the renormalization of these "new couplings". Instead (3.14) is treated as an effective theory to finite order in the latter (but to all orders in g_0^2) and is thus renormalizable order by order in a. It is in this sense that renormalized correlation functions are matched between the lattice at finite cutoff and the effective continuum theory.

This is analogous to the phenomenological approach of describing yet undetected substructures or the effects of heavy particles through higher–dimensional interaction terms. The most prominent example is probably Fermi's current–current interaction that approximates two weak–interaction vertices connected by the propagator of a W boson. In the low–energy limit $E \ll m_W$, the W-propagator can be neglected and Fermi's description becomes exact.

In this sense the additional terms in Symanzik's low–energy effective theory (3.14) represent "new physics" (namely the lattice artifacts) entering at a scale of a^{-1}. Naturally, this description can be valid only for energies small compared to the cutoff, i.e. lattice spacings fine compared to hadronic length scales.

In order to study how correlation functions approach their continuum limit, one also has to represent renormalized (composite) lattice fields in the effective theory. These effective fields

$$\phi_{\text{eff}} = \phi_0 + a\phi_1 + a^2\phi_2 + \ldots \tag{3.15}$$

are given as a sum of terms of increasing mass dimension that have the same lattice symmetries as the (composite) lattice field to be represented.

With the help of the effective continuum theory the connected renormalized n–point lattice correlation function

$$G_n(x_1, \ldots, x_n) = (Z_\phi)^n \langle \phi(x_1) \ldots \phi(x_n) \rangle_{\text{con}} \tag{3.16}$$

can be written in terms of expectation values with the QCD Lagrangian only

$$\begin{aligned} G_n(x_1, \ldots, x_n) \quad = \quad & \langle \phi_0(x_1) \ldots \phi_0(x_n) \rangle_{\text{con}} \\ & -a \int \mathrm{d}^4 y \langle \phi_0(x_1) \ldots \phi_0(x_n) \mathcal{L}_1(y) \rangle_{\text{con}} \\ & +a \sum_{k=1}^{n} \langle \phi_1(x_0) \ldots \phi_1(x_k) \ldots \phi_0(x_n) \rangle_{\text{con}} + \mathrm{O}(a^2) \ . \end{aligned} \tag{3.17}$$

The higher–dimensional terms from the action and the composite field now appear as operator insertions, thus explicitly showing the origin of the lattice artifacts. If the symmetries of the lattice action in question are such that the terms $\mathcal{L}_1$ and ϕ_1 are forbidden, correlation functions will approach the continuum with a rate proportional to a^2. This is the case for the lattice chiral symmetry of Ginsparg–Wilson fermions, which will be discussed in Section 4.1.

The Symanzik improvement programme aims at a removal of the lattice artifacts of a given action order by order in the lattice spacing. This is done by modifying the lattice action and composite fields such that the terms $\mathcal{L}_k$ and ϕ_k in the effective continuum theory vanish up to a fixed order k. If e.g. $\mathcal{L}_1$ is a linear combination of operators $\mathcal{O}_i$, improvement (of the action) to order a can be achieved by adding a term $\sum c_i \widehat{\mathcal{O}}_i$ to the action, where $\widehat{\mathcal{O}}_i$ is a lattice representation of $\mathcal{O}_i$ and c_i are suitably chosen chosen improvement coefficients. The same procedure is also applied to the fields ϕ.

While in principle the improvement programme can be applied to arbitrary orders in the lattice spacing, in practice the increasing number of possible improvement terms limits its application to a cancellation of the cutoff effects linear in the lattice spacing. For Wilson fermions $\mathrm{O}(a)$ improvement of the action and the isovector currents and densities will be discussed at the end of Section 4.2.

Chapter 4

Lattice QCD

In the path integral formulation fermions are represented by two Grassmann–valued fields, ψ and $\bar{\psi}$. On the lattice these become an assignment of $\bar{\psi}$ and ψ to each lattice site $x_\mu = an_\mu$, $n_\mu \in \mathbb{N}^4$. They carry color $(\alpha, \beta, \ldots)$ and Dirac $(A, B, \ldots)$ indices. A lattice action S combines the two lattice vectors into a scalar and is hence defined in terms of a matrix $M = D + m_0$, where D is the lattice Dirac operator and m_0 the bare quark mass

$$S = \sum_{x,y;\alpha,\beta;A,B} \bar{\psi}(x)^\alpha_A M(x,y)^{\alpha\beta}_{AB} \psi(y)^\beta_B \; . \tag{4.1}$$

In the following several choices for D will be discussed and in particular we will see which properties of the continuum Dirac operator $\gamma_\mu D_\mu$ can be preserved on the lattice.

4.1 Chiral symmetry on the lattice

As we have seen in Chapter 2, the global chiral symmetry is a central aspect of continuum QCD. Unfortunately it also seems to be the symmetry that is most difficult to obtain in a lattice formulation. In their 1981 paper [35] Nielson and Ninomiya gave a mathematical foundation to this finding. If we denote the Fourier space representation of the translation–invariant Dirac operator D by $\widetilde{D}(p)$, the famous Nielson–Ninomiya no–go theorem states [26] that there is no lattice Dirac operator that simultaneously has *all* of the following properties.

- [**locality**] $\widetilde{D}(p)$ is analytic in the momenta p_μ with period $2\pi/a$,
- [**small p limit**] For small momenta $\widetilde{D}(p)$ behaves like $i\gamma_\mu p_\mu + \mathrm{O}(ap^2)$,
- [**no doublers**] $\widetilde{D}(p)$ is invertible at all non–zero momenta (mod $2\pi/a$),
- [**chirality**] D anti–commutes with γ_5.

The first condition ensures that D is an essentially local operator, i.e. that in position space the coupling between sites decreases exponentially with their distance. Obviously the small momentum and invertibility conditions are required to obtain a continuum limit with the right number of particles and the correct dispersion relation. Finally, the last condition guarantees the invariance under the chiral transformations discussed at the end of Section 2.1. The violations of these properties are useful to classify the various fermion discretizations.

Directly transcribing the continuum action (2.8) on a space–time lattice using the covariant lattice derivatives (3.3) leads to the naïve lattice fermion action

$$S_n = a^4 \sum_x \bar{\psi}(x)\gamma_\mu \widetilde{\nabla}_\mu \psi(x) + m_0 \bar{\psi}(x)\psi(x). \tag{4.2}$$

This action is ultra–local and due to its Dirac structure it also inherited all the (isovector) chiral properties of its continuum counterpart. By construction, the behavior for small momenta is also correct. However, in the chiral limit $m_0 \to 0$ the inverse momentum–space propagator

$$S^{-1}(p) = m_0 + \frac{i}{a} \sum_\mu \gamma_\mu \sin(p_\mu a). \tag{4.3}$$

of this action has zeros on all corners of the Brillouin zone in addition to the one at $p = (0,0,0,0)$. These spurious poles of the propagator cannot be ignored, since they survive in the continuum limit. They describe additional unwanted particles, the so–called "doublers" and hence the naïve lattice fermions violate the third property mentioned above. To make things worse, the doublers come in pairs with opposite chirality, thus spoiling the $U(1)_\mathrm{A}$ axial anomaly [36].[1]

To achieve a correct continuum limit, Wilson added a second derivative term to the naïve action (4.2). This gives a mass of order a^{-1} to all doublers such that they decouple in the continuum. The locality of the action is not affected and also the small momentum behavior is only modified at $\mathrm{O}(ap^2)$. The Wilson fermion action with Wilson parameter r is given by

$$\begin{aligned} S_f &= a^4 \sum_x \bar{\psi}(x)(D_\mathrm{w} + m_0)\psi(x) \\ &= a^4 \sum_x \bar{\psi}(x)\gamma_\mu \widetilde{\nabla}_\mu \psi(x) - ar\bar{\psi}(x)\tfrac{1}{2}\nabla_\mu \nabla^\star_\mu \psi(x) + m_0 \bar{\psi}(x)\psi(x)\ . \end{aligned} \tag{4.4}$$

The Wilson term proportional to r ($0 < r \leq 1$, [38]) is diagonal in Dirac space and hence violates the last point in the no–go theorem. The properties of Wilson fermions and in particular the consequences of this explicit breaking of chiral

[1] One can define a different axial transformation to remove this cancellation [37], but this still produces the anomaly for 16 flavors.

symmetry (also with respect to the axial anomaly) will be discussed in more detail in the next section.

In 1982 Ginsparg and Wilson [39] suggested a way to evade the no–go theorem and preserve the consequences of chiral symmetry. They proposed to replace the condition $\{D, \gamma_5\} = 0$ with the milder condition

$$D\gamma_5 + \gamma_5 D = aD\gamma_5 D \qquad \text{(GW relation)}^2, \tag{4.5}$$

An action defined with a Dirac operator satisfying this relation is invariant under a continuous chiral symmetry, which becomes the continuum chiral symmetry as the lattice spacing a goes to zero. Indeed, it is easily verified that (4.5) implies the invariance of $\bar{\psi}D\psi$ under the transformation

$$\delta\psi = \gamma_5(1 - \tfrac{1}{2}aD)\psi \quad \text{and} \quad \delta\bar{\psi} = \bar{\psi}(1 - \tfrac{1}{2}aD)\gamma_5 \tag{4.6}$$

and also its isovector counterpart. Comparing this to the axial transformation in (2.30), it can be seen as a redefinition of γ_5 to $\hat{\gamma}_5 = \gamma_5(1 - aD/2)$.

Since one now has an exact chiral symmetry at *finite* lattice spacing, there exist exactly conserved (albeit rather complicated) isovector axial currents [40]. Also the axial anomaly with GW fermions appears not only in the continuum limit. Inserting $\hat{\gamma}_5$ into (2.31) one immediately obtains the anomaly in the form

$$\langle \partial_\mu A_\mu(x) \mathcal{O}_{\text{ext}} \rangle = -a \langle \mathcal{O}_{\text{ext}} \text{Tr}\,[\gamma_5 D] \rangle \ . \tag{4.7}$$

In [26] it is shown that the GW relation also implies that for any gauge background $-a\text{Tr}\,[\gamma_5 D] = 2N_{\text{f}} \times \text{index}(D)$, where N_{f} is the number of quark flavors and the index is the difference of the right– and left–handed zero modes of D. The topological interpretation of the anomaly is then obtained via the Atiyah–Singer index theorem [41], which (for smooth gauge configurations) states that

$$\text{index}(D) = \frac{g_0^2}{64\pi^2} \epsilon_{\mu\nu\rho\sigma} \int \mathrm{d}^4x \, F^a_{\mu\nu} F^a_{\rho\sigma} \ . \tag{4.8}$$

It took 15 years to find solutions to the GW relation for the interacting case of QCD. These now include the (classically perfect) fixed point action [42], domain wall fermions [43] and the related overlap formalism [44]. Tempted by the beautiful properties implied by the GW relation, attempts have been made at dynamical QCD simulations using overlap fermions [45, 46, 47]. However, currently available algorithms and computer resources essentially forbid a physical application except in the quenched case.

While already the *global* chiral symmetry of QCD is a very important aspect of the theory, its rôle in the electroweak theory is even more fundamental. There

[2] The original and more general form is actually $D\gamma_5 + \gamma_5 D = 2aDR\gamma_5 D$, where R is some local operator.

the flavor (or weak isospin) $SU(2)$ is promoted to a local gauge symmetry and its presence is therefore necessary to provide a renormalizable theory. The existence of solutions to the GW–relation is thus crucial to define a chiral gauge theory non–perturbatively (see [48] for a review). Hence they help in establishing the renormalizability of the gauge sector of the standard model beyond perturbation theory.

The "staggered" or Kogut–Susskind (KS) fermions [49, 50] represent a very different approach by trying to directly address the problem of fermion doubling. Through a unitary transformation of the fermionic fields the action is brought to a spin–diagonal form, which is used to reduce the doubling problem to a four–fold "taste" degeneracy. While KS fermions keep a remnant chiral symmetry, they do not completely solve the doubling problem and also the construction of operators with correct quantum numbers is far from trivial. An additional theoretical problem [51] with the locality of the staggered operator might lie in the "square–root–trick" [52], which is used to further reduce the number of fermion flavors. With respect to the anomaly, staggered fermions have the same properties as the naïve ones, i.e. the species doubling spoils an anomaly for any number of flavors different from four (or multiples thereof).

The last lattice fermion formulation we mention here is again based on the Wilson Dirac operator. The (in practice) most immediate consequence of its lack of chiral symmetry is the fact that it is not protected against zero–modes even at non–vanishing quark mass. In the so–called twisted mass formulation [53] of lattice QCD a term proportional to $i\gamma_5\tau^3$ (with the Pauli matrix τ^3 acting in flavor space) is added to the Wilson Dirac operator for two quark flavors. As a result this operator has a manifestly positive determinant. Also here part of the continuum chiral symmetry is recovered at the cost of breaking the vector flavor symmetry such that the total number of conserved currents remains the same as for (untwisted) Wilson fermions.

One particularity of this lattice fermion formulation is related to a spurionic symmetry of the terms appearing at O(a) in the Symanzik expansion (3.17). Using this symmetry it is possible to set up a twisted mass formulation such that O(a) lattice artifacts cancel in most physical observables without the need to tune improvement coefficients [54].

4.2 Wilson fermions

We will now proceed with a more detailed discussion of Wilson's fermion action (4.4). Inserting the expressions for the covariant derivatives (3.3) and fixing the Wilson parameter r to unity, it can be written as

$$S_f = a^4 \sum_x \Big\{ \frac{1}{2a} \bar{\psi}(x)\gamma_\mu \Big[U_\mu(x)\psi(x+\hat{\mu}) - U_\mu^\dagger(x-\hat{\mu})\psi(x-\hat{\mu}) \Big] \tag{4.9}$$

$$-\frac{1}{2a}\bar{\psi}(x)\Big[U_\mu(x)\psi(x+\hat{\mu}) - 2\psi(x) + U_\mu^\dagger(x-\hat{\mu})\psi(x-\hat{\mu})\Big] + m_0\bar{\psi}(x)\psi(x)\Big\}\ ,$$

where a sum over μ is still implied in all but the last expression. The action can be rearranged into a diagonal and off–diagonal part

$$S_f = a^4\sum_x \Big\{ -\frac{1}{2a}\sum_\mu \Big[\bar{\psi}(x)(1-\gamma_\mu)U_\mu(x)\psi(x+\hat{\mu}) + \bar{\psi}(x+\hat{\mu})(1+\gamma_\mu)U_\mu^\dagger(x)\psi(x)\Big] + \bar{\psi}(x)\Big(m_0 + \frac{4}{a}\Big)\psi(x)\Big\}\ . \tag{4.10}$$

In practice the *hopping parameter* $\kappa = (2am_0 + 8)^{-1}$ is used instead of the bare mass m_0. If one rescales the fields ψ and $\bar{\psi}$ by a factor $\sqrt{2\kappa}/a^{3/2}$, the Wilson action assumes the simple form

$$S_f = \sum_x \Big\{ -\kappa\sum_\mu \Big[\bar{\psi}(x)(1-\gamma_\mu)U_\mu(x)\psi(x+\hat{\mu}) + \bar{\psi}(x+\hat{\mu})(1+\gamma_\mu)U_\mu^\dagger(x)\psi(x)\Big] + \bar{\psi}(x)\psi(x)\Big\}. \tag{4.11}$$

The transformations of charge conjugation C, parity P and time reversal T listed in Table 4.1 are all discrete symmetries of the Wilson fermion action (this is of course also true for the plaquette gauge action). In addition it also inherited the γ_5–Hermiticity ($\gamma_5 D\gamma_5 = D^\dagger$ due to the use of the symmetric derivative $\widetilde{\nabla}_\mu$) from the continuum.

As already mentioned, chiral symmetry is broken at order a by the Wilson term and recovered only in the continuum. As a consequence the point of vanishing bare quark mass is no longer endowed with an enhanced symmetry (leading to the conservation of the axial current) and protected from renormalization. However, by tuning the bare quark mass m_0 to a non–zero value one can still find a point, where the axial current is conserved (up to cutoff effects). At this *critical*

C	$U_\mu(x) \xrightarrow{C} U_\mu^*(x)$	$\psi(x) \xrightarrow{C} C\bar{\psi}^T(x)$ $\bar{\psi}(x) \xrightarrow{C} -\psi^T(x)C^{-1}$ $C = i\gamma_0\gamma_2$
P $x \xrightarrow{P} x_P = (x_0, -\mathbf{x})$	$U_0(x) \xrightarrow{P} U_0(x_P)$ $U_k(x) \xrightarrow{P} U_k^\dagger(x_p-\hat{k})$	$\psi(x) \xrightarrow{P} \gamma_0\psi(x_P)$ $\bar{\psi}(x) \xrightarrow{P} \bar{\psi}(x_P)\gamma_0$
T $x \xrightarrow{T} x_T = (-x_0, \mathbf{x})$	$U_0(x) \xrightarrow{T} U_0^\dagger(x_T-\hat{0})$ $U_k(x) \xrightarrow{T} U_k(x_p)$	$\psi(x) \xrightarrow{T} T\psi(x_T)$ $\bar{\psi}(x) \xrightarrow{T} \bar{\psi}(x_T)T^{-1}$ $T = i\gamma_0\gamma_5$

Table 4.1: C,P and T transformations on the lattice.

mass $m_c(g_0^2)$ a quark mass derived from the PCAC relation (see Section 5.1) vanishes and thus the theory can be parameterized in terms of the bare subtracted quark mass $m_q = m_0 - m_c$. In perturbation theory the critical mass if found to be [55]

$$m_c(g_0^2) = -0.2701\, g_0^2 - 0.0430\, g_0^4 + \mathrm{O}(g_0^6)\ . \tag{4.12}$$

In addition to this *additive quark mass renormalization* the axial current itself requires a finite renormalization, which is discussed in Section 4.3. In analogy to Section 2.3 we now study the lattice currents associated with the vector and axial flavor transformations in more detail.

4.2.1 Vector currents

The isospin symmetry, which the continuum action possesses in the case of degenerate quarks, is not broken by the Wilson term. Hence a global isospin vector variation of the Wilson action vanishes and a local one, parameterized by $\omega^a(x)$, can be written as a divergence

$$\delta_V S_f = a^4 \sum_x -\omega^a(x)\partial_\mu^* \widetilde{V}_\mu^a(x)\ , \tag{4.13}$$

where ∂_μ^* is the backward lattice derivative and $\widetilde{V}_\mu^a(x)$ the split–point vector current

$$\widetilde{V}_\mu^a(x) = \tfrac{1}{2}\Big\{\bar\psi(x+\hat\mu)\tfrac{1}{2}\tau^a(1+\gamma_\mu)U_\mu^\dagger(x)\psi(x) - \bar\psi(x)\tfrac{1}{2}\tau^a(1-\gamma_\mu)U_\mu(x)\psi(x+\hat\mu)\Big\}\ . \tag{4.14}$$

Although one now has an exactly conserved vector current for Wilson fermions, in practice the local current

$$V_\mu^a(x) = \bar\psi(x)\gamma_\mu\tfrac{1}{2}\tau^a\psi(x) \tag{4.15}$$

is generally used for convenience since sources for correlation functions of this current are easier to construct. Not being a Noether current, it is not protected from renormalization. However, its normalization factor $Z_V(g_0^2)$ is calculated essentially as a by–product of the axial current renormalization discussed in Chapter 8.

4.2.2 Axial currents

Of more interest are the axial transformations. Let us first consider the case of naïve fermions, where also chiral symmetry is preserved on the lattice. The associated current $\widetilde{A}_\mu^a(x)$ is conserved at zero quark mass due to

$$\begin{aligned} \delta_A S_n &= a^4 \sum_x \omega(x)\Big[-\partial_\mu^*\widetilde{A}_\mu^a(x) + 2m_0 P^a(x)\Big]\ , \\ \text{with}\quad \widetilde{A}_\mu^a(x) &= \tfrac{1}{2}\Big\{\bar\psi(x+\hat\mu)\tfrac{1}{2}\tau^a\gamma_\mu\gamma_5 U_\mu^\dagger(x)\psi(x) + \bar\psi(x)\tfrac{1}{2}\tau^a\gamma_\mu\gamma_5 U_\mu(x)\psi(x+\hat\mu)\Big\}\ . \end{aligned}$$

At non–vanishing bare quark mass the divergence of this axial current is proportional to the pseudo–scalar density

$$P^a(x) = \bar{\psi}(x)\gamma_5 \tfrac{1}{2}\tau^a \psi(x) \ . \tag{4.16}$$

In this way naïve lattice fermions have the chiral symmetry of the continuum if the local axial current

$$A^a_\mu(x) = \bar{\psi}(x)\gamma_\mu\gamma_5 \tfrac{1}{2}\tau^a \psi(x) \tag{4.17}$$

is replaced by the split–point axial current $\widetilde{A}^a_\mu(x)$. However, this symmetry is broken by the Wilson term such that even at vanishing bare quark mass no conserved axial current can be defined. Denoting the axial variation of the Wilson term by $X^a(x)$ we obtain [56]

$$\begin{aligned} \delta_A S_f &= a^4 \sum_x \omega^a(x) \Big[-\partial^*_\mu \widetilde{A}^a_\mu(x) + 2m_0 P^a(x) + X^a(x) \Big] \ , \qquad \text{with} \\ X^a(x) &= -\tfrac{1}{2a} \sum_\mu \Big\{ \bar{\psi}(x)\tfrac{1}{2}\tau^a\gamma_5 U_\mu(x)\psi(x{+}\hat{\mu}) + \bar{\psi}(x{+}\hat{\mu})\tfrac{1}{2}\tau^a\gamma_5 U^\dagger_\mu(x)\psi(x) \\ &\qquad + \Big[x \to (x{-}\hat{\mu})\Big] - 4P^a(x) \Big\} \ . \end{aligned} \tag{4.18}$$

Here the explicit breaking of chiral symmetry by the Wilson term can be seen from the fact that X^a can not be written as the divergence of a current.

If Wilson fermions are an admissible regularization of QCD, it must be possible to reproduce the correct axial anomaly in the continuum limit. Performing an iso*singlet* axial transformation of the Wilson action one obtains eq. (4.18) with the replacement $(\frac{1}{2}\tau^a \to 1)$. It is precisely the isosinglet axial variation X of the Wilson term, which (under certain assumptions [57]) reproduces the correct axial anomaly

$$\lim_{a\to 0} X = \frac{N_\mathrm{f} g_0^2}{32\pi^2} \epsilon_{\mu\nu\rho\sigma} F^a_{\mu\nu} F^a_{\rho\sigma} \ . \tag{4.19}$$

4.2.3 Improvement

For the Wilson fermion action the $\mathcal{L}_1$ term in Symanzik's effective theory can contain the five expressions ($\sigma_{\mu\nu} = \frac{i}{2}[\gamma_\mu, \gamma_\nu]$)

$$\begin{aligned} &\mathcal{O}_1 = \bar{\psi} i\sigma_{\mu\nu} F_{\mu\nu} \psi \ , &&\mathcal{O}_2 = \bar{\psi} D_\mu D_\mu \psi + \bar{\psi} \overleftarrow{D}_\mu \overleftarrow{D}_\mu \psi \ , \\ &\mathcal{O}_3 = m_\mathrm{q} \mathrm{Tr}\,\{F_{\mu\nu}F_{\mu\nu}\} \ , &&\mathcal{O}_4 = m_\mathrm{q}\{\bar{\psi}\gamma_\mu D_\mu \psi - \bar{\psi}\gamma_\mu \overleftarrow{D}_\mu \psi\} \ , \\ &\mathcal{O}_5 = m_\mathrm{q}^2 \bar{\psi}\psi \ , \end{aligned} \tag{4.20}$$

since these are compatible with the symmetries (C,P,T and γ_5–Hermiticity) of the Wilson–Dirac operator. Note that none of these terms can appear in the effective action for a Dirac operator that satisfies the GW–relation (4.5).

Through formal manipulations of the Euclidean functional integral (which amount to an application of the classical field equations) two of these (e.g. $\mathcal{O}_2$

and $\mathcal{O}_4$) can be eliminated [34]. While this is necessary from a practical point of view, it restricts the improvement to on–shell quantities, i.e. correlation functions over finite distances. However, since in practice all physically relevant matrix elements are on–shell, this does not represent any loss of applicability

On the other hand, adding $\mathcal{O}_3$ and $\mathcal{O}_5$ merely amounts to a rescaling of the bare coupling and quark mass by factors 1+O(am_q). We will return to this point in the discussion of normalization factors. What remains is the Pauli term $\mathcal{O}_1$. On the lattice the field strength tensor can be represented by

$$\widehat{F}_{\mu\nu} = \frac{1}{8a^2}[Q_{\mu\nu} - Q_{\nu\mu}] \; , \tag{4.21}$$

$$\text{where} \quad Q_{\mu\nu}(x) = U_{x;\mu,\nu} + U_{x;-\nu,\mu} + U_{x;-\mu,-\nu} + U_{x;\nu,-\mu} \; , \tag{4.22}$$

to arrive at the action [58]

$$S_{\mathrm{SW}} = \sum_x \bar{\psi}(x)\Big[D_w + m_0 + ac_{\mathrm{sw}}\tfrac{i}{4}\sigma_{\mu\nu}\widehat{F}_{\mu\nu}\Big]\psi(x) \; . \tag{4.23}$$

The normalization of the improvement term is chosen such that the improvement coefficient $c_{\mathrm{sw}} = 1$ at tree–level in perturbation theory. In general however, c_{sw} depends on g_0^2 and a non–perturbative determination for the two–flavor case [59, 60] is summarized by the interpolating formula

$$c_{\mathrm{sw}}(g_0^2) = \frac{1 - 0.454g_0^2 - 0.175g_0^4 + 0.012g_0^6 + 0.045g_0^8}{1 - 0.720g_0^2} \; . \tag{4.24}$$

For the gauge action $\mathcal{L}_1$ vanishes and thus at O(a) no improvement is needed.

The number of possible improvement terms for the isovector axial and vector currents can be reduced using the same arguments as for the Wilson action. The on–shell improved currents are given by

$$(A_\mathrm{I})^a_\mu = A^a_\mu + ac_\mathrm{A}\tilde{\partial}_\mu P^a \; , \tag{4.25}$$

$$(V_\mathrm{I})^a_\mu = V^a_\mu + ac_\mathrm{V}\tilde{\partial}_\mu T^a_{\mu\nu}, \tag{4.26}$$

$$\text{where} \quad T^a_{\mu\nu}(x) = i\bar{\psi}(x)\sigma_{\mu\nu}\tfrac{1}{2}\tau^a\psi(x) \; . \tag{4.27}$$

The pseudo–scalar density $P^a(x)$ is already improved, i.e. no O(a) counter term with the correct symmetries exists. For the vector current correlation functions we will consider, the term proportional to c_V does not contribute. The 1–loop result for c_A is [61]

$$c_\mathrm{A}(g_0^2) = -0.00756g_0^2 + \mathrm{O}(g_0^4) \tag{4.28}$$

and a non–perturbative determination will be presented in Chapter 7.

4.3 Current renormalization

A scheme, in which the renormalization conditions are imposed on a set of correlation functions at a point (g_0, am_0) in bare parameter space, would result in renormalization factors, which depend on both the bare coupling and the bare mass as well as a renormalization scale $a\mu$. Inherently simpler are mass–independent schemes, where one imposes the normalization condition at zero quark mass with the consequence that no dependence of the renormalization factors on the quark mass is introduced [62].

Neglecting $\mathrm{O}(a)$ improvement, in such a scheme one would introduce renormalized parameters through e.g. $m_\mathrm{R} = Z_m m_\mathrm{q}$, where the subtracted mass $m_\mathrm{q} = m_0 - m_\mathrm{c}$ parameterizes deviations from the critical line and the renormalization factor depends on the bare coupling g_0^2 as well as the renormalization scale $a\mu$. As is discussed in [63], such a definition leads to uncanceled $\mathrm{O}(am)$ effects and is thus not compatible with the improvement programme. This can be understood from the fact that in Section 4.2.3 we ignored $\mathrm{O}(a)$ counterterms, which merely amounted to a rescaling of the bare parameters.

If we want to employ a massless renormalization scheme and at the same time have on–shell $\mathrm{O}(a)$ improvement, we need to allow for a more general form of renormalized quantities. These are expressed in terms of the modified bare coupling and quark mass

$$\tilde{g}_0^2 = g_0^2(1 + b_\mathrm{g} am_\mathrm{q}) \; , \tag{4.29}$$

$$\tilde{m}_\mathrm{q} = m_\mathrm{q}(1 + b_\mathrm{m} am_\mathrm{q}) \; , \tag{4.30}$$

where the b–coefficients are functions of g_0^2. The renormalized coupling and quark mass can then be written as

$$g_\mathrm{R}^2 = \tilde{g}_0^2 Z_g(\tilde{g}_0^2, a\mu) \tag{4.31}$$

$$m_\mathrm{R} = \tilde{m}_\mathrm{q} Z_m(\tilde{g}_0^2, a\mu) \; . \tag{4.32}$$

Also for local composite fields ϕ the $1+\mathrm{O}(am_\mathrm{q})$ counterterm is conventionally not included in the definition of the improved field ϕ_I, but rather in the renormalized field according to

$$\phi_\mathrm{R}(x) = Z_\phi(\tilde{g}_0^2, a\mu)(1 + b_\phi am_\mathrm{q})\phi_\mathrm{I}(x) \; . \tag{4.33}$$

In this context the isovector axial and vector currents are special since in the (massless) continuum limit they become the Noether currents of the flavor chiral symmetry and at finite lattice spacing their normalization can thus be fixed by imposing a continuum Ward identity. The latter is a local identity and hence the renormalization factors of the isovector axial and vector currents do not depend on a scale. In addition they approach unity for g_0^2 going to zero, i.e. when the flavor chiral symmetry is recovered [56, 64].

$$(A_{\mathrm{R}})^a_\mu = Z_{\mathrm{A}}(\tilde{g}_0^2)\,(1+b_{\mathrm{A}}am_{\mathrm{q}})(A_{\mathrm{I}})^a_\mu \,, \tag{4.34}$$
$$(V_{\mathrm{R}})^a_\mu = Z_{\mathrm{V}}(\tilde{g}_0^2)\,(1+b_{\mathrm{V}}am_{\mathrm{q}})(V_{\mathrm{I}})^a_\mu \,. \tag{4.35}$$

To one loop in perturbation theory [65, 66, 67] one finds that

$$Z_{\mathrm{A}} = 1 - 0.116458\, g_0^2 + \mathrm{O}(g_0^4) \,, \tag{4.36}$$
$$Z_{\mathrm{V}} = 1 - 0.129430\, g_0^2 + \mathrm{O}(g_0^4) \,. \tag{4.37}$$

One should point out again that we have ignored the existence of an exactly conserved vector current (4.14) for Wilson fermions and treat V^a_μ and A^a_μ on exactly the footing. The normalization of the split–point vector current (4.14) is given naturally, i.e. it does not renormalize.

The renormalization of the pseudo–scalar density

$$(P_{\mathrm{R}})^a(x) = Z_{\mathrm{P}}(1+b_{\mathrm{P}}am_q)P^a(x) \tag{4.38}$$

on the other hand will depend on the scale, at which the normalization condition is imposed, i.e. $Z_{\mathrm{P}} = Z_{\mathrm{P}}(\tilde{g}_0^2, a\mu)$.

A massless scheme requires that the normalization conditions are defined at vanishing quark mass. In a non–perturbative implementation this implies that numerical simulations have to be performed at zero (or at least very small) quark mass. With periodic boundary conditions such simulations are technically very difficult or even impossible since there is no lower bound on the spectrum of the Dirac operator. This problem is cured in the Schrödinger functional setup, which will be discussed in the following chapter, at the end of which we will define a renormalized quark mass in terms of correlation functions of renormalized composite fields.

Chapter 5

The Schrödinger functional

So far no boundary conditions have been specified since they would have been of no importance in the discussion of the local symmetries. It was thus implicitly assumed that we are working either in infinite volume or in finite volume with periodic boundary conditions for the fields. All numerical results report here were obtained in the Schrödinger functional (SF) setup, which employs periodic boundary conditions in the three spatial directions and fixed (Dirichlet) boundary conditions in time.

There are several advantages of this method compared to the torus, where all four directions are periodic. The Dirichlet boundary conditions provide an infrared cutoff (inversely proportional to the time extension T) to the Dirac operator [10].[1] The gluonic boundary conditions can be used to induce a color background field, which was employed e.g. in the definition of a running coupling [2, 68]. The fermionic boundary fields can serve as sources for correlation functions in an elegant way, particularly if a zero–momentum projection or wave–functions are required. This results in mesonic correlation functions with smaller statistical error than on the torus.

A vast literature (see e.g. [9, 10, 34, 69]) exists on the SF and we will therefore restrict the discussion here to the aspects required in the following chapters, in particular the ingredients required for the definition of the lattice SF with Wilson fermions. Some SF correlation functions needed in the axial current improvement (Chapter 7) and renormalization (Chapter 8) are also introduced.

The QCD Schrödinger functional is the propagation kernel of a field configuration $C, \bar{\rho}, \rho$ at Euclidean time 0 to a configuration $C', \bar{\rho}', \rho'$ at time T. Following Feynman, this is written as an integration over all interpolating field configurations

$$\mathcal{Z}[C, C'; \bar{\rho}, \rho; \bar{\rho}', \rho'] = \int_{A,\bar{\psi},\psi} \mathrm{e}^{-S[A,\bar{\psi},\psi]} \,. \tag{5.1}$$

[1] This can be rigorously shown only in the $g_0^2 \to 0$ limit.

5.1 Lattice SF with Wilson fermions

We consider an $L^3 \times T$ space–time cylinder, i.e. the set of sites $(k = 1, 2, 3)$

$$\{x \,|\, x/a \in \mathbb{Z}^4, 0 \leq x_0 \leq T, 0 \leq x_k < L\} \tag{5.2}$$

and the associated links $U_\mu(x)$.[2] The gauge links are spatially strictly periodic, while the fermionic fields are allowed to pick up a phase θ_k at the boundary

$$\begin{aligned} U_\mu(x+L\hat{k}/a) &= U_\mu(x) \\ \psi(x+L\hat{k}/a) &= \mathrm{e}^{i\theta_k}\psi(x) \\ \bar{\psi}(x+L\hat{k}/a) &= \mathrm{e}^{-i\theta_k}\bar{\psi}(x) \,. \end{aligned} \tag{5.3}$$

The Dirichlet boundary conditions are implemented via

$$U_k(x)|_{x_0=0} = \exp(C_k) \quad \text{and} \quad U_k(x)|_{x_0=T} = \exp(C'_k) \,, \tag{5.4}$$

where C_k is a traceless anti–Hermitian 3×3 matrix. Throughout this work we use $C_k = C'_k = 0$, i.e. no background field. From the lattice action it will be obvious that only half of the fermion fields components on the boundaries actually couple to the interior of the SF cylinder. The SF therefore becomes a well–defined boundary value problem by prescribing $(P_\pm = (1 \pm \gamma_0)/2)$

$$\begin{aligned} P_+\psi(x)|_{x_0=0} = \rho(\mathbf{x}) \,, \quad \bar{\psi}(x)P_-|_{x_0=0} = \bar{\rho}(\mathbf{x}) \,, \\ P_-\psi(x)|_{x_0=T} = \rho'(\mathbf{x}) \,, \quad \bar{\psi}(x)P_+|_{x_0=T} = \bar{\rho}'(\mathbf{x}) \,. \end{aligned} \tag{5.5}$$

While the fermionic boundary fields $(\rho, \ldots)$ are always set to zero, functional derivatives of the effective action with respect to them are used to define correlation functions involving the SF boundary. Thus, expectation values of composite fields $\mathcal{O}$ in the lattice Schrödinger functional are obtained from

$$\langle \mathcal{O} \rangle = \left\{ \frac{1}{\mathcal{Z}} \int \mathcal{D}U\mathcal{D}\bar{\psi}\mathcal{D}\psi \, \mathcal{O} \, \mathrm{e}^{-S[U,\bar{\psi},\psi]} \right\}_{\bar{\rho}'=\rho'=\bar{\rho}=\rho=0} \,. \tag{5.6}$$

In addition to the dynamical variables $U, \bar{\psi}$ and ψ, the composite fields may then also involve the "boundary fields" (see Appendix A for details)

$$\begin{aligned} \zeta(\mathbf{x}) &= \frac{\delta}{\delta\bar{\rho}(\mathbf{x})} \,, \quad \bar{\zeta}(\mathbf{x}) = -\frac{\delta}{\delta\rho(\mathbf{x})} \,, \\ \zeta'(\mathbf{x}) &= \frac{\delta}{\delta\bar{\rho}'(\mathbf{x})} \,, \quad \bar{\zeta}'(\mathbf{x}) = -\frac{\delta}{\delta\rho'(\mathbf{x})} \,. \end{aligned} \tag{5.7}$$

When acting on the Boltzmann factor in (5.6), these have the effect of inserting certain combinations of ψ and $\bar{\psi}$ close to the boundary, together with the

[2] Except for $U_0(x)$ when $x_0 = T$.

appropriate gauge field variables to ensure gauge covariance. While the lattice action $S[U,\bar{\psi},\psi]$ is in principle given by (3.4) and (4.23) together with the above boundary conditions, the issue of O(a) improvement needs to be re–addressed due to boundary effects.

In the presence of the Dirichlet boundary conditions, surface terms have to be added to the effective action (3.14). At O(a) this is [63]

$$\lim_{\epsilon\to 0}\int \mathrm{d}^3\mathbf{x}\{\mathcal{B}_1(\mathbf{x})|_{x_0=\epsilon}+\mathcal{B}_1'(\mathbf{x})|_{x_0=T-\epsilon}\}\ , \tag{5.8}$$

where $\mathcal{B}_1$ and $\mathcal{B}_1'$ are linear combinations of composite fields of mass dimension four. For the gauge action the only fields that can contribute are $\mathrm{Tr}\,\{F_{kl}F_{kl}\}$ and $\mathrm{Tr}\,\{F_{0k}F_{0k}\}$. On the lattice these are implemented by modifying the weight of the plaquettes *in* the boundaries ($c_\mathrm{s}/2$) and those *touching* the boundaries (c_t).

On–shell O(a) improvement of the fermion action can be achieved by e.g. adding the field products

$$\begin{aligned}\mathcal{O}_{11} &= \bar{\psi}P_+D_0\psi+\bar{\psi}\overleftarrow{D}_0P_-\psi\ ,\\ \mathcal{O}_{14} &= \bar{\psi}P_-\gamma_kD_k\psi-\bar{\psi}\overleftarrow{D}_k\gamma_kP_+\psi\ ,\end{aligned} \tag{5.9}$$

at $x_0=0$ and

$$\begin{aligned}\mathcal{O}_{12} &= \bar{\psi}P_-D_0\psi+\bar{\psi}\overleftarrow{D}_0P_+\psi\ ,\\ \mathcal{O}_{13} &= \bar{\psi}P_+\gamma_kD_k\psi-\bar{\psi}\overleftarrow{D}_k\gamma_kP_-\psi\ ,\end{aligned} \tag{5.10}$$

at $x_0=T$. The corresponding lattice discretizations of these terms are added to the action with coefficients $\tilde{c}_\mathrm{t}$ for the temporal derivatives and $\tilde{c}_\mathrm{s}$ for the spatial derivatives.

To keep the discussion transparent, the explicit form of the improved action is given in Appendix A. Here we want to note only that for our specific choice of boundary conditions the terms proportional to c_s and $\tilde{c}_\mathrm{s}$ do not contribute, while c_t and $\tilde{c}_\mathrm{t}$ are known perturbatively [70, 71]

$$c_\mathrm{t} = 1-0.089\,g_0^2-0.03\,g_0^4\ , \tag{5.11}$$

$$\tilde{c}_\mathrm{t} = 1-0.018\,g_0^2\ . \tag{5.12}$$

Unless T/a is very small, a non–perturbative knowledge of these coefficients is not necessary since the lattice artifacts they modify are surface effects and thus suppressed by a/T compared to the cutoff–effects from the bulk. Moreover, in [63] it is shown explicitly that these term can not contribute O(a) terms to matrix elements of the PCAC relation (since the latter holds exactly in the continuum theory).

The two–point functions are derived by taking functional derivatives of the generating functional and all the fermionic propagators involving the boundary and bulk quark fields are also given in Appendix A.

5.2 Fermionic correlation functions

We are interested in mesonic correlation functions, i.e. we want to excite states with the quantum numbers of isovector pseudo–scalar particles. In terms of the boundary fields (5.7) possible choices are

$$\mathcal{O}^a = a^6 \sum_{\mathbf{u},\mathbf{v}} \bar{\zeta}(\mathbf{u})\gamma_5 \tfrac{1}{2}\tau^a \zeta(\mathbf{v}) , \tag{5.13}$$

$$\mathcal{O}'^a = a^6 \sum_{\mathbf{u},\mathbf{v}} \bar{\zeta}'(\mathbf{u})\gamma_5 \tfrac{1}{2}\tau^a \zeta'(\mathbf{v}) . \tag{5.14}$$

With these operators both constituent quarks are projected to zero momentum separately. In Chapter 7 we will also consider generalizations of (5.13, 5.14), which make use of spatial trial wave functions to influence the excitations of pseudo–scalar states.

To obtain non–trivial expectation values in (5.6) the operator appearing there needs to be compatible with the lattice symmetries, in particular it must be invariant under parity and an isoscalar. Restricting ourselves to two quark bilinears, there are five possible combinations involving (5.13, 5.14)

$$f_{\mathrm{A}}(x_0) = -\frac{a^3}{3L^3} \sum_{\mathbf{x}} \langle A_0^a(x)\, \mathcal{O}^a \rangle , \tag{5.15}$$

$$f_{\mathrm{P}}(x_0) = -\frac{a^3}{3L^3} \sum_{\mathbf{x}} \langle P^a(x)\, \mathcal{O}^a \rangle , \tag{5.16}$$

$$g_{\mathrm{A}}(x_0) = \frac{a^3}{3L^3} \sum_{\mathbf{x}} \langle \mathcal{O}'^a\, A_0^a(x) \rangle , \tag{5.17}$$

$$g_{\mathrm{P}}(x_0) = -\frac{a^3}{3L^3} \sum_{\mathbf{x}} \langle \mathcal{O}'^a\, P^a(x) \rangle , \tag{5.18}$$

$$\text{and} \quad f_1 = -\frac{1}{3L^6} \langle \mathcal{O}'^a\, \mathcal{O}^a \rangle . \tag{5.19}$$

Their explicit form in terms of quark propagators is given in Appendix B.1. From these correlation functions one can define a current quark mass m through the PCAC relation (2.28). If the transformations (2.17) are applied in the interior, the boundary fields $\mathcal{O}$ and $\mathcal{O}'$ are "external" and we get

$$\tilde{\partial}_\mu \langle A_\mu^a \mathcal{O}^a \rangle = 2m \langle P^a \mathcal{O}^a \rangle \tag{5.20}$$

and thus e.g.

$$\frac{\tilde{\partial}_0 f_{\mathrm{A}}(T/2)}{2 f_{\mathrm{P}}(T/2)} \tag{5.21}$$

defines a bare current quark mass since the spatial derivatives vanish under periodic boundary conditions. The lattice artifacts, by which eq. (5.21) is affected can be reduced by using the improved axial current (4.25) to arrive at

$$m_{\mathrm{I}} = \frac{\tilde{\partial}_0 f_{\mathrm{A}}(T/2) + ac_{\mathrm{A}}\partial_0\partial_0^{\star} f_{\mathrm{P}}(T/2)}{2f_{\mathrm{P}}(T/2)} \tag{5.22}$$

as a possible estimator for an improved current quark mass. Of course, also g_{A} and g_{P} could be used instead. In fact, for vanishing background field ($C_k = C_k' = 0$) time–reflection is a symmetry of the SF and $f_{\mathrm{X}}(x_0) = g_{\mathrm{X}}(T-x_0)$. An average of f and g can then be used to improve the statistical precision.

Since their derivation is based on local symmetry transformations of the continuum action, the quark masses defined in this way are independent of the lattice extensions L and T up to cutoff effects of $\mathrm{O}(a^2)$ in the improved theory. This is explicitly shown in [61].

The Schrödinger functional also defines a (finite volume) renormalization scheme, which has been used e.g. in the calculation of the scale dependence of the SF coupling $\bar{g}^2$ [2]. In the SF scheme the renormalization scale μ is identified with the inverse box length L^{-1}. In the context of a project to determine the scale evolution of quark masses, the renormalization constant of the pseudo–scalar density has been determined non–perturbatively in this scheme [13, 14]. To this end one requires that a certain matrix element of $(P_{\mathrm{R}})^a$ is equal to its tree–level value c. The concrete requirement is that

$$Z_{\mathrm{P}}(g_0, L/a) = c\frac{\sqrt{3f_1}}{f_{\mathrm{P}}(T/2)} \tag{5.23}$$

at vanishing quark mass. One can then proceed and insert the renormalized currents into (5.22) to define a renormalized improved quark mass

$$\overline{m} = \frac{Z_{\mathrm{A}}(1+b_{\mathrm{A}}am_{\mathrm{q}})}{Z_{\mathrm{P}}(1+b_{\mathrm{P}}am_{\mathrm{q}})}\, m_{\mathrm{I}} + \mathrm{O}(a^2) \tag{5.24}$$

$$= \frac{Z_{\mathrm{A}}}{Z_{\mathrm{P}}}(1+(b_{\mathrm{A}}-b_{\mathrm{P}})\, am_{\mathrm{q}})\, m_{\mathrm{I}} + \mathrm{O}(a^2)\ . \tag{5.25}$$

Since Z_{A} depends only on the (modified) bare coupling, the entire scale (and scheme) dependence of the renormalized quark mass enters through the normalization of the pseudo–scalar density.

The evolution of $\overline{m}$ is then traced to very high energies, where the SF scheme can be related to a more common renormalization scheme like $\overline{\mathrm{MS}}$ by means of a 1–loop calculation. The application of this programme to the strange quark mass [15] is one of the immediate applications of the axial current improvement and renormalization presented here. In the quenched approximation this has been done in [13, 72]

Chapter 6

Algorithmic issues

The basics of our lattice theory as well as the framework, in which we implement the axial current improvement and renormalization, have now been laid out. However, before proceeding to a detailed discussion of the latter, it is necessary to detour into the more technical aspects of full QCD simulations.

6.1 Hybrid Monte Carlo algorithms

Since the fermionic action is bilinear in the quark fields, the Grassmann integral can be performed analytically, resulting in the determinant of the Dirac operator. This step is even necessary unless one can find an efficient way of dealing with the Grassmann fields directly. For two quark flavors one has (writing $M = D + m$)

$$\mathcal{Z} = \int \mathcal{D}U\mathcal{D}\bar{\psi}\mathcal{D}\psi \, \exp\Big\{ - S_g[U] - \sum_{\text{flavors}} \bar{\psi} M[U]\psi \Big\} \tag{6.1}$$

$$= \int \mathcal{D}U \; \mathrm{e}^{-S_g[U]} \det M[U]^2 \; . \tag{6.2}$$

Due to the γ_5–Hermiticity of M this can be expressed in terms of the positive matrix $Q^2 = Q^\dagger Q$ with $Q = \gamma_5 M$, such that $\det M^2 = \det QQ^\dagger$. With the introduction of a so–called pseudo–fermion field ϕ the determinant can be expressed as a *bosonic* Gaussian integral

$$\mathcal{Z} = \int \mathcal{D}U\mathcal{D}\phi \; \exp\left\{-S_g[U] - \phi^\dagger (QQ^\dagger)^{-1}\phi\right\} = \int \mathcal{D}U\mathcal{D}\phi \; \mathrm{e}^{-S_{\text{eff}}} \; . \tag{6.3}$$

To generate gauge field configurations distributed according to the effective action, the hybrid Monte Carlo (HMC) [73] algorithm evolves the gauge field in a fictitious time τ (molecular dynamics). This evolution is described by anti–Hermitian traceless momentum matrices $\pi_\mu(x)$

$$\frac{\partial}{\partial \tau} U_\mu(x) = \pi_\mu(x) U_\mu(x) \; . \tag{6.4}$$

Adding a Gaussian action for the momenta to S_{eff}, we obtain the Hamiltonian of the molecular dynamics (MD) evolution

$$H = S_{\text{eff}} - \tfrac{1}{2}\mathrm{Tr}\,\pi^2 \ . \tag{6.5}$$

The evolution equation of the momenta π is derived by requiring the Hamiltonian H to be a constant of the MD motion. The update of the momenta requires the computation of the "force", i.e. $\delta S_{\text{eff}}/\delta U$, which involves an inversion of $Q^\dagger Q$ for the fermionic contribution. For this inversion the conjugate gradient algorithm is used (see Section 6.2). Since the momenta don't couple to the gauge or pseudo–fermion fields they will have no effects on correlation functions involving U and ϕ. An HMC update step (trajectory) now proceeds from a starting configuration $U(0)$ according to

1. Generate a complex Gaussian random vector and apply Q to it, to obtain ϕ distributed according to (6.3);
2. Generate momenta according to (6.5) by drawing Gaussian components in the Lie algebra generators;
3. For fixed ϕ, numerically evolve U and π for a MD time τ_0 using a numerical approximation of Hamilton's equations of motion;
4. Accept $U(\tau_0)$ with a probability $\mathrm{e}^{-\Delta H}$, where $\Delta H = H(\tau_0) - H(0)$ (Metropolis step).

In case of rejection $U(0)$ becomes also the next configuration in the Markov chain. In the next trajectory new pseudo–fermion fields are used to estimate the determinant contribution and also the direction of evolution is again chosen randomly by using new Gaussian momenta (*refreshed* molecular dynamics). Several aspects of the HMC are worth mentioning at this points.

For the algorithm to satisfy detailed balance with respect to the effective action, the numerical integration scheme needs to be reversible and area preserving (in phase space). The molecular dynamics evolution is the computationally most expensive part of the HMC algorithm.

The simplest reversible and area preserving integration scheme, is the *leapfrog*. With $\delta\tau = \tau_0/n_{\text{step}}$ this is defined through

$$\begin{array}{rl} & \pi \;\rightarrow\; \pi - \delta S_{\text{eff}}/\delta U\cdot\delta\tau/2 \\ (n_{\text{step}}-1)\ \times & \left\{ \begin{array}{ccl} U & \rightarrow & \exp(\pi\delta\tau)U \\ \pi & \rightarrow & \pi - \delta S_{\text{eff}}/\delta U\cdot\delta\tau \end{array} \right\} \\ & U \;\rightarrow\; \exp(\pi\delta\tau)U \\ & \pi \;\rightarrow\; \pi - \delta S_{\text{eff}}/\delta U\cdot\delta\tau/2 \ . \end{array} \tag{6.6}$$

Throughout this work we always consider molecular dynamics trajectories of unit length, i.e. $\tau_0 = 1$ and $\delta\tau = 1/n_{\text{step}}$. The half–steps differ from the exact integration of Hamilton's equation by errors of order $\delta\tau^2$, whereas the $n_{\text{step}} = \mathrm{O}(1/\delta\tau)$

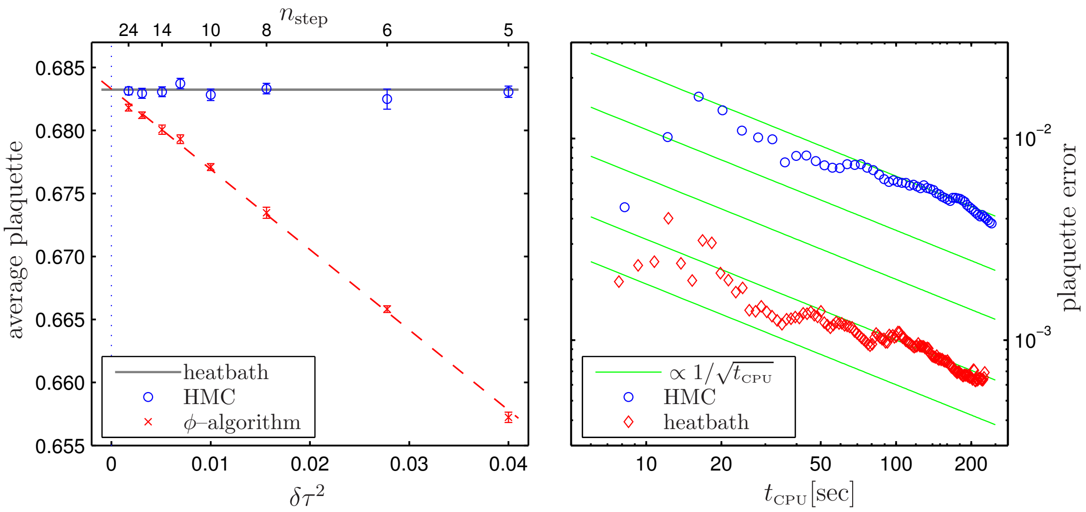

Figure 6.1: Left: Average plaquette from different algorithms in $SU(2)$ gauge theory on a 6^3 lattice with periodic boundary conditions at $\beta = 3.5$. Right: scaling of the error with CPU time t_{CPU} for heatbath and HMC in this setup.

intermediate steps each have errors of $\delta\tau^3$. More elaborate (and hence more expensive) schemes can increase the acceptance rate by lowering the violation of energy (Hamiltonian) conservation. If the accept/reject step at the end of the HMC trajectory is omitted, one generates a systematically wrong ensemble and an extrapolation to $\delta\tau = 0$ becomes necessary (ϕ–algorithm [74]). In this case observables are expected to differ by $\mathrm{O}(\delta\tau^2)$ from their correct value if a leapfrog integrator is employed.

While most of the computer time is spent in evaluating the fermionic force, one should note that already for pure gauge theory, the HMC itself is a rather inefficient algorithm. Although it globally moves the field configurations, in practice the autocorrelation times are large.

To illustrate these points, results from three–dimensional $SU(2)$ gauge theory are shown in Fig. 6.1. At this statistical precision the $\mathrm{O}(\delta\tau^2)$ errors from the leapfrog integration are clearly visible for the ϕ–algorithm (left plot). The HMC results for the average plaquette agree with the (much more precise) heatbath data for all values of the leapfrog step–size. A comparison of the statistical error as a function of the CPU time (right plot) shows that the heatbath gives a significantly more precise result for a given computational effort.

Many improvements to the ”basic” HMC described here have been proposed and tested to speed up full QCD simulations. This includes preconditioning and different pseudo–fermion representations of the fermion matrix as well as higher–order integration schemes for the MD evolution. However, so far none of these represent a real breakthrough in algorithmic development since the performance gain is in general quite moderate (i.e. factors of $\lesssim 2$ at most). The situation might be different for a recent promising proposal [75], which relies on a domain–decomposition of the fermion matrix. Here significant advantages in the region of small quark masses are expected.

Another possibility is to use in the MD evolution a different action (guidance Hamiltonian) than one really wants to simulate. This can be corrected either through an adjustment of the acceptance probability in the Metropolis step or by calculating a *reweighting factor* to be included in the data analysis. The latter possibility is employed in the polynomial hybrid Monte Carlo (PHMC) algorithm, which will be discussed in Section 6.6.

All of the simulations presented here are done using even–odd preconditioning [76], where the lattice sites are divided into an even and an odd part according to $\sum_\mu x_\mu$. Since the hopping term in the Wilson Dirac operator couples only even to odd sites, it is possible to rewrite Q in a form, where the non–trivial part acts only on the odd sites. As a result the effective condition number is reduced and inversions become computationally cheaper. We will denote the even–odd–preconditioned Hermitian Dirac operator by $\hat{Q}$.

Another improvement is the introduction of a second pseudo–fermion field as proposed in [77]. More precisely, the implementation we employed is the one discussed in [78], where the pseudo–fermion action from (6.3) is split according to

$$\begin{aligned} S_{F_1} &= \phi_1^\dagger (Q^2+\rho^2)^{-1}\phi_1 && (6.7) \\ \text{and} \quad S_{F_2} &= \phi_2^\dagger (\rho^{-2}+Q^{-2})\phi_2\,, && (6.8) \end{aligned}$$

such that

$$\det Q^2 = \int \mathcal{D}\phi_1 \mathcal{D}\phi_2 \, \mathrm{e}^{-S_{F_1}-S_{F_2}}\,. \tag{6.9}$$

With this split–up the fermionic forces in the MD evolution become smaller, such that larger step–sizes can be used in the numerical integration.

Finally, an improved Sexton–Weingarten [79] integrator is used in the molecular dynamics. It uses different time scales for the gauge and the fermionic part of the forces. A performance improvement results since the computationally cheaper gauge forces are evaluated more often. This scheme partially removes the integration errors of $\mathrm{O}(\delta\tau^3)$. In practice it is found that the Metropolis acceptance rate P_{acc} behaves as

$$-\log P_{\mathrm{acc}} \simeq 1 - P_{\mathrm{acc}} \propto \delta\tau^4\,, \tag{6.10}$$

thus indicating that the errors of $\mathrm{O}(\delta\tau^4)$ dominate.

An important quantity to monitor in an HMC simulation is the Hamiltonian violation ΔH during one molecular dynamics trajectory. In the large volume limit its distribution is Gaussian with mean and width related through [80]

$$2\langle \Delta H\rangle = \langle \Delta H^2\rangle - \langle \Delta H\rangle^2\,. \tag{6.11}$$

This relation holds for the simulation described in Table 7.1, while for the simulations in smaller volume (Tables 6.1 and D.1) deviations were observed. Only in the limit of an exact integration, $\delta\tau \to 0$, the mean (and hence also the variance) of ΔH vanish. However, from the detailed balance condition it is possible to show that even at finite step–size [81]

$$\langle \mathrm{e}^{-\Delta H} \rangle = 1 \tag{6.12}$$

on the generated ensemble (including of course the rejected proposals). A violation of this condition could indicate problems with reversibility in the numerical integration of the equations of motion.

6.2 Inverting the Dirac operator

To evaluate the fermionic contribution to the MD force and to calculate fermionic correlation functions, matrix elements of the quark propagator $S = M^{-1}$ need to be calculated on the gauge background produced in the Monte Carlo run. Depending on the specific correlator we need different linear combinations of matrix elements. These are obtained by inverting M on different sources q. Writing the Dirac indices $A, B, \ldots$ and color indices $\alpha, \beta, \ldots$ explicitly, we need to solve

$$M(x,y)^{\alpha\beta}_{AB} \cdot \widetilde{S}(y,z)^{\beta\gamma}_{BC} = q(x,z)^{\alpha\gamma}_{AC} \,. \tag{6.13}$$

Since the source for the inversion can only be a vector, we need one inversion for each combination of the "column" indices z, γ and C of q. Exploiting the linearity of (6.13), one can add different sources to obtain the corresponding linear combination of columns of S with a single inversion. For a given source y the solution x of $Mx{=}y$ is found by minimizing the residue

$$r = \frac{||Mx - y||^2}{||y||^2} \,. \tag{6.14}$$

Since M is a large sparse matrix, iterative conjugate gradient methods provide an efficient tool for this task. The most commonly used version is the stabilized biconjugate gradient (BiCGstab) [82]. However, we found that in cases where the matrix M is rather ill–conditioned, it can happen that the BiCGstab does not converge to a solution.

This poses a problem in particular because during the iteration, the residue r is not computed according to (6.14). To save an additional application of M, the current residue is computed from its value during the previous iteration (iterated residue). Thus, due to accumulation of roundoff the iterated residue might become small, indicating that a solution has been found, while the real residue is still of O(1).

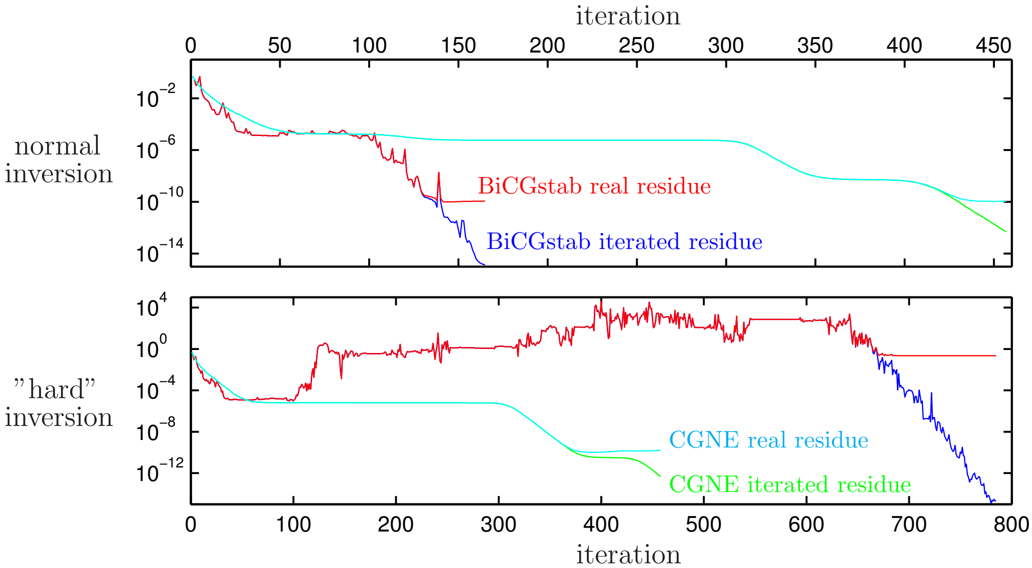

Figure 6.2: Solver residues as a function of the iteration number. For difficult inversions (lower plot) the BiCGstab might indicate a convergence in the iterated residue although no solution has been found.

The simple conjugate gradient (CGNE)[1] solver has a much smoother convergence behavior and is very stable even when applied to ill–conditioned problems. Fig. 6.2 shows the real and the iterated residue for BiCGstab and CGNE during the iterations of a normal inversion and one, where BiCGstab did not converge to a solution. For CGNE the real and iterated residues start to differ only when the single–precision limit is approached.[2]

To account for the known insufficiencies of the BiCGstab while still making use of its superior performance, we perform the inversions for the calculation of correlation functions in the following way. We start by first running the BiCGstab solver until the required precision or the maximum number of iterations, O(100), is reached. This is followed by a CGNE inversion starting from the BiCGstab result with a maximum number of O(1000) iterations, although for a "normal" inversion only O(1) CGNE iterations are performed until the required precision is obtained. To compensate for precision loss due to roundoff, the CGNE is restarted up to ten times with the previously found solution. The real residue is always recomputed after the entire inversion and monitored in the data analysis program.

[1]NE stands for normal equation, $M^\dagger M x = M^\dagger y$. CG itself applies only to positive matrices.
[2] Apart from global sums all our calculations are carried out in single–precision arithmetics.

6.3 Data analysis

As mentioned earlier, the field configurations in a Markov chain produced by a hybrid Monte Carlo algorithm can be strongly (auto)correlated in Monte Carlo time. This needs to be taken into account in order to obtain reliable error estimates for quantities measured in such simulations.

Traditionally this is done by combining a number of consecutive measurements into *bins* and then performing a naïve error analysis on the binned data (jackknife analysis). However, it has been shown [83] that this procedure is only suboptimal concerning the reliability of the error estimate.

For all our data analysis we use the explicit numerical integration of the autocorrelation function for primary and derived observables from [83]. The integrated autocorrelation time τ_{int} enters the error estimate σ in the form that the number of estimates N is "effectively" reduced according to

$$\sigma^2 = \frac{2\tau_{\mathrm{int}}}{N}\nu \ , \tag{6.15}$$

where ν is the variance of the quantity in question. While the latter is a property of the observable and hence of the theory one is simulating, the size of the statistical error is also influenced by τ_{int}, which depends on the algorithm used to generate the Markov chain. This method also provides us with an error of τ_{int} and hence we can directly assess the reliability of our error estimate, i.e. the error of the error.

6.4 Sampling problems on coarse lattices

In order to motivate the choice of simulation algorithms in the evaluation of the axial current normalization condition (Chapter 8) we now proceed to a more detailed discussion of the algorithmic difficulties we faced. This concerns the simulations at the coarsest lattice spacing we consider, $a \simeq 0.1\,\mathrm{fm}$ at a bare gauge coupling of $\beta = 5.2$.

It has long been established that in the corresponding quenched situation cutoff–effects are compatible with Symanzik's description (Section 3.3) and a continuum extrapolation can be started there. However, over the last years more and more evidence has been accumulated that for *dynamical* improved Wilson fermions at this lattice spacing the cutoff–effects are much larger than expected. As an extreme example, for three flavors the existence of a phase transition in the β–κ–plane has been numerically conjectured and is interpreted as a lattice artifact [84]. A summary of large scaling violations in the two–flavor–theory is given in ref. [85].

In the following we will establish that the algorithmic problems we encountered in the MD integration and the efficient simulation of the canonical ensemble can also be interpreted as cutoff–effects. More precisely, at the infrared end of the spectrum of the Dirac operator we find a behavior different from what one would expect close to the continuum.

One of the important results will be our finding that the distortion of the Dirac spectrum makes it advantageous to deviate from importance sampling. In this context we study the behavior of the polynomial hybrid Monte Carlo (PHMC) algorithm [86, 87] in this situation and find it a very useful tool for a detailed investigation of the properties of the small eigenvalues of the Dirac operator.

In Table 6.1 we list the lattice sizes and bare parameters for the simulations discussed in this chapter. In all cases we have $T = 9/4\ L$ for the time extension T. The bare quark mass m is defined through (5.22), where we used the perturbative value of c_{A} from eq. (4.28). In the algorithm column 'H_2' refers to the HMC with two pseudo–fermion fields described at the end of Section 6.1 and 'P_n' stands for PHMC with a polynomial of degree n. This algorithm will be introduced in Section 6.6. To gain more statistics, each simulation was performed with 16 independent replica.

run	L/a	β	κ	Lm	algo.	N_{traj}	$\delta\tau$	P_{acc}
[A1]	8	5.2	0.13550	0.205(10)	H_2	16·500	1/16	91%
[A2]	8	5.2	0.13515	0.307(9)	H_2	16·520	1/25	97%
[A3]	8	5.2	0.13515	0.314(8)	P_{140}	16·500	1/26	87%
[A4]	8	5.2	0.13550	0.195(7)	P_{140}	16·400	1/25	85%
[A5]	8	6.0	0.13421	0.193(3)		— quenched —		
[A6]	12	5.5	0.13606	0.287(3)	H_2	16·240	1/20	91%
[A7]	12	6.26	0.13495	0.295(3)		— quenched —		

Table 6.1: Summary of simulation parameters.

6.5 Instabilities in the molecular dynamics integration

We have seen that in the numerical approximation to the molecular dynamics evolution the Hamiltonian is conserved up to powers of the step–size $\delta\tau$ employed in the integration. Apart from these (usually small) deviations, under certain conditions the currently used integration schemes can become unstable and produce very large Hamiltonian violations ΔH. For a more detailed discussion see ref. [88], where a connection between these instabilities and large driving forces in the MD is proposed in analogy to a harmonic oscillator model. In this model the

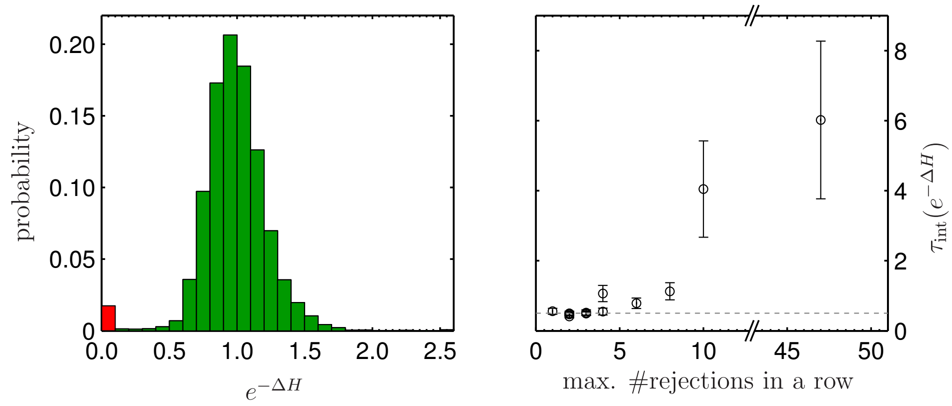

Figure 6.3: $e^{-\Delta H}$ from run [A1]. Left plot: histogram. Right plot: our estimates of $\tau_{\rm int}$ in units of MD time separately for the 16 replica. In our normalization $\tau_{\rm int} = 0.5$ means no autocorrelation (dotted line).

integrator becomes unstable when the product of the force and the integration step–size exceeds a certain threshold.

Large (positive) values of ΔH result in a rejection of the configuration proposed by the MD. In a histogram of $e^{-\Delta H}$ these contribute to bins close to zero while the distribution is peaked around one, indicating that in most cases the numerical integrator performs as expected. They can also lead to an unusual autocorrelation of this quantity, making the Monte Carlo error estimate difficult. In particular this applies also to the integrated autocorrelation time of $e^{-\Delta H}$ itself. This is due to the long periods of rejection in the Metropolis step, which sometimes follow large ΔH values.

Fig. 6.3 shows a histogram of $e^{-\Delta H}$ and also its integrated autocorrelation time from one of our simulations. In this data set there are several series of large ΔH values, during which the proposed configurations were rejected. In the distribution of $e^{-\Delta H}$ these lead to an additional peak close to zero. One also sees from the right–hand plot that $e^{-\Delta H}$ is noticeably autocorrelated only when a large number of proposals were rejected in a row. As argued above in these cases the error of $\tau_{\rm int}$ could be underestimated. These two effects might cause some concerns when using $\langle e^{-\Delta H}\rangle - 1$ as an indicator for the absence of reversibility violations [78].

Spikes in ΔH have been observed by several collaborations using (improved) Wilson fermions in various setups (e.g. different gauge actions and volumes) at relatively large lattice spacings [59, 88, 89, 90]. There these spikes have been traced back to large values of the driving force in the MD evolution and also their dependence on the quark mass has been investigated.

Here we want to clarify a point, which is essentially implied by the previ-

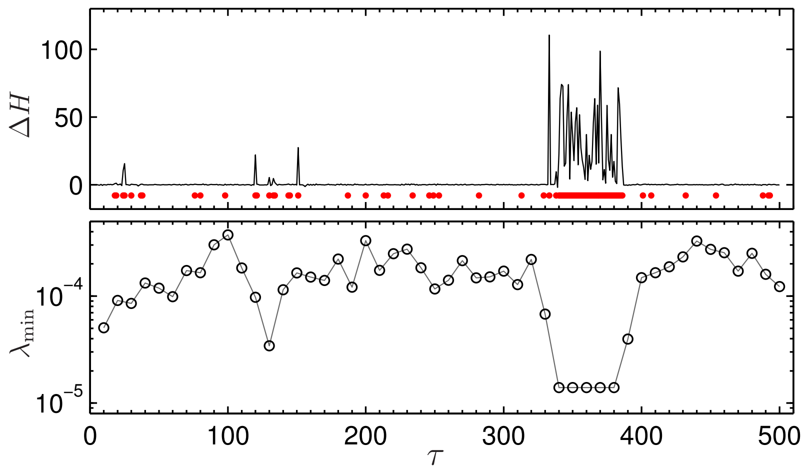

Figure 6.4: Monte Carlo history for one replicum of run [A1] with a long period of rejection. Configurations where the new proposal was rejected are marked by a dot. At $\tau \simeq 340$ the algorithm gets stuck with a configuration carrying an exceptionally low smallest eigenvalue $\lambda_{\min}$ of $\hat{Q}^2$.

ous observations [89, 91], namely the strong correlation between spikes in ΔH and small eigenvalues of the Dirac operator.[3] In this way we hope to be able to separate physical effects from cutoff–effects, i.e. the occurrence of unphysically small eigenvalues. The low–lying eigenvalues are computed using the method described in [92]. In Fig. 6.4 we clearly see a long period of rejection (corresponding to the rightmost data point in Fig. 6.3) caused by the presence of a very small eigenvalue. Although we did not measure them, this is expected to produce large fermionic contributions to the driving forces since they involve an inverse power of the Dirac operator.

We found the observed *average* $\lambda_{\min}$ to be close to its tree–level estimate with Schrödinger functional boundary conditions [10]. However, the *smallest* $\lambda_{\min}$ is an order of magnitude below that and we therefore consider these eigenvalues unphysical and will later establish their nature as cutoff–effects.

Finally, following the procedure of ref. [78], the absence of global reversibility violations is explicitly verified even for trajectories resulting in large values of ΔH. Nevertheless our experience shows that the increased cost of using a smaller $\delta\tau$ such that no long periods of rejection occur is more than compensated by the reduction in autocorrelation time of all observables. The reason is that already a small decrease of the integration step–size greatly reduces the Hamiltonian viola-

[3] Here and in the following we will always refer to the eigenvalues of the square of the Hermitian even–odd preconditioned Dirac operator $\hat{Q}^2$ in the Schrödinger functional. For its precise definition see ref. [78].

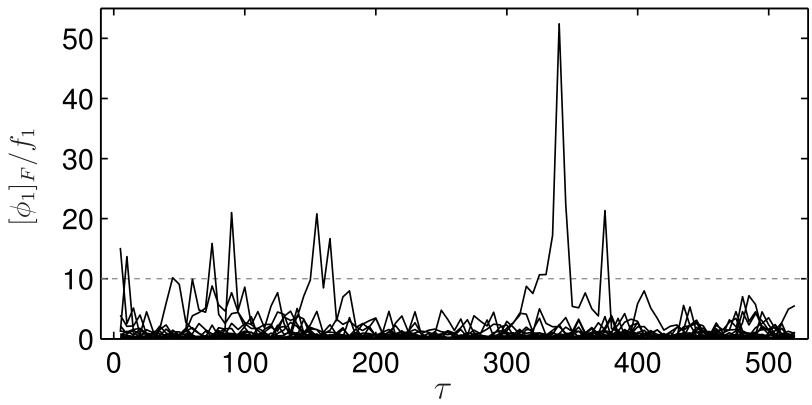

Figure 6.5: Monte Carlo history for the $N_{\rm rep}=16$ replica of run [A2] showing the normalized $[\phi_1]_{\rm F}$.

tions. For example, repeating run [A1] with a step–size of 1/20 instead of 1/16, the longest period of rejection was 4 (instead of 47) consecutive trajectories. Such a rapidly changing behavior also supports the picture of integrator instabilities from [88], where an abrupt increase of Hamiltonian violations is predicted when a certain $\delta\tau$ threshold is exceeded.

6.6 MC estimates of fermionic observables

We concluded in the previous section that unphysically small eigenvalues of $\hat{Q}^2$ produce algorithmic problems only on a practical and not on a theoretical level. But apart from slowing down the algorithm these small eigenvalues also cause problems in the MC evaluation of fermionic Green's functions.

As an example we consider the Schrödinger functional correlation function f_1 as defined in eq. (5.19). It is the correlation between pseudo–scalar composite fields at the first and last time–slice, respectively. We will denote its value on a given gauge field configuration by $[\phi_1]_{\rm F}$.[4] Fig. 6.5 shows the MC history of the normalized $[\phi_1]_{\rm F}$ for the 16 replica of run [A2]. Here τ refers to the molecular dynamics time for each replicum. While on this scale the bulk of the data are below one and hence not visible, there are several peaks, which give a significant contribution to the mean value. These spikes also affect the error estimate $\sigma(f_1)$ through both the variance and the integrated autocorrelation time. For statistically accessible quantities the error should approach a $1/\sqrt{\tau}$ behavior in the limit $\tau\to\infty$. In this respect we found f_1 and all other fermionic correlation functions we considered to be very hard to measure. Even when averaging over 16 replica,

[4] From eq. (B.13) it follows that $[\phi_1]_{\rm F} = {\rm Tr}\,\overline{S}_T\overline{S}_T^{\dagger}/2L^3$.

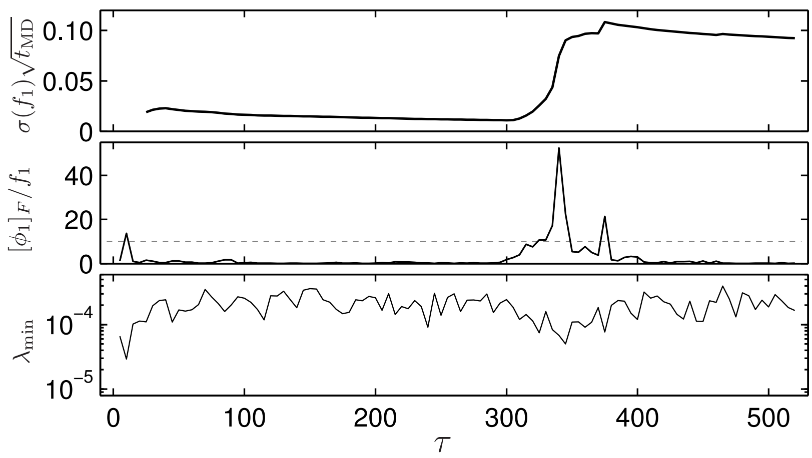

Figure 6.6: Normalized $[\phi_1]_{\rm F}$ and smallest eigenvalue from one "sick" replicum of run [A2]. Evidently the spike in $[\phi_1]_{\rm F}$ is dominating the statistical error $\sigma(f_1)$.

this asymptotic behavior does not set in after $\tau \simeq 500$.

The reason is the rare occurrence of very large values of $[\phi_1]_{\rm F}$, which appear to be correlated with small eigenvalues of $\hat{Q}^2$. However, this effect is washed out by using several replica. We therefore show in Fig. 6.6 the MC history of $[\phi_1]_{\rm F}$, $\lambda_{\rm min}$ and our error estimate for f_1 for one replicum of run [A2] with such a spike in $[\phi_1]_{\rm F}$. Indeed, for each spike in $[\phi_1]_{\rm F}$ the smallest eigenvalue drops below its average. That the converse is not true could be ascribed to a lack of overlap of the eigenvector corresponding to $\lambda_{\rm min}$ with the source needed to compute the quark propagator. Quantitatively, for the correlation between $[\phi_1]_{\rm F}$ and $\lambda_{\rm min}$ we measure a value of $C_{[\phi_1]_{\rm F},\lambda_{\rm min}} = -0.33(4)$ if we use all replica and $-0.46(6)$ from the replicum shown in Fig. 6.6 alone. Here we used as a definition of the correlation $C_{A,B}$ between two (primary) observables A and B

$$C_{A,B} = \frac{\langle AB\rangle - \langle A\rangle\langle B\rangle}{\sqrt{\Big\langle A^2 - \langle A\rangle^2\Big\rangle\Big\langle B^2 - \langle B\rangle^2\Big\rangle}}\,, \quad \text{so that} \quad -1 \leq C_{A,B} \leq 1\,. \tag{6.16}$$

Even though in the limit of infinite statistics configurations carrying very small eigenvalues are given the correct weight, depending on the algorithm this might be badly approximated for a typical ensemble size. Similar arguments referring in particular to the HMC algorithm motivated the introduction of the polynomial hybrid Monte Carlo (PHMC) algorithm in refs. [87, 93, 94].

Hence the difficulty in measuring fermionic correlation functions might be an efficiency problem related to the choice of the algorithm. To check this conjecture we employ a second algorithm and compare ensembles generated by HMC (with two pseudo–fermion fields) with PHMC ensembles. Indeed, PHMC can be tuned in such a way that it enhances the occurrence of configurations carrying small eigenvalues, thus resulting in a better sampling of this region of configuration space. A reweighting step is introduced to render the algorithm exact. As a preparation for the following discussions we want to recall some properties and introduce the notations concerning the PHMC.

6.6.1 The PHMC algorithm

One of the main ideas of the PHMC algorithm is to deliberately move away from importance sampling by using an approximation to the fermionic part of the lattice QCD action. More precisely, in an HMC algorithm the inverse of $\hat{Q}^2$ is replaced by a polynomial $P_{n,\epsilon}(\hat{Q}^2)$ of degree n. Here $P_{n,\epsilon}(x)$ approximates $1/x$ in the range $\epsilon \leq x \leq 1$. As a consequence this algorithm stochastically implements the weight $\mathcal{D}U \det P_{n,\epsilon}^{-1}(\hat{Q}^2)e^{-S_g}$, whereas standard HMC generates ensembles according to $\mathcal{D}U \det \hat{Q}^2 e^{-S_g}$. Denoting averages over the PHMC ensemble by $\langle \ldots \rangle_P$, the correct sample average of an observable $\langle O \rangle$ can then be written as

$$\langle O \rangle = \langle O\omega \rangle_P \ , \ \text{where} \ \ \omega = \frac{W}{\langle W \rangle_P} \ , \tag{6.17}$$

and we introduce the reweighting factor W as a (partially) [5] stochastic estimate of $\det\{\hat{Q}^2 P_{n,\epsilon}(\hat{Q}^2)\}$. When using Chebyshev polynomials the relative approximation error of $P_{n,\epsilon}$ is bounded by $\delta \simeq 2\exp(-2\sqrt{\epsilon}n)$ in the range $\epsilon \leq x \leq 1$.

To give an impression of the rôle of ϵ and δ we plot in Fig. 6.7 a set of polynomials $P_{n,\epsilon}(x)$ for typical (in our simulations) values of these parameters and compare them with $1/x$ in the region of small x. Depending on the smallest eigenvalue of $\hat{Q}^2$ the parameters ϵ and n have to be tuned such that the reweighting factor does not fluctuate too much. The authors of ref. [87] suggested to take ϵ of the same order as $\langle \lambda_{\min} \rangle$ and in practice used $\epsilon \simeq 2\langle \lambda_{\min} \rangle$ and $\delta \lesssim 0.01$.

Recalling that PHMC replaces $\det \hat{Q}^2$ in the HMC weight with $\det P_{n,\epsilon}^{-1}(\hat{Q}^2)$ and observing from Fig. 6.7 that $P_{n,\epsilon}(x)$ is smaller than $1/x$ for $x \leq \epsilon$, the aforementioned property of enhancing the occurrence of small eigenvalues is evident. At this point we would like to note that the fermionic contribution to the driving force in the PHMC is bounded from above since $P_{n,\epsilon}(x)$ is finite even at $x = 0$. In this way the polynomial provides a regularized inversion of $\hat{Q}^2$, thus also addressing the problems mentioned in Section 6.5.

6.6.2 HMC vs. PHMC

Coming back to the comparison of samples from HMC and PHMC, we repeated run [A2] with PHMC using a polynomial of degree 140 and $\epsilon = 6 \cdot 10^{-4}$, resulting

[5] Through the separate treatment of the lowest eigenvalues of $\hat{Q}^2$ the infrared part of W is evaluated exactly.

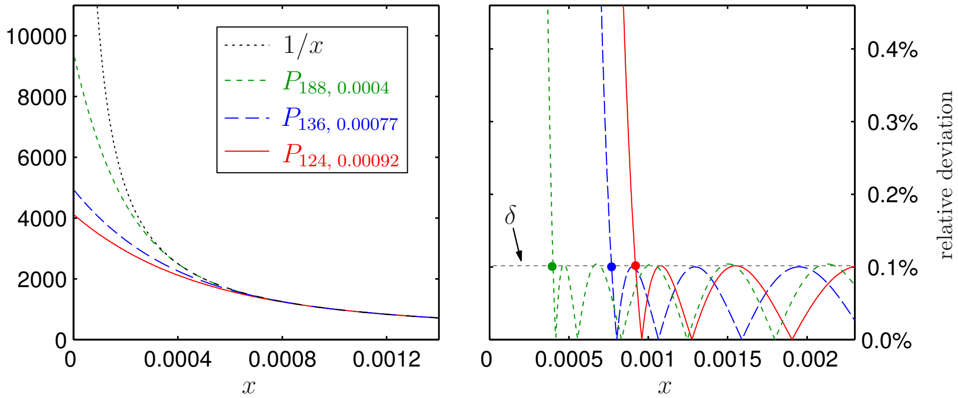

Figure 6.7: Three different Chebyshev polynomials approximating $1/x$, all with $\delta = 0.001$. The right–hand plot shows the relative deviation from $1/x$ as a function of x. There the points (ϵ, δ) are marked by dots.

in $\delta \simeq 0.002$. The ratio $\epsilon/\langle\lambda_{\min}\rangle$ turned out to be around 2.7. In Fig. 6.8 we plot for this run the MC history of $[\phi_1]_{\mathrm{F}}$ and of $[\phi_1]_{\mathrm{F}} \cdot \omega$, which enters into eq. (6.17) if we consider $O = [\phi_1]_{\mathrm{F}}$, i.e.

$$f_1 = \langle [\phi_1]_{\mathrm{F}} \rangle = \langle [\phi_1]_{\mathrm{F}} \cdot \omega \rangle_P = \frac{\langle [\phi_1]_{\mathrm{F}} \cdot W \rangle_P}{\langle W \rangle_P} \, . \tag{6.18}$$

We first observe that apart from removing the largest spikes the inclusion of the reweighting factor does not seem to significantly change the relative fluctuations. This means that the parameters of the polynomial have been chosen properly. Events where $[\phi_1]_{\mathrm{F}}$ assumes a value O(10) times larger than f_1 are no longer isolated as in Fig. 6.5 but happen frequently, which means that the PHMC algorithm can more easily explore the associated regions in configuration space. This is what allows a reliable error estimate as shown in the upper part of Fig. 6.8, i.e. with 16 replica the asymptotic behavior of the error sets in after $\tau \simeq 100$.

The advantage of using PHMC instead of HMC can be clearly seen by considering the spread of $\sigma(f_1)\sqrt{\tau}$ among the replica. We analyzed this quantity in extensions of runs [A2] and [A3]. The result is shown in figure Fig. 6.9, where the shaded areas represent the range of values covered by the 16 replica as a function of the MD time. In the limit of infinite statistics all replica should converge to the same value, which need not be the same for the two algorithms because of reweighting and different autocorrelation times. We see that the spread for the HMC data is more than twice as large as for PHMC, i.e. the error on f_1 is significantly harder to estimate with HMC.

What we are suggesting here is that the algorithm should be chosen depending on the type of observables and the parameter values. From our experience we

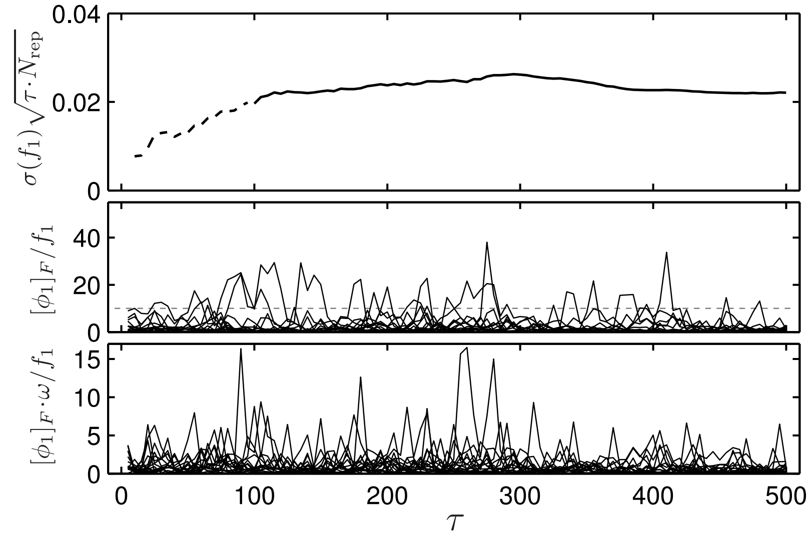

Figure 6.8: Monte Carlo history for the 16 replica of run [A3] showing the correlation function $[\phi_1]_{\mathrm{F}}$ and the product $[\phi_1]_{\mathrm{F}} \cdot \omega$, where ω is the normalized reweighting factor. Our error estimate of f_1 shows the expected scaling behavior as soon as the run is long enough for a reliable extraction of τ_{int}.

conclude that PHMC sampling might just be more effective than HMC when computing fermionic quantities that are sensitive to small eigenvalues.

To gain some more insight into the difference in sampling we consider the distribution of λ_{min} since this is where we expect the largest effect. The distributions are analyzed by treating $\Lambda_{\mathrm{bin}} = \chi_{\mathrm{bin}}(\lambda_{\mathrm{min}})$ as a primary observable. Here χ_{bin} denotes the characteristic function of each given bin in the histogram. We then perform our normal error analysis for $\langle \Lambda_{\mathrm{bin}} \rangle$, where eq. (6.17) has to be used if it is a PHMC sample. For comparison $\langle \Lambda_{\mathrm{bin}} \rangle_P$ is also analyzed in this case.

The histograms in the upper part of Fig. 6.10 compare the results from 200 independent measurements produced by HMC and PHMC (runs [A2] and [A3], respectively). As expected the distributions agree within errors. For the PHMC run we also plot the unreweighted histogram, i.e. $\langle \Lambda_{\mathrm{bin}} \rangle_{\mathrm{P}}$. Here we again confirm that with the parameters we chose for the polynomial the PHMC produces more configurations with small eigenvalues than HMC. As a consequence of the reweighting the errors at the infrared end of the spectrum should be smaller for the PHMC data. This is explicitly verified in the lower part of the plot where we show the ratio of the errors on $\langle \Lambda_{\mathrm{bin}} \rangle$ from the two algorithms. One can see that below $\approx 7 \cdot 10^{-5}$ the error from PHMC is at least a factor two smaller than from HMC, with a more pronounced difference towards even smaller eigenvalues. The advantage in using PHMC to sample this part of the spectrum is significant and we will make use of this in the following discussion.

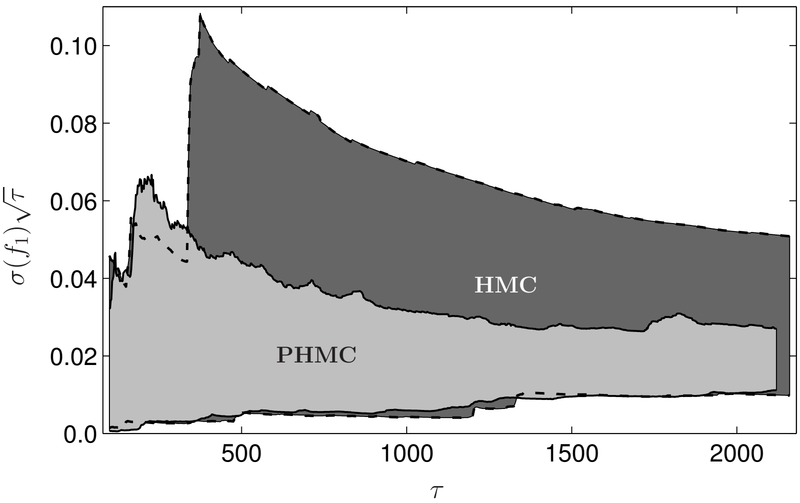

Figure 6.9: Monte Carlo history of $\sigma(f_1)\sqrt{\tau}$ from extensions of runs [A2] and [A3]. For the two algorithms we show the ranges covered by the 16 replica.

6.7 Comparison to the quenched case

In the previous section we studied various problems related to the occurrence of small eigenvalues. All the data presented there were produced at bare parameter values, which correspond to relatively large quark masses and small volumes. These small eigenvalues might therefore have a different nature from the "physical" ones expected to show up in large volumes and/or close to the chiral limit. Here and in the next section we will establish them as cutoff–effects.

To this end we made an additional simulation at the parameters of run [A2] and calculated the ten lowest–lying eigenvalues λ_i, $i = 1 \ldots 10$. In Fig. 6.11 the smallest eigenvalue, λ_1, is denoted by an open symbol. It seems that while λ_2 through λ_{10} form a rather compact band, the lowest eigenvalue fluctuates to very small values quite independently of the others. It is expected and has been shown numerically [95] that the spectrum of the Dirac operator depends quite strongly on the bare gauge coupling. A well–defined lower bound should be recovered close to the continuum limit only. Therefore we take the strong fluctuations of $\lambda_{\min}$ as an indication for the presence of large cutoff–effects. Here we should point out that the eigenvalues of the Dirac operator are not on–shell quantities and hence the Symanzik improvement programme does not necessarily reduce cutoff–effects here. Quenched experience even suggests that the opposite might be true [96].

The occurrence of small eigenvalues at these bare parameters poses a somewhat unexpected problem in dynamical simulations. Comparing the quenched situation to the $N_f = 2$ dynamical case, the naïve expectation is that at fixed bare parameters the probability of finding configurations with small eigenvalues

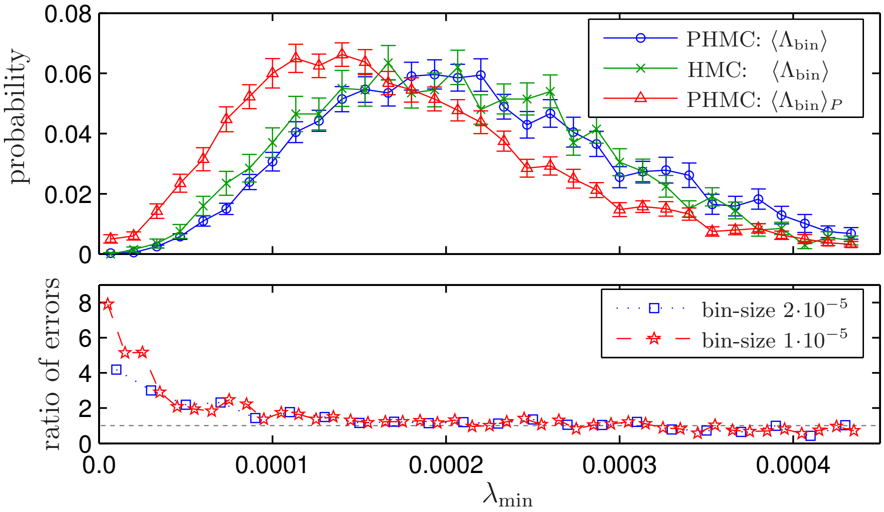

Figure 6.10: Upper panel: histograms of $\lambda_{\rm min}$, i.e. $\langle\Lambda_{\rm bin}\rangle$ vs. 'bin', from runs [A2] and [A3]. For run [A3] we also show $\langle\Lambda_{\rm bin}\rangle_P$. Lower panel (from the same data): ratio of the error on $\langle\Lambda_{\rm bin}\rangle$ from HMC to that from PHMC.

should be reduced by the determinant. To us the more relevant question seems to be whether small eigenvalues are suppressed in a situation where the physical parameters (e.g. volume and pseudo–scalar mass) are kept constant.

Using the quenched data from ref. [72] and the dynamical data from refs. [97] and [98] (where an estimate of $r_0/a = 5.21(6)$ for $\beta = 5.2$ can be found) we chose the parameters of the quenched run [A5] such that the lattice spacing and the (large volume) pseudo–scalar mass are matched to run [A4]. This was found to occur at almost equal bare current quark mass (see Lm in Table 6.1). In Fig. 6.12 we compare the distributions of $\lambda_{\rm min}$ for these two runs. Two comments are in order here:

- For the dynamical run the mean value is shifted up from $1.44(1)\cdot 10^{-4}$ to $1.72(5)\cdot 10^{-4}$. This agrees with the naïve expectation but in a physically matched comparison it is a non–trivial observation.
- The distribution itself is significantly broader compared to the quenched case and in particular it is falling off more slowly towards zero. This means that even though $\langle\lambda_{\rm min}\rangle$ is larger for $N_f = 2$ the probability of finding *very* small eigenvalues is enhanced.

The second point, i.e. that the lower bound of $\lambda_{\rm min}$ is less well–defined, seems to imply that at a lattice spacing of $a \approx 0.1\,$fm the cutoff–effects are much larger in the $N_f = 2$ case. To substantiate this we will compare the distribution of $\lambda_{\rm min}$ to that from a run at finer lattice spacing and matched physical parameters.

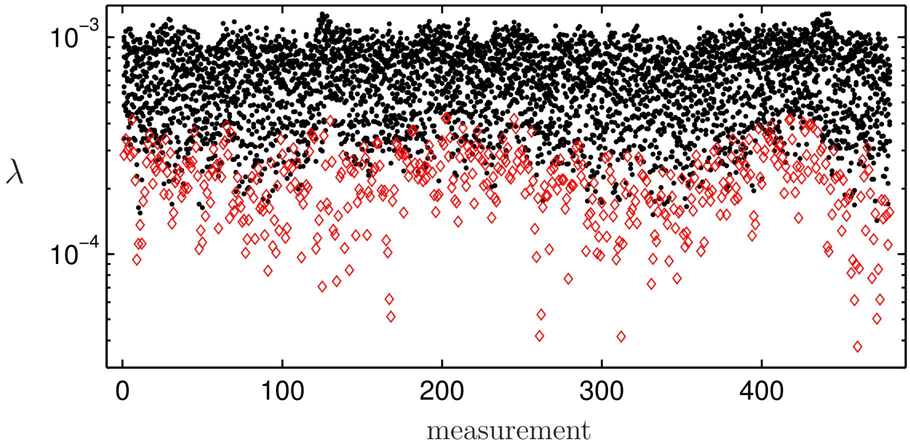

Figure 6.11: Monte Carlo history of the ten lowest eigenvalues at the parameters of run [A2]. The open symbols denote $\lambda_{\min}$.

6.8 Finer lattices

Apart from cutoff–effects, in the massless theory the Schrödinger functional coupling $\bar{g}^2$ is a function of the box size L only [9, 10]. We measured it on a small lattice of extension $L/a=4$ at $\beta = 5.2$, obtaining a value of $\bar{g}^2=3.7(1)$. We then extrapolated to this value the $L/a=6$ data used in ref. [99] as a function of β. Our result from the matching is that for the two–flavor theory a bare gauge coupling of $\beta = 5.5$ roughly corresponds to a lattice spacing, which is 1.5 times smaller than at $\beta=5.2$. This estimate will be confirmed by other non–perturbative data as well as the perturbative evolution of a in Chapter 7.

Hoping that the algorithmic difficulties arising from cutoff–effects would be much smaller in this situation, we simulated a $12^3\times 27$ lattice at this value of β (run [A6]) using the HMC algorithm. With the κ we chose (and ignoring the change in renormalization factors) the bare quark mass Lm is roughly matched to the heavier runs at $\beta=5.2$. We therefore compare run [A6] with run [A3].

Normally, a constant acceptance requires a decrease of the MD integration step–size if ones goes to finer lattices at fixed physical conditions. This argument is based on the scaling of the small eigenvalues[6], which influence the MD driving force. We found that $\langle\lambda_{\min}\rangle$ in run [A6] is a factor two smaller than in run [A3]. Nevertheless, at $\beta=5.5$ the step–size necessary for a certain ($\simeq 90\%$) acceptance is roughly the same as at $\beta = 5.2$. This indicates that the value of $\delta\tau$ we had to use in the HMC runs at $\beta=5.2$ was dictated by the occurrence of extremely small eigenvalues rather than by the average smallest eigenvalue. In addition,

[6] As the squared Dirac operator, its eigenvalues have mass dimension two and should thus behave like a^2.

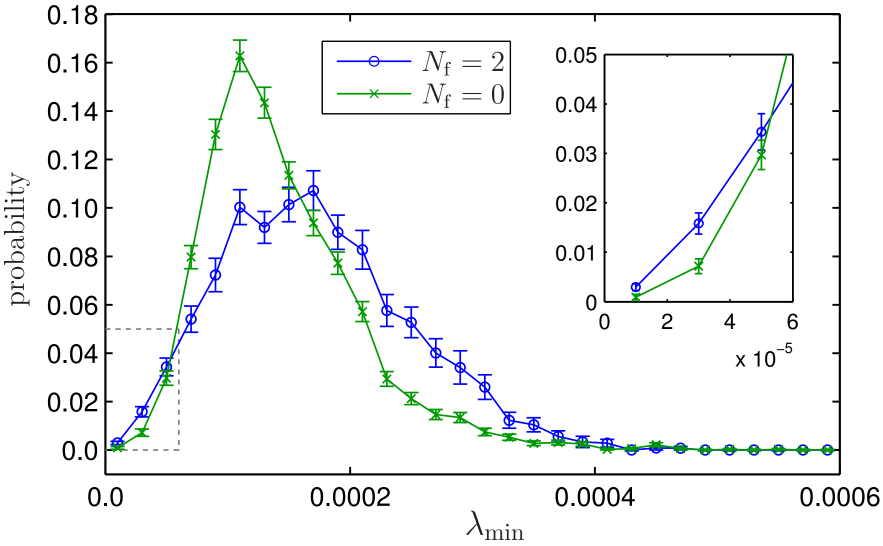

Figure 6.12: The histograms of λ_{min} from run [A4] ($N_f = 2$) and run [A5] ($N_f = 0$). Despite its higher mean value the dynamical data show a much larger probability of finding very small eigenvalues.

where in run [A1] at the same average acceptance a maximum of 47 proposals were rejected in a row, the maximum for run [A6] is 4 trajectories. For this reason $e^{-\Delta H}$ shows no autocorrelation and its distribution is well separated from zero.

Concerning fermionic observables, we have not observed spikes and hence expect the error to scale properly. However, for an accurate estimate of the error on e.g. f_1 our present statistics is not sufficient. One should note that *ratios* of correlators are easier to estimate since usually numerator and denominator are correlated, which reduces the impact of statistical fluctuations. This applies to essentially all relevant quantities, including the axial current improvement and renormalization constants discussed in the next chapters.

The reason for these effects is the change in the distribution of λ_{min}. To compensate for the different lattice spacing, Fig. 6.13 compares $\lambda_{\text{min}}/\langle\lambda_{\text{min}}\rangle$ from runs [A3] and [A6]. One can clearly see that at the finer lattice spacing the probability of finding a smallest eigenvalue less than half its average is greatly reduced compared to $\beta = 5.2$. The width of the distribution is smaller in this case and in particular the spectrum is now clearly separated from zero. Quantitatively, the normalized variance of λ_{min} is reduced from 0.18(1) to 0.13(2).

This comparison explicitly shows that the long tail of the eigenvalue distribution we observed at $a \simeq 0.1\,\text{fm}$, and which caused the problems we have discussed, is a cutoff–effect. Matching also run [A6] to a quenched simulation (run [A7]), we again found an upward shift of $\langle\lambda_{\text{min}}\rangle$ for the dynamical case. In addition, at

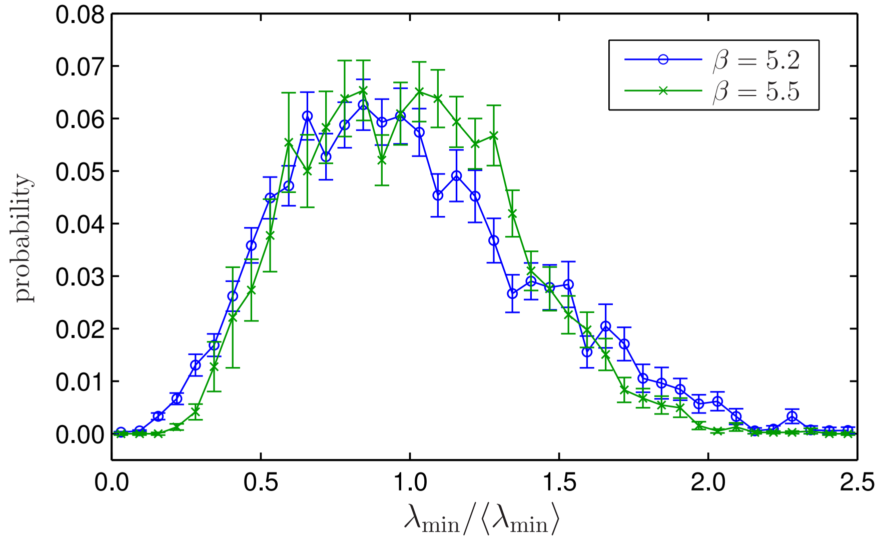

Figure 6.13: Normalized distributions of $\lambda_{\min}$ from runs [A3] ($\beta = 5.2$) and [A6] ($\beta = 5.5$). While the data from the coarse lattice stretch almost to zero, the $\beta = 5.5$ data seem to have a more well–defined lower bound.

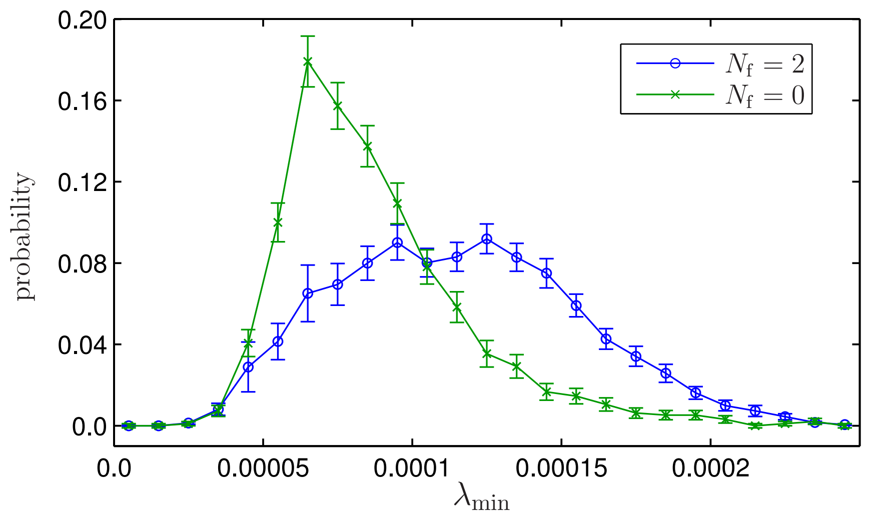

Figure 6.14: The histograms of $\lambda_{\min}$ from run [A6] ($N_f = 2$) and run [A7] ($N_f = 0$). At this finer lattice spacing the lower end of the spectrum appears to be similar in the quenched and the dynamical case.

this finer lattice spacing, the tails of the distributions of $\lambda_{\rm min}$ look already very similar to each other as shown in Fig. 6.14.

6.9 Conclusions

At a lattice cutoff of approximately 2 GeV, corresponding to $a \simeq 0.1\,\rm fm$, we have studied the behavior and performance of HMC–type algorithms in an intermediate size volume of $1\,\rm fm^4$. We discussed problems related to the occurrence of small eigenvalues in two–flavor dynamical simulations with improved Wilson fermions. We found these small eigenvalues to be responsible for large Hamiltonian violations in the molecular dynamics. Even for integration step–sizes such that the acceptance is $80 \sim 90\%$ those can still cause long periods of rejection, thus degrading algorithmic performance. However, in spite of employing only single–precision arithmetics we never observed reversibility violations.

In addition, those eigenvalues make the estimate of fermionic quantities very difficult. The naïve intuition is that the fermionic determinant should suppress small eigenvalues compared to the quenched case. Through a direct comparison at matched physical parameters we indeed verified that $\langle \lambda_{\rm min} \rangle$ is larger with two dynamical flavors. On the other hand there is no obvious expectation for the tail of the distribution and we observed that it extends further towards zero than in the quenched case. Given the infrared cutoff induced by the Schrödinger functional boundary conditions and the quark mass we interpret this as a lattice artifact. We were able to confirm this picture with a simulation at finer lattice spacing, where the spectrum turned out to have a much sharper lower bound.

In our study we found that the PHMC algorithm is more efficient than HMC (with two pseudo–fermions) in incorporating the contribution to the path integral of configurations carrying small eigenvalues. In other words, the distortion of the spectrum by cutoff–effects actually makes it advantageous to deviate from importance sampling. Also without such special problems we found PHMC at least comparable in performance to HMC (in our implementations).

We want to emphasize that the problems discussed here do not occur only in the Schrödinger functional setup. Without this infrared regulator they are expected to show up already at larger quark masses.

Due to the in a sense ”more robust” nature of PHMC one might ask why one should not use it in all simulations. The reason is that with decreasing lattice spacing the smallest eigenvalues will also decrease, which in turn requires a smaller ϵ in the construction of the polynomial as otherwise the fluctuations of the reweighting factor will render the algorithm inefficient.

However, a smaller lower bound in the polynomial approximation implies a larger degree of the polynomial (at constant relative deviation δ). In the current implementation of the PHMC, single precision restricts the degree to ≈ 140 since otherwise roundoff problems appear in the construction of the polynomial.

We therefore used the PHMC only in the simulation for the axial current renormalization at $\beta = 5.2$ and 5.29. The simulations for the axial current improvement condition are performed with a smaller time extension and larger quark mass. Therefore one can safely use HMC at all lattice spacings we consider.

Chapter 7

Axial current improvement

In the quenched approximation, the improvement coefficients c_{sw} and c_{A} have been determined non-perturbatively in the relevant range of bare coupling (or lattice spacings) in [12]. The improvement conditions, from which they have been determined, were derived from the chiral symmetry of the theory in the continuum limit.

More precisely, the PCAC relation (2.28) was required to hold at finite lattice spacing [12, 61, 63]. As will be detailed in the next section, the PCAC relation is considered considered with different external states. In [12, 61, 63], finite volume states were chosen, formulated in the framework of the Schrödinger functional. Later, a determination of c_{A} was performed by evaluating the PCAC relation in large volume [100, 101] at several values of the lattice spacing. While at $a \approx 0.1\,\mathrm{fm}$ these results for c_{A} differ quite significantly from the finite volume definition [12], at smaller lattice spacings the difference decreases.

For the interpretation of this difference, one should keep in mind that beyond perturbation theory the improvement coefficients themselves are affected by $\mathrm{O}(a)$ ambiguities. In some detail this has been discussed and demonstrated numerically in [102]. The $\mathrm{O}(a)$ ambiguity simply corresponds to the fact that in the implementation of the improvement programme the theory is treated only up to $\mathrm{O}(a^2)$ effects. Thus any change of $\mathrm{O}(a)$ of the improvement coefficients only contributes to the terms ϕ_2 and $\mathcal{L}_2$ in (3.14, 3.15) and does therefore not invalidate $\mathrm{O}(a)$ improvement.

While this obviously forbids a unique definition of the improved theory, the $\mathrm{O}(a)$ ambiguities can be made to disappear smoothly if the improvement condition is evaluated with all physical scales kept fixed, e.g. in units of r_0 (3.13), while only the lattice spacing is varied [102]. This is what is meant by a "line of constant physics" (LCP).

Since Symanzik's effective theory describes the lattice artifacts only asymptotically (Section 3.3) it can only be valid for matrix elements dominated by states with energy $E \ll a^{-1}$. It is therefore important to make sure that the improvement conditions are also imposed using low energy states. So far, the methods of

[100, 101] have not yet been implemented such as to satisfy these conditions.

In [103], two improvement conditions for c_{A}, were studied, for which one can choose the kinematic parameters such that the above criteria are satisfied. They are formulated in finite volume with Schrödinger functional boundary conditions, which furthermore helps to render the numerical evaluation feasible in full QCD. These improvement conditions will be discussed in the next section, where we motivate our choice of one of them to compute c_{A} in the $N_{\mathrm{f}}=2$ theory.

7.1 Strategy and techniques

Before going into the details of our strategy and techniques let us comment again on the constant physics condition. In order to keep the physical volume constant, we need to know how the lattice spacing depends on β. With this knowledge we can tune β such that a certain L/a corresponds to a prescribed value of L (or L/r_0). However, this tuning of the volume is not critical in the evaluation of c_{A}, since the latter depends on the volume only through effects of order a/L.[1] A relative uncertainty Δ in the physical volume L (or equivalently in r_0) thus implies a relative uncertainty in c_{A}, which is proportional to $a/L \cdot \Delta$. As a consequence, even if Δ varies a bit in the considered range of lattice spacings, this is quite irrelevant, in particular if Δ is a smooth function of the lattice spacing. Therefore the constant physics condition with respect to the volume has to be enforced with only moderate precision.

In the remainder of this section we will state in more detail how the constant physics condition is implemented. We will also discuss the methods in [12, 103] to determine c_{A}, with emphasis on the one we finally used.

7.1.1 Constant physics condition

With two degenerate flavors of light quarks, the theory has two bare parameters, β and m_0. Roughly speaking, the bare quark mass m_0 controls the physical quark mass and the bare coupling determines the lattice spacing, defined at vanishing quark mass (for a more precise discussion see [63, 85]). Non–perturbative estimates of

$$t_{r_0}(\beta) = \frac{[r_0/a](5.2)}{[r_0/a](\beta)} \,, \tag{7.1}$$

are available in a limited range of β [97, 104]. In [2], the results of [97, 104] were extrapolated to zero quark mass. Taking directly these values for $[r_0/a](\beta)$, we have the points with error bars in Fig. 7.1. From those we roughly estimated the location of the filled points, using the perturbative dependence of the lattice spacing on β as a guideline. For our action this is given to three loops in [105], which builds on various steps carried out in [106, 107, 108, 109, 110, 111, 112].

[1] Effects of order am will be discussed later.

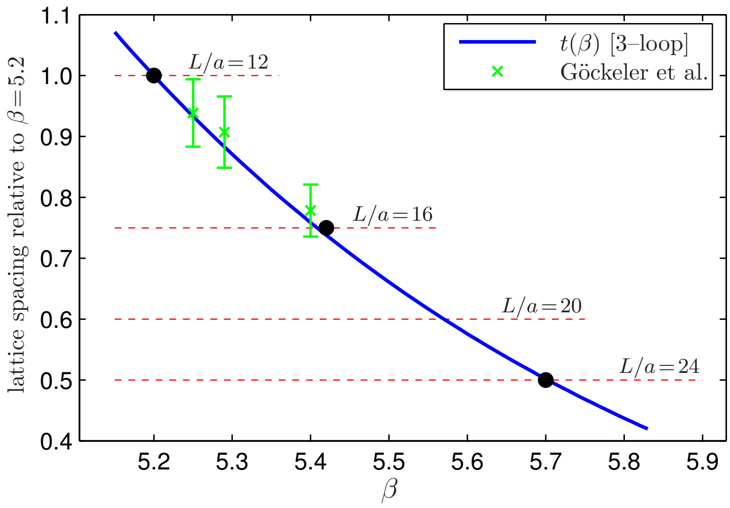

Figure 7.1: The evolution of the lattice spacing a with the inverse bare gauge coupling β from perturbation theory in the lattice scheme and large volume data [104] for the scale r_0. The filled points correspond to our "scaled" simulations.

Applied as a pure expansion in the bare coupling (no tadpole improvement), one has

$$\frac{a(g_0^2)}{a((g_0')^2)} = e^{-[g_0^{-2}-(g_0')^{-2}]/2b_0}[g_0^2/(g_0')^2]^{-b_1/2b_0^2}\left[1+q\,[g_0^2-(g_0')^2]+\mathrm{O}\left((g_0')^4\right)\right],$$
$$q = 0.4529(1)\,, \quad g_0 < g_0'\,. \tag{7.2}$$

The evolution of the lattice spacing relative to our reference point at $(g_0')^2 = 6/5.2$ is then expressed by the function $t(\beta) = a(6/\beta)/a(6/5.2)$, which is plotted as a thick line in the graph. It confirms that the filled points are very reasonable choices. Note that other forms of applying bare perturbation theory (differing from eq. (7.2) in the g_0^4-term) would give somewhat different results, but since we are interested in a rather limited range in g_0^2 this is of no great importance. Later we will show that systematic uncertainties in c_A introduced by this approximate scale setting are negligible. Finally, we keep the PCAC mass (5.22), evaluated with an average of f_X and g_X approximately constant.

7.1.2 Improvement conditions for the axial current

In this section we discuss criteria for the choice of the improvement condition. Quark masses derived from the PCAC relation are of the form

$$m(x;\alpha,\beta) = \frac{\langle\alpha|\tilde{\partial}_\mu (A_\mathrm{I})^a_\mu(x)|\beta\rangle}{2\langle\alpha|P^a(x)|\beta\rangle}\,. \tag{7.3}$$

Since this mass is obtained from an operator identity, it is independent of the states $|\alpha\rangle$ and $|\beta\rangle$ as well as the insertion point x up to cutoff–effects. Enforcing this independence at *finite* lattice spacing leads to possible definitions of improvement conditions [103]. Inserting the expression for the improved current (4.25) in the previous equation, the quark mass can be written as $m = r + ac_{\rm A}s + \mathrm{O}(a^2)$ with

$$r(x;\alpha,\beta) = \frac{\langle\alpha|\tilde{\partial}_\mu A^a_\mu(x)|\beta\rangle}{2\langle\alpha|P^a(x)|\beta\rangle} \tag{7.4}$$

and

$$s(x;\alpha,\beta) = \frac{\langle\alpha|\partial_\mu\partial^*_\mu P^a(x)|\beta\rangle}{2\langle\alpha|P^a(x)|\beta\rangle} \,. \tag{7.5}$$

If we now consider two sets of external states and two insertion points, the improvement condition $m(x;\alpha,\beta) = m(y;\gamma,\delta)$ yields

$$-\,c_{\rm A} = \frac{\Delta r}{a\Delta s} = \frac{1}{a}\cdot\frac{r(x;\alpha,\beta) - r(y;\gamma,\delta)}{s(x;\alpha,\beta) - s(y;\gamma,\delta)} \,. \tag{7.6}$$

The "sensitivity" to $c_{\rm A}$ of an improvement condition is therefore given by $a\Delta s$, since it is this term, which is multiplied by $c_{\rm A}$ in the current quark masses.

Once a reasonably large sensitivity is achieved, all improvement conditions at constant physics are equally valid in the sense that $\mathrm{O}(a)$ effects are removed in on-shell quantities. However, the way in which *higher–order* lattice artifacts are modified will depend on the concrete choice of the improvement condition. In particular, if states with energy not so far from the cutoff are involved, large $\mathrm{O}(a^2)$ effects might be introduced.

To discuss the different improvement conditions we need to generalize the Schrödinger function correlators introduced in Section 5.2. Instead of projecting both boundary quarks to zero momentum separately (5.13,5.14), we now use boundary fields products, which depend on spatial trial "wave functions" $\omega(\mathbf{x})$ [113]. In the following we will use

$$f_{\rm A}(x_0;\omega) = -\frac{a^3}{3L^{3/2}}\sum_{\mathbf{x}}\langle A^a_0(x)\,\mathcal{O}^a(\omega)\rangle \,, \tag{7.7}$$

$$f_{\rm P}(x_0;\omega) = -\frac{a^3}{3L^{3/2}}\sum_{\mathbf{x}}\langle P^a(x)\,\mathcal{O}^a(\omega)\rangle \,, \tag{7.8}$$

and

$$f_1(\omega',\omega) = -\frac{1}{3L^3}\langle\mathcal{O}'^a(\omega')\,\mathcal{O}^a(\omega)\rangle \,, \tag{7.9}$$

which depend on the pseudo–scalar operator

$$\mathcal{O}^a(\omega) = a^6\sum_{\mathbf{x},\mathbf{y}}\bar{\zeta}(\mathbf{x})\gamma_5\tau^a\tfrac{1}{2}\omega(\mathbf{x}-\mathbf{y})\zeta(\mathbf{y}) \tag{7.10}$$

at the $x_0 = 0$ boundary and the corresponding operator $\mathcal{O}'^a(\omega')$ at the upper boundary of the SF cylinder.

The Schrödinger functional version of eqs. (7.4) and (7.5) is then given by

$$r(x_0;\omega) = \frac{\tilde{\partial}_0 f_\mathrm{A}(x_0;\omega)}{2 f_\mathrm{P}(x_0;\omega)} \tag{7.11}$$

and

$$s(x_0;\omega) = \frac{\partial_0 \partial_0^* f_\mathrm{P}(x_0;\omega)}{2 f_\mathrm{P}(x_0;\omega)}\ . \tag{7.12}$$

To determine c_A in the $N_\mathrm{f} = 0$ theory [12], Δr and Δs were originally defined through a variation of the periodicity angle θ of the fermion fields, while keeping $x_0 = T/2$ and $\omega = const$ fixed. For this method the sensitivity $a\Delta s$ is quite low when $L \gtrsim 0.8\,\mathrm{fm}$, $T = 2L$. In addition, with dynamical fermions different values of θ would require separate simulations. We therefore consider this method as too expensive and disregard it in the following. In the quenched approximation two alternatives have been explored in [103].

Requiring the quark mass to be independent of x_0 (for fixed θ and $\omega = const$) is technically easy to implement. However, also in this case the sensitivity is small unless large values of θ are used. Moreover, the contribution of excited states is not well controlled, because one insertion point must be rather close to a boundary to achieve a sufficiently large sensitivity. Thus, energies which are not far removed from the cutoff may contribute.

The simultaneous requirements of large sensitivity and control of excited–state contribution can be fulfilled more easily with the second method, where variations of the wave function ω have been considered. Ideally, one would like to use two wave functions $\omega_{\pi,0}$ and $\omega_{\pi,1}$, such that the corresponding operator $\mathcal{O}^a(\omega)$ couples only to the ground and first excited state in the pseudo–scalar channel, respectively. As one can easily see from eq. (7.12) the sensitivity to c_A is then proportional to $m_{\pi,1}^2 - m_{\pi,0}^2$, where $m_{\pi,n}$ denotes the mass of the nth excited state in the pseudo–scalar channel. Higher excited states are (by definition) not contributing and in principle the method can be used for rather small T. Hence, we find this the most attractive method both from a theoretical and practical point of view. In the next section we will detail our approximation to this ideal situation.

7.1.3 Wave functions

We will now proceed to the more technical aspects of our method. In order to approximate $\omega_{\pi,0}$ and $\omega_{\pi,1}$ consider a set of N wave functions. Given a vector u in this N–dimensional space, projected correlation functions are defined as (u, f_A) and $(u, f_1 u)$, i.e. f_A is regarded as a vector and f_1 as a matrix in this space. It is useful to represent $f_{\rm X}$ ($\rm X = A, P$) and f_1 as [114]

$$
\begin{aligned}
f_{\rm X}(x_0;\omega_i) &= \sum_{n=0}^{M-1} F_{\rm X}^n v_i^n e^{-m_{\pi,n}x_0} + \mathrm{O}(e^{-m_{\pi,M}x_0}) + \mathrm{O}(e^{-m_{\rm G}(T-x_0)}) \;, \qquad (7.13)\\
f_1(\omega_i,\omega_j) &= \sum_{n=0}^{M-1} v_i^n v_j^n e^{-m_{\pi,n}T} + \mathrm{O}(e^{-m_{\pi,M}T}) + \mathrm{O}(e^{-m_{\rm G}T}) \;, \qquad (7.14)
\end{aligned}
$$

where n labels the states in the pseudo–scalar channel in increasing energy and v_i^n is the overlap of such a state with the one generated by the action of $\mathcal{O}^a(\omega_i)$ on the SF boundary state. The mass $m_{\rm G}$ belongs to the lowest excitation in the scalar channel, the 0^{++} glueball and the coefficients $F_{\rm X}^n$ are proportional to the decay constant of the nth state. Here we have suppressed the explicit volume dependence of all quantities.

Knowledge of v^n would allow the construction of vectors u^n, such that – up to corrections of order $e^{-m_{\pi,M}T}$ – the correlation $(u^n, f_{\rm A})$ receives contribution from the nth state only. These u^n may be computed from the v^n by a Gram-Schmidt orthonormalization. Clearly, u^0 and u^1 can then be used to approximate $\omega_{\pi,0}$ and $\omega_{\pi,1}$.

An approximation to the v^n can be obtained from the eigenvectors of the positive symmetric matrix f_1. We denote the normalized eigenvectors of f_1 by $\eta^0, \eta^1, \ldots$ corresponding to eigenvalues $\lambda^0 > \lambda^1 > \ldots$ and apply eq. (7.14) to η^0 to obtain[2]

$$v^0(v^0,\eta^0)\mathrm{e}^{-m_{\pi,0}T} + \mathrm{O}(\mathrm{e}^{-m_{\pi,1}T}) = \lambda^0\eta^0 \;. \qquad (7.15)$$

Clearly λ_0 is of order $|v_0|^2\mathrm{e}^{-m_{\pi,0}T}$, which is inserted to rewrite the previous equation in terms of the normalized vectors $\hat{v}^n = v^n/|v^n|$

$$\hat{v}^0(\hat{v}^0,\eta^0) = \eta^0 + \mathrm{O}(\mathrm{e}^{-(m_{\pi,1}-m_{\pi,0})T}) \;. \qquad (7.16)$$

Since $\hat{v}^0$ and η^0 are normalized vectors, it follows that $(\hat{v}^0,\eta^0) = 1$ up the error term given above. Together with the orthogonality of the eigenvalues of f_1 this implies

$$
\begin{aligned}
||\hat{v}^0 - \eta^0||^2 &= \mathrm{O}(e^{-(m_{\pi,1}-m_{\pi,0})T}) \qquad (7.17)\\
\text{and}\quad (\eta^1,\hat{v}^0) &= \mathrm{O}(e^{-(m_{\pi,1}-m_{\pi,0})T}) \;. \qquad (7.18)
\end{aligned}
$$

Thus, to the order indicated above, $\hat{v}^0$ is given by η^0 and η^1 is orthogonal to the "ground state vector" $\hat{v}^0$. As eigenvectors of a symmetric matrix the η^n are already orthogonal and we therefore use the approximation

$$\omega_{\pi,0} \simeq \sum_i \eta_i^0\omega_i \qquad \text{and} \qquad \omega_{\pi,1} \simeq \sum_i \eta_i^1\omega_i \qquad (7.19)$$

[2] The glueball contribution will be dropped from now on.

to obtain correlators, which are (for intermediate x_0) dominated by the ground and first excited state, respectively. We note in passing that the ratios v_i^n/v_j^n have a continuum limit if the wave functions are properly scaled with the lattice spacing.

In our simulations we restrict ourselves to a basis consisting of three (spatially periodic) wave functions defined by

$$\begin{aligned}
\omega_i(\mathbf{x}) &= N_i^{-1} \sum_{\mathbf{n}\in\mathbf{Z}^3} \overline{\omega}_i(|\mathbf{x}-\mathbf{n}L|)\,,\; i=1,\ldots,3\,,\\
\overline{\omega}_1(r) &= r_0^{-3/2}\,\mathrm{e}^{-r/a_0}\,,\quad \overline{\omega}_2(r) = r_0^{-5/2}\,r\,\mathrm{e}^{-r/a_0}\,,\\
\overline{\omega}_3(r) &= r_0^{-3/2}\,\mathrm{e}^{-r/(2a_0)}\;,
\end{aligned}\tag{7.20}$$

where a_0 is some physical length scale. We thus keep it fixed in units of L, choosing $a_0 = L/6$. The sum over $\mathbf{n}$ is required to preserve the spatial periodicity. In practice the summation is stopped when the norm of ω no longer changes within single precision arithmetics. The (dimensionless) coefficients N_i are fixed to normalize the wave function via $a^3\sum_{\mathbf{x}}\omega_i^2(\mathbf{x}) = 1$. In this context the correlation functions introduced in Section 5.2 can be regarded as belonging to the flat wave function $\omega_0(\mathbf{x}) = L^{-3/2}$, where both quarks are projected to zero momentum separately. In this case $\mathbf{x}$ and $\mathbf{y}$ in eq. (7.10) are uncorrelated and thus full translational invariance can be used without performing additional inversions of the Dirac operator (see Appendix B.1.1). In the general case $\omega_{1\ldots3}$ we replace one of the spatial sums in eq. (7.10) by a sum over eight far separated points, which means that one performs eight times as many inversions. This additional computational effort is still small compared to the cost of the inversions in the HMC update.

7.2 Numerical computation

7.2.1 Results for the improvement coefficient

Table 7.1 summarizes the parameters of our simulations for the axial current improvement constant. The values of the other improvement coefficients are given in Sections 4.2 and 5.1.

The β values for run [C2] and [C3] have been chosen such that L/r_0 is approximately the same as in run [C1], which corresponds to $L \simeq 1.2\,\mathrm{fm}$. In exploratory quenched studies [103] this volume was found to be sufficient for the described projection method to work. N_{meas} is the number of estimates of c_{A} (with the number of replica denoted explicitly), separated by τ_{meas} in Monte Carlo time. The autocorrelation of these measurements turned out to be negligible. The column labeled $am/t(\beta)$ refers to the bare quark mass $m = r(T/2;\omega_0)+ac_{\mathrm{A}}s(T/2;\omega_0)$, cf. eqs. (7.11, 7.12), which is equivalent to (5.22). The 1–loop value of c_{A} from [61]

run	L/a	T/a	β	κ	$N_{\rm meas}$	$\tau_{\rm meas}$	$am/t(\beta)$	$-c_{\rm A}$
[C1]	12	12	5.20	0.135600	4×80	5	0.0151(9)	0.0638(23)
[C2]	16	16	5.42	0.136300	1×200	4	0.0171(5)	0.0420(21)
[C3]	24	24	5.70	0.136490	2×60	4	0.0151(4)	0.0243(36)
[C4]	12	12	5.20	0.135050	4×39	5	0.0363(6)	0.0697(31)
[C5]	16	20	5.57	0.136496	1×285	8	0.0154(4)	0.0366(36)
[C6]	24	24	6.12	0.136139	2×21	12	0.0002(4)	0.0244(21)

Table 7.1: Summary of simulation parameters and results for $c_{\rm A}$. Runs [C1]-[C3] are at constant physics.

is used here. We tuned the hopping parameter κ in order to keep $am/t(\beta)$ fixed when varying β, thus ignoring (presumably small) changes in the renormalization factors. Note that we have chosen a finite, but small bare quark mass of around 30 MeV. Such a mass helps (in addition to the Dirichlet boundary conditions) to reduce the cost of the simulations. Results from the remaining simulations are used to discuss systematic uncertainties in our determination of $c_{\rm A}$.

We employed the hybrid Monte Carlo algorithm with two pseudo–fermion fields as described in Section 6.1. For all observables we have checked the expected scaling of the statistical error with the sample size and thus verified the absence of the problems described in Sections 6.5 and 6.6 at the volumes and masses we consider here. For run [C2] Fig. 7.2 shows how the error of our estimate for $c_{\rm A}$ (see below) behaves as a function of the Monte Carlo time τ. One can see that already after approximately 200 trajectories the region of statistical scaling is reached.

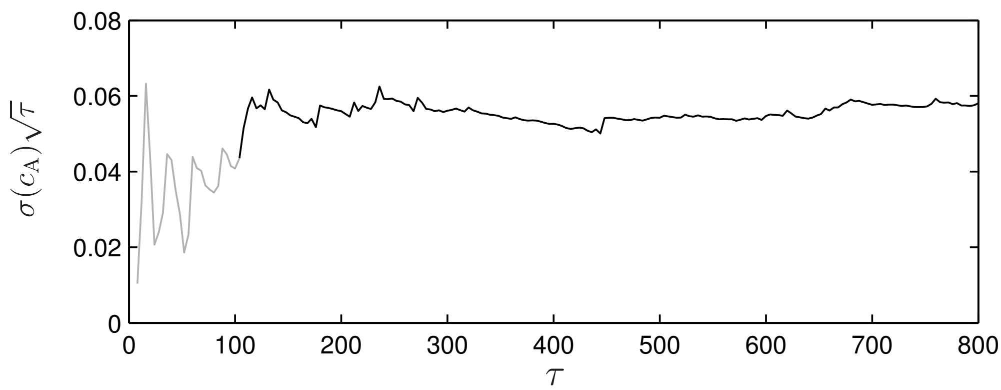

Figure 7.2: The error on $c_{\rm A}$ vs. the Monte Carlo time for run [C2].

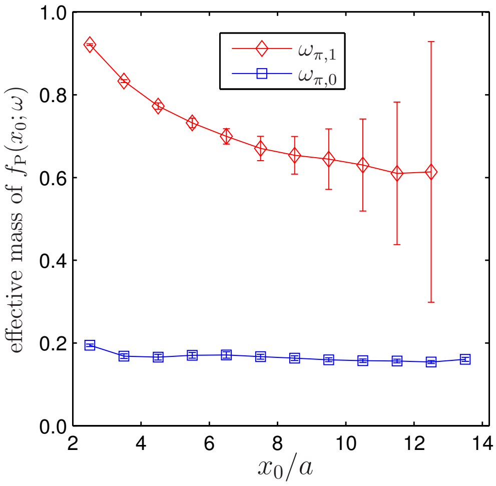

Figure 7.3: The effective mass in lattice units of the projected correlation functions (η^0, f_P) and (η^1, f_P) from run [C2].

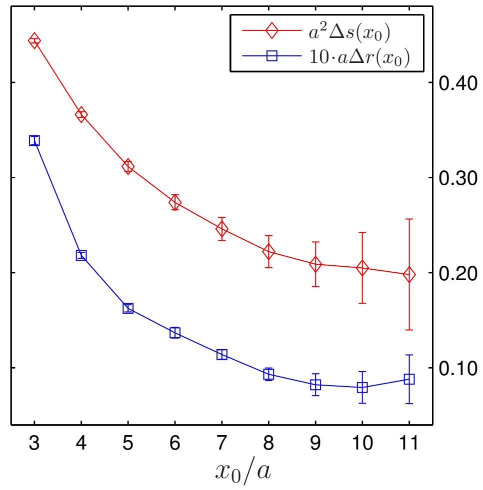

Figure 7.4: $\Delta s(x_0)$ and $\Delta r(x_0)$ determined from $\omega_{\pi,0}$ and $\omega_{\pi,1}$ in run [C2].

In Fig. 7.3 we show the effective masses from $f_\mathrm{P}(x_0;\omega_{\pi,0})$ and $f_\mathrm{P}(x_0;\omega_{\pi,1})$ as obtained in run [C2]. Two distinct signals are clearly visible, which indicates that the described approximate projection method works well at these parameters. The energy of the first excited state is not far away from a^{-1}, suggesting that in even smaller volumes the residual $\mathrm{O}(a^2)$ effects would grow rapidly. In the spirit of the remark after eq. (7.19) at the other values of β we used the same linear combination of wave functions to define $\omega_{\pi,0}$ and $\omega_{\pi,1}$, namely

$$\begin{aligned} \eta^0 &= [\,0.5172, \quad 0.6023, \quad 0.6081\,] \\ \text{and} \quad \eta^1 &= [\,0.8545, \ -0.3233, \ -0.4066\,]\,, \end{aligned} \tag{7.21}$$

which are the ones determined in run [C2]. When scaled in units of r_0, this yields effective masses similar to those shown in Fig. 7.3. Results from a redetermination of $\eta^{(0)}$ and $\eta^{(1)}$ in the other matched simulations agree with eq. (7.21) to a high precision. In fact, one can easily distinguish the matched and unmatched runs using e.g. η^0. Comparing the two 24^4 runs

$$\text{[C3]} \qquad \eta^0 = [\,0.5173(2), 0.6024(1), 0.6079(1)\,]\,, \tag{7.22}$$
$$\text{and [C6]} \qquad \eta^0 = [\,0.5126(2), 0.6042(1), 0.6101(1)\,]\,, \tag{7.23}$$

it is clear that the eigenvector η^0 from run [C3] is in good agreement with (7.21), while a significant deviation is seen in run [C6].

In Fig. 7.3 the error on the effective mass of the first excited state is seen to be quite large, but what actually enters the computation of c_{A} is the error of

$$\Delta r(x_0) = r(x_0;\omega_{\pi,1}) - r(x_0;\omega_{\pi,0}) \quad (7.24)$$

$$\text{and } \Delta s(x_0) = s(x_0;\omega_{\pi,1}) - s(x_0;\omega_{\pi,0}) \,. \quad (7.25)$$

These profit from statistical correlations of the correlation functions entering their definition and thus have smaller statistical errors as can be seen in Fig. 7.4, where we plot $a\Delta r$ and $a^2\Delta s$ from the same data used in Fig. 7.3.

Fig. 7.5 collects results for the "effective" $c_{\mathrm{A}}(x_0) = -\Delta r(x_0)/a\Delta s(x_0)$ from the matched runs [C1]-[C3]. We see little variation for $x_0 \gtrsim 6a$, which we take as another signal that high energy states, which could contribute large O(a) ambiguities in the improvement condition, are reasonably suppressed in this region. We complete our definition of c_{A} with the choice $x_0 = T/2$, which is at the same time scaled in physical units and in agreement with the $x_0 \gtrsim 6a$ bound for all our lattices.

Finally, c_{A} is plotted as a function of g_0^2 in Fig. 7.6. The solid line is a smooth interpolation of the data from the matched simulations, constrained in addition by 1–loop perturbation theory:

$$c_{\mathrm{A}}(g_0^2) = -0.00756\, g_0^2 \times \frac{1 - 0.4485\, g_0^2}{1 - 0.8098\, g_0^2} \,. \quad (7.26)$$

It is our final result, valid in the range $0.98 \leq g_0^2 \leq 1.16$ within the errors of the data points (at most 0.004).

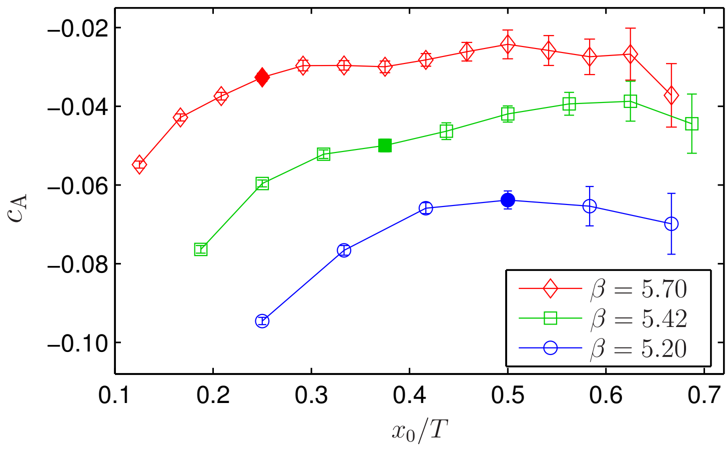

Figure 7.5: Effective c_{A} as determined from $\omega_{\pi,0}$ and $\omega_{\pi,1}$ for runs [C1]-[C3]. Points with $x_0/a = 6$ are marked by filled symbols.

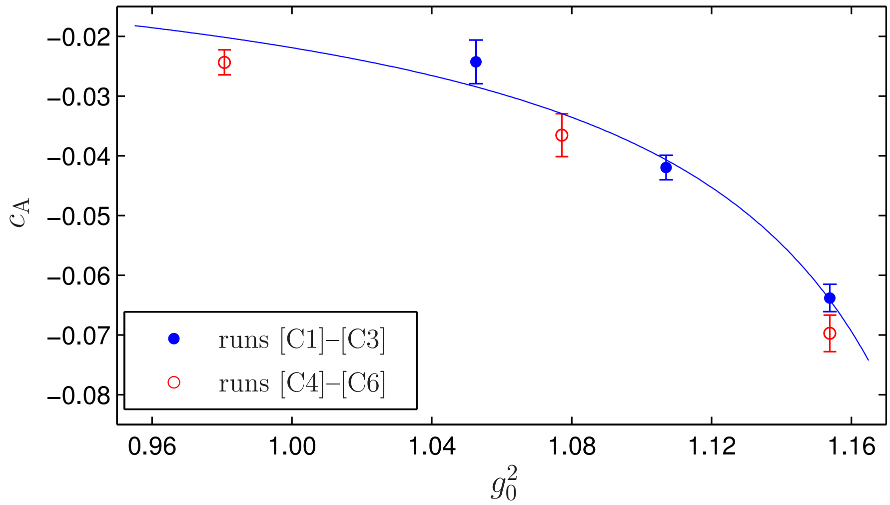

Figure 7.6: Simulation results for c_A. The solid line represents a fit of the data points at constant physics (filled circles).

This non-perturbative result is quite far away form 1–loop perturbation theory, in particular at the coarsest lattice spacing. For $\beta = 5.2$, the perturbative value of $c_A = -0.0087$ is almost an order of magnitude smaller.

Of course this has a significant impact if simulation data are now analyzed using the non–perturbative c_A instead of its 1–loop value. Using e.g. data from [115], we see that the effect on the result for the pseudo–scalar decay constant at this lattice spacing is as large as 10%.

7.2.2 Uncertainties due to deviations from the "constant physics" condition

We should check whether the volumes in our runs [C1]-[C3] are scaled sufficiently precisely or if systematic errors need to be added to the statistical ones on c_A to cover possible violations of the constant physics condition. Table 1 shows that the bare PCAC mass has been kept constant to within about 10%. A renormalized quark mass would differ by the multiplication with a Z-factor, which is a slowly (namely logarithmically) varying function of a. Considering the restricted range of lattice spacings we cover, such factors can be safely ignored. Run [C4] is done with a quark mass which is more than twice as large as the one in run [C1], with otherwise identical parameters. The barely significant difference in c_A confirms that the small deviations from the "constant mass" condition can be neglected.

We also need to examine the impact of the uncertainty in L due to our perturbative (or asymptotic) scaling of the lattice spacing. It has been argued in Section 7.1 that the difference to a proper non-perturbative scaling is rather small. Also, estimating a possible change by comparing 3–loop to 2–loop and non–perturbative scaling, gives a deviation in $t(\beta)$ which is smaller than 10% in the whole range of Fig. 7.1 and thus the same maximum deviation applies to L/a. That this is negligible can be seen from a comparison of run [C5] to the interpolating formula (7.26). In run [C5], L/a is 20% lower than the proper value, but c_A does not differ significantly from the fit curve. As will be discussed in the next section, comparison with significantly smaller volumes at *smaller* β values can lead to enhanced $\mathrm{O}(a^2)$ effects.

Finally, by run [C6] we verify that the dependence of c_A on the kinematic parameters disappears quickly when going to even larger values of β. In this run we used gauge configurations from the calculation of Z_P [78]. Although those were produced at $m=0$, $\theta=0.5$ and a much smaller volume[3], the resulting c_A is only approximately two standard deviations away from our fit.

7.3 Discussion

For the $\mathrm{O}(a)$-improved action with non-perturbative c_sw [59], we have determined the improvement coefficient c_A for $\beta \geq 5.2$, which roughly corresponds to $a \leq 0.1\,\mathrm{fm}$. The improvement condition was evaluated on a line of constant physics, which is necessary in the situation when $\mathrm{O}(a)$ ambiguities in the improvement coefficients are not negligible.

That this is indeed the case here can be seen from an additional run at $\beta=5.42$. Decreasing L/a from 16 to 12 at constant T/a gives $c_\mathrm{A} = -0.0559(21)$, which is about 25% larger in magnitude than its value on our line of constant physics. This can be understood from the fact that the energy levels in the pseudo–scalar channel increase if the volume is decreased. But in order to safely exclude large $\mathrm{O}(a)$ ambiguities, improvement conditions should only involve states with energy $E \ll a^{-1}$. On this requirement we had to compromise more than we would have liked to do already in our LCP volume, where the maximum values for Ea are about 0.7. With larger energies in smaller volume it is only to be expected that the value of c_A changes in trying to compensate the larger $\mathrm{O}(a^2)$ effects.

Although one could have improved the situation, i.e. made Ea smaller, by going to somewhat larger values of L (and T), this would have made the numerical computation much more expensive.

Large $\mathrm{O}(a^2)$ effects have indeed been found in the $N_\mathrm{f} = 2$, $\mathrm{O}(a)$-improved theory [85] at $\beta = 5.2$ and these may well be related to the not so small $\mathrm{O}(a)$ ambiguity in c_A that we just mentioned.

This can only be investigated further by studying the scaling violations in quantities such as $F_\pi r_0$ after improvement and renormalization. The next step after successfully implementing non–perturbative improvement for the axial current

[3] If one would extend $t(\beta)$ to this value, this would indicate a required lattice volume of 43^4.

is therefore its (also non–perturbative) renormalization, which will be discussed in the next chapter.

Clearly, the method described here may also be useful to compute $c_{\rm A}$ in the three flavor case, where $c_{\rm sw}$ is known non–perturbatively with plaquette and Iwasaki gauge actions [60, 116, 117].

Chapter 8

Axial current renormalization

After the successful non–perturbative improvement of the axial current, we can now turn to the problem of its normalization. In the quenched case [11], a non–perturbative renormalization of the isovector axial current was achieved by requiring certain continuum chiral Ward identities to hold at finite lattice spacing. These relate matrix elements of the axial and vector currents and thus link the normalization of the two. The local vector current is normalized by enforcing isospin symmetry, again in the form of an integrated Ward identity.

In fact, the situation is similar to the calculation of $c_{\rm A}$. Also here the results (i.e. $Z_{\rm A}$ and $Z_{\rm V}$) are ambiguous due to cutoff effects and in order to obtain them as smooth functions of g_0^2 we need to evaluate our normalization conditions on a line of constant physics, keeping all length scales fixed. As discussed in Section 4.3, the normalization conditions have to be set up at vanishing quark mass since we want to implement a mass–independent renormalization scheme.

While this is in principle possible in the Schrödinger functional, we have seen in Chapter 6 that cutoff effects make simulations at small quark masses and coarse lattice spacings difficult. Although this problem is addressed efficiently through the use of the PHMC algorithm, it is still desirable to formulate the normalization conditions such that they have only very little dependence on the quark mass. This is the point where we improve the method employed in the quenched case [11] by deriving a normalization condition from the axial Ward identity including the mass term. This new normalization condition naturally reduces to the previously used one in the chiral limit, but numerical results can now be more easily extrapolated in the quark mass.

After deriving the normalization conditions for the isovector currents, the advantage of using the new condition is demonstrated through its chiral extrapolation in a quenched example. Then the results for two dynamical flavors are presented and summarized in interpolating formulae. We also discuss systematic errors due to deviations from the line of constant physics and other variations of the normalization condition.

8.1 Continuum Ward identities

In Section 2.3 we considered Ward identities derived from the flavor chiral symmetry of the continuum QCD Lagrangian. Here we will generalize these to matrix elements, where (part of) the operator insertion has support in the region, where the field transformations are performed. As a result eqs. (2.27) and (2.28) will be modified by terms containing the variation of this "internal" operator.

8.1.1 VWI

Again we consider only the case of two degenerate quarks flavors and pick a region $\mathcal{R}$ with a smooth boundary $\partial\mathcal{R}$. Suppose $\mathcal{O}_{\rm int}$ and $\mathcal{O}_{\rm ext}$ are polynomials in the basic fields localized in the interior and exterior of this region, respectively. If we perform a field transformation with support in $\mathcal{R}$, the variation of the external operator $\mathcal{O}_{\rm ext}$ vanishes and for the case of an isovector vector transformation it follows that

$$\begin{aligned}\langle(\delta_V\mathcal{O}_{\rm int})\mathcal{O}_{\rm ext}\rangle &= \langle\delta_V\mathcal{O}_{\rm int}\mathcal{O}_{\rm ext}\rangle \overset{(2.24)}{=} \langle(\delta_V S)\mathcal{O}_{\rm int}\mathcal{O}_{\rm ext}\rangle \\ &\overset{(2.18)}{=} \int_{\mathcal{R}} \mathrm{d}^4x\,\omega^a(x)\left\langle -\partial_\mu V_\mu^a(x)\mathcal{O}_{\rm int}\mathcal{O}_{\rm ext}\right\rangle\,,\end{aligned}$$

where $\delta_V\mathcal{O}_{\rm int} = \omega^a(y)\,\delta_V^a\mathcal{O}_{\rm int}$ if y denotes the point, where $\mathcal{O}$ lives. We now take ω^a to be a constant in $\mathcal{R}$. Using Gauss' law the integrated vector current Ward identity (VWI) is obtained

$$\left\langle(\delta_V^a\mathcal{O}_{\rm int})\mathcal{O}_{\rm ext}\right\rangle = -\int_{\partial\mathcal{R}} \mathrm{d}\sigma_\mu(x)\left\langle V_\mu^a(x)\mathcal{O}_{\rm int}\mathcal{O}_{\rm ext}\right\rangle\,. \tag{8.1}$$

8.1.2 AWI

The same construction is also valid for the axial current variation except that the mass term in (2.19) cannot be written as a surface integral[1]

$$\begin{aligned}\left\langle(\delta_A^a\mathcal{O}_{\rm int})\mathcal{O}_{\rm ext}\right\rangle &\overset{(2.19)}{=} -\int_{\partial\mathcal{R}} \mathrm{d}\sigma_\mu(x)\left\langle A_\mu^a(x)\mathcal{O}_{\rm int}\mathcal{O}_{\rm ext}\right\rangle \\ &\quad +2m\int_{\mathcal{R}} \mathrm{d}^4x\left\langle P^a(x)\mathcal{O}_{\rm int}\mathcal{O}_{\rm ext}\right\rangle\,.\end{aligned} \tag{8.2}$$

The axial Ward identity (AWI, 8.2) will later be used for massless quarks with $\mathcal{O}_{\rm int}$ equal to the axial current component A_ν^b at some point $y\in\mathcal{R}$. for this case we have

$$\begin{aligned}\int_{\partial\mathcal{R}} \mathrm{d}\sigma_\mu(x)\left\langle A_\mu^a(x)A_\nu^b(y)\mathcal{O}_{\rm ext}\right\rangle &= -\left\langle\left(\delta_A^a A_\nu^b(y)\right)\mathcal{O}_{\rm ext}\right\rangle \\ &\overset{(2.17)}{=} i\epsilon^{abc}\left\langle V_\nu^c(y)\mathcal{O}_{\rm ext}\right\rangle\,.\end{aligned} \tag{8.3}$$

[1] Due to additive mass renormalization, it is the current quark mass, e.g. (5.22), rather than the bare quark mass, which appears in the integrated Ward identity.

8.1.3 Euclidean proof of the Goldstone theorem

As an immediate application of the integrated Ward identities with operator insertions we will now show that a non–zero *chiral condensate* $\langle\bar{\psi}\psi\rangle$ leads to long–ranged current–density correlation functions [34], which in turn implies a massless propagating particle. This is the basis for the conjectured mechanism of spontaneous chiral symmetry breaking.

We know from (2.28) that for all $x \neq 0$ and zero quark mass the correlation function $\langle\partial_\mu A^a_\mu(x)P^a(0)\rangle$ vanishes. From Lorentz invariance one can then conclude that the integrated version is of the form

$$\langle A^a_\mu(x)P^a(0)\rangle = k\frac{x_\mu}{(x^2)^2} \ . \tag{8.4}$$

The constant k can be fixed by applying (8.2) with a sphere of radius r around the origin as the region $\mathcal{R}$, $m = 0$, $\mathcal{O}_{\text{int}} = P^a(0)$ and $\mathcal{O}_{\text{ext}} = 1$, which gives

$$\int_{|x|=r} \mathrm{d}\sigma_\mu(x)\langle A^a_\mu(x)P^a(0)\rangle = -\langle\delta^a_A P^a(0)\rangle = -\tfrac{3}{2}\langle\bar{\psi}\psi\rangle \ . \tag{8.5}$$

In the last step the definition (2.14) has been applied to the pseudo–scalar density (2.20). Since the integrand's divergence is zero everywhere except at the origin, in an application of Gauss's law the entire contribution would come from the contact term at the origin. However, we can simply plug (8.4) into (8.5) and solve the trivial integral directly. The result is the surface of the 4–sphere times k such that

$$-\tfrac{3}{2}\langle\bar{\psi}\psi\rangle = k2\pi^2 \tag{8.6}$$

and we finally arrive at

$$\langle A^a_\mu(x)P^a(0)\rangle = -\frac{3}{4\pi^2}\langle\bar{\psi}\psi\rangle\frac{x_\mu}{(x^2)^2} \ . \tag{8.7}$$

Thus, if the chiral condensate $\langle\bar{\psi}\psi\rangle$ is non–zero, the correlation function on the left–hand side of (8.7) has *no* exponential decay and therefore the energy spectrum of the theory has no gap. The massless particles propagating in the correlation function (8.7) are the Goldstone bosons of the broken chiral symmetry.

8.2 Normalization conditions

The normalization conditions for the isovector currents are obtained by deriving an identity between matrix elements in the continuum from the isovector symmetries of the QCD action. The renormalized improved currents on the lattice are then required to satisfy these identities at finite lattice spacing. This results in conditions for the renormalization factors Z_{A} and Z_{V}, cf. eqs. (4.34, 4.35).

In a massless renormalization scheme these conditions have to be set up a vanishing quark mass. If numerical simulations at the critical point are not possible, the normalization factors become the result of a chiral extrapolation.

We improve the methods employed for the calculation of Z_{A} in the quenched theory [11] by including the mass term in the integrated Ward identity (8.2). Of course, one still has to extrapolate to the chiral limit, but we will show that in practice the mass dependence of this normalization condition is extremely small.

8.2.1 The vector current

Our starting point is the continuum vector Ward identity (8.1) and we take the region $\mathcal{R}$ to be the entire Euclidean space for times smaller than some positive x_0. As internal operator we use the pseudo–scalar density at time zero and as external operator the pseudo–scalar density at time $T > x_0$. The surface integral then becomes a spatial integral over the time component of the vector current. Applying (2.13) to (2.20) gives

$$\delta_V^b P^c(x) = -i\epsilon^{bcd} P^d(x) \; . \tag{8.8}$$

In this setup the vector Ward identity becomes

$$\begin{aligned} \Big\langle (\delta_V^b P^c(0,\mathbf{u})) P^a(T,\mathbf{v}) \Big\rangle &= -\int \mathrm{d}^3\mathbf{x} \left\langle V_0^b(x_0,\mathbf{x}) P^c(0,\mathbf{u}) P^a(T,\mathbf{v}) \right\rangle \\ i\epsilon^{bcd} \Big\langle P^d(0,\mathbf{u}) P^a(T,\mathbf{v}) \Big\rangle &= \int \mathrm{d}^3\mathbf{x} \left\langle P^a(T,\mathbf{v}) V_0^b(x_0,\mathbf{x}) P^c(0,\mathbf{u}) \right\rangle . \end{aligned}$$

The physical interpretation of this relation is that the isospin charge $\int \mathrm{d}^3\mathbf{x} V_0^b(x)$ generates an infinitesimal isospin rotation of the state created by P^c, which transforms according to the vector representation of the exact isospin symmetry.

If the open isospin indices on the right–hand side are contracted in a totally antisymmetric way with $i\epsilon^{abc}$, the result is

$$-2\Big\langle P^a(T,\mathbf{v}) P^a(0,\mathbf{u}) \Big\rangle = i\epsilon^{abc} \int \mathrm{d}^3\mathbf{x} \left\langle P^a(T,\mathbf{v}) V_0^b(x_0,\mathbf{x}) P^c(0,\mathbf{u}) \right\rangle . \tag{8.9}$$

On the lattice we now construct these matrix elements in the framework of the Schrödinger functional. We use the boundary field products (5.13) and (5.14) to create initial and final states that transform according to the vector representation of the exact isospin symmetry and insert the renormalized improved vector current (4.35). We demand that the correlation function

$$f_{\mathrm{V}}^{\mathrm{R}}(x_0) = \frac{a^3}{6L^6} \sum_{\mathbf{x}} i\epsilon^{abc} \langle \mathcal{O}'^a (V_{\mathrm{R}})_0^b(x) \mathcal{O}^c \rangle \; , \tag{8.10}$$

is equal to

$$f_1 = -\frac{1}{3L^6} \langle \mathcal{O}'^a \mathcal{O}^a \rangle \; , \tag{8.11}$$

which corresponds to (8.9) when $\mathbf{u}$ and $\mathbf{v}$ are summed over all of space. In the improved theory it defines the renormalized vector current up to an $\mathrm{O}(a^2)$ uncertainty

$$f_{\mathrm{V}}^{\mathrm{R}}(x_0) = f_1 + \mathrm{O}(a^2) \;, \tag{8.12}$$

since both correlation functions approach their (common) continuum limit with this rate. Note that we do not need to include the renormalization factors for the (multiplicatively renormalizable) boundary quark fields here because they appear on both sides and thus cancel. With the obvious definition of $f_{\mathrm{V}}^{\mathrm{I}}(x_0)$

$$f_{\mathrm{V}}^{\mathrm{I}}(x_0) = \frac{a^3}{6L^6}\sum_{\mathbf{x}} i\epsilon^{abc}\langle \mathcal{O}'^a (V_{\mathrm{I}})_0^b(x)\mathcal{O}^c\rangle \;, \tag{8.13}$$

equation (8.12) then gives

$$Z_{\mathrm{V}}(1+b_{\mathrm{V}}am_{\mathrm{q}})f_{\mathrm{V}}^{\mathrm{I}}(x_0) \overset{(4.35)}{=} f_1 + \mathrm{O}(a^2) \;. \tag{8.14}$$

One can easily evaluate the contribution of the $\mathrm{O}(a)$ counterterm appearing in the definition (4.26) of the improved vector current to the correlation function $f_{\mathrm{V}}^{\mathrm{I}}(x_0)$. If we introduce the correlation function for the bare unimproved current,

$$f_{\mathrm{V}}(x_0) = \frac{a^3}{6L^6}\sum_{\mathbf{x}} i\epsilon^{abc}\langle \mathcal{O}'^a V_0^b(x)\mathcal{O}^c\rangle \;, \tag{8.15}$$

it follows that

$$\begin{aligned} f_{\mathrm{V}}^{\mathrm{I}}(x_0) - f_{\mathrm{V}}(x_0) &\overset{(4.26)}{\propto} \sum_{\mathbf{x}} \epsilon^{abc}\Big\langle \mathcal{O}'^a \tilde{\partial}_\nu T_{0\nu}^b(x)\mathcal{O}^c\Big\rangle \\ &\overset{(4.27)}{\propto} \sum_{\mathbf{x}} \epsilon^{abc}\Big\langle \mathcal{O}'^a \tilde{\partial}_\nu [\bar{\psi}(x)\sigma_{0\nu}\tau^b\psi(x)]\mathcal{O}^c\Big\rangle \;. \end{aligned} \tag{8.16}$$

Since $\sigma_{0\nu} = \frac{i}{2}[\gamma_0,\gamma_\nu]$ is antisymmetric in its Dirac indices, we have $\sigma_{00}=0$. The contribution of the improvement term to the correlation function will therefore contain the expression

$$\sum_{\mathbf{x}} \tilde{\partial}_k[\bar{\psi}(x)\sigma_{0k}\tau^b\psi(x)] \;, \tag{8.17}$$

which vanishes identically if we impose periodic boundary conditions in the spatial directions. We can therefore conclude that $f_{\mathrm{V}}^{\mathrm{I}}(x_0) = f_{\mathrm{V}}(x_0)$ and from equation (8.14) it follows that

$$Z_{\mathrm{V}}(\tilde{g}_0^2)(1+b_{\mathrm{V}}am_{\mathrm{q}})f_{\mathrm{V}}(x_0) = f_1 + \mathrm{O}(a^2) \;. \tag{8.18}$$

By evaluating the correlation functions f_1 and $f_{\mathrm{V}}(x_0)$ through numerical simulation one is thus able to compute the normalization factor $Z_{\mathrm{V}}(1+b_{\mathrm{V}}am_{\mathrm{q}})$. In particular, to calculate Z_{V} it suffices to consider the theory at vanishing quark mass. Equation (8.18) also implies that $f_{\mathrm{V}}(x_0)$ is independent of x_0 up to cutoff effects. In a numerical evaluation one can therefore increase the statistical accuracy by averaging over a range of x_0 values. More details will be given in Section 8.3.

Derivation in the operator formalism

The vector current normalization condition can also be derived in the operator formalism of the Schrödinger functional with boundary states S and S'. The fact that the charge is conserved implies that the corresponding charge operator, denoted by $\hat{Q}^b$, commutes with the transfer matrix $\mathbb{T}$. The correlation function (8.10) now reads

$$
\begin{aligned}
f_{\mathrm{V}}^{\mathrm{R}}(x_0) &= \frac{1}{6L^6} i\epsilon^{abc}\langle S'|\hat{\mathcal{O}}'^a\mathbb{T}^{(T-x_0)}\hat{Q}^b\mathbb{T}^{x_0}\hat{\mathcal{O}}^c|S\rangle \\
&= \frac{1}{6L^6} i\epsilon^{abc}\langle S'|\hat{\mathcal{O}}'^a\mathbb{T}^{T}\hat{Q}^b\hat{\mathcal{O}}^c|S\rangle \; .
\end{aligned}
$$

Since $\hat{Q}^b|S\rangle = 0$ we can replace $\hat{Q}^b\hat{\mathcal{O}}^c$ by its commutator and since the boundary fields are isospin vectors we have $[\hat{Q}^b, \hat{\mathcal{O}}^c] = -i\epsilon^{bcd}\hat{\mathcal{O}}^d$ in the continuum. The physical interpretation is that the isovector charge generates an infinitesimal isospin rotation as in (8.8). In an $\mathrm{O}(a)$ improved lattice theory this argumentation holds up to $\mathrm{O}(a^2)$ and therefore

$$
\begin{aligned}
f_{\mathrm{V}}^{\mathrm{R}}(x_0) &= -\frac{1}{6L^6}\underbrace{\epsilon^{abc}\epsilon^{bcd}}_{=2\delta^{ad}}\langle S'|\hat{\mathcal{O}}'^a\mathbb{T}^{T}\hat{\mathcal{O}}^d|S\rangle + \mathrm{O}(a^2) \\
&= -\frac{1}{3L^6}\langle \mathcal{O}'^a\mathcal{O}^a\rangle + \mathrm{O}(a^2) \; , \qquad (8.19)
\end{aligned}
$$

where in the last line we have switched back to the path integral form to recover the result (8.12).

8.2.2 The axial current

We will start with a derivation of the normalization condition used in [11], where the quark is set to zero in the beginning. This will later be generalized to $m \neq 0$.

Massless case

For vanishing quark mass our starting point is the Ward identity (8.3). Contracting the isospin indices gives

$$
\begin{aligned}
\int_{\partial\mathcal{R}} \mathrm{d}\sigma_\mu(x)\,\epsilon^{abc}\Big\langle A_\mu^a(x)A_\nu^b(y)\mathcal{O}_{\mathrm{ext}}\Big\rangle &\overset{(8.3)}{=} i\underbrace{\epsilon^{abc}\epsilon^{abd}}_{2\delta^{cd}}\Big\langle V_\nu^d(y)\mathcal{O}_{\mathrm{ext}}\Big\rangle \\
&= 2i\Big\langle V_\nu^c(y)\mathcal{O}_{\mathrm{ext}}\Big\rangle \; . \qquad (8.20)
\end{aligned}
$$

This relation is now transcribed to the $\mathrm{O}(a)$ improved lattice theory with $\mathcal{R}$ being the region between the hyper-planes at $x_0 = y_0 \pm t$ and $\nu = 0$. With periodic boundary conditions in the spatial directions the surface integration in (8.20) results in the difference between the axial charge at times $y_0 \pm t$, i.e.

$$a^3 \sum_{\mathbf{x}} \epsilon^{abc} \Big\langle \Big[(A_{\rm R})_0^a(y_0{+}t, \mathbf{x}) - (A_{\rm R})_0^a(y_0{-}t, \mathbf{x}) \Big] (A_{\rm R})_0^b(y) \mathcal{O}_{\rm ext} \Big\rangle \\ = 2i \Big\langle (V_{\rm R})_0^c(y) \mathcal{O}_{\rm ext} \Big\rangle + \mathrm{O}(a^2) \ . \qquad (8.21)$$

On-shell improvement is effective in (8.21) since the fields in the correlation functions are localized at non-zero distances from each other. Equation (8.21) is summed over $\mathbf{y}$ to obtain the axial charge. In the form of (8.21) the integrated Ward identity requires three different time–slices, where the axial charge is inserted.

Using the conservation of the (renormalized) axial current the two insertions at $y_0{-}t$ and y_0, associated with the lower surface of $\mathcal{R}$, can (simultaneously) be shifted to y_0 and $y_0{+}t$. We thus arrive at

$$a^6 \sum_{\mathbf{x},\mathbf{y}} \epsilon^{abc} \Big\langle (A_{\rm R})_0^a(x) (A_{\rm R})_0^b(y) \mathcal{O}_{\rm ext} \Big\rangle = a^3 \sum_{\mathbf{y}} i \Big\langle (V_{\rm R})_0^c(y) \mathcal{O}_{\rm ext} \Big\rangle + \mathrm{O}(a^2) \ , \qquad (8.22)$$

where $x_0 = y_0{+}t$. Since t was arbitrary, the above equation holds for all insertion points x_0 and y_0 such that $0 < y_0 < x_0 < T$.

At this point we have a relation that would allow us to calculate the axial current renormalization from the vector current renormalization. We can make things even simpler by choosing the field product $\mathcal{O}_{\rm ext}$ such that the correlation function $f_{\rm V}^{\rm R}(y_0)$ appears on the right–hand side of equation (8.22). This amounts to setting

$$\mathcal{O}_{\rm ext} = -\frac{1}{6L^6} \epsilon^{cde} \mathcal{O}'^d \mathcal{O}^e \ , \qquad (8.23)$$

since with this definition equation (8.22) becomes

$$
\begin{aligned}
-\frac{a^6}{6L^6}\sum_{\mathbf{x},\mathbf{y}} \epsilon^{abc}\epsilon^{cde}\Big\langle \mathcal{O}'^d (A_\mathrm{R})_0^a(x)(A_\mathrm{R})_0^b(y)\mathcal{O}^e\Big\rangle \qquad (8.24)\\
\stackrel{(8.22)}{=} \quad -\frac{a^3}{6L^6}\sum_{\mathbf{y}} i\epsilon^{cde}\Big\langle \mathcal{O}'^d (V_\mathrm{R})_0^c(y)\mathcal{O}^e\Big\rangle + \mathrm{O}(a^2)\\
= \quad \frac{a^3}{6L^6}\sum_{\mathbf{y}} i\epsilon^{abc}\Big\langle \mathcal{O}'^a (V_\mathrm{R})_0^b(y)\mathcal{O}^c\Big\rangle + \mathrm{O}(a^2)\\
\stackrel{(8.10)}{=} \quad f_\mathrm{V}^\mathrm{R}(y_0) + \mathrm{O}(a^2)\,. \qquad (8.25)
\end{aligned}
$$

The normalization condition for the vector current (8.12) allows us to replace $f_\mathrm{V}^\mathrm{R}(y_0)$ by f_1. If we define the unrenormalized version of the correlator (8.24) as

$$
f_\mathrm{AA}^\mathrm{I}(x_0,y_0) = -\frac{a^6}{6L^6}\sum_{\mathbf{x},\mathbf{y}} \epsilon^{abc}\epsilon^{cde}\Big\langle \mathcal{O}'^d (A_\mathrm{I})_0^a(x)(A_\mathrm{I})_0^b(y)\mathcal{O}^e\Big\rangle\,, \qquad (8.26)
$$

one can conclude from (8.25) that

$$
Z_\mathrm{A}^2 f_\mathrm{AA}^\mathrm{I}(y_0{+}t, y_0) = f_1 + \mathrm{O}(a^2) \qquad (8.27)
$$

for all times $t > 0$ such that $0 < y_0$ and $y_0{+}t < T$. As in (8.12) the normalization of the boundary quark fields cancel. The axial current normalization constant Z_A can thus be determined by computing the two correlation functions f_1 and $f_\mathrm{AA}^\mathrm{I}(y_0{+}t, y_0)$ at vanishing quark mass.

Numerical simulations (see Section 8.3.1) show that the above relation has a very pronounced mass dependence. Since the quark mass was neglected from the very beginning in its derivation, this should not come as a surprise. In the following we will derive a normalization condition from the full PCAC relation.

Non-vanishing PCAC mass

Since we use a mass–independent renormalization scheme the normalization condition for the axial current can not be set up at finite quark mass. Instead our goal is to derive a normalization condition, which has a smaller mass dependence than (8.27), such that in practice the chiral extrapolation is easier. To this end we now use the axial Ward identity (8.2) with the same operator $\mathcal{O}_\mathrm{int} = A_\nu^b(y)$, where again the point y is somewhere in the interior of $\mathcal{R}$. After anti–symmetrically contracting the isospin indices the result for an arbitrary mass m reads

$$
\begin{aligned}
\int_{\partial\mathcal{R}} \mathrm{d}\sigma_\mu(x)\,\epsilon^{abc}\Big\langle A_\mu^a(x)A_\nu^b(y)\mathcal{O}_\mathrm{ext}\Big\rangle\\
-2m\int_{\mathcal{R}} \mathrm{d}^4x\,\epsilon^{abc}\Big\langle P^a(x)A_\nu^b(y)\mathcal{O}_\mathrm{ext}\Big\rangle \;=\; 2i\Big\langle V_\nu^c(y)\mathcal{O}_\mathrm{ext}\Big\rangle\,. \qquad (8.28)
\end{aligned}
$$

Already here we note that the volume integral contains a contact–term, i.e. a contribution from the composite operator $\epsilon^{abc}P^a(x)A_\nu^b(y)$ as x approaches the (fixed) y. The operator product expansion implies that the leading contribution in the $x \to y$ limit comes from $V_\nu^c(x)$. From power counting it then follows that the composite operator cannot diverge faster than $|x-y|^{-3}$, such that we receive a finite contribution under the four–dimensional integral over $\mathcal{R}$.

We choose the same region $\mathcal{R}$ and set $\nu=0$ as in the massless case. Together with an additional spatial integration over $\mathbf{y}$ the result is

$$\begin{aligned}\int \mathrm{d}^3\mathbf{y} \int \mathrm{d}^3\mathbf{x}\, \epsilon^{abc} \Big[\Big\langle A_0^a(y_0+t,\mathbf{x}) A_0^b(y_0,\mathbf{y}) \mathcal{O}_{\mathrm{ext}}\Big\rangle - \Big\langle A_0^a(y_0-t,\mathbf{x}) A_0^b(y_0,\mathbf{y}) \mathcal{O}_{\mathrm{ext}}\Big\rangle\Big] \\ -2m \int \mathrm{d}^3\mathbf{y} \int \mathrm{d}^3\mathbf{x} \int_{y_0-t}^{y_0+t} \mathrm{d}x_0\, \epsilon^{abc} \Big\langle P^a(x_0,\mathbf{x}) A_0^b(y_0,\mathbf{y}) \mathcal{O}_{\mathrm{ext}}\Big\rangle \\ = 2i \int \mathrm{d}^3\mathbf{y} \,\Big\langle V_0^c(y_0,\mathbf{y}) \mathcal{O}_{\mathrm{ext}}\Big\rangle \,. \qquad (8.29)\end{aligned}$$

In the massless case the two contributions from the surface integration were the same due to current conservation and the anti–symmetric isospin structure. Here we have to use the partial conservation of the axial current to transform the second term of the surface integral. This will cancel the lower part (y_0-t to y_0) of the volume integral. The detailed calculation is given in Appendix C and the result is

$$\begin{aligned}i \int \mathrm{d}^3\mathbf{y} \,\Big\langle V_0^c(y_0,\mathbf{y}) \mathcal{O}_{\mathrm{ext}}\Big\rangle = \\ \int \mathrm{d}^3\mathbf{y} \int \mathrm{d}^3\mathbf{x}\, \epsilon^{abc} \Big\langle A_0^a(y_0+t,\mathbf{x}) A_0^b(y_0,\mathbf{y}) \mathcal{O}_{\mathrm{ext}}\Big\rangle \\ -2m \int \mathrm{d}^3\mathbf{y} \int \mathrm{d}^3\mathbf{x} \int_{y_0}^{y_0+t} \mathrm{d}x_0\, \epsilon^{abc} \Big\langle P^a(x_0,\mathbf{x}) A_0^b(y_0,\mathbf{y}) \mathcal{O}_{\mathrm{ext}}\Big\rangle \,. \qquad (8.30)\end{aligned}$$

As before a normalization condition for the axial current on the lattice is obtained by demanding that eq. (8.30) in terms of the renormalized currents holds at non–zero lattice spacing. Inserting the same external operator (8.23) as before will again allow us to replace the matrix–element of the vector current with the correlation function f_1. As a result of the contact term O(a) improvement fails in the correlator multiplying the mass term. On the lattice we therefore expect corrections of order am at finite mass in addition to the overall $\mathrm{O}(a^2)$ uncertainty and thus have

$$\begin{aligned}-\frac{a^6}{6L^6} \sum_{\mathbf{x},\mathbf{y}} \epsilon^{abc}\epsilon^{cde} \Big\langle \mathcal{O}'^d (A_\mathrm{R})_0^a(y_0+t,\mathbf{x}) (A_\mathrm{R})_0^b(y_0,\mathbf{y}) \mathcal{O}^e \Big\rangle \\ +\frac{2ma^7}{6L^6} \sum_{x_0=y_0}^{y_0+t} w(x_0) \sum_{\mathbf{x},\mathbf{y}} \epsilon^{abc}\epsilon^{cde} \Big\langle \mathcal{O}'^d P_\mathrm{R}^a(x) (A_\mathrm{R})_0^b(y) \mathcal{O}^e \Big\rangle \\ = f_1 + \mathrm{O}(a^2) + \mathrm{O}(am) \,. \qquad (8.31)\end{aligned}$$

The weight factor $w(x_0)$ is needed to implement the trapezoidal rule in the discretization of the time integral in (8.30), i.e. that the boundary terms $x_0 = y_0$ and $y_0 + t$ should only contribute with the weight 1/2. It is given by

$$w(x_0) = \begin{cases} 1/2, & x_0 \in \{y_0, y_0{+}t\} \\ 1, & \text{otherwise}\ . \end{cases} \tag{8.32}$$

If we set $m = 0$ in (8.31) we immediately recover the normalization condition used in [11], i.e. (8.25). With the definitions (8.26) and (4.34) the normalization condition can be written as

$$\begin{aligned} &Z_{\mathrm{A}}^2(1{+}b_{\mathrm{A}}am_{\mathrm{q}})^2 f_{\mathrm{AA}}^{\mathrm{I}}(y_0{+}t, y_0) \\ &+\frac{2m_{\mathrm{R}}a^7}{6L^6}\sum_{x_0=y_0}^{y_0+t} w(x_0)\sum_{\mathbf{x},\mathbf{y}} \epsilon^{abc}\epsilon^{cde}\Big\langle \mathcal{O}'^d P_{\mathrm{R}}^a(x)(A_{\mathrm{R}})_0^b(y)\mathcal{O}^e\Big\rangle = f_1 + \mathrm{O}(a^2) + \mathrm{O}(am)\ . \end{aligned}$$

Since there is no improvement term for the pseudo-scalar density we now define the new correlation function

$$\tilde{f}_{\mathrm{PA}}^{\mathrm{I}}(y_0{+}t, y_0) \ = \ -\frac{a^7}{6L^6}\sum_{x_0=y_0}^{y_0+t} w(x_0)\sum_{\mathbf{x},\mathbf{y}} \epsilon^{abc}\epsilon^{cde}\Big\langle \mathcal{O}'^d P^a(x)(A_{\mathrm{I}})_0^b(y)\mathcal{O}^e\Big\rangle\ . \tag{8.33}$$

From the PCAC relation we conclude that the product mP renormalizes with the same factor as A_μ. Thus, the final form for the normalization condition derived from the Ward identity with mass term is given by

$$\begin{aligned} Z_{\mathrm{A}}^2(1{+}b_{\mathrm{A}}am_{\mathrm{q}})^2\Big(f_{\mathrm{AA}}^{\mathrm{I}}(y_0{+}t, y_0) - 2m\tilde{f}_{\mathrm{PA}}^{\mathrm{I}}(y_0{+}t, y_0)\Big) &= \\ f_1 + \mathrm{O}(am) + \mathrm{O}(a^2)\ . \end{aligned} \tag{8.34}$$

8.3 Numerical computation

Before going into the details of the simulations, we need to specify our choice of kinematic parameters in the numerical evaluation of the conditions (8.18) and (8.34).

The spatial boundary conditions are strictly periodic ($\theta_k = 0$) and to accommodate the two insertion points in (8.34) in a symmetric way, we choose a $T = 9/4L$ geometry. The background field (C_k and C_k') is set to zero and the improvement coefficients have the values specified in Sections 4.2 and 5.1. The axial current improvement coefficient c_{A} is given by (7.26).

As first discussed in [11] and further detailed in [102], we need to evaluate the normalization conditions on a line of constant physics, keeping all length scales fixed. This ensures that the $\mathrm{O}(a^2)$ ambiguities in the normalization factors vanish smoothly when the perturbative regime is approached. In addition, the normalization conditions have to be set up at zero quark mass since we are implementing a mass–independent renormalization scheme as detailed in Section 4.3.

To keep the volume constant, we again employ the approximate scale setting given by $t(\beta)$, cf. eq. (7.2). We point out that in the present case a deviation from the line of constant physics can change the result by $\mathrm{O}(a^2)$ only, whereas in the computation of c_A such deviations would show up at $\mathrm{O}(a)$. In addition to three lattice resolutions matched in this way, we simulated at three larger values of β and fixed $L/a = 8$, which results in very small volumes. This was done in order to verify that our non–perturbative estimate smoothly connects to the perturbative predictions, eqs. (4.36) and (4.37).

Our "reference" volume is an $8^3 \times 18$ lattice at $\beta = 5.2$, which corresponds to the coarsest lattice spacing. At all other lattice spacings the systematic error in Z_A and Z_V due to a mismatch in the volume is estimated by varying the lattice resolution L/a. To check for smoothness of $Z_\mathrm{A}(g_0^2)$ additional simulations were performed in an unmatched $8^3 \times 18$ volume at $\beta = 5.29$ without an estimate of the systematic error.

These last simulations as well as all but the heaviest run at $\beta = 5.2$ were done with the PHMC algorithm. All others employ the HMC with two pseudo–fermions as discussed in Section 6.1. For all runs it could be verified that the problems described in Sections 6.5 and 6.6 are absent.

For reference we collect again the precise non–perturbative definitions of Z_V and Z_A. In the simulations both the PCAC mass and the estimate for Z_V are averaged over a few time–slices in the middle of the lattice. No such time average is performed for the correlation functions f_AA^I and $\tilde{f}_\mathrm{PA}^\mathrm{I}$.

$$Z_\mathrm{A}(g_0^2) = \lim_{m\to 0} \sqrt{\frac{f_1}{f_\mathrm{AA}^\mathrm{I}(2T/3,T/3) - 2m\tilde{f}_\mathrm{PA}^\mathrm{I}(2T/3,T/3)}}\,, \tag{8.35}$$

$$Z_\mathrm{V}(g_0^2) = \lim_{m\to 0} \frac{1}{N_t} \sum_{x_0=t_1}^{t_2} \frac{f_1}{f_\mathrm{V}(x_0)}\,, \tag{8.36}$$

$$m = \frac{1}{N_t} \sum_{x_0=t_1}^{t_2} \frac{\tilde{\partial}_0\Big[f_\mathrm{A}(x_0)+g_\mathrm{A}(T-x_0)\Big]+ac_\mathrm{A}\partial_0\partial_0^\star\Big[f_\mathrm{P}(x_0)+g_\mathrm{P}(T-x_0)\Big]}{2\Big[f_\mathrm{P}(x_0)+g_\mathrm{P}(T-x_0)\Big]}\,, \tag{8.37}$$

$$\text{where} \quad \begin{cases} t_1 = \frac{T-2}{2},\ t_2 = \frac{T+2}{2},\ N_t = 3 & \text{for } T \text{ even.} \\ t_1 = \frac{T-3}{2},\ t_2 = \frac{T+3}{2},\ N_t = 4 & \text{for } T \text{ odd.} \end{cases} \tag{8.38}$$

8.3.1 Implementation notes and quenched example

The starting point in the implementation of the correlation functions for the axial normalization condition were the APEmille TAO codes of the ALPHA collaboration. These already include the correlation functions f_A, f_P, g_A and g_P.

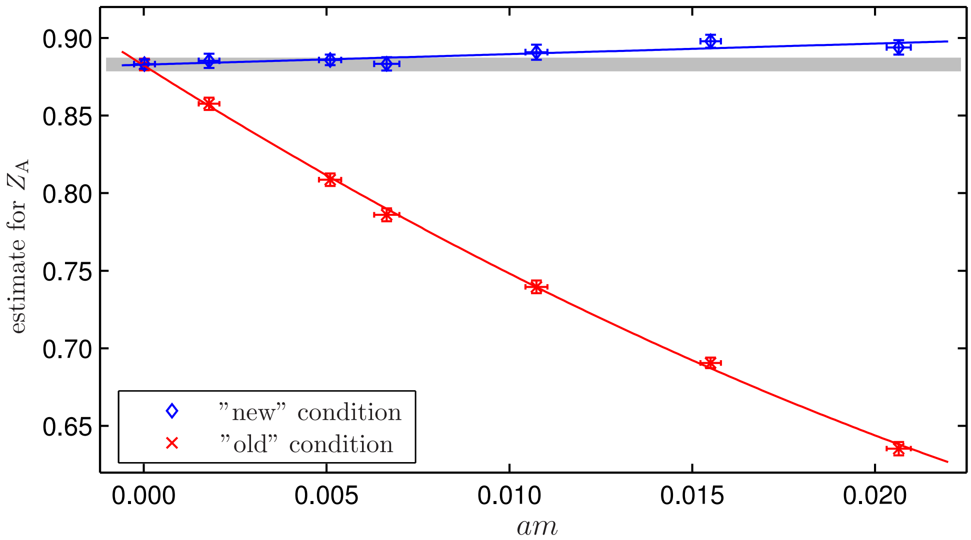

Figure 8.1: Mass dependence of the old and new normalization conditions for the axial current evaluated in the quenched approximation. The parameters are $\beta = 8.0$, volume $= 8^3 \times 18$ and $\kappa \in [0.1325, 0.133168]$.

The correlation functions $f_{\rm V}$, $f^{\rm I}_{\rm AA}$ and $\tilde{f}^{\rm I}_{\rm PA}$ have been implemented in the quenched code (which uses SSOR preconditioning [118]) as well as the even–odd preconditioned HMC and PHMC codes. An additional version (derived from the quenched one) exists, which measures the correlation functions on a saved gauge configuration. A detailed discussion of all correlation functions and in particular of $f^{\rm I}_{\rm AA}$ and $\tilde{f}^{\rm I}_{\rm PA}$ and their Wick contractions is given in Appendix B.1.

The code for $f^{\rm I}_{\rm AA}$ as well as the analysis program have been checked against those used in [11]. Agreement was found both statistically (i.e. at a given set of bare parameters) as well as on a given gauge configuration.

As a first test of the new axial current normalization condition, we consider sets of quenched $8^3 \times 18$ gauge configurations at $\beta = 8.0$ and various values of the hopping parameter κ. The lattice spacing and hence the volume are extremely small[2] such that the fluctuations of the gauge field are strongly suppressed and one can (in the Schrödinger functional) easily simulate at the critical point.

The results are shown in Fig. 8.1, where one can see that the lightest mass (with $\kappa = 0.133168$) is exactly at the critical point. We show the estimate for $Z_{\rm A}$ defined in (8.35) as well as the one from the old condition [11], where the term $m\tilde{f}^{\rm I}_{\rm PA}$ is neglected. As expected from the argumentation in the previous section, the new condition has a significantly smaller mass dependence. At these

[2]In the quenched approximation $\beta = 6.0$ implies $a \simeq 0.1$ fm and hence corresponds to $\beta = 5.2$ in the two–flavor case.

parameter values using the new condition reduces the linear coefficient of a fit in am from $-14.9(8)$ to $0.7(2)$, which is consistent with our $\mathrm{O}(am)$ expectation. With a value of 0.97(2) the slope in the estimate of Z_V from (8.36), which is not shown in the plot, is similar to that of Z_A with the new condition.

Due to the large slope, an extrapolation of results from the old normalization condition of the axial current should take into account the error in the quark mass as well as the correlation between am and the Z_A estimate. In contrast, with the small slope from the new condition the extra– or interpolation is essentially flat and uncertainties in the location of the critical point do not propagate to the determination of Z_A.

Note that in the shown quark mass range the old normalization condition already shows non–linear effects in am. Since a is extremely small here, the physical quark mass is already quite large and such a behavior is thus not unexpected.

8.3.2 Results for the normalization factors

The results of all simulations are collected in Appendix D, while in Table 8.1 we show only the results of the chiral extrapolations (8.35) and (8.36).

In most cases at least one simulation is very close to the critical point and in some cases we actually perform an *inter*polation in am. As can be seen from the table, this results in a very precise estimate of the critical hopping parameter κ_c. The latter is obtained by extrapolating the PCAC mass am linearly in $1/\kappa$.

β	L/a	T/a	κ_c	Z_A	Z_V
5.200	8	18	0.135856(18)	0.7141(123)	0.7397(12)
5.500	12	27	0.136733(8)	0.7882(35)(39)	0.7645(22)(18)
5.715	16	36	0.136688(11)	0.8037(38)(7)	0.7801(15)(27)
5.290	8	18	0.136310(22)	0.7532(79)	0.7501(13)
7.200	8	18	0.134220(21)	0.8702(16)(7)	0.8563(5)(45)
8.400	8	18	0.132584(7)	0.8991(25)(7)	0.8838(13)(45)
9.600	8	18	0.131405(3)	0.9132(11)(7)	0.9038(3)(45)

Table 8.1: Results of the chiral extrapolations to extract Z_A (8.35) and Z_V (8.36).

As already mentioned the volumes of the simulations at $\beta = 5.2$, 5.5 and 5.715 are matched in the same way as for the c_A simulations, cf. eq. (7.2), while for $\beta \geq 7.2$ the volumes are much smaller.[3] The second set of errors for $Z_\mathrm{A/V}$ represent an estimate of the systematic uncertainties due a mismatch in the lattice

[3]The (compared to Chapter 7) different β, such that $t(\beta) = 0.5$ is due to the use of a version of eq. (7.2), which differs by $\mathrm{O}(g_0^4)$ terms.

spacing/volume. They will be discussed in Section 8.3.3. An exception are the simulations at $\beta = 5.2$, which is the reference volume and $\beta = 5.29$, which was performed only to qualitatively confirm the observed rapid change of $Z_{\rm A}(g_0^2)$ in this region of the coupling.

Fig. 8.2 shows the critical mass $am_{\rm c} = (2\kappa_c)^{-1} - 4$ as determined in the simulations and compares it to the (continuum) perturbative prediction. The non–monotonic behavior of the additive mass renormalization at $g_0^2 > 1$ is similar to the one found in the quenched case (see e.g. [11]) and is clearly a non–perturbative phenomenon. In contrast, for the largest values of β simulated, the numerical results are already close to the the two–loop formula (4.12).

The chiral extrapolation of our estimate for $Z_{\rm A}$ at the coarsest lattice spacing, $\beta = 5.2$, is plotted in Fig. 8.3. Apart from the significantly larger errors the situation is very similar to the quenched one from Fig. 8.1, showing that also in the dynamical case the new normalization condition has only a very small mass dependence. As a result, the errors on am and the correlation of am with the estimate for $Z_{\rm A}$ are irrelevant for the extrapolation. Note however, that the mass range in *lattice units* is the same in both plots, which implies that (ignoring renormalization factors of order one) the physical masses in the dynamical case are much smaller since a is much larger. As a result, also for the old normalization condition all mass effects now show a linear behavior.

The slopes of the two estimate as functions of am are also very similar to the quenched case. Due to the large statistical errors the slope for the new condition is consistent with zero (0.4 with an error of 1.2) and for the old condition we obtain -14(1). Again, the slope of the estimate for $Z_{\rm V}$ (0.64(9), not shown) is comparable to that from the new condition for $Z_{\rm A}$. In the quenched case [11] the slope (in $am_{\rm q}$) of $f_1/(Z_{\rm V} f_{\rm V})$ could be used to determine the $\mathrm{O}(am_{\rm q})$ improvement coefficient $b_{\rm V}$, cf. eq. (8.18). This was possible because for $N_{\rm f} = 0$ the bare and modified gauge couplings coincide ($b_{\rm g} = 0$). This is no longer true in the dynamical case [63, 71] and hence the slope one finds is not entirely due to $b_{\rm V}$.

In order to keep the discussion transparent, we will now restrict ourselves to the new normalization condition. The final results for $Z_{\rm A}$ and $Z_{\rm V}$ are shown in Fig. 8.4 as a function of g_0^2. The errors plotted there are obtained by linearly summing the statistical and systematic errors. Also shown are the 1–loop estimates (4.36) and (4.37).

One can see that our results for both $Z_{\rm A}$ and $Z_{\rm V}$ lie on smooth curves and we can therefore (as for $c_{\rm A}$) describe the non–perturbative data in form of a rational function of g_0^2 (Pade fit). In this fit the difference of the linear terms of numerator and denominator is constrained to the 1–loop value, which ensures a smooth matching with perturbation theory as g_0^2 approaches zero.

The fit is performed with the sum of the errors from Table 8.1 and the data points at $\beta = 5.29$ are excluded since no estimate of the systematics is available in this case. With the perturbative input (4.36) and (4.37) we thus arrive at the

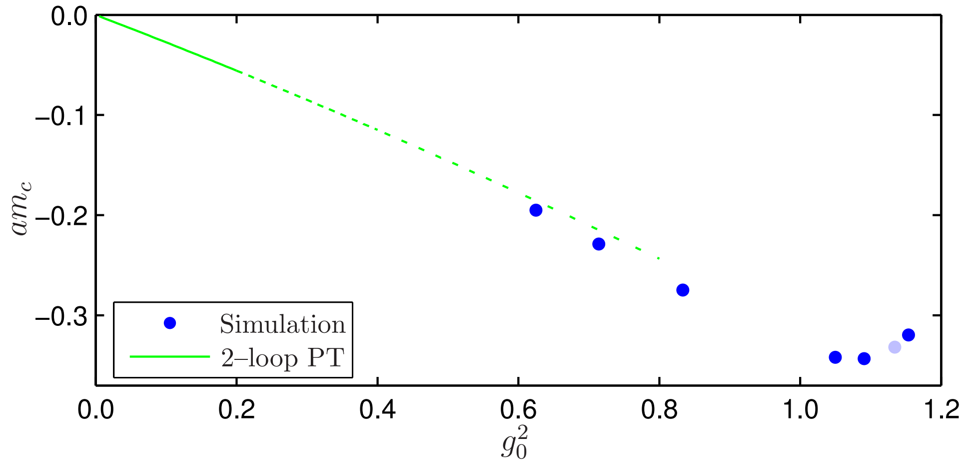

Figure 8.2: The critical mass am_c (errors are much smaller than the symbols) as a function of the bare gauge coupling g_0^2. For $g_0^2 < 0.8$ the non–perturbative data start to approach the two–loop prediction (4.12) from [55].

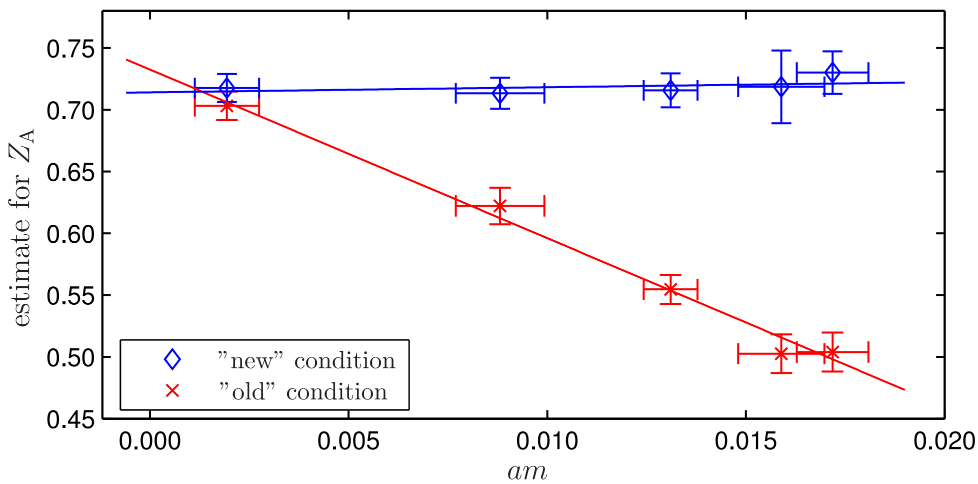

Figure 8.3: The chiral extrapolation of the result from the axial current normalization conditions at $\beta = 5.2$.

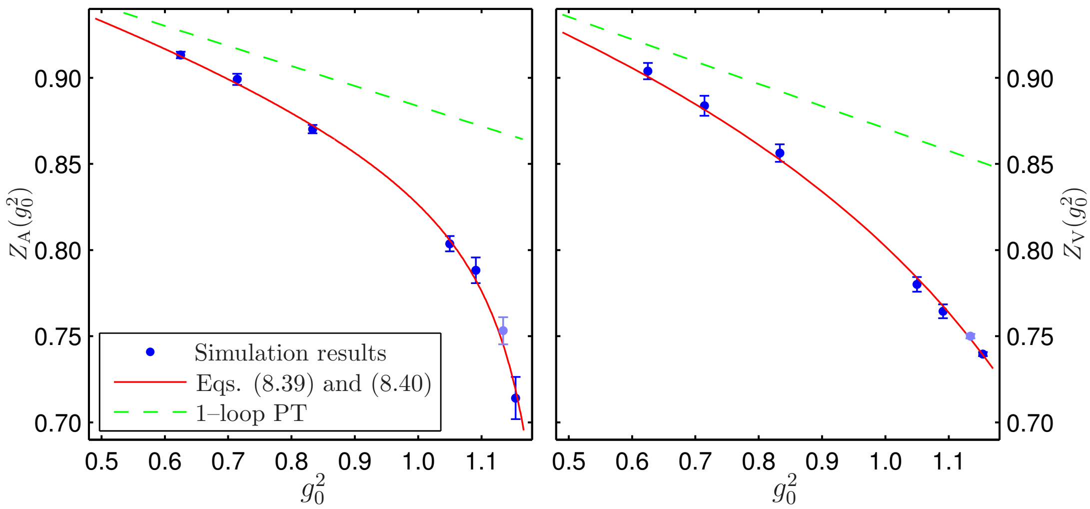

Figure 8.4: The normalization factors Z_A and Z_V as a function of g_0^2, together with the 1–loop results (dashed line) and the Pade interpolating formulae (solid line). The data points at $\beta = 5.29$ (lighter color) are excluded from the fit.

interpolating formulae

$$Z_\mathrm{A}(g_0^2) = \frac{1 - 0.918\, g_0^2 + 0.062\, g_0^4 + 0.020\, g_0^6}{1 - 0.8015\, g_0^2}\,, \tag{8.39}$$

$$Z_\mathrm{V}(g_0^2) = \frac{1 - 0.6715\, g_0^2 + 0.0388\, g_0^4}{1 - 0.5421\, g_0^2}\,. \tag{8.40}$$

The low value of Z_A at $\beta = 5.2$ requires that the Z_A data are fitted with a polynomial of third degree in the numerator, while the Z_V data can be well described including only quadratic terms in g_0^2 in the numerator. For Z_V we find agreement at the 1% level with the results from [119], where isospin charge conservation is imposed for nucleon matrix elements of the local vector current in large volume.

The maximal absolute deviations of the fit from the simulation data are 0.0056 (corresponding to $0.7\,\sigma$ or 0.7%) for Z_A at $\beta = 5.5$ and 0.004 ($0.9\,\sigma$ or 0.5%) for Z_V at $\beta = 5.715$. Considering that all the data in one fit are statistically independent since they come from different simulations, these fluctuations are rather small. For future application we propose to either use the data from Table 8.1 directly or the interpolating formulae (8.39) and (8.40). To Z_V we ascribe an absolute error of 0.005 and for Z_A the absolute error decreases from 0.01 at $\beta = 5.2$ to 0.005 at $\beta = 5.7$.

We note that for a lattice spacing of roughly 0.1 fm, corresponding to $\beta = 5.2$, our non–perturbative estimate of Z_A is almost 20% smaller than the 1–loop value, while in the quenched case [11] this difference was only 10% at the same lattice spacing.[4]

8.3.3 Systematic uncertainties

Close to the continuum the dependence of the normalization factors on the lattice size is expected to be of order $(a/L)^2$ [11] in the improved theory. This implies that effects in Z_{A} and Z_{V} due to deviations from the line of constant physics, i.e. the constant physical volume condition, should be strongly suppressed.

To check for these effects, at $\beta = 5.5$ and 5.715 the simulations closest to the critical point were repeated on smaller lattices ($L/a = 8$ instead of 12 at $\beta = 5.5$ and $L/a = 12$ instead of 16 at $\beta = 5.715$). From our approximate matching (see Chapter 7) we estimate the uncertainty in L (measured in units of L at $\beta = 5.2$) to increase up to at most 10% in the range $5.2 < \beta < 5.715$. We assume that the uncertainty in L grows linearly in β and therefore assign a 6% error to L at $\beta = 5.5$ and 10% at $\beta = 5.715$. Together with the difference in the estimates of Z_{A} and Z_{V} this gives the systematic errors quoted in Table 8.1 through a linear propagation of the error.

Our simulations confirm the expectation of small volume dependence. The largest difference is seen at $\beta = 5.5$ ($L/a = 12$ vs. 8), where it is 0.022(7) corresponding to a 3% effect in Z_{A} for a 33% change in L.

For the runs with $\beta \geq 7.2$ the matched L/a would be extremely large. On the other hand the volume dependence of the normalization factors should become smaller as we are approaching the perturbative regime. In practice the simulations are thus performed at $L/a = 8$ and the systematic error is estimated from additional runs at the coarsest of these lattice spacings, i.e. at $\beta = 7.2$, by taking the difference of Z_{A} and Z_{V} between $L/a = 8$ and 16. While for the Z_{A} estimate the volume dependence is hardly visible, in the case of Z_{V} the large volume ($L/a = 16$) results in a (statistically) significantly lower value. This is the reason for the larger systematic error of Z_{V} for $\beta \geq 7.2$.

As already mentioned, the simulations at $\beta = 5.29$ (again with a $8^3 \times 18$ lattice) were done to check that the large difference in Z_{A} when going from $\beta = 5.2$ to 5.5 is bridged smoothly. At this value of β the matched volume would be $L/a = 9$, which is not accessible with our machine (APE geometry restrictions) and code (even–odd preconditioning). Although the results were excluded from the fits for this reason, also the $\beta = 5.29$ data are well reproduced by the interpolating formulae (see Fig. 8.4), which implies that possible systematic effects are not visible at the given statistical precision.

[4] Although in [11] $Z_{\mathrm{A}}^{\mathrm{con}}$ (see next section) was considered, this comparison is still meaningful since the difference from our definition of Z_{A} was found to be negligible already for $a \simeq 0.1\,\mathrm{fm}$.

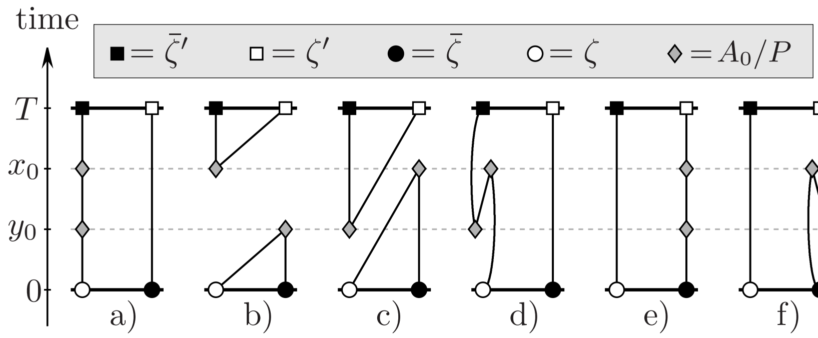

Figure 8.5: Quark diagrams for $f^{\mathrm{I}}_{\mathrm{AA}}$ with non–vanishing isospin factors. The gray diamonds indicate the insertions at times y_0 and x_0.

8.3.4 Comparison with alternative normalization conditions

In this section we consider two variants of the definition of Z_{A} (8.35) and study the difference in the results for $Z_{\mathrm{A}}(g_0^2)$. This provides us with an estimate for the magnitude of the cutoff effects to be expected at the considered lattice spacings.

The Wick contractions of $f^{\mathrm{I}}_{\mathrm{AA}}(x_0, y_0)$ are derived in Appendix B.1 with the result that for the chosen isospin assignment only the quark diagrams shown in Fig. 8.5 contribute. Diagrams related by an exchange $y_0 \leftrightarrow x_0$ have the same isospin factors with opposite signs. This follows directly from (8.26), where such an exchange corresponds to $\epsilon^{abc} \leftrightarrow \epsilon^{bac}$. Among the quark diagrams are the two disconnected diagrams b) and c), where no quark propagator connects the boundaries.

Following [120], we now argue that in the massless continuum limit the contribution of the disconnected diagrams vanishes. Thus we consider diagram b) without improvement, i.e. the current insertions are just axial charges.

In this diagram, termed $[gf]_{\mathrm{AA}}(x_0, y_0)$ in Appendix B.2, the spatial insertion points $\mathbf{x}$ and $\mathbf{y}$ are integrated over such that it is a function of x_0 and y_0 only. In fact, since we are in the chiral limit, the axial charge is conserved and hence the diagram is independent of the insertion points in the two regions $x_0 < y_0$ and $x_0 > y_0$. If the two insertion meet, contact terms may arise, which we need to treat separately.

To this end we restrict the spatial integration to $|\mathbf{x} - \mathbf{y}| > \epsilon$ and let the insertion times approach one another from either region. No contact terms can appear due to the finite spatial separation. If the integrand has a divergence weaker than $|\mathbf{x} - \mathbf{y}|^{-3}$, the contribution to the spatial integral from the region $|\mathbf{x} - \mathbf{y}| \leq \epsilon$ vanishes as we make it smaller and smaller. In this case we can take the limit $\epsilon \to 0$ and conclude that the order of x_0 and y_0 does not play any rôle. This would imply $[gf]_{\mathrm{AA}}(x_0, y_0) = [gf]_{\mathrm{AA}}(y_0, x_0)$, i.e. the diagrams b) and c) have the same value. Since their isospin factors have opposite signs, their contribution to $f_{\rm AA}$ cancels.

This argumentation shows that in the massless continuum theory the disconnected quark diagrams b) and c) do not contribute if the composite field $A_0(x)A_0(y)$ has a divergence weaker than $|\mathbf{x}-\mathbf{y}|^{-3}$. To decide this we consider the matrix elements of two axial charges between pseudo–scalar states and assign the flavor quantum numbers such that diagram b) is the only Wick contraction. Using four valence quark species u, d, s and c this amounts to

$$\langle \pi_{ud}|\,(A_0)_{du}(x)(A_0)_{cs}(y)|\pi_{sc}\rangle\ . \tag{8.41}$$

It is now immediately clear that such a flavor assignment excludes a single quark bilinear as the leading contribution in the operator product expansion of $A_0(x)A_0(y)$. Hence the latter has (if any) a divergence weaker than $|\mathbf{x}-\mathbf{y}|^{-3}$ in the limit $|\mathbf{x}-\mathbf{y}|\rightarrow\epsilon$ and the contribution from the excluded integration region vanishes.

Since the correlation functions approach their continuum value with a rate proportional to a^2, we can conclude that on the lattice the contribution from the disconnected diagrams is a cutoff effect of this order.

If, in contrast, we would consider the diagrams a) and d), which also differ by a sign, they are still independent of the insertion times in the regions $x_0<y_0$ and $x_0>y_0$. However, in the above argumentation the flavor structure would be

$$\langle \pi_{ud}|\,(A_0)_{ds}(x)(A_0)_{sc}(y)|\pi_{cu}\rangle \tag{8.42}$$

and hence the operator product could mix with e.g. $(V_0)_{dc}$ or the scalar density. This, by dimensional analysis, produces a factor $|\mathbf{x}-\mathbf{y}|^{-3}$ in the integrand at leading order of the OPE and thus, after integrating, a logarithmically divergent contact term. Therefore, no statement about the contribution of the connected diagrams can be made from this argument.

In more physical terms this can be understood directly from the quark diagrams. Even if the insertion points coincide when we move them around (on a fixed gauge background), in b) there is no propagator connecting them and the axial charges thus don't "see" each other. Doing this with diagram d) changes the propagator $\sum_{\mathbf{x},\mathbf{y}} S(x;y)$ and in particular it gives a contact term at zero separation.

As is shown in Fig. 8.6, we can numerically confirm that the contribution of the disconnected diagrams to $f_{\rm AA}^{\rm I}$ vanishes in the continuum limit. According to Appendix B.2 the contribution is

$$\begin{aligned} f_{\rm AA}^{\rm I}\Big|_{\rm disconnected} = \;& [gf]_{\rm AA}(x_0,y_0)-[gf]_{\rm AA}(y_0,x_0) \\ & +ac_{\rm A}\tilde\partial_0^x\Big\{-[gf]_{\rm PA}(x_0,y_0)-[gf]_{\rm AP}(y_0,x_0)\Big\} \\ & +ac_{\rm A}\tilde\partial_0^y\Big\{[gf]_{\rm AP}(x_0,y_0)+[gf]_{\rm PA}(y_0,x_0)\Big\} \end{aligned}$$

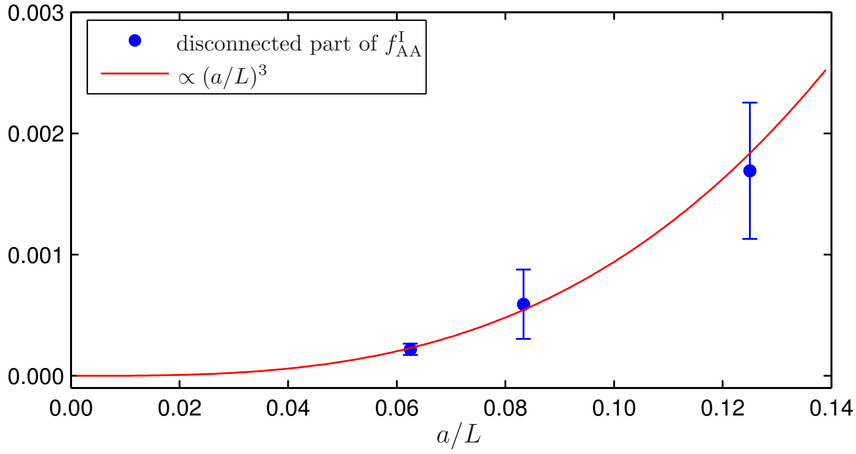

Figure 8.6: Data from the simulations at $\beta = 5.2$, 5.5 and 5.715 extrapolated to the chiral limit. As expected the contributions from the disconnected diagrams vanishes in the continuum limit with a rate that is faster than linear in a.

$$+a^2 c_{\rm A}^2 \tilde{\partial}_0^x \, \tilde{\partial}_0^y \left\{ [gf]_{\rm PP}(y_0, x_0) - [gf]_{\rm PP}(x_0, y_0) \right\} , \quad (8.43)$$

where we have $y_0 = T/3$ and $x_0 = 2T/3$. In Fig. 8.6 we plot data from the matched simulations and neglect any systematic effects from volume mismatch. One can clearly see that the above term approaches zero *faster* than linear in the lattice spacing and is in fact compatible with an a^3 effect.

The correlation function multiplying the mass term, $\tilde{f}_{\rm PA}^{\rm I}$, only influences the slope of the chiral extrapolation but not the result for $Z_{\rm A}$ in the chiral limit. We are therefore free to also drop the disconnected diagrams for this correlator. An estimate of $Z_{\rm A}$ using (8.35), where only the connected part of the correlation functions enter, should therefore agree with the original definition up to $\mathrm{O}(a^2)$. We will denote this by $Z_{\rm A}^{\rm con}$.

In the quenched case [11] $Z_{\rm A}$ was also determined from the connected quark diagrams only. The authors approach the above conclusion from a different point. Their argument exploits the freedom to choose different external operators in the Ward identity (8.22). Instead of (8.23), one could use

$$\mathcal{O}_{\rm ext} = \frac{-i}{6L^6} \mathcal{O}'_i \tfrac{1}{2}(\tau^c)_{ij} \mathcal{O}_j + \frac{i}{6L^6} \mathcal{K}'_i \tfrac{1}{2}(\tau^c)_{ji} \mathcal{K}_j \;, \quad (8.44)$$

$$\text{where} \quad \mathcal{O}'_i = a^6 \sum_{\mathbf{u},\mathbf{v}} \bar{\zeta}'_i(\mathbf{u}) \gamma_5 \xi'(\mathbf{v}) \;, \qquad \mathcal{O}_i = a^6 \sum_{\mathbf{u},\mathbf{v}} \bar{\xi}(\mathbf{u}) \gamma_5 \zeta_i(\mathbf{v}) \;, \quad (8.45)$$

$$\mathcal{K}'_i = a^6 \sum_{\mathbf{u},\mathbf{v}} \bar{\xi}'(\mathbf{u}) \gamma_5 \zeta'_i(\mathbf{v}) \;, \qquad \mathcal{K}_i = a^6 \sum_{\mathbf{u},\mathbf{v}} \bar{\zeta}_i(\mathbf{u}) \gamma_5 \xi(\mathbf{v}) \;. \quad (8.46)$$

Here i and j are flavor indices and ξ denotes the boundary field for a third quark species, which is taken to be an isospin singlet. Therefore no Wick contraction

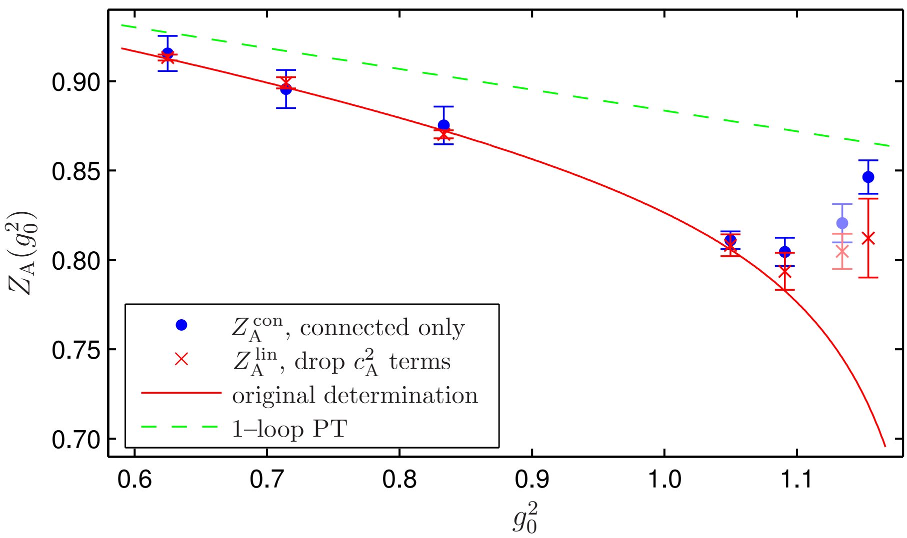

Figure 8.7: Changing the definition of Z_A at $O(a^2)$ has significant effect on the result for bare gauge couplings $g_0^2 \gtrsim 1.1$.

exists that connects it to the axial current with the result that no disconnected diagrams can appear. Since the external operator in the Ward identity is arbitrary, the resulting Z_A agrees with the original one up to cutoff effects and one thus again reaches the same conclusion. Note that the first argument takes place at the level of quark diagrams and is thus valid for any number of valence and sea quarks, whereas the external operator (8.44) explicitly assumes the existence of three valence quarks flavors.

If the improved axial current is inserted into the correlator f_{AA}^I, we obtain expressions proportional to c_A^2 as in the last line of (8.43). Since we implement improvement only to $O(a)$, we could have decided to drop these as just another source of $O(a^2)$ ambiguities. Thus, keeping only improvement terms *lin*ear in c_A provides us with another estimate of the axial current normalization constant, which we denote by Z_A^{lin}.[5]

We can now repeat the whole analysis – chiral limit at each value of β and estimate of volume dependence – to extract $Z_A(g_0^2)$ from the estimates Z_A^{con} and Z_A^{lin}. The result of this exercise is shown in Fig. 8.7, where it is compared to the interpolating formula (8.39) for the original estimate. We note that for $\beta \geq 5.7$ ($g_0^2 < 1.1$) the central values agree with the interpolating formula (8.39). The increased errors for Z_A^{con} at $\beta \geq 7.2$ are due to the rather large dependence on L/a we found at $\beta = 7.2$ (see Appendix D).

[5] One might be tempted to also consider $Z_A^{con,lin}$, but in practice the contribution of the c_A^2 term to the connected part is negligible and hence $Z_A^{con,lin} \simeq Z_A^{con}$.

However, much more noticeable are the $\mathrm{O}(a^2)$ effects in the range of $g_0^2 \simeq 1.1$ and above, corresponding to $\beta \lesssim 5.4$. The agreement with the original determination in form of the Pade fit is rapidly lost and at $\beta = 5.2$ we see a (statistically significant) deviation of 15% (for $Z_\mathrm{A}^\mathrm{con}$).

This might be surprising, given that in Fig. 8.6 the $\beta = 5.2$ estimate of the disconnected part is only two standard deviations from zero. It is, however, of similar magnitude as the connected part and the small error in the resulting Z_A is due to the correlation of numerator and denominator in (8.35).

From the above observations and Fig. 8.7 it is clear that it is essentially the last term in (8.43), which is responsible for the monotonic behavior in our original estimate. The large contribution of this term is in turn related to the fact that in the volumes and time extensions we consider here, the f_P correlator still shows a strong exponential decay *even at the critical point*. This means that it receives large contributions from excited states in the pseudo–scalar channel [114] and therefore its effective mass large.

These deviations and even the apparent non–monotonic behavior one obtains from $Z_\mathrm{A}^\mathrm{con}$ and $Z_\mathrm{A}^\mathrm{lin}$ do not signify any theoretical problems. It is, however, another sign that even after a successful implementation of the improvement programme the lattice artifacts in the two–flavor theory can be large for $\beta \lesssim 5.4$ and a continuum extrapolation remains necessary to make reliable physical predictions. In particular, care should be taken that such extrapolations are *not* dominated by the data from simulations with $\beta = 5.3$ or lower.

In the quenched case the $\mathrm{O}(a^2)$ effects from the disconnected diagrams are significantly smaller at a lattice spacing $a \simeq 0.1\,\mathrm{fm}$. In fact, at a statistical precision of the order of 1% these effects are not visible at all.

8.4 Summary

We have formulated an integrated Ward identity, derived from the isovector chiral symmetry of the continuum action, as a normalization condition for the axial current on the lattice. Through the use of the massive Ward identity we were able to improve the method from [11] with respect to its mass dependence.

The normalization condition was implemented in terms of correlation functions in the Schrödinger functional framework and evaluated on a line of constant physics in order to achieve a smooth disappearance of the $\mathrm{O}(a^2)$ uncertainties. Through additional simulations at very small lattice spacings and volumes we verified that our non–perturbative definition approaches the perturbative prediction at small bare gauge coupling. Simulations were done at or near the critical point and owing to the new normalization condition, which keeps track of the mass term in the PCAC relation, any chiral extrapolations were extremely flat. Systematic effects due to deviations from the constant volume condition are also estimated and turn out to be small. The results are well described by an interpolating formula $Z_{\mathrm{A}}(g_0^2)$ in the range of bare couplings considered.

Enforcing isospin symmetry with the same programme, we obtain at the same time a non–perturbative determination of the normalization constant $Z_{\mathrm{V}}(g_0^2)$ of the local vector current.

We found large $\mathrm{O}(a^2)$ uncertainties in Z_{A} at $\beta \lesssim 5.4$ by varying the definition of Z_{A}, which indicate that despite improvement the cutoff effects in this range of lattice spacings can be large. Together with the algorithmic issues discussed in Chapter 6 these findings corroborate the worries expressed in [85] about the status of simulations with improved dynamical Wilson fermions at the currently accessible lattice spacings. This merely emphasizes that cutoff effects in physical quantities can be controlled only if a continuum extrapolation with several lattice resolutions is performed.

Finally, the method employed here can also be used to obtain Z_{A} with other actions formulated in the Schrödinger functional. This includes in particular the $\mathrm{O}(a)$ improved three flavor theory with either Iwasaki or plaquette gauge action [60, 116, 117].

Chapter 9

Conclusions

The main result of this work is the non–perturbative determination of the axial current improvement and normalization constants for the lattice theory with two flavors of dynamical Wilson fermions.

With this regularization we have thus shown that normalization conditions can be imposed at the non–perturbative level such that isovector chiral symmetries are realized in the continuum limit. Since we work with an improved theory, chiral Ward–Takahashi identities are then satisfied up to $\mathrm{O}(a^2)$ at finite lattice spacing.

In the course of the implementation of this programme algorithmic difficulties were encountered in the numerical simulations. A more detailed investigation revealed that those are related to features of the infrared spectrum of the Wilson–Dirac operator. More precisely, it was found that at a given lattice spacing the inclusion of the fermion determinant enhances the probability of finding very small eigenvalues, which is contrary to the usual intuition. This effect disappears rapidly as the lattice spacing is decreased and is thus interpreted as a lattice artifact.

This spectral distortion is responsible for problems in the molecular dynamics evolution of the hybrid Monte Carlo algorithm as well as in the efficient sampling of observables sensitive to small eigenvalues. One of the important results is that in this situation it can be advantageous to deviate from importance sampling. In practice we found the polynomial hybrid Monte Carlo algorithm with reweighting to be an efficient tool in the parameter range we considered.

The non–perturbative determination of c_{sw}, the improvement coefficient of the Wilson fermion action, has been known for some time already [59]. However, for a complete removal of the $\mathrm{O}(a)$ lattice artifacts also the composite fields need to be improved. We have completed this programme for the axial current, accomplishing a necessary step on the way to a non–perturbative normalization of the latter.

The non–perturbative determination of the axial current improvement constant c_{A} was implemented in the Schrödinger functional framework using spatial wave functions in the composite boundary fields. In this way we could obtain a large sensitivity by explicitly projecting to the ground and first excited state in the pseudo–scalar channel and requiring the current quark mass derived from the PCAC relation to be the same in both cases. With this method the contribution of excited states is well controlled and we were thus able to ensure that the unavoidable $\mathrm{O}(a)$ ambiguities in c_A remain small. To achieve a smooth disappearing of the latter in the perturbative limit we evaluated the improvement condition on a line of constant physics. Lacking a non–perturbative estimate of the evolution of the lattice spacing with the bare gauge coupling, we used (in a small range of bare gauge couplings) an estimate based on the three–loop lattice β–function for improved Wilson fermions.

In the next step we implemented the non–perturbative renormalization of the improved axial current. Similarly to the determination of the improvement coefficient this is also achieved by enforcing a continuum Ward identity at finite lattice spacing. We improved the method used in the quenched case [11] to obtain a normalization condition whose dependence on the quark mass is only a cutoff effect, thus alleviating the need for a chiral extrapolation.

Similar to c_A, beyond perturbation theory $Z_\mathrm{A}(g_0^2)$ is affected by an intrinsic $\mathrm{O}(a^2)$ ambiguity, which vanishes smoothly in the continuum limit if the normalization condition is evaluated on a line of constant physics. However, in the case of Z_A we need to evaluate this condition at zero quark mass at each lattice spacing and Z_A is thus the result of an extra– or interpolation in the quark mass. To match the volumes we use the same estimate of $\partial a/\partial g_0^2$ as in the determination of c_A and with additional simulations at large β we verify that our definition of Z_A smoothly matches with perturbation theory. With little additional effort we also extracted the local vector current normalization factor $Z_\mathrm{V}(g_0^2)$ from the same simulation data by enforcing isospin symmetry at finite lattice spacing.

The dependence of a non–perturbative definition of Z_A on the lattice size is expected to be of order $(a/L)^2$ close to the continuum. In our estimate of the systematic effects in Z_A due to deviations from the constant physics condition, we indeed observed only very little volume dependence. However, at lattice spacings $a \gtrsim 0.07\,\mathrm{fm}$ large ambiguities in Z_A were found by changing the normalization condition at $\mathrm{O}(a^2)$. Together with the cutoff effects in the spectrum (Chapter 6) these findings add to the evidence collected in [85] that the lattice artifacts with dynamical improved Wilson fermions at the current lattice spacings are much larger than initially expected from quenched experience. One might even suspect the proximity of a phase transition in bare parameter space in analogy to [84]. Such an extreme example of a lattice artifact would surely invalidate the Symanzik expansion (3.17).

Setting these worries aside, the results for c_A and Z_A can now readily be applied. The most immediate application would be to $\mathrm{O}(a)$ improve and renormalize the bare pseudo–scalar decay constants computed in [97, 98, 115]. As already mentioned in Section 7.2, using the non–perturbative c_A lowers the result from [115] by 10% at $\beta = 5.2$. With a 20% decrease compared to the 1–loop estimate (again at $\beta = 5.2$) the non–perturbative Z_{A} will also have a large effect when used to renormalize existing data.

The methods developed and implemented here can easily be applied to other actions formulated in the Schrödinger functional framework. This includes improved gauge actions [28] as well as theories with more than two dynamical quark flavors [60, 116, 117].

Within the research programme of the ALPHA collaboration, the results obtained here are an essential step in the computation of the pseudo–scalar meson decay constant F_{PS} needed to reliably convert the Λ parameter from [2] into physical units. In the short term, together with data from [14] $Z_{\mathrm{A}}(g_0^2)$ will be used in a fully non–perturbative calculation of the strange quark mass [15] following the strategy of [13, 72].

Bibliography

[1] J. D. Bjorken. Asymptotic sum rules at infinite momentum. *Phys. Rev.*, 179: 1547–1553, 1969.

[2] Michele Della Morte et al. Computation of the strong coupling in QCD with two dynamical flavours. *Nucl. Phys.*, B713:378–406, 2005.

[3] Kenneth G. Wilson. Confinement of quarks. *Phys. Rev.*, D10:2445–2459, 1974.

[4] S. Aoki et al. Quenched light hadron spectrum. *Phys. Rev. Lett.*, 84:238–241, 2000.

[5] A. Ukawa. Computational cost of full QCD simulations experienced by CP-PACS and JLQCD Collaborations. *Nucl. Phys. Proc. Suppl.*, 106:195–196, 2002.

[6] K. Symanzik. Continuum limit and improved action in lattice theories. 1. Principles and ϕ^4 theory. *Nucl. Phys.*, B226:187, 1983.

[7] K. Symanzik. Continuum limit and improved action in lattice theories. 2. O(N) nonlinear sigma model in perturbation theory. *Nucl. Phys.*, B226:205, 1983.

[8] K. Symanzik. Some topics in quantum field theory. *Mathematical Problems in Theoretical Physics, eds. R. Schrader et al., Lecture Notes in Physics*, 153:47–58, 1982. Presented at 6th Int. Conf. on Mathematical Physics, Berlin, West Germany, Aug 11-21, 1981.

[9] Martin Lüscher, Rajamani Narayanan, Peter Weisz, and Ulli Wolff. The Schrödinger functional: A renormalizable probe for non–Abelian gauge theories. *Nucl. Phys.*, B384:168–228, 1992.

[10] Stefan Sint. On the Schrödinger functional in QCD. *Nucl. Phys.*, B421:135–158, 1994.

[11] Martin Lüscher, Stefan Sint, Rainer Sommer, and Hartmut Wittig. Non–perturbative determination of the axial current normalization constant in O(a) improved lattice QCD. *Nucl. Phys.*, B491:344–364, 1997.

[12] Martin Lüscher, Stefan Sint, Rainer Sommer, Peter Weisz, and Ulli Wolff. Non–perturbative O(a) improvement of lattice QCD. *Nucl. Phys.*, B491:323–343, 1997.

[13] Stefano Capitani, Martin Lüscher, Rainer Sommer, and Hartmut Wittig. Non–perturbative quark mass renormalization in quenched lattice QCD. *Nucl. Phys.*, B544:669–698, 1999.

[14] F. Knechtli et al. Running quark mass in two flavor QCD. *Nucl. Phys. Proc. Suppl.*, 119:320–322, 2003.

[15] Michele Della Morte, Roland Hoffmann, Francesco Knechtli, Juri Rolf, Rainer Sommer, Ines Wetzorke, and Ulli Wolff. Non–perturbative quark mass renormalization in two–flavor QCD. 2005.

[16] R. Hoffmann, F. Knechtli, J. Rolf, R. Sommer, and U. Wolff. Non–perturbative renormalization of the axial current with improved Wilson quarks. *Nucl. Phys. Proc. Suppl.*, 129:423–425, 2004.

[17] Michele Della Morte, Roland Hoffmann, Francesco Knechtli, and Ulli Wolff. Impact of large cutoff–effects on algorithms for improved Wilson fermions. *Comput. Phys. Commun.*, 165:49–58, 2005.

[18] M. Della Morte, R. Hoffmann, F. Knechtli, and U. Wolff. Cutoff effects in the spectrum of dynamical Wilson fermions. *Nucl. Phys. Proc. Suppl.*, 140:862–864, 2005.

[19] Michele Della Morte, Roland Hoffmann, and Rainer Sommer. Non–perturbative improvement of the axial current for dynamical Wilson fermions. *JHEP*, 03:029, 2005.

[20] Michele Della Morte, Roland Hoffmann, Francesco Knechtli, Rainer Sommer, and Ulli Wolff. Non–perturbative renormalization of the axial current with dynamical Wilson fermions. *JHEP*, 07:007, 2005.

[21] Chen-Ning Yang and R. L. Mills. Conservation of isotopic spin and isotopic gauge invariance. *Phys. Rev.*, 96:191–195, 1954.

[22] Christof Gattringer, Roland Hoffmann, and Stefan Schaefer. Setting the scale for the Lüscher–Weisz action. *Phys. Rev.*, D65:094503, 2002.

[23] Gerard 't Hooft. On the phase transition towards permanent quark confinement. *Nucl. Phys.*, B138:1, 1978.

[24] J. Gasser and H. Leutwyler. Quark masses. *Phys. Rept.*, 87:77–169, 1982.

[25] Kazuo Fujikawa. Path integral measure for gauge invariant fermion theories. *Phys. Rev. Lett.*, 42:1195, 1979.

[26] Martin Lüscher. Exact chiral symmetry on the lattice and the Ginsparg–Wilson relation. *Phys. Lett.*, B428:342–345, 1998.

[27] M. Lüscher and P. Weisz. On–shell improved lattice gauge theories. *Commun. Math. Phys.*, 97:59, 1985.

[28] Y. Iwasaki. Renormalization group analysis of lattice theories and improved lattice action. 2. Four–dimensional non–Abelian SU(N) gauge model. Tsukuba preprint, 1983. UTHEP-118.

[29] M. Creutz. Monte Carlo study of quantized SU(2) gauge theory. *Phys. Rev.*, D21:2308–2315, 1980.

[30] N. Cabibbo and E. Marinari. A new method for updating SU(N) matrices in computer simulations of gauge theories. *Phys. Lett.*, B119:387–390, 1982.

[31] Michael Creutz. Overrelaxation and Monte Carlo simulation. *Phys. Rev.*, D36: 515, 1987.

[32] R. Sommer. A new way to set the energy scale in lattice gauge theories and its applications to the static force and α_s in $SU(2)$ Yang-Mills theory. *Nucl. Phys.*, B411:839–854, 1994.

[33] Silvia Necco and Rainer Sommer. The $N_f = 0$ heavy quark potential from short to intermediate distances. *Nucl. Phys.*, B622:328–346, 2002.

[34] Martin Lüscher. Advanced lattice QCD. 1998. Published in Proceedings of the Les Houches Summer School, 28 July-5 September 1997, Edited by R. Gupta, A. Morel, E. de Rafael, F. David.

[35] Holger Bech Nielsen and M. Ninomiya. No–go theorem for regularizing chiral fermions. *Phys. Lett.*, B105:219, 1981.

[36] Luuk H. Karsten and Jan Smit. Lattice fermions: Species doubling, chiral invariance, and the triangle anomaly. *Nucl. Phys.*, B183:103, 1981.

[37] H. S. Sharatchandra, H. J. Thun, and P. Weisz. Susskind fermions on a Euclidean lattice. *Nucl. Phys.*, B192:205, 1981.

[38] I. Montvay and G Münster. *Quantum Fields on a Lattice*. Cambridge University Press, Cambridge, 1991.

[39] Paul H. Ginsparg and Kenneth G. Wilson. A remnant of chiral symmetry on the lattice. *Phys. Rev.*, D25:2649, 1982.

[40] P. Hasenfratz, S. Hauswirth, T. Jorg, F. Niedermayer, and K. Holland. Testing the fixed–point QCD action and the construction of chiral currents. *Nucl. Phys.*, B643:280–320, 2002.

[41] M. F. Atiyah and I. M. Singer. The index of elliptic operators. 5. *Annals Math.*, 93:139–149, 1971.

[42] P. Hasenfratz. Prospects for perfect actions. *Nucl. Phys. Proc. Suppl.*, 63:53–58, 1998.

[43] David B. Kaplan. A method for simulating chiral fermions on the lattice. *Phys. Lett.*, B288:342–347, 1992.

[44] Herbert Neuberger. Exactly massless quarks on the lattice. *Phys. Lett.*, B417: 141–144, 1998.

[45] Z. Fodor, S. D. Katz, and K. K. Szabo. Dynamical overlap fermions, results with hybrid Monte Carlo algorithm. *JHEP*, 08:003, 2004.

[46] N. Cundy, S. Krieg, A. Frommer, Th. Lippert, and K. Schilling. Dynamical overlap simulations using HMC. *Nucl. Phys. Proc. Suppl.*, 140:841–843, 2005.

[47] Thomas DeGrand and Stefan Schaefer. Physics issues in simulations with dynamical overlap fermions. *Phys. Rev.*, D71:034507, 2005.

[48] Martin Lüscher. Chiral gauge theories revisited. 2000.

[49] John B. Kogut and Leonard Susskind. Hamiltonian formulation of Wilson's lattice gauge theories. *Phys. Rev.*, D11:395, 1975.

[50] Leonard Susskind. Lattice fermions. *Phys. Rev.*, D16:3031–3039, 1977.

[51] B. Bunk, M. Della Morte, K. Jansen, and F. Knechtli. Locality with staggered fermions. *Nucl. Phys.*, B697:343–362, 2004.

[52] E. Marinari, G. Parisi, and C. Rebbi. Monte Carlo simulation of the massive Schwinger model. *Nucl. Phys.*, B190:734, 1981.

[53] Roberto Frezzotti, Pietro Antonio Grassi, Stefan Sint, and Peter Weisz. Lattice QCD with a chirally twisted mass term. *JHEP*, 08:058, 2001.

[54] R. Frezzotti and G. C. Rossi. Chirally improving Wilson fermions. I: O(a) improvement. *JHEP*, 08:007, 2004.

[55] H. Panagopoulos and Y. Proestos. The critical hopping parameter in O(a) improved lattice QCD. *Phys. Rev.*, D65:014511, 2002.

[56] Marco Bochicchio, Luciano Maiani, Guido Martinelli, Gian Carlo Rossi, and Massimo Testa. Chiral symmetry on the lattice with Wilson fermions. *Nucl. Phys.*, B262:331, 1985.

[57] Werner Kerler. Axial vector anomaly in lattice gauge theory. *Phys. Rev.*, D23: 2384, 1981.

[58] B. Sheikholeslami and R. Wohlert. Improved continuum limit lattice action for QCD with Wilson fermions. *Nucl. Phys.*, B259:572, 1985.

[59] Karl Jansen and Rainer Sommer. O(a) improvement of lattice QCD with two flavors of Wilson quarks. *Nucl. Phys.*, B530:185–203, 1998.

[60] N. Yamada et al. Non-perturbative O(a) improvement of Wilson quark action in three-flavor QCD with plaquette gauge action. 2004.

[61] M. Lüscher and P. Weisz. O(a) improvement of the axial current in lattice QCD to one–loop order of perturbation theory. *Nucl. Phys.*, B479:429–458, 1996.

[62] Steven Weinberg. New approach to the renormalization group. *Phys. Rev.*, D8: 3497–3509, 1973.

[63] Martin Lüscher, Stefan Sint, Rainer Sommer, and Peter Weisz. Chiral symmetry and O(a) improvement in lattice QCD. *Nucl. Phys.*, B478:365–400, 1996.

[64] M. Testa. Some observations on broken symmetries. *JHEP*, 04:002, 1998.

[65] E. Gabrielli, G. Martinelli, C. Pittori, G. Heatlie, and Christopher T. Sachrajda. Renormalization of lattice two fermion operators with improved nearest neighbor action. *Nucl. Phys.*, B362:475–486, 1991.

[66] M. Göckeler et al. Perturbative renormalisation of bilinear quark and gluon operators. *Nucl. Phys. Proc. Suppl.*, 53:896–898, 1997.

[67] Stefan Sint,. private notes, 1996.

[68] Martin Lüscher, Rainer Sommer, Peter Weisz, and Ulli Wolff. A precise determination of the running coupling in the SU(3) Yang–Mills theory. *Nucl. Phys.*, B413:481–502, 1994.

[69] Rainer Sommer. Non-perturbative renormalization of QCD. 1997.

[70] Achim Bode, Peter Weisz, and Ulli Wolff. Two–loop computation of the Schrödinger functional in lattice QCD. *Nucl. Phys.*, B576:517–539, 2000.

[71] Stefan Sint and Peter Weisz. Further results on O(a) improved lattice QCD to one-loop order of perturbation theory. *Nucl. Phys.*, B502:251–268, 1997.

[72] Joyce Garden, Jochen Heitger, Rainer Sommer, and Hartmut Wittig. Precision computation of the strange quark's mass in quenched QCD. *Nucl. Phys.*, B571: 237–256, 2000.

[73] S. Duane, A. D. Kennedy, B. J. Pendleton, and D. Roweth. Hybrid Monte Carlo. *Phys. Lett.*, B195:216–222, 1987.

[74] Steven A. Gottlieb, W. Liu, D. Toussaint, R. L. Renken, and R. L. Sugar. Hybrid molecular dynamics algorithms for the numerical simulation of quantum chromodynamics. *Phys. Rev.*, D35:2531–2542, 1987.

[75] Martin Lüscher. Lattice QCD and the Schwarz alternating procedure. *JHEP*, 05: 052, 2003.

[76] Thomas A. DeGrand and Pietro Rossi. Conditioning techniques for dynamical fermions. *Comput. Phys. Commun.*, 60:211–214, 1990.

[77] Martin Hasenbusch. Speeding up the hybrid Monte Carlo algorithm for dynamical fermions. *Phys. Lett.*, B519:177–182, 2001.

[78] Michele Della Morte et al. Simulating the Schrödinger functional with two pseudo–fermions. *Comput. Phys. Commun.*, 156:62–72, 2003.

[79] J. C. Sexton and D. H. Weingarten. Hamiltonian evolution for the hybrid Monte Carlo algorithm. *Nucl. Phys.*, B380:665–678, 1992.

[80] Sourendu Gupta, A. Irback, F. Karsch, and B. Petersson. The acceptance probability in the hybrid Monte Carlo method. *Phys. Lett.*, B242:437–443, 1990.

[81] M. Creutz. Global Monte Carlo algorithms for many fermion systems. *Phys. Rev.*, D38:1228–1238, 1988.

[82] H. A. van der Vorst. Bicgstab: a fast and smoothly converging variant of BiCG for the solution of nonsymmetric linear systems. *SIAM J. Sci. Stat. Comput.*, 13 (2):631–644, 1992. ISSN 0196-5204.

[83] Ulli Wolff. Monte Carlo errors with less errors. *Comput. Phys. Commun.*, 156: 143–153, 2004.

[84] S. Aoki et al. Non–trivial phase structure of $N_f = 3$ QCD with O(a) improved Wilson fermions at zero temperature. *Nucl. Phys. Proc. Suppl.*, 106:263–265, 2002.

[85] **ALPHA, CP-PACS, JLQCD** Collaborations, R. Sommer, et al. Large cutoff effects of dynamical Wilson fermions. *Nucl. Phys. Proc. Suppl.*, 129:405–407, 2004.

[86] Philippe de Forcrand and Tetsuya Takaishi. Fast fermion Monte Carlo. *Nucl. Phys. Proc. Suppl.*, 53:968–970, 1997.

[87] Roberto Frezzotti and Karl Jansen. A polynomial hybrid Monte Carlo algorithm. *Phys. Lett.*, B402:328–334, 1997.

[88] Balint Joo et al. Instability in the molecular dynamics step of hybrid Monte Carlo in dynamical fermion lattice QCD simulations. *Phys. Rev.*, D62:114501, 2000.

[89] Yusuke Namekawa et al. Exploring QCD at small sea quark masses with improved Wilson–type quarks. *Nucl. Phys. Proc. Suppl.*, 119:335–337, 2003.

[90] C. R. Allton et al. Improved Wilson QCD simulations with light quark masses. *Phys. Rev.*, D70:014501, 2004.

[91] R. Frezzotti. Wilson fermions with chirally twisted mass. *Nucl. Phys. Proc. Suppl.*, 119:140–148, 2003.

[92] Thomas Kalkreuter and Hubert Simma. An accelerated conjugate gradient algorithm to compute low lying eigenvalues: A study for the Dirac operator in SU(2) lattice QCD. *Comput. Phys. Commun.*, 93:33–47, 1996.

[93] Roberto Frezzotti and Karl Jansen. The PHMC algorithm for simulations of dynamical fermions. I: Description and properties. *Nucl. Phys.*, B555:395–431, 1999.

[94] Roberto Frezzotti and Karl Jansen. The PHMC algorithm for simulations of dynamical fermions. II: Performance analysis. *Nucl. Phys.*, B555:432–453, 1999.

[95] Pilar Hernandez, Karl Jansen, and Martin Lüscher. Locality properties of Neuberger's lattice Dirac operator. *Nucl. Phys.*, B552:363–378, 1999.

[96] Thomas DeGrand, Anna Hasenfratz, and Tamas G. Kovacs. Instantons and exceptional configurations with the clover action. *Nucl. Phys.*, B547:259–280, 1999.

[97] S. Aoki et al. Light hadron spectroscopy with two flavors of O(a) improved dynamical quarks. *Phys. Rev.*, D68:054502, 2003.

[98] C. R. Allton et al. Effects of non–perturbatively improved dynamical fermions in QCD at fixed lattice spacing. *Phys. Rev.*, D65:054502, 2002.

[99] Achim Bode et al. First results on the running coupling in QCD with two massless flavors. *Phys. Lett.*, B515:49–56, 2001.

[100] Tanmoy Bhattacharya, Rajan Gupta, Weon-Jong Lee, and Stephen R. Sharpe. O(a) improved renormalization constants. *Phys. Rev.*, D63:074505, 2001.

[101] S. Collins, C. T. H. Davies, G. P. Lepage, and J. Shigemitsu. A non–perturbative determination of the O(a) improvement coefficient $c_{\rm A}$ and the scaling of f_π and $m_{\overline{\rm MS}}$. *Phys. Rev.*, D67:014504, 2003.

[102] Marco Guagnelli et al. Non–perturbative results for the coefficients b_m and $b_A - b_P$ in $O(a)$ improved lattice QCD. *Nucl. Phys.*, B595:44–62, 2001.

[103] S. Dürr and M. Della Morte. Exploring two non–perturbative definitions of $c_{\rm A}$. *Nucl. Phys. Proc. Suppl.*, 129:417–419, 2004.

[104] M. Göckeler et al. Determination of light and strange quark masses from full lattice QCD. 2004.

[105] A. Bode and H. Panagopoulos. The three–loop beta–function of QCD with the clover action. *Nucl. Phys.*, B625:198–210, 2002.

[106] Anna Hasenfratz and Peter Hasenfratz. The connection between the lambda parameters of lattice and continuum QCD. *Phys. Lett.*, B93:165, 1980.

[107] Hikaru Kawai, Ryuichi Nakayama, and Koichi Seo. Comparison of the lattice lambda parameter with the continuum lambda parameter in massless QCD. *Nucl. Phys.*, B189:40, 1981.

[108] P. Weisz. On the connection between the lambda parameters of Euclidean lattice and continuum QCD. *Phys. Lett.*, B100:331, 1981.

[109] Stefan Sint and Rainer Sommer. The running coupling from the QCD Schrödinger functional: A one–loop analysis. *Nucl. Phys.*, B465:71–98, 1996.

[110] Martin Lüscher and Peter Weisz. Computation of the relation between the bare lattice coupling and the MS coupling in SU(N) gauge theories to two loops. *Nucl. Phys.*, B452:234–260, 1995.

[111] B. Allés, A. Feo, and H. Panagopoulos. The three–loop beta function in SU(N) lattice gauge theories. *Nucl. Phys.*, B491:498–512, 1997.

[112] C. Christou, A. Feo, H. Panagopoulos, and E. Vicari. The three–loop beta–function of SU(N) lattice gauge theories with Wilson fermions. *Nucl. Phys.*, B525:387–400, 1998.

[113] Heiko Molke. *Improved interpolating fields in the Schrödinger functional.* PhD thesis, Humboldt Universität zu Berlin, 2004.

[114] Marco Guagnelli, Jochen Heitger, Rainer Sommer, and Hartmut Wittig. Hadron masses and matrix elements from the QCD Schrödinger functional. *Nucl. Phys.*, B560:465–481, 1999.

[115] A. C. Irving, C. McNeile, C. Michael, K. J. Sharkey, and H. Wittig. Is the up-quark massless? *Phys. Lett.*, B518:243–251, 2001.

[116] S. Aoki et al. Non–perturbative determination of $c_{\rm sw}$ in three–flavor dynamical QCD. *Nucl. Phys. Proc. Suppl.*, 119:433–435, 2003.

[117] K. I. Ishikawa et al. Study of finite volume effects in the non–perturbative determination of $c_{\rm sw}$ with the SF method in full three–flavor lattice QCD. *Nucl. Phys. Proc. Suppl.*, 129:444–446, 2004.

[118] Marco Guagnelli and Jochen Heitger. SSOR preconditioning in simulations of the QCD Schrödinger functional. *Comput. Phys. Commun.*, 130:12–21, 2000.

[119] T. Bakeyev et al. Non–perturbative renormalisation and improvement of the local vector current for quenched and unquenched Wilson fermions. *Phys. Lett.*, B580: 197–208, 2004.

[120] M. Lüscher and S. Sint,. private communication, 2003.

Appendix A

Improved action for the Schrödinger functional

The O(a) improved action of the QCD Schrödinger functional [63] is given by (the functional dependence on $U, \bar{\psi}$ and ψ is suppressed)

$$S_{\rm impr} = S_g + S_f + \delta S_v + \delta S_{f,b} \; . \tag{A.1}$$

The improvement of the gauge action (3.4) is implemented through

$$S_g[U] = \frac{1}{g_0^2} \sum_p w(p) {\rm Tr} \, \{1 - U_p\} \; , \tag{A.2}$$

where the weight for the oriented plaquette p is given by

$$w(p) \;\; = \;\; \begin{cases} 1, \text{ for } p \text{ in the interior of the SF} \\ c_{\rm t}, \text{ for } p \textit{ touching} \text{ the } x_0 = 0 \text{ or } T \text{ boundaries} \\ \frac{1}{2} c_{\rm s}, \text{ for } p \textit{ in} \text{ the boundary.} \end{cases} \tag{A.3}$$

A sufficient condition for the $c_{\rm s}$ term *not* to contribute are Abelian and spatially homogeneous boundary fields C_k and C'_k. This condition is not only fulfilled for vanishing background field (the setup employed here), but for all boundary gauge fields so far considered in the SF [2, 59].

The fermionic action is given by (4.4) in the interior of the SF cylinder and the boundary improvement terms (5.9) and (5.10) are transcribed on the lattice as

$$\delta S_{f,b} \;\; = \;\; a^4 \sum_{\mathbf{x}} \; (\tilde{c}_{\rm s} - 1)[\widehat{\mathcal{O}}_s(\mathbf{x}) + \widehat{\mathcal{O}}'_s(\mathbf{x})] \; + \; (\tilde{c}_{\rm t} - 1)[\widehat{\mathcal{O}}_t(\mathbf{x}) - \widehat{\mathcal{O}}'_t(\mathbf{x})] \; , \tag{A.4}$$

with the boundary and near–boundary operators

$$\widehat{\mathcal{O}}_s(\mathbf{x}) \;\; = \;\; \bar{\rho}(\mathbf{x}) \gamma_k \widetilde{\nabla}_k \rho(\mathbf{x}) \; , \tag{A.5}$$

$$\widehat{\mathcal{O}}'_s(\mathbf{x}) \;\; = \;\; \bar{\rho}'(\mathbf{x}) \gamma_k \widetilde{\nabla}_k \rho'(\mathbf{x}) \; , \tag{A.6}$$

$$\widehat{\mathcal{O}}_t(\mathbf{x}) \;\; = \;\; \left\{ \bar{\psi}(x) P_+ \nabla_0^\star \psi(x) + \bar{\psi}(x) \overleftarrow{\nabla}_0^\star P_- \psi(x) \right\}_{x_0 = a} \; , \tag{A.7}$$

$$\widehat{\mathcal{O}}'_t(\mathbf{x}) \;\; = \;\; \left\{ \bar{\psi}(x) P_- \nabla_0 \psi(x) + \bar{\psi}(x) \overleftarrow{\nabla}_0 P_+ \psi(x) \right\}_{x_0 = T - a} \; . \tag{A.8}$$

While $\widehat{\mathcal{O}}_t$ and $\widehat{\mathcal{O}}'_t$ couple to the dynamical variables close to the boundaries, $\widehat{\mathcal{O}}_s$ and $\widehat{\mathcal{O}}'_s$ depend on the fermionic boundary fields $\rho, \bar{\rho}, \rho'$ and $\bar{\rho}'$ only. Since they are set to zero, a knowledge of $\tilde{c}_{\mathrm{s}}$ is not necessary.

The entire fermionic part of (A.1) is expressed in (δD summarizes the volume and boundary improvement)

$$S_{f,\mathrm{impr}} = \sum_x \bar{\psi}(x)[D + \delta D + m_0]\psi(x) \ , \tag{A.9}$$

and for a given gauge field configuration $U_\mu(x)$ the quark propagator $S(x;y)$ is thus defined as [61]

$$(D + \delta D + m_0)S(x;y) = a^{-4}\delta_{xy} \ , \ 0 < x_0 < T \ , \tag{A.10}$$

and the boundary conditions

$$P_+ S(x;y)\Big|_{x_0=0} = P_- S(x;y)\Big|_{x_0=T} = 0 \ , \tag{A.11}$$

where color and spin indices have been suppressed. The basic two-point correlations are obtained [61] by differentiating the generating functional with respect to the source fields. The result can be expressed in terms of the quark propagator $S(x;y)$.

$$\begin{aligned}
\left[\psi(x)\bar{\psi}(y)\right]_{\mathrm{F}} &= S(x;y) && \text{(A.12)}\\
\left[\psi(x)\bar{\zeta}(\mathbf{y})\right]_{\mathrm{F}} &= \tilde{c}_{\mathrm{t}} S(x;a,\mathbf{y})U_0(0,\mathbf{y})^{-1}P_+ && \text{(A.13)}\\
\left[\psi(x)\bar{\zeta}'(\mathbf{y})\right]_{\mathrm{F}} &= \tilde{c}_{\mathrm{t}} S(x;T-a,\mathbf{y})U_0(T-a,\mathbf{y})P_- && \text{(A.14)}\\
\left[\zeta(\mathbf{x})\bar{\psi}(y)\right]_{\mathrm{F}} &= \tilde{c}_{\mathrm{t}} P_- U_0(0,\mathbf{x})S(a,\mathbf{x};y) && \text{(A.15)}\\
\left[\zeta'(\mathbf{x})\bar{\psi}(y)\right]_{\mathrm{F}} &= \tilde{c}_{\mathrm{t}} P_+ U_0(T-a,\mathbf{x})^{-1}S(T-a,\mathbf{x};y) && \text{(A.16)}\\
\left[\zeta(\mathbf{x})\bar{\zeta}'(\mathbf{y})\right]_{\mathrm{F}} &= \tilde{c}_{\mathrm{t}}^2 P_- U_0(0,\mathbf{x})S(a,\mathbf{x};T-a,\mathbf{y})U_0(T-a,\mathbf{y})P_- && \text{(A.17)}\\
\left[\zeta'(\mathbf{x})\bar{\zeta}(\mathbf{y})\right]_{\mathrm{F}} &= \tilde{c}_{\mathrm{t}}^2 P_+ U_0(T-a,\mathbf{x})^{-1}S(T-a,\mathbf{x};a,\mathbf{y})U_0(0,\mathbf{y})^{-1}P_+ && \text{(A.18)}
\end{aligned}$$

The correlators $\left[\zeta\bar{\zeta}\right]_{\mathrm{F}}$ and $\left[\zeta'\bar{\zeta}'\right]_{\mathrm{F}}$ are not needed since the isospin factor for such a Wick contraction vanishes for isovector boundary field of the type (5.13) and (5.14).

Appendix B

Correlation functions

B.1 Summed two-point correlators

We introduce the quark propagator from the lower boundary to the point x

$$\begin{aligned} \overline{S}(x) &= \frac{\tilde{c}_{\mathrm{t}} a^3}{L^{3/2}} \sum_{\mathbf{y}} S(x; a, \mathbf{y}) U_0(0, \mathbf{y})^{-1} P_+ && \text{(B.1)} \\ \Rightarrow \quad \overline{S}(x)^\dagger &= \frac{\tilde{c}_{\mathrm{t}} a^3}{L^{3/2}} \sum_{\mathbf{y}} P_+ U_0(0, \mathbf{y}) S(x; a, \mathbf{y})^\dagger \\ &= \frac{\tilde{c}_{\mathrm{t}} a^3}{L^{3/2}} \sum_{\mathbf{y}} P_+ U_0(0, \mathbf{y}) \gamma_5 S(a, \mathbf{y}; x) \gamma_5 \ , && \text{(B.2)} \end{aligned}$$

the quark propagator from the upper boundary to the point x

$$\begin{aligned} \overline{R}(x) &= \frac{\tilde{c}_{\mathrm{t}} a^3}{L^{3/2}} \sum_{\mathbf{y}} S(x; T-a, \mathbf{y}) U_0(T-a, \mathbf{y}) P_- && \text{(B.3)} \\ \Rightarrow \quad \overline{R}(x)^\dagger &= \frac{\tilde{c}_{\mathrm{t}} a^3}{L^{3/2}} \sum_{\mathbf{y}} P_- U_0(T-a, \mathbf{y})^{-1} \gamma_5 S(T-a, \mathbf{y}; x) \gamma_5 \ , && \text{(B.4)} \end{aligned}$$

and the boundary-to-boundary propagator

$$\begin{aligned} \overline{S}_T &= \tilde{c}_{\mathrm{t}} a^3 \sum_{\mathbf{x}} -U_0(T-a, \mathbf{x})^{-1} P_+ \overline{S}(T-a, \mathbf{x}) && \text{(B.5)} \\ \Rightarrow \quad \overline{S}_T^\dagger &= \tilde{c}_{\mathrm{t}} a^3 \sum_{\mathbf{x}} -\overline{S}(T-a, \mathbf{x})^\dagger P_+ U_0(T-a, \mathbf{x}) \ . && \text{(B.6)} \end{aligned}$$

Of course $\overline{S}_T$ can also be obtained through a summation of $\overline{R}(x)$

$$\begin{aligned} \gamma_5 \overline{S}_T \gamma_5 &\overset{(B.1)}{=} \frac{\tilde{c}_{\mathrm{t}}^2 a^6}{L^{3/2}} \sum_{\mathbf{x},\mathbf{y}} -U_0(T-a, \mathbf{x})^{-1} P_- \gamma_5 S(T-a, \mathbf{x}; a, \mathbf{y}) \gamma_5 U_0(0, \mathbf{y})^{-1} P_- \\ &\overset{(B.4)}{=} \tilde{c}_{\mathrm{t}} a^3 \sum_{\mathbf{y}} -\overline{R}(a, \mathbf{y})^\dagger U_0(0, \mathbf{y})^{-1} P_- \ . \end{aligned}$$

With these definitions we can express the basic two–point functions as

$$\frac{a^3}{L^{3/2}}\sum_{\mathbf{y}}\left[\psi(x)\bar{\zeta}(\mathbf{y})\right]_{\mathrm{F}} \stackrel{(A.13)}{=} \frac{a^3\tilde{c}_{\mathrm{t}}}{L^{3/2}}\sum_{\mathbf{y}} S(x;a,\mathbf{y})U_0(0,\mathbf{y})^{-1}P_+ \stackrel{(B.1)}{=} \overline{S}(x)\;, \tag{B.7}$$

$$\frac{a^3}{L^{3/2}}\sum_{\mathbf{y}}\left[\psi(x)\bar{\zeta}'(\mathbf{y})\right]_{\mathrm{F}} \stackrel{(A.14)}{=} \frac{a^3\tilde{c}_{\mathrm{t}}}{L^{3/2}}\sum_{\mathbf{y}} S(x;T-a,\mathbf{y})U_0(T-a,\mathbf{y})P_- \stackrel{(B.3)}{=} \overline{R}(x)\;. \tag{B.8}$$

The $\overline{S}(x)$ and $\overline{R}(x)$ propagators inherit the γ_5–Hermiticity from $S(x;y)$

$$\begin{aligned}
\frac{a^3}{L^{3/2}}\sum_{\mathbf{y}}\left[\zeta(\mathbf{y})\bar{\psi}(x)\right]_{\mathrm{F}} &\stackrel{(A.15)}{=} \frac{a^3\tilde{c}_{\mathrm{t}}}{L^{3/2}}\sum_{\mathbf{y}} P_-U_0(0,\mathbf{y})S(a,\mathbf{y};x)\\
&= \frac{a^3\tilde{c}_{\mathrm{t}}}{L^{3/2}}\sum_{\mathbf{y}}\left[S(a,\mathbf{y};x)^{\dagger}U_0(0,\mathbf{y})^{-1}P_-\right]^{\dagger}\\
&= \frac{a^3\tilde{c}_{\mathrm{t}}}{L^{3/2}}\sum_{\mathbf{y}}\left[\gamma_5 S(a,\mathbf{y};x)^{\dagger}\gamma_5 U_0(0,\mathbf{y})^{-1}P_+\gamma_5\right]^{\dagger}\gamma_5\\
&\stackrel{(B.1)}{=} \gamma_5\overline{S}(x)^{\dagger}\gamma_5\;,
\end{aligned}\tag{B.9}$$

$$\begin{aligned}
\frac{a^3}{L^{3/2}}\sum_{\mathbf{y}}\left[\zeta'(\mathbf{y})\bar{\psi}(x)\right]_{\mathrm{F}} &\stackrel{(A.16)}{=} \frac{a^3\tilde{c}_{\mathrm{t}}}{L^{3/2}}\sum_{\mathbf{y}} P_+U_0(T-a,\mathbf{y})^{-1}S(T-a,\mathbf{y};x)\\
&= \frac{a^3\tilde{c}_{\mathrm{t}}}{L^{3/2}}\sum_{\mathbf{y}}\left[S(T-a,\mathbf{y};x)^{\dagger}U_0(T-a,\mathbf{y})P_+\right]^{\dagger}\\
&= \frac{a^3\tilde{c}_{\mathrm{t}}}{L^{3/2}}\sum_{\mathbf{y}}\left[\gamma_5 S(T-a,\mathbf{y};x)^{\dagger}\gamma_5 U_0(T-a,\mathbf{y})P_-\gamma_5\right]^{\dagger}\gamma_5\\
&\stackrel{(B.3)}{=} \gamma_5\overline{R}(x)^{\dagger}\gamma_5\;.
\end{aligned}\tag{B.10}$$

For the spatially averaged boundary-to-boundary correlators one obtains

$$\begin{aligned}
\frac{a^6}{L^{3/2}}\sum_{\mathbf{x},\mathbf{y}}\left[\zeta(\mathbf{y})\bar{\zeta}'(\mathbf{x})\right]_{\mathrm{F}} &\stackrel{(A.17)}{=} \frac{a^6\tilde{c}_{\mathrm{t}}^2}{L^{3/2}}\sum_{\mathbf{x},\mathbf{y}} P_-U_0(0,\mathbf{y})S(a,\mathbf{y};T-a,\mathbf{x})U_0(T-a,\mathbf{x})P_-\\
&= \frac{a^6\tilde{c}_{\mathrm{t}}^2}{L^{3/2}}\sum_{\mathbf{x},\mathbf{y}}\gamma_5 P_+U_0(0,\mathbf{y})\gamma_5 S(a,\mathbf{y};T-a,\mathbf{x})\gamma_5 U_0(T-a,\mathbf{x})P_+\gamma_5\\
&\stackrel{(B.2)}{=} a^3\tilde{c}_{\mathrm{t}}\sum_{\mathbf{x}}\gamma_5\overline{S}(T-a,\mathbf{x})^{\dagger}U_0(T-a,\mathbf{x})P_+\gamma_5\\
&\stackrel{(B.6)}{=} -\gamma_5\overline{S}_T^{\dagger}\gamma_5\;,
\end{aligned}\tag{B.11}$$

$$
\begin{aligned}
\frac{a^6}{L^{3/2}}\sum_{\mathbf{x},\mathbf{y}}\left[\zeta'(\mathbf{x})\bar\zeta(\mathbf{y})\right]_{\mathrm{F}} &\stackrel{(A.18)}{=} \frac{a^6\tilde c_{\mathrm t}^2}{L^{3/2}}\sum_{\mathbf{x},\mathbf{y}} P_+U_0(T-a,\mathbf{x})^{-1}S(T-a,\mathbf{x};a,\mathbf{y})U_0(0,\mathbf{y})^{-1}P_+ \\
&\stackrel{(B.1)}{=} a^3\tilde c_{\mathrm t}\sum_{\mathbf{x}} P_+U_0(T-a,\mathbf{x})^{-1}\overline{S}(T-a,\mathbf{x}) \\
&\stackrel{(B.5)}{=} -\overline{S}_T\ . \qquad \text{(B.12)}
\end{aligned}
$$

B.1.1 2–point functions

To derive explicit expressions for f_1, $f_{\mathrm X}$ and $g_{\mathrm X}$ in terms of the propagators defined above, we use $A, B, \ldots$ for the Dirac indices and $i, j, \ldots$ for the indices in $SU(2)$ isospin space. Inserting equations (5.13, 5.14) into (5.19) yields

$$
\begin{aligned}
f_1 &= -\frac{1}{3L^6}\left\langle \mathcal{O}'^a\mathcal{O}^a\right\rangle \\
&= -\frac{a^{12}}{3L^6}\sum_{\mathbf{x},\mathbf{y},\mathbf{x}',\mathbf{y}'}\left\langle (\bar\zeta')_i^A(\mathbf{y}')\gamma_5^{AB}\tfrac12\tau^a_{ij}(\zeta')_j^B(\mathbf{x}')\bar\zeta_m^C(\mathbf{y})\gamma_5^{CD}\tfrac12\tau^a_{mn}\zeta_n^D(\mathbf{x})\right\rangle .
\end{aligned}
$$

We now perform the Wick contractions of the fields and since the propagator is isospin diagonal, each contraction requires the corresponding isospin indices to be the same. Due to their Grassmann nature, the sign changes when the order of fields is changed

$$
\begin{aligned}
\zeta'\bar\zeta', \zeta\bar\zeta &\;\to\; \delta_{ij}\delta_{mn} &&\to\; \tfrac14\tau^a_{ij}\tau^a_{mn}\delta_{ij}\delta_{mn} = \tfrac14(\mathrm{Tr}\,\tau^a)^2 = 0\ , \\
\zeta\bar\zeta', \zeta'\bar\zeta &\;\to\; -\delta_{in}\delta_{mj} &&\to\; -\tfrac14\tau^a_{nj}\tau^a_{jn} = -\tfrac14\mathrm{Tr}\,(\tau^a)^2 = -\tfrac32\ .
\end{aligned}
$$

The Dirac indices give the order of the propagators and Dirac–matrices and we are left with a trace in Dirac and color space

$$
\begin{aligned}
f_1 &= \frac{a^{12}}{2L^6}\sum_{\mathbf{x},\mathbf{y},\mathbf{x}',\mathbf{y}'}\left\langle \mathrm{Tr}\left\{\left[\zeta(\mathbf{x})\bar\zeta'(\mathbf{y}')\right]_{\mathrm F}\gamma_5\left[\zeta'(\mathbf{x}')\bar\zeta(\mathbf{y})\right]_{\mathrm F}\gamma_5\right\}\right\rangle_U \\
&\stackrel{(B.12)}{=} -\frac{a^6}{2L^{9/2}}\sum_{\mathbf{x},\mathbf{y}'}\left\langle \mathrm{Tr}\left\{\left[\zeta(\mathbf{x})\bar\zeta'(\mathbf{y}')\right]_{\mathrm F}\gamma_5\overline{S}_T\gamma_5\right\}\right\rangle_U \\
&\stackrel{(B.11)}{=} \frac{1}{2L^3}\left\langle \mathrm{Tr}\left\{\gamma_5\overline{S}_T^\dagger\gamma_5\gamma_5\overline{S}_T\gamma_5\right\}\right\rangle_U = \frac{1}{2L^3}\left\langle \mathrm{Tr}\,\overline{S}_T\overline{S}_T^\dagger\right\rangle_U . \qquad \text{(B.13)}
\end{aligned}
$$

In the same manner we evaluate the correlation function $f_{\mathrm P}$ (5.16)

$$
\begin{aligned}
f_{\mathrm P}(x_0) &= -\frac{a^3}{3L^3}\sum_{\mathbf{x}}\left\langle P^a(x)\mathcal{O}^a\right\rangle \\
&= -\frac{a^9}{3L^3}\sum_{\mathbf{x},\mathbf{u},\mathbf{v}}\left\langle \bar\psi_i^A(x)\gamma_5^{AB}\tfrac12\tau^a_{ij}\psi_j^B(x)\bar\zeta_m^C(\mathbf{u})\gamma_5^{CD}\tfrac12\tau^a_{mn}\zeta_n^D(\mathbf{v})\right\rangle .
\end{aligned}
$$

This is of the same structure as for f_1 and hence the only non–trivial Wick contraction is $[\psi\bar{\zeta}]$, $[\zeta\bar{\psi}]$ with an isospin factor of $-3/2$

$$
\begin{aligned}
f_{\rm P}(x_0) &= \frac{a^9}{2L^3}\sum_{\mathbf{x},\mathbf{u},\mathbf{v}}\left\langle \mathrm{Tr}\left\{\ [\psi(x)\bar{\zeta}(\mathbf{u})]_{\rm F}\,\gamma_5\,[\zeta(\mathbf{v})\bar{\psi}(x)]_{\rm F}\,\gamma_5\right\}\right\rangle_U \\
&\overset{(B.7)}{=} \frac{a^6}{2L^{3/2}}\sum_{\mathbf{x},\mathbf{v}}\left\langle \mathrm{Tr}\left\{\overline{S}(x)\gamma_5\,[\zeta(\mathbf{v})\bar{\psi}(x)]_{\rm F}\,\gamma_5\right\}\right\rangle_U \\
&\overset{(B.9)}{=} \frac{a^3}{2}\sum_{\mathbf{x}}\left\langle \mathrm{Tr}\left\{\overline{S}(x)\gamma_5\gamma_5\overline{S}(x)^\dagger\gamma_5\gamma_5\right\}\right\rangle_U \\
&= \frac{a^3}{2}\sum_{\mathbf{x}}\left\langle \mathrm{Tr}\left\{\overline{S}(x)\overline{S}(x)^\dagger\right\}\right\rangle_U . \qquad \text{(B.14)}
\end{aligned}
$$

The correlation function $f_{\rm A}(x_0)$ (5.15) differs from $f_{\rm P}(x_0)$ only by an additional γ_0 following $\bar{\psi}(x)$. We therefore have

$$
\begin{aligned}
f_{\rm A}(x_0) &= \frac{a^6}{2L^{3/2}}\sum_{\mathbf{x},\mathbf{v}}\left\langle \mathrm{Tr}\left\{\overline{S}(x)\gamma_5\,[\zeta(\mathbf{v})\bar{\psi}(x)]_{\rm F}\,\gamma_0\gamma_5\right\}\right\rangle_U \\
&\overset{(B.9)}{=} \frac{a^3}{2}\sum_{\mathbf{x}}\left\langle \mathrm{Tr}\left\{\overline{S}(x)\gamma_5\gamma_5\overline{S}(x)^\dagger\gamma_5\gamma_0\gamma_5\right\}\right\rangle_U \\
&= -\frac{a^3}{2}\sum_{\mathbf{x}}\left\langle \mathrm{Tr}\left\{\overline{S}(x)\overline{S}(x)^\dagger\gamma_0\right\}\right\rangle_U . \qquad \text{(B.15)}
\end{aligned}
$$

These results can also be used to evaluate $g_{\rm P}(x_0)$ (5.18) if one makes the replacement

$$
[\bar{\psi}(x),\psi(x),\bar{\zeta}(\mathbf{u}),\zeta(\mathbf{v})] \quad\longrightarrow\quad [\bar{\zeta}'(\mathbf{u}),\zeta'(\mathbf{v}),\bar{\psi}(x),\psi(x)]
$$

in eq. (B.14). The result is

$$
\begin{aligned}
g_{\rm P}(x_0) &= \frac{a^9}{2L^3}\sum_{\mathbf{x},\mathbf{u},\mathbf{v}}\left\langle \mathrm{Tr}\left\{\ [\zeta'(\mathbf{v})\bar{\psi}(x)]_{\rm F}\,\gamma_5\,[\psi(x)\bar{\zeta}'(\mathbf{u})]_{\rm F}\,\gamma_5\right\}\right\rangle_U \\
&\overset{(B.8)}{=} \frac{a^6}{2L^{3/2}}\sum_{\mathbf{x},\mathbf{v}}\left\langle \mathrm{Tr}\left\{\ [\zeta'(\mathbf{v})\bar{\psi}(x)]_{\rm F}\,\gamma_5\overline{R}(x)\gamma_5\right\}\right\rangle_U \\
&\overset{(B.10)}{=} \frac{a^3}{2}\sum_{\mathbf{x}}\left\langle \mathrm{Tr}\left\{\gamma_5\overline{R}(x)^\dagger\gamma_5\gamma_5\overline{R}(x)\gamma_5\right\}\right\rangle_U \\
&= \frac{a^3}{2}\sum_{\mathbf{x}}\left\langle \mathrm{Tr}\left\{\overline{R}(x)\overline{R}(x)^\dagger\right\}\right\rangle_U . \qquad \text{(B.16)}
\end{aligned}
$$

Again the corresponding axial correlator is obtained by inserting γ_0. Due to the different sign in (5.17) we need to put a γ_0 between $\bar{\psi}$ and the following γ_5 to obtain

$$
g_{\rm A}(x_0) = -\frac{a^6}{2L^{3/2}}\sum_{\mathbf{x},\mathbf{v}}\left\langle \mathrm{Tr}\left\{\ [\zeta'(\mathbf{v})\bar{\psi}(x)]_{\rm F}\,\gamma_0\gamma_5\overline{R}(x)\gamma_5\right\}\right\rangle_U
$$

$$\stackrel{(B.10)}{=} -\frac{a^3}{2}\sum_{\mathbf{x}}\left\langle \mathrm{Tr}\left\{\gamma_5\overline{R}(x)^\dagger\gamma_5\gamma_0\gamma_5\overline{R}(x)\gamma_5\right\}\right\rangle_U$$
$$= \frac{a^3}{2}\sum_{\mathbf{x}}\left\langle \mathrm{Tr}\left\{\overline{R}(x)\overline{R}^\dagger(x)\gamma_0\right\}\right\rangle_U . \qquad \text{(B.17)}$$

B.1.2 3–point functions

Inserting equations (5.13, 5.14) into (8.15) yields

$$\begin{aligned} f_{\mathrm{V}}(x_0) &= \frac{a^3}{6L^6}\sum_{\mathbf{x}} i\epsilon^{abc}\langle\mathcal{O}'^a V_0^b(x)\mathcal{O}^c\rangle \\ &= \frac{a^{15}}{6L^6}\sum_{\mathbf{x,u,v,w,z}} i\epsilon^{abc}\Big\langle(\bar\zeta')_i^A(\mathbf{u})\gamma_5^{AB}\tfrac{1}{2}\tau_{ij}^a(\zeta')_j^B(\mathbf{v}) \\ &\qquad\times\bar\psi_k^C(x)\gamma_0^{CD}\tfrac{1}{2}\tau_{kl}^b\psi_l^D(x)\bar\zeta_m^E(\mathbf{w})\gamma_5^{EF}\tfrac{1}{2}\tau_{mn}^c\zeta_n^F(\mathbf{z})\Big\rangle . \end{aligned}$$

The only contractions with non-vanishing isospin-factors are those where no fields on the same time-slice are paired, namely

$$\begin{aligned} \psi\bar\zeta',\zeta\bar\psi,\zeta'\bar\zeta &\;\rightarrow\; -\delta_{il}\delta_{kn}\delta_{mj} \;\rightarrow\; -\tfrac{1}{8}\epsilon^{abc}\tau_{lj}^a\tau_{nl}^b\tau_{jn}^c = -\tfrac{1}{8}\epsilon^{abc}\mathrm{Tr}\,\tau^a\tau^c\tau^b = \tfrac{3}{2}i\,, \\ \zeta\bar\zeta',\zeta'\bar\psi,\psi\bar\zeta &\;\rightarrow\; -\delta_{in}\delta_{kj}\delta_{ml} \;\rightarrow\; -\tfrac{1}{8}\epsilon^{abc}\tau_{nj}^a\tau_{jl}^b\tau_{ln}^c = -\tfrac{1}{8}\epsilon^{abc}\mathrm{Tr}\,\tau^a\tau^b\tau^c = -\tfrac{3}{2}i\,. \end{aligned}$$

Again the Dirac indices give the order of the propagators and the Dirac-matrices

$$f_{\mathrm{V}}(x_0) = \frac{a^{15}}{4L^6}\sum_{\substack{\mathbf{x,u,v}\\ \mathbf{w,z}}}\Big\langle \begin{array}{l} -\,\mathrm{Tr}\left\{\left[\psi(x)\bar\zeta'(\mathbf{u})\right]_{\mathrm{F}}\gamma_5\left[\zeta'(\mathbf{v})\bar\zeta(\mathbf{w})\right]_{\mathrm{F}}\gamma_5\left[\zeta(\mathbf{z})\bar\psi(x)\right]_{\mathrm{F}}\gamma_0\right\} \\ +\mathrm{Tr}\left\{\left[\zeta(\mathbf{w})\bar\zeta'(\mathbf{v})\right]_{\mathrm{F}}\gamma_5\left[\zeta'(\mathbf{u})\bar\psi(x)\right]_{\mathrm{F}}\gamma_0\left[\psi(x)\bar\zeta(\mathbf{z})\right]_{\mathrm{F}}\gamma_5\right\}\end{array}\Big\rangle_U ,$$

where we have renamed the arguments of the boundary fields ($\mathbf{u}\leftrightarrow\mathbf{v}$ and $\mathbf{w}\leftrightarrow\mathbf{z}$) in the second trace under the sum. Using equations (B.8) and (B.10) the propagators from the bulk to the upper boundary can be written in terms of $\overline{R}$ and $\overline{R}^\dagger$.

$$f_{\mathrm{V}}(x_0) = \frac{a^{12}}{4L^{9/2}}\sum_{\substack{\mathbf{x,v}\\ \mathbf{w,z}}}\Big\langle\mathrm{Tr}\Big\{ \begin{array}{l} -\,\overline{R}(x)\gamma_5\left[\zeta'(\mathbf{v})\bar\zeta(\mathbf{w})\right]_{\mathrm{F}}\gamma_5\left[\zeta(\mathbf{z})\bar\psi(x)\right]_{\mathrm{F}}\gamma_0 \\ +\left[\zeta(\mathbf{w})\bar\zeta'(\mathbf{v})\right]_{\mathrm{F}}\gamma_5\gamma_5\overline{R}(x)^\dagger\gamma_5\gamma_0\left[\psi(x)\bar\zeta(\mathbf{z})\right]_{\mathrm{F}}\gamma_5\end{array}\Big\}\Big\rangle_U .$$

In the next step we insert the expressions for the boundary-to-boundary propagators $\overline{S}_T$ and $\overline{S}_T^\dagger$ from equations (B.11) and (B.12), respectively, and then use $\gamma_5\gamma_5 = 1$ in both traces

$$\begin{aligned} f_{\mathrm{V}}(x_0) = \frac{a^6}{4L^3}\sum_{\mathbf{x,z}}\Big\langle\mathrm{Tr}\Big\{&\overline{R}(x)\gamma_5\overline{S}_T\gamma_5\left[\zeta(\mathbf{z})\bar\psi(x)\right]_{\mathrm{F}}\gamma_0 \\ &-\gamma_5\overline{S}_T^\dagger\gamma_5\overline{R}(x)^\dagger\gamma_5\gamma_0\left[\psi(x)\bar\zeta(\mathbf{z})\right]_{\mathrm{F}}\gamma_5\Big\}\Big\rangle_U . \end{aligned}$$

Again we use $\gamma_5\gamma_5 = 1$ and $\gamma_5\gamma_0 = -\gamma_0\gamma_5$ as well as the cyclic property of the trace. After inserting the propagators (B.7) and (B.9) we thus end up with

$$f_{\mathrm{V}}(x_0) = \frac{a^3}{4L^{3/2}}\sum_{\mathbf{x}}\Big\langle\mathrm{Tr}\left\{\overline{R}(x)\gamma_5\overline{S}_T\overline{S}(x)^\dagger\gamma_5\gamma_0 + \overline{S}_T^\dagger\gamma_5\overline{R}(x)^\dagger\gamma_0\gamma_5\overline{S}(x)\right\}\Big\rangle_U .$$

We now see that the expression is of the form $\mathrm{Tr}\,(X + X^\dagger) = 2\mathrm{Re}\,\mathrm{Tr}\,X$ and the final result is therefore

$$f_{\mathrm{V}}(x_0) = \frac{a^3}{2L^{3/2}} \sum_{\mathbf{x}} \left\langle \mathrm{Re}\,\mathrm{Tr}\left\{ \overline{S}(x)^\dagger \gamma_5 \gamma_0 \overline{R}(x) \gamma_5 \overline{S}_T \right\} \right\rangle_U . \tag{B.18}$$

B.1.3 4–point functions

Preliminaries

We start by inserting the expression (4.25) for the improved axial current into (8.26) to arrive at

$$\begin{aligned}
f^{\mathrm{I}}_{\mathrm{AA}}(x_0, y_0) &= -\frac{a^6}{6L^6} \sum_{\mathbf{x},\mathbf{y}} \epsilon^{abc}\epsilon^{cde} \left\langle \mathcal{O}'^d (A_{\mathrm{I}})^a_0(x)(A_{\mathrm{I}})^b_0(y) \mathcal{O}^e \right\rangle \\
&= -\frac{a^6}{6L^6} \sum_{\mathbf{x},\mathbf{y}} \epsilon^{abc}\epsilon^{cde} \Big\langle \mathcal{O}'^d \Big[A^a_0(x) + ac_{\mathrm{A}} \tilde{\partial}^x_0 P^a(x) \Big] \\
&\qquad\qquad \times \Big[A^b_0(y) + ac_{\mathrm{A}} \tilde{\partial}^y_0 P^b(y) \Big] \mathcal{O}^e \Big\rangle \\
&= -\frac{a^6}{6L^6} \sum_{\mathbf{x},\mathbf{y}} \epsilon^{abc}\epsilon^{cde} \Big\langle \mathcal{O}'^d \Big[A^a_0(x) A^b_0(y) + ac_{\mathrm{A}} \tilde{\partial}^x_0 P^a(x) A^b_0(y) \\
&\qquad\qquad + A^a_0(x) ac_{\mathrm{A}} \tilde{\partial}^y_0 P^b(y) + ac_{\mathrm{A}} \tilde{\partial}^x_0 P^a(x) ac_{\mathrm{A}} \tilde{\partial}^y_0 P^b(y) \Big] \mathcal{O}^e \Big\rangle \\
&= f_{\mathrm{AA}} + ac_{\mathrm{A}} [\tilde{\partial}^x_0 f_{\mathrm{PA}} + \tilde{\partial}^y_0 f_{\mathrm{AP}}] + a^2 c^2_{\mathrm{A}}\, \tilde{\partial}^x_0 \tilde{\partial}^y_0 f_{\mathrm{PP}} \; .
\end{aligned} \tag{B.19}$$

Here we have introduced the notation

$$f_{\mathrm{XY}}(x_0, y_0) = -\frac{a^6}{6L^6} \sum_{\mathbf{x},\mathbf{y}} \epsilon^{abc}\epsilon^{cde} \left\langle \mathcal{O}'^d X^a(x) Y^b(y) \mathcal{O}^e \right\rangle, \;\; X, Y \in \{A_0, P\} \; . \tag{B.20}$$

In order to evaluate these correlation functions in a closed form we define the Dirac matrices

$$\Xi = \begin{cases} \gamma_0\gamma_5 \;, & \text{if} \quad X = A_0 \\ \gamma_5 \quad , & \text{if} \quad X = P \end{cases} , \qquad \Upsilon = \begin{cases} \gamma_0\gamma_5 \;, & \text{if} \quad Y = A_0 \\ \gamma_5 \quad , & \text{if} \quad Y = P \end{cases} , \quad \text{so that}$$

$$X^a(x) = \bar{\psi}(x) \Xi \tfrac{1}{2}\tau^a \psi(x) \;\; \text{and} \;\; Y^a(y) = \bar{\psi}(y) \Upsilon \tfrac{1}{2}\tau^a \psi(y) \; . \tag{B.21}$$

Wick contractions for f_{XY}

As before the first step is the insertion of the explicit expressions for the boundary fields (5.13, 5.14) and the currents/densities (B.21) into (B.20). We suppress the time arguments of the correlation function to arrive at

$$\begin{aligned}
f_{\mathrm{XY}} \;=\; -\frac{a^{18}}{6L^6} \sum_{\substack{\mathbf{x},\mathbf{y},\mathbf{u}\\ \mathbf{v},\mathbf{w},\mathbf{z}}} \epsilon^{abc}\epsilon^{cde} \Big\langle & (\bar{\zeta}')^A_i(\mathbf{u}) \gamma_5^{AB} \tfrac{1}{2}\tau^d_{ij} (\zeta')^B_j(\mathbf{v}) \bar{\psi}^C_k(x) \Xi^{CD} \tfrac{1}{2}\tau^a_{kl} \psi^D_l(x) \\
& \times \bar{\psi}^E_s(y) \Upsilon^{EF} \tfrac{1}{2}\tau^b_{st} \psi^F_t(y) \bar{\zeta}^G_m(\mathbf{w}) \gamma_5^{GH} \tfrac{1}{2}\tau^e_{mn} \zeta^H_n(\mathbf{z}) \Big\rangle \; .
\end{aligned}$$

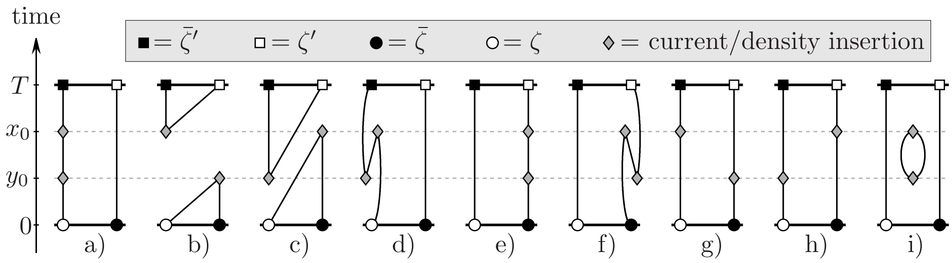

Figure B.1: Wick contractions of the correlation function $f_{\mathrm{XY}}(x_0, y_0)$. The gray diamonds indicate the insertions of Y and X at times y_0 and x_0.

Since we have two currents/densities in the bulk we need to keep track of the space–time locations, which we now write as indices. The number of possible Wick contractions is significantly larger than for the two– or three–point functions.

$$
\begin{array}{llll}
a) & \psi_x\bar{\zeta}'_{\mathbf{u}}, \psi_y\bar{\psi}_x,\ \zeta_{\mathbf{z}}\bar{\psi}_y,\ \zeta'_{\mathbf{v}}\bar{\zeta}_{\mathbf{w}} & f) & \zeta_{\mathbf{z}}\bar{\zeta}'_{\mathbf{u}} \quad \psi_y\bar{\psi}_x,\ \zeta'_{\mathbf{v}}\bar{\psi}_y, \psi_x\bar{\zeta}_{\mathbf{w}}, \\
b) & \psi_x\bar{\zeta}'_{\mathbf{u}},\ \zeta'_{\mathbf{v}}\bar{\psi}_x,\ \zeta_{\mathbf{z}}\bar{\psi}_y, \psi_y\bar{\zeta}_{\mathbf{w}} & g) & \psi_x\bar{\zeta}'_{\mathbf{u}} \quad \zeta_{\mathbf{z}}\bar{\psi}_x,\ \zeta'_{\mathbf{v}}\bar{\psi}_y, \psi_y\bar{\zeta}_{\mathbf{w}}, \\
c) & \psi_y\bar{\zeta}'_{\mathbf{u}},\ \zeta_{\mathbf{z}}\bar{\psi}_x,\ \zeta'_{\mathbf{v}}\bar{\psi}_y, \psi_x\bar{\zeta}_{\mathbf{w}} & h) & \psi_y\bar{\zeta}'_{\mathbf{u}} \quad \zeta'_{\mathbf{v}}\bar{\psi}_x,\ \zeta_{\mathbf{z}}\bar{\psi}_y, \psi_x\bar{\zeta}_{\mathbf{w}}, \\
d) & \psi_y\bar{\zeta}'_{\mathbf{u}},\ \zeta_{\mathbf{z}}\bar{\psi}_x, \psi_x\bar{\psi}_y,\ \zeta'_{\mathbf{v}}\bar{\zeta}_{\mathbf{w}} & i) & \zeta_{\mathbf{z}}\bar{\zeta}'_{\mathbf{u}} \quad \psi_y\bar{\psi}_x, \psi_x\bar{\psi}_y,\ \zeta'_{\mathbf{v}}\bar{\zeta}_{\mathbf{w}}, \\
e) & \zeta_{\mathbf{z}}\bar{\zeta}'_{\mathbf{u}},\ \zeta'_{\mathbf{v}}\bar{\psi}_x, \psi_x\bar{\psi}_y, \psi_y\bar{\zeta}_{\mathbf{w}} & &
\end{array}
$$

Isospin factors

The calculation of the isospin factors corresponding to the contractions a) to i) is lengthy but straightforward. With the notation $\mathrm{Tr}\,(\tau^a \ldots \tau^e) = \mathrm{Tr}_{\,a\ldots e}$ the result is

$$
\begin{array}{llllll}
a) & -\delta^{il}\delta^{kt}\delta^{sn}\delta^{mj} & \Rightarrow & -\frac{1}{16}\epsilon^{abc}\epsilon^{cde}\tau^d_{lj}\tau^a_{tl}\tau^b_{nt}\tau^e_{jn} & = -\frac{1}{16}\epsilon^{abc}\epsilon^{cde}\,\mathrm{Tr}_{\,deba} & = -3/2 \\
b) & +\delta^{il}\delta^{kj}\delta^{sn}\delta^{mt} & \Rightarrow & \frac{1}{16}\epsilon^{abc}\epsilon^{cde}\tau^d_{lj}\tau^a_{jl}\tau^b_{nt}\tau^e_{tn} & = \frac{1}{16}\epsilon^{abc}\epsilon^{cde}\,\mathrm{Tr}_{\,da}\mathrm{Tr}_{\,be} & = 3/2 \\
c) & +\delta^{it}\delta^{kn}\delta^{sj}\delta^{ml} & \Rightarrow & \frac{1}{16}\epsilon^{abc}\epsilon^{cde}\tau^d_{tj}\tau^a_{nl}\tau^b_{jt}\tau^e_{ln} & = \frac{1}{16}\epsilon^{abc}\epsilon^{cde}\,\mathrm{Tr}_{\,db}\mathrm{Tr}_{\,ae} & = -3/2 \\
d) & -\delta^{it}\delta^{kn}\delta^{sl}\delta^{mj} & \Rightarrow & -\frac{1}{16}\epsilon^{abc}\epsilon^{cde}\tau^d_{tj}\tau^a_{nl}\tau^b_{lt}\tau^e_{jn} & = -\frac{1}{16}\epsilon^{abc}\epsilon^{cde}\,\mathrm{Tr}_{\,deab} & = 3/2 \\
e) & -\delta^{in}\delta^{kj}\delta^{sl}\delta^{mt} & \Rightarrow & -\frac{1}{16}\epsilon^{abc}\epsilon^{cde}\tau^d_{nj}\tau^a_{jl}\tau^b_{lt}\tau^e_{tn} & = -\frac{1}{16}\epsilon^{abc}\epsilon^{cde}\,\mathrm{Tr}_{\,dabe} & = -3/2 \\
f) & -\delta^{in}\delta^{kt}\delta^{sj}\delta^{ml} & \Rightarrow & -\frac{1}{16}\epsilon^{abc}\epsilon^{cde}\tau^d_{nj}\tau^a_{tl}\tau^b_{jt}\tau^e_{ln} & = -\frac{1}{16}\epsilon^{abc}\epsilon^{cde}\,\mathrm{Tr}_{\,dbae} & = 3/2 \\
g) & -\delta^{il}\delta^{kn}\delta^{sj}\delta^{mt} & \Rightarrow & -\frac{1}{16}\epsilon^{abc}\epsilon^{cde}\tau^d_{lj}\tau^a_{nl}\tau^b_{jt}\tau^e_{tn} & = -\frac{1}{16}\epsilon^{abc}\epsilon^{cde}\,\mathrm{Tr}_{\,dbea} & = 0 \\
h) & -\delta^{it}\delta^{kj}\delta^{sn}\delta^{ml} & \Rightarrow & -\frac{1}{16}\epsilon^{abc}\epsilon^{cde}\tau^d_{tj}\tau^a_{jl}\tau^b_{nt}\tau^e_{ln} & = -\frac{1}{16}\epsilon^{abc}\epsilon^{cde}\,\mathrm{Tr}_{\,daeb} & = 0 \\
i) & +\delta^{in}\delta^{kt}\delta^{sl}\delta^{mj} & \Rightarrow & \frac{1}{16}\epsilon^{abc}\epsilon^{cde}\tau^d_{nj}\tau^a_{tl}\tau^b_{lt}\tau^e_{jn} & = \frac{1}{16}\epsilon^{abc}\epsilon^{cde}\,\mathrm{Tr}_{\,de}\mathrm{Tr}_{\,ab} & = 0\,.
\end{array}
$$

Combining this result with the contractions gives the propagators that need to be evaluated. Keeping track of the Dirac indices gives the order of the propagators in the non–vanishing contractions

$$
\begin{array}{rr}
a) & -\frac{3}{2}\mathrm{Tr}\,\left\{\left[\psi_x\bar{\zeta}'_{\mathbf{u}}\right]_{\mathrm{F}}\gamma_5\left[\zeta'_{\mathbf{v}}\bar{\zeta}_{\mathbf{w}}\right]_{\mathrm{F}}\gamma_5\left[\zeta_{\mathbf{z}}\bar{\psi}_y\right]_{\mathrm{F}}\Upsilon\left[\psi_y\bar{\psi}_x\right]_{\mathrm{F}}\Xi\right\} \\
b) & \frac{3}{2}\mathrm{Tr}\,\left\{\left[\psi_x\bar{\zeta}'_{\mathbf{u}}\right]_{\mathrm{F}}\gamma_5\left[\zeta'_{\mathbf{v}}\bar{\psi}_x\right]_{\mathrm{F}}\Xi\right\}\mathrm{Tr}\,\left\{\left[\zeta_{\mathbf{z}}\bar{\psi}_y\right]_{\mathrm{F}}\Upsilon\left[\psi_y\bar{\zeta}_{\mathbf{w}}\right]_{\mathrm{F}}\gamma_5\right\} \\
c) & -\frac{3}{2}\mathrm{Tr}\,\left\{\left[\psi_y\bar{\zeta}'_{\mathbf{u}}\right]_{\mathrm{F}}\gamma_5\left[\zeta'_{\mathbf{v}}\bar{\psi}_y\right]_{\mathrm{F}}\Upsilon\right\}\mathrm{Tr}\,\left\{\left[\zeta_{\mathbf{z}}\bar{\psi}_x\right]_{\mathrm{F}}\Xi\left[\psi_x\bar{\zeta}_{\mathbf{w}}\right]_{\mathrm{F}}\gamma_5\right\} \\
d) & \frac{3}{2}\mathrm{Tr}\,\left\{\left[\psi_y\bar{\zeta}'_{\mathbf{u}}\right]_{\mathrm{F}}\gamma_5\left[\zeta'_{\mathbf{v}}\bar{\zeta}_{\mathbf{w}}\right]_{\mathrm{F}}\gamma_5\left[\zeta_{\mathbf{z}}\bar{\psi}_x\right]_{\mathrm{F}}\Xi\left[\psi_x\bar{\psi}_y\right]_{\mathrm{F}}\Upsilon\right\} \\
e) & -\frac{3}{2}\mathrm{Tr}\,\left\{\left[\zeta_{\mathbf{z}}\bar{\zeta}'_{\mathbf{u}}\right]_{\mathrm{F}}\gamma_5\left[\zeta'_{\mathbf{v}}\bar{\psi}_x\right]_{\mathrm{F}}\Xi\left[\psi_x\bar{\psi}_y\right]_{\mathrm{F}}\Upsilon\left[\psi_y\bar{\zeta}_{\mathbf{w}}\right]_{\mathrm{F}}\gamma_5\right\} \\
f) & \frac{3}{2}\mathrm{Tr}\,\left\{\left[\zeta_{\mathbf{z}}\bar{\zeta}'_{\mathbf{u}}\right]_{\mathrm{F}}\gamma_5\left[\zeta'_{\mathbf{v}}\bar{\psi}_y\right]_{\mathrm{F}}\Upsilon\left[\psi_y\bar{\psi}_x\right]_{\mathrm{F}}\Xi\left[\psi_x\bar{\zeta}_{\mathbf{w}}\right]_{\mathrm{F}}\gamma_5\right\}\ .
\end{array}
$$

The general correlator f_{XY}

If we keep the arguments of the fields as indices, the correlation function f_{XY} can now be written as

$$\begin{aligned} f_{\mathrm{XY}} = \frac{a^{18}}{4L^6} \sum_{\substack{\mathbf{x},\mathbf{y},\mathbf{u}\\ \mathbf{v},\mathbf{w},\mathbf{z}}} \Big\langle & \ \mathrm{Tr}\left\{ \left[\psi_x \bar{\zeta}'_{\mathbf{u}}\right]_{\mathrm{F}} \gamma_5 \left[\zeta'_{\mathbf{v}} \bar{\zeta}_{\mathbf{w}}\right]_{\mathrm{F}} \gamma_5 \left[\zeta_{\mathbf{z}} \bar{\psi}_y\right]_{\mathrm{F}} \Upsilon \left[\psi_y \bar{\psi}_x\right]_{\mathrm{F}} \Xi \right\} \\ & - \mathrm{Tr}\left\{ \left[\psi_x \bar{\zeta}'_{\mathbf{u}}\right]_{\mathrm{F}} \gamma_5 \left[\zeta'_{\mathbf{v}} \bar{\psi}_x\right]_{\mathrm{F}} \Xi \right\} \mathrm{Tr}\left\{ \left[\zeta_{\mathbf{z}} \bar{\psi}_y\right]_{\mathrm{F}} \Upsilon \left[\psi_y \bar{\zeta}_{\mathbf{w}}\right]_{\mathrm{F}} \gamma_5 \right\} \\ & + \mathrm{Tr}\left\{ \left[\psi_y \bar{\zeta}'_{\mathbf{u}}\right]_{\mathrm{F}} \gamma_5 \left[\zeta'_{\mathbf{v}} \bar{\psi}_y\right]_{\mathrm{F}} \Upsilon \right\} \mathrm{Tr}\left\{ \left[\zeta_{\mathbf{z}} \bar{\psi}_x\right]_{\mathrm{F}} \Xi \left[\psi_x \bar{\zeta}_{\mathbf{w}}\right]_{\mathrm{F}} \gamma_5 \right\} \\ & - \mathrm{Tr}\left\{ \left[\psi_y \bar{\zeta}'_{\mathbf{u}}\right]_{\mathrm{F}} \gamma_5 \left[\zeta'_{\mathbf{v}} \bar{\zeta}_{\mathbf{w}}\right]_{\mathrm{F}} \gamma_5 \left[\zeta_{\mathbf{z}} \bar{\psi}_x\right]_{\mathrm{F}} \Xi \left[\psi_x \bar{\psi}_y\right]_{\mathrm{F}} \Upsilon \right\} \\ & + \mathrm{Tr}\left\{ \left[\zeta_{\mathbf{z}} \bar{\zeta}'_{\mathbf{u}}\right]_{\mathrm{F}} \gamma_5 \left[\zeta'_{\mathbf{v}} \bar{\psi}_x\right]_{\mathrm{F}} \Xi \left[\psi_x \bar{\psi}_y\right]_{\mathrm{F}} \Upsilon \left[\psi_y \bar{\zeta}_{\mathbf{w}}\right]_{\mathrm{F}} \gamma_5 \right\} \\ & - \mathrm{Tr}\left\{ \left[\zeta_{\mathbf{z}} \bar{\zeta}'_{\mathbf{u}}\right]_{\mathrm{F}} \gamma_5 \left[\zeta'_{\mathbf{v}} \bar{\psi}_y\right]_{\mathrm{F}} \Upsilon \left[\psi_y \bar{\psi}_x\right]_{\mathrm{F}} \Xi \left[\psi_x \bar{\zeta}_{\mathbf{w}}\right]_{\mathrm{F}} \gamma_5 \right\} \Big\rangle_U . \end{aligned}$$

Using eqs. (A.12), (B.7), (B.10), (B.11) and (B.12) as well as the properties of the Dirac matrices, one arrives at

$$\begin{aligned} f_{\mathrm{XY}} = \frac{a^6}{4L^{3/2}} \sum_{\mathbf{x},\mathbf{y}} \Big\langle & - \mathrm{Tr}\left\{ \overline{R}(x)\gamma_5 \overline{S}_T \overline{S}(y)^\dagger \gamma_5 \Upsilon S(y;x) \Xi \right\} \\ & - L^{3/2} \mathrm{Tr}\left\{ \overline{R}(x)\overline{R}(x)^\dagger \gamma_5 \Xi \right\} \mathrm{Tr}\left\{ \overline{S}(y)^\dagger \gamma_5 \Upsilon \overline{S}(y) \right\} \\ & + L^{3/2} \mathrm{Tr}\left\{ \overline{R}(y)\overline{R}(y)^\dagger \gamma_5 \Upsilon \right\} \mathrm{Tr}\left\{ \overline{S}(x)^\dagger \gamma_5 \Xi \overline{S}(x) \right\} \\ & + \mathrm{Tr}\left\{ \overline{R}(y)\gamma_5 \overline{S}_T \overline{S}(x)^\dagger \gamma_5 \Xi \, S(x;y) \Upsilon \right\} \\ & - \mathrm{Tr}\left\{ \overline{S}_T^\dagger \gamma_5 \overline{R}(x)^\dagger \gamma_5 \Xi \, \gamma_5 S(y;x)^\dagger \gamma_5 \Upsilon \overline{S}(y) \right\} \\ & + \mathrm{Tr}\left\{ \overline{S}_T^\dagger \gamma_5 \overline{R}(y)^\dagger \gamma_5 \Upsilon \gamma_5 S(x;y)^\dagger \gamma_5 \Xi \, \overline{S}(x) \right\} \Big\rangle_U . \end{aligned}$$

If we now specialize to the four cases f_{PP}, f_{AA}, f_{AP} and f_{PA}, the connected contributions will combine to form pairs of Hermitian conjugates.

$\boxed{f_{\mathrm{PP}} \Rightarrow \Xi = \Upsilon = \gamma_5}$

$$\begin{aligned} f_{\mathrm{PP}} = \frac{a^6}{4L^{3/2}} \sum_{\mathbf{x},\mathbf{y}} \Big\langle & - 2\mathrm{Re}\,\mathrm{Tr}\left\{ \overline{R}(x)\gamma_5 \overline{S}_T \overline{S}(y)^\dagger S(y;x) \gamma_5 \right\} \\ & - L^{3/2} \mathrm{Tr}\left\{ \overline{R}(x)\overline{R}(x)^\dagger \right\} \mathrm{Tr}\left\{ \overline{S}(y)\overline{S}(y)^\dagger \right\} \\ & + L^{3/2} \mathrm{Tr}\left\{ \overline{R}(y)\overline{R}(y)^\dagger \right\} \mathrm{Tr}\left\{ \overline{S}(x)\overline{S}(x)^\dagger \right\} \\ & + 2\mathrm{Re}\,\mathrm{Tr}\left\{ \overline{R}(y)\gamma_5 \overline{S}_T \overline{S}(x)^\dagger S(x;y) \gamma_5 \right\} \Big\rangle_U . \end{aligned} \tag{B.22}$$

$\boxed{f_{\mathrm{AA}} \Rightarrow \Xi = \Upsilon = \gamma_0\gamma_5}$

$$f_{\mathrm{AA}} = \frac{a^6}{4L^{3/2}} \sum_{\mathbf{x},\mathbf{y}} \Big\langle + 2\mathrm{Re}\,\mathrm{Tr}\left\{ \overline{R}(x)\gamma_5 \overline{S}_T \overline{S}(y)^\dagger \gamma_0 S(y;x) \gamma_0 \gamma_5 \right\}$$

$$
\begin{aligned}
&-L^{3/2}\mathrm{Tr}\,\left\{\overline{R}(x)\overline{R}(x)^\dagger\gamma_0\right\}\,\mathrm{Tr}\,\left\{\overline{S}(y)\overline{S}(y)^\dagger\gamma_0\right\}\\
&+L^{3/2}\mathrm{Tr}\,\left\{\overline{R}(y)\overline{R}(y)^\dagger\gamma_0\right\}\,\mathrm{Tr}\,\left\{\overline{S}(x)\overline{S}(x)^\dagger\gamma_0\right\}\\
&-2\mathrm{Re}\,\mathrm{Tr}\,\left\{\overline{R}(y)\gamma_5\overline{S}_T\overline{S}(x)^\dagger\gamma_0\,S(x;y)\gamma_0\gamma_5\right\}\Big\rangle_U\,. \qquad \text{(B.23)}
\end{aligned}
$$

$\boxed{f_{\mathrm{AP}} \Rightarrow \Xi = \gamma_0\gamma_5,\ \Upsilon = \gamma_5}$

$$
\begin{aligned}
f_{\mathrm{AP}} \;=\; \frac{a^6}{4L^{3/2}}\sum_{\mathbf{x},\mathbf{y}}\Big\langle &-2\mathrm{Re}\,\mathrm{Tr}\,\left\{\overline{R}(x)\gamma_5\overline{S}_T\overline{S}(y)^\dagger S(y;x)\gamma_0\gamma_5\right\}\\
&+L^{3/2}\mathrm{Tr}\,\left\{\overline{R}(x)\overline{R}(x)^\dagger\gamma_0\right\}\,\mathrm{Tr}\,\left\{\overline{S}(y)\overline{S}(y)^\dagger\right\}\\
&-L^{3/2}\mathrm{Tr}\,\left\{\overline{R}(y)\overline{R}(y)^\dagger\right\}\,\mathrm{Tr}\,\left\{\overline{S}(x)\overline{S}(x)^\dagger\gamma_0\right\}\\
&-2\mathrm{Re}\,\mathrm{Tr}\,\left\{\overline{R}(y)\gamma_5\overline{S}_T\overline{S}(x)^\dagger\gamma_0 S(x;y)\gamma_5\right\}\Big\rangle_U\,. \qquad \text{(B.24)}
\end{aligned}
$$

$\boxed{f_{\mathrm{PA}} \Rightarrow \Xi = \gamma_5,\ \Upsilon = \gamma_0\gamma_5}$

$$
\begin{aligned}
f_{\mathrm{PA}} \;=\; \frac{a^6}{4L^{3/2}}\sum_{\mathbf{x},\mathbf{y}}\Big\langle &+2\mathrm{Re}\,\mathrm{Tr}\,\left\{\overline{R}(x)\gamma_5\overline{S}_T\overline{S}(y)^\dagger\gamma_0 S(y;x)\gamma_5\right\}\\
&+L^{3/2}\mathrm{Tr}\,\left\{\overline{R}(x)\overline{R}(x)^\dagger\right\}\,\mathrm{Tr}\,\left\{\overline{S}(y)\overline{S}(y)^\dagger\gamma_0\right\}\\
&-L^{3/2}\mathrm{Tr}\,\left\{\overline{R}(y)\overline{R}(y)^\dagger\gamma_0\right\}\,\mathrm{Tr}\,\left\{\overline{S}(x)\overline{S}(x)^\dagger\right\}\\
&+2\mathrm{Re}\,\mathrm{Tr}\,\left\{\overline{R}(y)\gamma_5\overline{S}_T\overline{S}(x)^\dagger S(x;y)\gamma_0\gamma_5\right\}\Big\rangle_U\,. \qquad \text{(B.25)}
\end{aligned}
$$

Evaluation of $\tilde{f}_{\mathrm{PA}}^{\mathrm{I}}$

Inserting the expression (4.25) for the improved axial current into (8.33) gives

$$
\begin{aligned}
\tilde{f}_{\mathrm{PA}}^{\mathrm{I}}(y_0{+}t,y_0) \;&=\; -\frac{a^7}{6L^6}\sum_{x_0=y_0}^{y_0+t} w(x_0)\sum_{\mathbf{x},\mathbf{y}}\epsilon^{abc}\epsilon^{cde}\Big\langle\mathcal{O}'^{d}P^a(x)[A_0^b(y)+ac_{\mathrm{A}}\tilde{\partial}_0^y P^b(y)]\mathcal{O}^e\Big\rangle\\
&\overset{(B.20)}{=}\; a\sum_{x_0=y_0}^{y_0+t} w(x_0)\Big[f_{\mathrm{PA}}(x_0,y_0)+ac_{\mathrm{A}}\tilde{\partial}_0^y f_{\mathrm{PP}}(x_0,y_0)\Big]\,. \qquad \text{(B.26)}
\end{aligned}
$$

B.2 Simplifying the correlation functions

We now specify an explicit (chiral) representation of the Euclidean Dirac matrices

$$\gamma_\mu = \begin{pmatrix} 0 & e_\mu \\ e_\mu^\dagger & 0 \end{pmatrix}, \text{ with the } 2\times 2 \text{ matrices } e_0 = -1, \quad e_k = -i\sigma_k \ ,$$

where $k = 1,2,3$ and σ_k are the Pauli matrices. With $\gamma_5 = \gamma_0\gamma_1\gamma_2\gamma_3$ and $P_\pm = \frac{1}{2}(1 \pm \gamma_0)$ we then have

$$\gamma_5 = \begin{pmatrix} 1 & 0 \\ 0 & -1 \end{pmatrix}, \ P_+ = \frac{1}{2}\begin{pmatrix} 1 & -1 \\ -1 & 1 \end{pmatrix} \text{ and } P_- = \frac{1}{2}\begin{pmatrix} 1 & 1 \\ 1 & 1 \end{pmatrix} .$$

If we write the four components explicitly we see that for all matrices X, Y in Dirac space we can conclude that

$$\begin{aligned} 0 = XP_+ \ &\Rightarrow \ 0 = 2(XP_+)_{A*} = (X_{A1}-X_{A3},\ X_{A2}-X_{A4},\ X_{A3}-X_{A1},\ X_{A4}-X_{A2}) \\ &\Rightarrow \ \underline{0 = X_{A1}-X_{A3} = X_{A2}-X_{A4}} \ , \end{aligned} \tag{B.27}$$

$$\begin{aligned} 0 = XP_- \ &\Rightarrow \ 0 = 2(XP_-)_{A*} = (X_{A1}+X_{A3},\ X_{A2}+X_{A4},\ X_{A1}+X_{A3},\ X_{A2}+X_{A4}) \\ &\Rightarrow \ \underline{0 = X_{A1}+X_{A3} = X_{A2}+X_{A4}} \ , \end{aligned} \tag{B.28}$$

$$\begin{aligned} 0 = P_+Y \ &\Rightarrow \ 0 = 2(P_+Y)_{*B} = (Y_{1B}-Y_{3B},\ Y_{2B}-Y_{4B},\ Y_{3B}-Y_{1B},\ Y_{4B}-Y_{2B})^T \\ &\Rightarrow \ \underline{0 = Y_{1B}-Y_{3B} = Y_{2B}-Y_{4B}} \ , \end{aligned} \tag{B.29}$$

$$\begin{aligned} 0 = P_-Y \ &\Rightarrow \ 0 = 2(P_-Y)_{*B} = (Y_{1B}+Y_{3B},\ Y_{2B}+Y_{4B},\ Y_{1B}+Y_{3B},\ Y_{2B}+Y_{4B})^T \\ &\Rightarrow \ \underline{0 = Y_{1B}+Y_{3B} = Y_{2B}+Y_{4B}} \ . \end{aligned} \tag{B.30}$$

From equations (B.1) - (B.5) we can now derive relations between the Dirac components of the summed correlators (only Dirac indices are written explicitly)

$$0 \overset{(B.1)}{=} \overline{S}P_- \quad \Rightarrow \quad 0 \overset{(B.28)}{=} \overline{S}_{A1}+\overline{S}_{A3} = \overline{S}_{A2}+\overline{S}_{A4} \ , \tag{B.31}$$

$$0 \overset{(B.2)}{=} P_-\overline{S}^\dagger \quad \Rightarrow \quad 0 \overset{(B.30)}{=} (\overline{S}^\dagger)_{1B}+(\overline{S}^\dagger)_{3B} = (\overline{S}^\dagger)_{2B}+(\overline{S}^\dagger)_{4B} \ , \tag{B.32}$$

$$0 \overset{(B.3)}{=} \overline{R}P_+ \quad \Rightarrow \quad 0 \overset{(B.27)}{=} \overline{R}_{A1}-\overline{R}_{A3} = \overline{R}_{A2}-\overline{R}_{A4} \ , \tag{B.33}$$

$$0 \overset{(B.4)}{=} P_+\overline{R}^\dagger \quad \Rightarrow \quad 0 \overset{(B.29)}{=} (\overline{R}^\dagger)_{1B}-(\overline{R}^\dagger)_{3B} = (\overline{R}^\dagger)_{2B}-(\overline{R}^\dagger)_{4B} \ , \tag{B.34}$$

$$0 \overset{(B.1)}{=} \overline{S}_TP_- \quad \Rightarrow \quad 0 \overset{(B.28)}{=} (\overline{S}_T)_{A1}+(\overline{S}_T)_{A3} = (\overline{S}_T)_{A2}+(\overline{S}_T)_{A4} \ , \tag{B.35}$$

$$0 \overset{(B.5)}{=} P_-\overline{S}_T \quad \Rightarrow \quad 0 \overset{(B.30)}{=} (\overline{S}_T)_{1B}+(\overline{S}_T)_{3B} = (\overline{S}_T)_{2B}+(\overline{S}_T)_{4B} \ , \tag{B.36}$$

$$\begin{aligned} 0 \overset{(B.5)}{=} P_-\overline{S}_T \quad &\Rightarrow \quad \gamma_5P_-\overline{S}_T = 0 \ \Rightarrow \ P_+(\gamma_5\overline{S}_T) = 0 \\ &\Rightarrow \quad 0 \overset{(B.29)}{=} (\gamma_5\overline{S}_T)_{1B}-(\gamma_5\overline{S}_T)_{3B} = (\gamma_5\overline{S}_T)_{2B}-(\gamma_5\overline{S}_T)_{4B} \ . \end{aligned} \tag{B.37}$$

B.2.1 Explicit form of the correlation functions

$\boxed{f_1}$

We use $A, B, \ldots$ for the Dirac indices and $\alpha, \beta, \ldots$ for color indices.

$$\begin{aligned}
\mathrm{Tr}\,\overline{S}_T\overline{S}_T^\dagger &= \sum_{A,B=1}^{4}\sum_{\alpha,\beta=1}^{3}\left(\overline{S}_T\right)_{AB}^{\alpha\beta}\left(\overline{S}_T^\dagger\right)_{BA}^{\beta\alpha} = \sum_{A,B=1}^{4}\sum_{\alpha,\beta=1}^{3}\left(\overline{S}_T\right)_{AB}^{\alpha\beta}\left\{\left(\overline{S}_T\right)_{AB}^{\alpha\beta}\right\}^* \\
&= \sum_{A,B=1}^{4}\sum_{\alpha,\beta=1}^{3}\left|\left(\overline{S}_T\right)_{AB}^{\alpha\beta}\right|^2 \overset{(B.35)}{=} 2\sum_{A=1}^{4}\sum_{B=1}^{2}\sum_{\alpha,\beta=1}^{3}\left|\left(\overline{S}_T\right)_{AB}^{\alpha\beta}\right|^2 \\
&\overset{(B.36)}{=} 4\sum_{A,B=1}^{2}\sum_{\alpha,\beta=1}^{3}\left|\left(\overline{S}_T\right)_{AB}^{\alpha\beta}\right|^2 .
\end{aligned} \tag{B.38}$$

The final form for the correlation function f_1 from (B.13) is therefore

$$f_1 \overset{(B.38)}{=} \frac{2}{L^3}\left\langle \sum_{A,B=1}^{2}\sum_{\alpha,\beta=1}^{3}\left|\left(\overline{S}_T\right)_{AB}^{\alpha\beta}\right|^2\right\rangle_U . \tag{B.39}$$

For the more complicated correlation functions it will be useful to introduce a modified sum convention, where all Dirac indices that are restricted to $\{1, 2\}$ are written in square brackets. In this notation we have

$$f_1 = \frac{2}{L^3}\left\langle \left(\overline{S}_T\right)_{[A][B]}^{\alpha\beta}\left(\overline{S}_T^\dagger\right)_{[B][A]}^{\beta\alpha}\right\rangle_U . \tag{B.40}$$

$\boxed{f_{\mathrm{V}}(x_0)}$

The correlation function $f_{\mathrm{V}}(x_0)$ from $(B.18)$ contains the trace of $\overline{S}^\dagger\gamma_5\gamma_0\overline{R}\gamma_5\overline{S}_T$. Using equation (B.33) and (B.37) one can see that the Dirac index contracting $\overline{R}$ and $\gamma_5\overline{S}_T$ can be restricted to $\{1, 2\}$ if a factor of 2 is included. Since in this representation γ_5 is equal to the unit matrix if the indices are restricted to $\{1, 2\}$ the γ_5 in front of $\overline{S}_T$ can be dropped, i.e.

$$\ldots\overline{R}_{AB}(\gamma_5\overline{S}_T)_{BC}\ldots \;=\; \ldots 2\overline{R}_{A[B]}(\overline{S}_T)_{[B]C}\ldots$$

Similarly, using equations (B.32) and (B.35) the contracting Dirac index between $\overline{S}_T$ and $\overline{S}^\dagger$ can be restricted to $\{1, 2\}$ if another factor of 2 is included

$$\ldots(\overline{S}_T)_{AB}(\overline{S}^\dagger)_{BC}\ldots \;=\; \ldots 2(\overline{S}_T)_{A[B]}(\overline{S}^\dagger)_{[B]C}\ldots$$

The result for $f_{\mathrm{V}}(x_0)$ is then

$$f_{\mathrm{V}}(x_0) = \frac{2a^3}{L^{3/2}}\left\langle\sum_{\mathbf{x}}\mathrm{Re}\left[(\overline{S}(x)^\dagger)_{[A]B}^{\alpha\beta}(\gamma_5\gamma_0)_{BC}\overline{R}(x)_{C[D]}^{\beta\gamma}(\overline{S}_T)_{[D][A]}^{\gamma\alpha}\right]\right\rangle_U .$$

Since the combination $\overline{S} \cdot \overline{S}_T^\dagger$ will appear in all f_{XY} as well as f_V, we define

$$\overline{P}(x)^{\beta\gamma}_{B[D]} = \frac{1}{2}\left[\overline{S}(x)\left(\overline{S}_T\right)^\dagger\right]^{\beta\gamma}_{B[D]} = \overline{S}(x)^{\beta\alpha}_{B[A]}\left[\left(\overline{S}_T\right)^\dagger\right]^{\alpha\gamma}_{[A][D]} \; . \tag{B.41}$$

The final result for $f_{\mathrm{V}}(x_0)$ is then

$$\begin{aligned} f_{\mathrm{V}}(x_0) &= \frac{2a^3}{L^{3/2}}\left\langle \sum_{\mathbf{x}} \mathrm{Re}\left\{ (\overline{S}_T)^{\gamma\alpha}_{[D][A]}(\overline{S}(x)^\dagger)^{\alpha\beta}_{[A]B}(\gamma_5\gamma_0)_{BC}\overline{R}(x)^{\beta\gamma}_{C[D]}\right\}\right\rangle_U \\ &\overset{(B.41)}{=} \frac{2a^3}{L^{3/2}}\left\langle \sum_{\mathbf{x}} \mathrm{Re}\left\{ \left[\overline{P}(x)^\dagger\right]^{\gamma\beta}_{[D]B}(\gamma_5\gamma_0)_{BC}\overline{R}(x)^{\beta\gamma}_{C[D]}\right\}\right\rangle_U \; . \end{aligned} \tag{B.42}$$

$\boxed{f_{\mathrm{A}},\, f_{\mathrm{P}},\, g_{\mathrm{A}},\, g_{\mathrm{P}}}$

In addition to the above simplifications we also have

$$(B.31) \wedge (B.32) \;\rightarrow\; \ldots\overline{S}_{AB}(\overline{S}^\dagger)_{BC}\ldots \;=\; \ldots 2\overline{S}_{A[B]}(\overline{S}^\dagger)_{[B]C}\cdots \tag{B.43}$$

$$(B.33) \wedge (B.34) \;\rightarrow\; \ldots\overline{R}_{AB}(\overline{R}^\dagger)_{BC}\ldots \;=\; \ldots 2\overline{R}_{A[B]}(\overline{R}^\dagger)_{[B]C}\cdots \tag{B.44}$$

With these the correlators f_{P}, f_{A}, g_{P} and g_{A} can be written as

$$f_{\mathrm{P}}(x_0) \overset{(B.14)}{=} a^3\sum_{\mathbf{x}}\left\langle \overline{S}(x)^{\alpha\beta}_{A[B]}\left(\overline{S}(x)^\dagger\right)^{\beta\alpha}_{[B]A}\right\rangle_U \tag{B.45}$$

$$f_{\mathrm{A}}(x_0) \overset{(B.15)}{=} -a^3\sum_{\mathbf{x}}\left\langle \overline{S}(x)^{\alpha\beta}_{A[B]}\left(\overline{S}(x)^\dagger\right)^{\beta\alpha}_{[B]C}(\gamma_0)_{CA}\right\rangle_U \tag{B.46}$$

$$g_{\mathrm{P}}(x_0) \overset{(B.16)}{=} a^3\sum_{\mathbf{x}}\left\langle \overline{R}(x)^{\alpha\beta}_{A[B]}\left(\overline{R}(x)^\dagger\right)^{\beta\alpha}_{[B]A}\right\rangle_U \tag{B.47}$$

$$g_{\mathrm{A}}(x_0) \overset{(B.17)}{=} a^3\sum_{\mathbf{x}}\left\langle \overline{R}(x)^{\alpha\beta}_{A[B]}\left(\overline{R}(x)^\dagger\right)^{\beta\alpha}_{[B]C}(\gamma_0)_{CA}\right\rangle_U \; . \tag{B.48}$$

$\boxed{f_{\mathrm{XY}}(x_0, y_0)}$

The expressions for f_{XY} can be written in the same form as f_{V} with the definitions

$$\overline{N_5}(x, y_0)^{\gamma\alpha}_{C[A]} = a^3\sum_{\mathbf{y}}\left[S(x;y)\gamma_5\overline{R}(y)\right]^{\gamma\alpha}_{C[A]} \; , \tag{B.49}$$

$$\overline{N_{05}}(x, y_0)^{\gamma\alpha}_{C[A]} = a^3\sum_{\mathbf{y}}\left[S(x;y)\gamma_0\gamma_5\overline{R}(y)\right]^{\gamma\alpha}_{C[A]} \; . \tag{B.50}$$

Using these, the expression (B.22) for f_{PP} becomes

$$
\begin{aligned}
f_{\mathrm{PP}} \;&=\; \frac{a^6}{L^{3/2}}\sum_{\mathbf{x},\mathbf{y}}\Big\langle L^{3/2}\left\{\overline{R}(y)^{\alpha\beta}_{A[B]}(\overline{R}(y)^{\dagger})^{\beta\alpha}_{[B]A}\right\}\left\{\overline{S}(x)^{\gamma\delta}_{D[E]}(\overline{S}(x)^{\dagger})^{\delta\gamma}_{[E]D}\right\} \\
&\qquad\qquad +2\mathrm{Re}\left\{(\overline{S}_T)^{\alpha\beta}_{[A][B]}\left(\overline{S}(x)^{\dagger}\right)^{\beta\gamma}_{[B]C}\left(S(x;y)\gamma_5\overline{R}(y)\right)^{\gamma\alpha}_{C[A]}\right\} \\
&\qquad\qquad -\{x\longleftrightarrow y\}\Big\rangle_U \\
&\overset{(B.41)}{=} \frac{a^6}{L^{3/2}}\sum_{\mathbf{x},\mathbf{y}}\Big\langle L^{3/2}\left\{\overline{R}(y)^{\alpha\beta}_{A[B]}(\overline{R}(y)^{\dagger})^{\beta\alpha}_{[B]A}\right\}\left\{\overline{S}(x)^{\gamma\delta}_{D[E]}(\overline{S}(x)^{\dagger})^{\delta\gamma}_{[E]D}\right\} \\
&\qquad\qquad +2\mathrm{Re}\left\{\left(\overline{P}(x)^{\gamma\alpha}_{C[A]}\right)^{*}\left(S(x;y)\gamma_5\overline{R}(y)\right)^{\gamma\alpha}_{C[A]}\right\} \\
&\qquad\qquad -\{x\longleftrightarrow y\}\Big\rangle_U \\
&\overset{(B.49)}{=} \frac{a^6}{L^{3/2}}\Big\langle L^{3/2}\sum_{\mathbf{x},\mathbf{y}}\left\{\overline{R}(y)^{\alpha\beta}_{A[B]}(\overline{R}(y)^{\dagger})^{\beta\alpha}_{[B]A}\right\}\left\{\overline{S}(x)^{\gamma\delta}_{D[E]}(\overline{S}(x)^{\dagger})^{\delta\gamma}_{[E]D}\right\} \\
&\qquad\qquad +\frac{2}{a^3}\mathrm{Re}\sum_{\mathbf{x}}\left\{\left(\overline{P}(x)^{\gamma\alpha}_{C[A]}\right)^{*}\overline{N_5}(x,y_0)^{\gamma\alpha}_{C[A]}\right\} \\
&\qquad\qquad -\{x\longleftrightarrow y\}\Big\rangle_U\,.
\end{aligned}
$$

The disconnected parts are built from the propagator products, which also appear in f_{P} and g_{P}. However, this is done on *each* gauge configuration and we therefore have to define new correlation functions

$$
\begin{aligned}
[gf]_{\mathrm{PP}}(x_0,y_0) \;&=\; a^6\sum_{\mathbf{x},\mathbf{y}}\Big\langle\left\{\overline{R}(x)^{\alpha\beta}_{A[B]}(\overline{R}(x)^{\dagger})^{\beta\alpha}_{[B]A}\right\}\left\{\overline{S}(y)^{\gamma\delta}_{D[E]}(\overline{S}(y)^{\dagger})^{\delta\gamma}_{[E]D}\right\}\Big\rangle_U \\
[gf]_{\mathrm{AA}}(x_0,y_0) \;&=\; -a^6\sum_{\mathbf{x},\mathbf{y}}\Big\langle\left\{\overline{R}(x)^{\alpha\beta}_{A[B]}(\overline{R}(x)^{\dagger})^{\beta\alpha}_{[B]C}(\gamma_0)_{CA}\right\} \\
&\qquad\qquad \times\left\{\overline{S}(y)^{\gamma\delta}_{D[E]}(\overline{S}(y)^{\dagger})^{\delta\gamma}_{[E]F}(\gamma_0)_{FD}\right\}\Big\rangle_U \\
[gf]_{\mathrm{AP}}(x_0,y_0) \;&=\; a^6\sum_{\mathbf{x},\mathbf{y}}\Big\langle\left\{\overline{R}(x)^{\alpha\beta}_{A[B]}(\overline{R}(x)^{\dagger})^{\beta\alpha}_{[B]C}(\gamma_0)_{CA}\right\}\left\{\overline{S}(y)^{\gamma\delta}_{D[E]}(\overline{S}(y)^{\dagger})^{\delta\gamma}_{[E]D}\right\}\Big\rangle_U \\
[gf]_{\mathrm{PA}}(x_0,y_0) \;&=\; -a^6\sum_{\mathbf{x},\mathbf{y}}\Big\langle\left\{\overline{R}(x)^{\alpha\beta}_{A[B]}(\overline{R}(x)^{\dagger})^{\beta\alpha}_{[B]A}\right\}\left\{\overline{S}(y)^{\gamma\delta}_{D[E]}(\overline{S}(y)^{\dagger})^{\delta\gamma}_{[E]F}(\gamma_0)_{FD}\right\}\Big\rangle_U\,.
\end{aligned}
$$

Without any additional effort these correlation functions can be constructed from the estimates for f_{X} and g_{X} in the analysis program. Inserting them into the last expression for f_{PP} gives

$$
\begin{aligned}
f_{\mathrm{PP}} \;=\; \frac{2a^3}{L^{3/2}}\Big\langle &- \mathrm{Re}\sum_{\mathbf{y}}\Big\{\Big(\overline{P}(y)^{\gamma\alpha}_{C[A]}\Big)^*\,\overline{N_5}(y,x_0)^{\gamma\alpha}_{C[A]}\Big\} \\
&+\mathrm{Re}\sum_{\mathbf{x}}\Big\{\Big(\overline{P}(x)^{\gamma\alpha}_{C[A]}\Big)^*\,\overline{N_5}(x,y_0)^{\gamma\alpha}_{C[A]}\Big\}\Big\rangle_U \\
&-[gf]_{\mathrm{PP}}(x_0,y_0)+[gf]_{\mathrm{PP}}(y_0,x_0)\;.
\end{aligned}
\tag{B.51}
$$

In the expression (B.23) for f_{AA} again two indices in each line can be restricted, thus giving an overall factor of 4

$$
\begin{aligned}
f_{\mathrm{AA}} \;&=\; \frac{a^6}{L^{3/2}}\sum_{\mathbf{x},\mathbf{y}}\Big\langle +2\mathrm{Re}\Big\{(\overline{S}_T)^{\alpha\beta}_{[A][B]}\Big(\overline{S}(y)^\dagger\Big)^{\beta\gamma}_{[B]C}(\gamma_0)_{CD}\left(S(y;x)\gamma_0\gamma_5\overline{R}(x)\right)^{\gamma\alpha}_{D[A]}\Big\} \\
&\qquad +L^{3/2}\Big\{\overline{R}(y)^{\alpha\beta}_{A[B]}(\overline{R}(y)^\dagger)^{\beta\alpha}_{[B]C}(\gamma_0)_{CA}\Big\} \\
&\qquad\qquad \times\Big\{\overline{S}(x)^{\gamma\delta}_{D[E]}(\overline{S}(x)^\dagger)^{\delta\gamma}_{[E]F}(\gamma_0)_{FD}\Big\}\Big\rangle_U \\
&\qquad -\{x\longleftrightarrow y\}\Big\rangle_U \\
&\overset{(B.41)}{=} \frac{a^6}{L^{3/2}}\sum_{\mathbf{x},\mathbf{y}}\Big\langle +2\mathrm{Re}\Big\{\Big(\overline{P}(y)^{\gamma\alpha}_{C[A]}\Big)^*(\gamma_0)_{CD}\left(S(y;x)\gamma_0\gamma_5\overline{R}(x)\right)^{\gamma\alpha}_{D[A]}\Big\} \\
&\qquad +L^{3/2}\Big\{\overline{R}(y)^{\alpha\beta}_{A[B]}(\overline{R}(y)^\dagger)^{\beta\alpha}_{[B]C}(\gamma_0)_{CA}\Big\} \\
&\qquad\qquad \times\Big\{\overline{S}(x)^{\gamma\delta}_{D[E]}(\overline{S}(x)^\dagger)^{\delta\gamma}_{[E]F}(\gamma_0)_{FD}\Big\} \\
&\qquad -\{x\longleftrightarrow y\}\Big\rangle_U \\
&\overset{(B.50)}{=} \frac{2a^3}{L^{3/2}}\Big\langle +\mathrm{Re}\sum_{\mathbf{y}}\Big\{\Big(\overline{P}(y)^{\gamma\alpha}_{C[A]}\Big)^*(\gamma_0)_{CD}\overline{N_{05}}(y,x_0)^{\gamma\alpha}_{D[A]}\Big\} \\
&\qquad -\mathrm{Re}\sum_{\mathbf{x}}\Big\{\Big(\overline{P}(x)^{\gamma\alpha}_{C[A]}\Big)^*(\gamma_0)_{CD}\overline{N_{05}}(x,y_0)^{\gamma\alpha}_{D[A]}\Big\}\Big\rangle_U \\
&\quad +[gf]_{\mathrm{AA}}(x_0,y_0)-[gf]_{\mathrm{AA}}(y_0,x_0)\;.
\end{aligned}
\tag{B.52}
$$

The evaluation of f_{AP} and f_{PA} from equations (B.24) and (B.25) is now entirely straightforward. However, the antisymmetry under the exchange $x \leftrightarrow y$ is obtained only when the two are combined.

$$
\begin{aligned}
f_{\mathrm{AP}} &= \frac{a^6}{L^{3/2}} \sum_{\mathbf{x},\mathbf{y}} \Big\langle -2\mathrm{Re}\left\{ (\overline{S}_T)^{\alpha\beta}_{[A][B]} \left(\overline{S}(y)^\dagger\right)^{\beta\gamma}_{[B]C} \left(S(y;x)\gamma_0\gamma_5\overline{R}(x)\right)^{\gamma\alpha}_{C[A]} \right\} \\
&\qquad + L^{3/2}\left\{ \overline{R}(x)^{\alpha\beta}_{A[B]} (\overline{R}(x)^\dagger)^{\beta\alpha}_{[B]C} (\gamma_0)_{CA} \right\} \left\{ \overline{S}(y)^{\gamma\delta}_{D[E]} (\overline{S}(y)^\dagger)^{\delta\gamma}_{[E]D} \right\} \\
&\qquad - L^{3/2}\left\{ \overline{R}(y)^{\alpha\beta}_{A[B]} (\overline{R}(y)^\dagger)^{\beta\alpha}_{[B]A} \right\} \left\{ \overline{S}(x)^{\gamma\delta}_{D[E]} (\overline{S}(x)^\dagger)^{\delta\gamma}_{[E]F} (\gamma_0)_{FD} \right\} \\
&\qquad - 2\mathrm{Re}\left\{ (\overline{S}_T)^{\alpha\beta}_{[A][B]} \left(\overline{S}(x)^\dagger\right)^{\beta\gamma}_{[B]C} (\gamma_0)_{CD} \left(S(x;y)\gamma_5\overline{R}(y)\right)^{\gamma\alpha}_{D[A]} \right\} \Big\rangle_U \\
&\overset{(B.41)}{=} \frac{a^6}{L^{3/2}} \sum_{\mathbf{x},\mathbf{y}} \Big\langle -2\mathrm{Re}\left\{ \left(\overline{P}(y)^{\gamma\alpha}_{C[A]}\right)^* \left(S(y;x)\gamma_0\gamma_5\overline{R}(x)\right)^{\gamma\alpha}_{C[A]} \right\} \\
&\qquad + L^{3/2}\left\{ \overline{R}(x)^{\alpha\beta}_{A[B]} (\overline{R}(x)^\dagger)^{\beta\alpha}_{[B]C} (\gamma_0)_{CA} \right\} \left\{ \overline{S}(y)^{\gamma\delta}_{D[E]} (\overline{S}(y)^\dagger)^{\delta\gamma}_{[E]D} \right\} \\
&\qquad - L^{3/2}\left\{ \overline{R}(y)^{\alpha\beta}_{A[B]} (\overline{R}(y)^\dagger)^{\beta\alpha}_{[B]A} \right\} \left\{ \overline{S}(x)^{\gamma\delta}_{D[E]} (\overline{S}(x)^\dagger)^{\delta\gamma}_{[E]F} (\gamma_0)_{FD} \right\} \\
&\qquad - 2\mathrm{Re}\left\{ \left(\overline{P}(x)^{\gamma\alpha}_{C[A]}\right)^* (\gamma_0)_{CD} \left(S(x;y)\gamma_5\overline{R}(y)\right)^{\gamma\alpha}_{D[A]} \right\} \Big\rangle_U \\
&= \frac{2a^3}{L^{3/2}} \Big\langle -\mathrm{Re}\sum_{\mathbf{y}} \left\{ \left(\overline{P}(y)^{\gamma\alpha}_{C[A]}\right)^* \overline{N_{05}}(y,x_0)^{\gamma\alpha}_{C[A]} \right\} \\
&\qquad -\mathrm{Re}\sum_{\mathbf{x}} \left\{ \left(\overline{P}(x)^{\gamma\alpha}_{C[A]}\right)^* (\gamma_0)_{CD} \overline{N_5}(x,y_0)^{\gamma\alpha}_{D[A]} \right\} \Big\rangle_U \\
&\quad + [gf]_{\mathrm{AP}}(x_0,y_0) + [gf]_{\mathrm{PA}}(y_0,x_0)\,.
\end{aligned} \tag{B.53}
$$

$$
\begin{aligned}
f_{\mathrm{PA}} &= \frac{a^6}{L^{3/2}} \sum_{\mathbf{x},\mathbf{y}} \Big\langle +2\mathrm{Re}\left\{ (\overline{S}_T)^{\alpha\beta}_{[A][B]} \left(\overline{S}(y)^\dagger\right)^{\beta\gamma}_{[B]C} (\gamma_0)_{CD} \left(S(y;x)\gamma_5\overline{R}(x)\right)^{\gamma\alpha}_{D[A]} \right\} \\
&\qquad + L^{3/2}\left\{ \overline{R}(x)^{\alpha\beta}_{A[B]} (\overline{R}(x)^\dagger)^{\beta\alpha}_{[B]A} \right\} \left\{ \overline{S}(y)^{\gamma\delta}_{D[E]} (\overline{S}(y)^\dagger)^{\delta\gamma}_{[E]F} (\gamma_0)_{FD} \right\} \\
&\qquad - L^{3/2}\left\{ \overline{R}(y)^{\alpha\beta}_{A[B]} (\overline{R}(y)^\dagger)^{\beta\alpha}_{[B]C} (\gamma_0)_{CA} \right\} \left\{ \overline{S}(x)^{\gamma\delta}_{D[E]} (\overline{S}(x)^\dagger)^{\delta\gamma}_{[E]D} \right\} \\
&\qquad + 2\mathrm{Re}\left\{ (\overline{S}_T)^{\alpha\beta}_{[A][B]} \left(\overline{S}(x)^\dagger\right)^{\beta\gamma}_{[B]C} \left(S(x;y)\gamma_0\gamma_5\overline{R}(y)\right)^{\gamma\alpha}_{C[A]} \right\} \Big\rangle_U \\
&\overset{(B.41)}{=} \frac{a^6}{L^{3/2}} \sum_{\mathbf{x},\mathbf{y}} \Big\langle +2\mathrm{Re}\left\{ \left(\overline{P}(y)^{\gamma\alpha}_{C[A]}\right)^* (\gamma_0)_{CD} \left(S(y;x)\gamma_5\overline{R}(x)\right)^{\gamma\alpha}_{D[A]} \right\} \\
&\qquad + L^{3/2}\left\{ \overline{R}(x)^{\alpha\beta}_{A[B]} (\overline{R}(x)^\dagger)^{\beta\alpha}_{[B]A} \right\} \left\{ \overline{S}(y)^{\gamma\delta}_{D[E]} (\overline{S}(y)^\dagger)^{\delta\gamma}_{[E]F} (\gamma_0)_{FD} \right\} \\
&\qquad - L^{3/2}\left\{ \overline{R}(y)^{\alpha\beta}_{A[B]} (\overline{R}(y)^\dagger)^{\beta\alpha}_{[B]C} (\gamma_0)_{CA} \right\} \left\{ \overline{S}(x)^{\gamma\delta}_{D[E]} (\overline{S}(x)^\dagger)^{\delta\gamma}_{[E]D} \right\} \\
&\qquad + 2\mathrm{Re}\left\{ \left(\overline{P}(x)^{\gamma\alpha}_{C[A]}\right)^* \left(S(x;y)\gamma_0\gamma_5\overline{R}(y)\right)^{\gamma\alpha}_{C[A]} \right\} \Big\rangle_U \\
&= \frac{2a^3}{L^{3/2}} \Big\langle +\mathrm{Re}\sum_{\mathbf{y}} \left\{ \left(\overline{P}(y)^{\gamma\alpha}_{C[A]}\right)^* (\gamma_0)_{CD} \overline{N_5}(y,x_0)^{\gamma\alpha}_{D[A]} \right\}
\end{aligned}
$$

$$
\begin{aligned}
&+\mathrm{Re}\sum_{\mathbf{x}}\Big\{\Big(\overline{P}(x)^{\gamma\alpha}_{C[A]}\Big)^{*}\,\overline{N_{05}}(x,y_0)^{\gamma\alpha}_{C[A]}\Big\}\Big\rangle_U \\
&-[gf]_{\mathrm{PA}}(x_0,y_0)-[gf]_{\mathrm{AP}}(y_0,x_0)\,. \qquad \text{(B.54)}
\end{aligned}
$$

We can now plug the expressions (B.51) to (B.54) back into (B.19) to obtain

$$
\begin{aligned}
f^{\mathrm{I}}_{\mathrm{AA}}(x_0,y_0) &= f_{\mathrm{AA}}(x_0,y_0)+ac_A[\tilde{\partial}^x_0 f_{\mathrm{PA}}(x_0,y_0)+\tilde{\partial}^y_0 f_{\mathrm{AP}}(x_0,y_0)] \\
&\quad +a^2c_A^2\tilde{\partial}^x_0\tilde{\partial}^y_0 f_{\mathrm{PP}}(x_0,y_0) \\
&= \frac{2a^3}{L^{3/2}}\Big\langle\mathrm{Re}\sum_{\mathbf{y}}\Big\{\Big(\overline{P}(y)^{\gamma\alpha}_{C[A]}\Big)^{*}(\gamma_0)_{CD}\Big[\overline{N_{05}}(y,x_0)+ac_A\tilde{\partial}^x_0\overline{N_5}(y,x_0)\Big]^{\gamma\alpha}_{D[A]}\Big\}\Big\rangle_U \\
&\quad -ac_A\tilde{\partial}^y_0\Big[\frac{2a^3}{L^{3/2}}\Big\langle\mathrm{Re}\sum_{\mathbf{y}}\Big\{\Big(\overline{P}(y)^{\gamma\alpha}_{C[A]}\Big)^{*}\Big[\overline{N_{05}}(y,x_0)+ac_A\tilde{\partial}^x_0\overline{N_5}(y,x_0)\Big]^{\gamma\alpha}_{C[A]}\Big\}\Big] \\
&\quad -\frac{2a^3}{L^{3/2}}\Big\langle\mathrm{Re}\sum_{\mathbf{x}}\Big\{\Big(\overline{P}(x)^{\gamma\alpha}_{C[A]}\Big)^{*}(\gamma_0)_{CD}\Big[\overline{N_{05}}(x,y_0)+ac_A\tilde{\partial}^y_0\overline{N_5}(x,y_0)\Big]^{\gamma\alpha}_{D[A]}\Big\}\Big\rangle_U \\
&\quad +ac_A\tilde{\partial}^x_0\Big[\frac{2a^3}{L^{3/2}}\Big\langle\mathrm{Re}\sum_{\mathbf{x}}\Big\{\Big(\overline{P}(x)^{\gamma\alpha}_{C[A]}\Big)^{*}\Big[\overline{N_{05}}(x,y_0)+ac_A\tilde{\partial}^y_0\overline{N_5}(x,y_0)\Big]^{\gamma\alpha}_{C[A]}\Big\}\Big\rangle_U\Big] \\
&\quad +[gf]_{\mathrm{AA}}(x_0,y_0)-[gf]_{\mathrm{AA}}(y_0,x_0)+ac_A\tilde{\partial}^x_0\Big[-[gf]_{\mathrm{PA}}(x_0,y_0)-[gf]_{\mathrm{AP}}(y_0,x_0)\Big] \\
&\quad +ac_A\tilde{\partial}^y_0\Big[[gf]_{\mathrm{AP}}(x_0,y_0)+[gf]_{\mathrm{PA}}(y_0,x_0)\Big] \\
&\quad +a^2c_A^2\tilde{\partial}^x_0\tilde{\partial}^y_0\Big[[gf]_{\mathrm{PP}}(y_0,x_0)-[gf]_{\mathrm{PP}}(x_0,y_0)\Big]\,. \qquad \text{(B.55)}
\end{aligned}
$$

The expressions in square brackets, which multiply the $\overline{P}$ propagator, can be obtained with one additional inversion for x_0 and y_0 and each combination of external indices $[A]$ and α. More details about the necessary inversions are given in Sections B.2.2 and B.2.3. If it is necessary to keep $f^{\mathrm{I}}_{\mathrm{AA}}$ as an explicit function of c_A more inversions are needed.

The correlation function $\tilde{f}^{\mathrm{I}}_{\mathrm{PA}}(y_0+t,y_0)$ (B.26) multiplying the mass term in the integrated Ward identity can also be expanded in the same way.

$$
\begin{aligned}
\tilde{f}^{\mathrm{I}}_{\mathrm{PA}}(y_0+t,y_0) &= a\sum_{x_0=y_0}^{y_0+t}w(x_0)\Big[f_{\mathrm{PA}}(x_0,y_0)+c_Aa\tilde{\partial}^y_0 f_{\mathrm{PP}}(x_0,y_0)\Big] \\
&= \frac{2a^4}{L^{3/2}}\Big\langle\mathrm{Re}\sum_{x_0=y_0}^{y_0+t}w(x_0)\sum_{\mathbf{x}}\Big\{\Big(\overline{P}(x)^{\gamma\alpha}_{C[A]}\Big)^{*}\Big[\overline{N_{05}}(x,y_0)\Big]^{\gamma\alpha}_{C[A]}\Big\}\Big\rangle_U \\
&\quad +ac_A\Big[\frac{2a^4}{L^{3/2}}\Big\langle\mathrm{Re}\sum_{x_0=y_0}^{y_0+t}w(x_0)\sum_{\mathbf{x}}\Big\{\Big(\overline{P}(x)^{\gamma\alpha}_{C[A]}\Big)^{*}\Big[\tilde{\partial}^y_0\overline{N_5}(x,y_0)\Big]^{\gamma\alpha}_{C[A]}\Big\}\Big\rangle_U\Big] \\
&\quad +\frac{2a^4}{L^{3/2}}\Big\langle\mathrm{Re}\sum_{\mathbf{y}}\Big\{\Big(\overline{P}(y)^{\gamma\alpha}_{C[A]}\Big)^{*}(\gamma_0)_{CD}\Big[\sum_{x_0=y_0}^{y_0+t}w(x_0)\overline{N_5}(y,x_0)^{\gamma\alpha}_{D[A]}\Big]\Big\}\Big\rangle_U \\
&\quad -c_Aa\Big[\frac{2a^4}{L^{3/2}}\sum_{x_0=y_0}^{y_0+t}w(x_0)\,\tilde{\partial}^y_0\Big\langle\mathrm{Re}\sum_{\mathbf{y}}\Big\{\Big(\overline{P}(y)^{\gamma\alpha}_{C[A]}\Big)^{*}\Big[\overline{N_5}(y,x_0)^{\gamma\alpha}_{C[A]}\Big]\Big\}\Big\rangle_U\Big]
\end{aligned}
$$

$$+c_A a^2 \sum_{x_0=y_0}^{y_0+t} w(x_0) \left[\tilde{\partial}_0^y \Big(-[gf]_{\rm PP}(x_0,y_0) + [gf]_{\rm PP}(y_0,x_0) \Big) \right]$$
$$+a \sum_{x_0=y_0}^{y_0+t} w(x_0) \Big(-[gf]_{\rm PA}(x_0,y_0) - [gf]_{\rm AP}(y_0,x_0) \Big) \ . \tag{B.56}$$

B.2.2 Sources for the inversion of the Dirac operator

With the definition of the propagator $S(x;y)$ as the inverse of the Dirac operator[1]

$$D(x,y)^{\alpha\beta}_{AB} \cdot S(y;z)^{\beta\gamma}_{BC} = a^{-4}\delta_{xz}\delta_{\alpha\gamma}\delta_{AC} \ , \tag{B.57}$$

one can easily calculate the action of D on the summed correlators.

$$\begin{aligned}
D(x,y)^{\alpha\beta}_{AB}\overline{S}(y)^{\beta\gamma}_{B[C]} &\overset{(B.1)}{=} \frac{\tilde{c}_{\rm t}a^3}{L^{3/2}} \sum_{\mathbf{z}} D(x,y)^{\alpha\beta}_{AB} S(y;a,\mathbf{z})^{\beta\delta}_{BD} [U_0(0,\mathbf{z})^{-1}]_{\delta\gamma}[P_+]_{D[C]} \\
&\overset{(B.57)}{=} \frac{\tilde{c}_{\rm t}a^3}{L^{3/2}} \sum_{\mathbf{z}} a^{-4}\delta_{x_0,a}\delta^{(3)}_{\mathbf{xz}}\delta_{\alpha\delta}\delta_{AD} \left[U_0(0,\mathbf{z})^{-1}\right]_{\delta\gamma} [P_+]_{D[C]} \\
&= \frac{\tilde{c}_{\rm t}}{aL^{3/2}} \delta_{a,x_0} \left[U_0(0,\mathbf{x})^{-1}\right]_{\alpha\gamma} [P_+]_{A[C]} \ ,
\end{aligned} \tag{B.58}$$

$$D(x,y)^{\alpha\beta}_{AB}\overline{R}(y)^{\beta\gamma}_{B[C]} \overset{(B.3)}{=} \frac{\tilde{c}_{\rm t}}{aL^{3/2}} \delta_{T-a,x_0} \left[U_0(T-a,\mathbf{x})\right]_{\alpha\gamma} [P_-]_{A[C]} \ . \tag{B.59}$$

The right–hand sides of equations (B.58) and (B.59) are therefore the sources to be used in the calculation of $\overline{S}(x)$ and $\overline{R}(x)$. For all index combinations of these propagators that were used, six inversions, corresponding to the possible combinations of γ and $[C]$, are needed. Similarly we obtain for the expressions containing the full propagator $S(x;y)$

$$\begin{aligned}
D(z,y)^{\beta\gamma}_{BC}\, a^3 \sum_{\mathbf{x}} \left[S(y;x)\Gamma\overline{R}(x)\right]^{\gamma\alpha}_{C[A]} &= D(z,y)^{\beta\gamma}_{BC}\, a^3 \sum_{\mathbf{x}} S(y,x)^{\gamma\delta}_{CD}\Gamma_{DE}\left[\overline{R}(x)\right]^{\delta\alpha}_{E[A]} \\
&= \sum_{\mathbf{x}} a^{-1}\delta_{zx}\delta_{BD}\delta_{\beta\delta}\Gamma_{DE}\left[\overline{R}(x)\right]^{\delta\alpha}_{E[A]} \\
&= a^{-1}\delta_{z_0x_0}\Gamma_{BE}\left[\overline{R}(z)\right]^{\beta\alpha}_{E[A]} \ .
\end{aligned} \tag{B.60}$$

Thus, to calculate $\overline{N}_5$ and $\overline{N}_{05}$, the knowledge of the full propagator $S(x;y)$ is not necessary. Instead, one uses $\overline{R}$ as the source for an inversion to obtain the desired product of propagators. When $\overline{N}_5$ is used with a time derive, this is included in the source, such that e.g. $\tilde{\partial}_0^x\overline{N_5}(y,x_0)$ also requires only one inversion. The same applies to the correlator

$$\sum_{x_0=y_0}^{y_0+t} w(x_0)\overline{N_5}(y,x_0)^{\gamma\alpha}_{D[A]} \ ,$$

appearing in both the bare and the improvement term of $\tilde{f}^{\rm I}_{\rm PA}$.

[1] Here D stands symbolically for $D+\delta D+m_0$ from (A.10).

B.2.3 Counting inversions

Here we give the structure of the program that calculates the correlation function necessary for the estimate of Z_{A}. We write $f_{\mathrm{AA}}^{\mathrm{I}}$ as `fAA1`+c_{A}`fAA2`+c_{A}^2`fAA3` and $\tilde{f}_{\mathrm{PA}}^{\mathrm{I}}$ as `fPA1`+c_{A}`fPA2`. On a given gauge configuration the program proceeds according to

for all γ and $[C]$ {
Solve for $\overline{S}(\star)_{\star[C]}^{\star\gamma}$ and
accumulate result into f_{P}, f_{A}, $\overline{S}_T$, f_1 and $\overline{P}$. }

for all γ and $[C]$ {
Solve for $\overline{R}(\star)_{\star[C]}^{\star\gamma}$ and
accumulate result into g_{P}, g_{A}, f_{V}.

Solve for $\overline{N}_{05}(\star, x_0)_{\star[C]}^{\star\gamma}$ and
accumulate result into `fAA1` and `fAA2`.

Solve for $\tilde{\partial}_0^x \overline{N}_5(\star, x_0)_{\star[C]}^{\star\gamma}$ and
accumulate result into `fAA2` and `fAA3`.

Solve for $\overline{N}_{05}(\star, y_0)_{\star[C]}^{\star\gamma}$ and
accumulate result into `fAA1`, `fAA2` and `fPA1`.

Solve for $\tilde{\partial}_0^y \overline{N}_5(\star, y_0)_{\star[C]}^{\star\gamma}$ and
accumulate result into `fAA2`, `fAA3` and `fPA2`.

Solve for $\sum_{x_0=y_0}^{y_0+t} \overline{N_5}(\star, x_0)_{\star[C]}^{\star\gamma}$ and
accumulate result into `fPA1` and `fPA2`. }

The "accumulate into…" corresponds to the trace over color and (restricted) Dirac indices in the correlation functions. For the connected correlators this is done by taking the scalar product of $\overline{P}$ with the result of the inversion, taking into account temporal derivatives or sums and the correct combination of Dirac indices as given by (B.55) and (B.56).

Thus, a calculation of f_{A}, f_{P} and f_1 needs six inversions on each gauge configuration, while six more are required for g_{A}, g_{P} and f_{V}. A total of 36 is needed for the correlation function $f_{\mathrm{AA}}^{\mathrm{I}}$ and only six more for the volume correlator $\tilde{f}_{\mathrm{PA}}^{\mathrm{I}}$. However, even this is negligible compared to the cost of the inversions in the molecular dynamics. One should note that if the value of c_{A} were fixed at run–time, two of the additional inversions could be saved by using the linearity of the Dirac equation, e.g. by solving

$$
\begin{aligned}
D(z,y)_{BC}^{\beta\gamma}\Big[\overline{N_{05}}(y,x_0) + a c_A \tilde{\partial}_0^x \overline{N_5}(y,x_0)\Big]_{C[A]}^{\gamma\alpha} \\
\stackrel{(B.60)}{=} a^{-1}\delta_{z_0 x_0}(\gamma_0\gamma_5)_{BE}\left[\overline{R}(z)\right]_{E[A]}^{\beta\alpha} \\
+\frac{c_A}{2a}\delta_{z_0,x_0+a}(\gamma_5)_{BE}\left[\overline{R}(z)\right]_{E[A]}^{\beta\alpha} \\
-\frac{c_A}{2a}\delta_{z_0,x_0-a}(\gamma_5)_{BE}\left[\overline{R}(z)\right]_{E[A]}^{\beta\alpha} \ ,
\end{aligned}
$$

thus reducing the total number of inversions from 42 to 30. An overview is given in table Table B.1.

correlation functions	# inversions
f_{A}, f_{P}, f_1	6
f_{A}, f_{P}, f_1, g_{A}, g_{P}, f_{V}	12
f_{A}, f_{P}, f_1, g_{A}, g_{P}, f_{V}, $f_{\mathrm{AA}}^{\mathrm{I}}$	36 (24)
f_{A}, f_{P}, f_1, g_{A}, g_{P}, f_{V}, $f_{\mathrm{AA}}^{\mathrm{I}}$, $\tilde{f}_{\mathrm{PA}}^{\mathrm{I}}$	42 (30)

Table B.1: Number of inversions needed to compute the correlation functions. The numbers in parenthesis refer to the case, where the value of c_{A} is fixed at run–time.

Appendix C

Transforming the integrated Ward identity

We start by isolating the contact term in the volume integration in (8.29)

$$
\begin{aligned}
&-2m\int\mathrm{d}^3\mathbf{y}\int\mathrm{d}^3\mathbf{x}\int_{y_0-t}^{y_0+t}\mathrm{d}x_0\,\epsilon^{abc}\Big\langle P^a(x_0,\mathbf{x})A_0^b(y_0,\mathbf{y})\mathcal{O}_{\rm ext}\Big\rangle \\
&= \; -2m\int\mathrm{d}^3\mathbf{y}\int\mathrm{d}^3\mathbf{x}\int_{y_0+\epsilon}^{y_0+t}\mathrm{d}x_0\,\epsilon^{abc}\Big\langle P^a(x_0,\mathbf{x})A_0^b(y_0,\mathbf{y})\mathcal{O}_{\rm ext}\Big\rangle \\
&\quad -2m\int\mathrm{d}^3\mathbf{y}\int\mathrm{d}^3\mathbf{x}\int_{y_0-\epsilon}^{y_0+\epsilon}\mathrm{d}x_0\,\epsilon^{abc}\Big\langle P^a(x_0,\mathbf{x})A_0^b(y_0,\mathbf{y})\mathcal{O}_{\rm ext}\Big\rangle \\
&\quad -2m\int\mathrm{d}^3\mathbf{y}\int\mathrm{d}^3\mathbf{x}\int_{y_0-t}^{y_0-\epsilon}\mathrm{d}x_0\,\epsilon^{abc}\Big\langle P^a(x_0,\mathbf{x})A_0^b(y_0,\mathbf{y})\mathcal{O}_{\rm ext}\Big\rangle \,. \qquad \text{(C.1)}
\end{aligned}
$$

We will now use the partial conservation of the axial current to relate the two contributions from the surface integral in eq.(8.29). Using $\int\mathrm{d}^3\mathbf{x}\,\partial_k f_k(x)=0$ (for periodic spatial boundary conditions) the partial conservation reads as an operator identity

$$
\begin{aligned}
\int\mathrm{d}^3\mathbf{y}\,\partial_0 A_0^b(y) &= \int\mathrm{d}^3\mathbf{y}\,\partial_\mu A_\mu^b(y) = 2m\int\mathrm{d}^3\mathbf{y}P^b(y) \qquad \Rightarrow \\
\int\mathrm{d}^3\mathbf{y}A_0^b(y_0-t,\mathbf{y}) &= \int\mathrm{d}^3\mathbf{y}A_0^b(y_0-\epsilon,\mathbf{y}) - 2m\int_{y_0-t}^{y_0-\epsilon}\mathrm{d}x_0\int\mathrm{d}^3\mathbf{y}P^b(x_0,\mathbf{y})\,. \qquad \text{(C.2)}
\end{aligned}
$$

We will also use (C.2) in the form

$$
\int\mathrm{d}^3\mathbf{x}A_0^a(y_0,\mathbf{x}) = \int\mathrm{d}^3\mathbf{x}A_0^a(y_0+t,\mathbf{x}) - 2m\int_{y_0}^{y_0+t}\mathrm{d}x_0\int\mathrm{d}^3\mathbf{x}\,P^a(x_0,\mathbf{x})\,. \qquad \text{(C.3)}
$$

These relations can be used only in matrix elements with fields that are not located in the integration region since otherwise the axial variation of the latter will appear as an additional term. We therefore have to be careful how far we can shift the current insertions. Due to the antisymmetry of ϵ^{abc} the second expression in the first line of equation (8.29) can be rewritten as

$$
\int\mathrm{d}^3\mathbf{y}\int\mathrm{d}^3\mathbf{x}\,\epsilon^{abc}\Big\langle A_0^a(y_0,\mathbf{x})A_0^b(y_0-t,\mathbf{y})\mathcal{O}_{\rm ext}\Big\rangle
$$

$$
\begin{aligned}
&\overset{(C.2)}{=} \int \mathrm{d}^3\mathbf{y} \int \mathrm{d}^3\mathbf{x}\, \epsilon^{abc} \Big\langle A_0^a(y_0,\mathbf{x}) A_0^b(y_0-\epsilon,\mathbf{y}) \mathcal{O}_{\mathrm{ext}} \Big\rangle \\
&\qquad -2m \int \mathrm{d}^3\mathbf{y} \int \mathrm{d}^3\mathbf{x} \int_{y_0-t}^{y_0-\epsilon} \mathrm{d}x_0\, \epsilon^{abc} \Big\langle A_0^a(y_0,\mathbf{x}) P^b(x_0,\mathbf{y}) \mathcal{O}_{\mathrm{ext}} \Big\rangle \\
&\overset{(C.3)}{=} \int \mathrm{d}^3\mathbf{y} \int \mathrm{d}^3\mathbf{x}\, \epsilon^{abc} \Big\langle A_0^a(y_0+t,\mathbf{x}) A_0^b(y_0-\epsilon,\mathbf{y}) \mathcal{O}_{\mathrm{ext}} \Big\rangle \\
&\qquad -2m \int \mathrm{d}^3\mathbf{y} \int \mathrm{d}^3\mathbf{x} \int_{y_0}^{y_0+t} \mathrm{d}x_0\, \epsilon^{abc} \Big\langle P^a(x_0,\mathbf{x}) A_0^b(y_0-\epsilon,\mathbf{y}) \mathcal{O}_{\mathrm{ext}} \Big\rangle \\
&\qquad +2m \int \mathrm{d}^3\mathbf{y} \int \mathrm{d}^3\mathbf{x} \int_{y_0-t}^{y_0-\epsilon} \mathrm{d}x_0\, \epsilon^{abc} \Big\langle P^a(x_0,\mathbf{y}) A_0^b(y_0,\mathbf{x}) \mathcal{O}_{\mathrm{ext}} \Big\rangle \,. \qquad \text{(C.4)}
\end{aligned}
$$

The last term cancels the last integral in the split up integration (C.1) and in the limit $\epsilon \to 0$ the first combines with the result from the integration over the upper surface. Thus, inserting (C.4) and (C.1) into equation (8.29) yields

$$
\begin{aligned}
&2i \int \mathrm{d}^3\mathbf{y} \, \Big\langle V_0^c(y_0,\mathbf{y}) \mathcal{O}_{\mathrm{ext}} \Big\rangle = \\
&\lim_{\epsilon\to 0}\; 2 \int \mathrm{d}^3\mathbf{y} \int \mathrm{d}^3\mathbf{x}\, \epsilon^{abc} \Big\langle A_0^a(y_0+t,\mathbf{x}) A_0^b(y_0,\mathbf{y}) \mathcal{O}_{\mathrm{ext}} \Big\rangle \\
&\qquad -2m \int \mathrm{d}^3\mathbf{y} \int \mathrm{d}^3\mathbf{x} \int_{y_0}^{y_0+t} \mathrm{d}x_0\, \epsilon^{abc} \Big\langle P^a(x_0,\mathbf{x}) A_0^b(y_0-\epsilon,\mathbf{y}) \mathcal{O}_{\mathrm{ext}} \Big\rangle \\
&\qquad -2m \int \mathrm{d}^3\mathbf{y} \int \mathrm{d}^3\mathbf{x} \int_{y_0+\epsilon}^{y_0+t} \mathrm{d}x_0\, \epsilon^{abc} \Big\langle P^a(x_0,\mathbf{x}) A_0^b(y_0,\mathbf{y}) \mathcal{O}_{\mathrm{ext}} \Big\rangle \\
&\qquad -2m \int \mathrm{d}^3\mathbf{y} \int \mathrm{d}^3\mathbf{x} \int_{y_0-\epsilon}^{y_0+\epsilon} \mathrm{d}x_0\, \epsilon^{abc} \Big\langle P^a(x_0,\mathbf{x}) A_0^b(y_0,\mathbf{y}) \mathcal{O}_{\mathrm{ext}} \Big\rangle \,. \qquad \text{(C.5)}
\end{aligned}
$$

In the third line we can replace $A_0^b(y_0-\epsilon)$ by $A_0^b(y_0)$ if we start the time integration at $y_0+\epsilon$. This preserves the order of the operator insertions and allows us to combine two of the time integrations with the result given by

$$
\begin{aligned}
&i\int\!\mathrm{d}^3\mathbf{y}\;\Big\langle V_0^c(y_0,\mathbf{y})\mathcal{O}_{\mathrm{ext}}\Big\rangle = \\
&\lim_{\epsilon\to 0}\int\!\mathrm{d}^3\mathbf{y}\int\!\mathrm{d}^3\mathbf{x}\,\epsilon^{abc}\Big\langle A_0^a(y_0{+}t,\mathbf{x})A_0^b(y_0,\mathbf{y})\mathcal{O}_{\mathrm{ext}}\Big\rangle \\
&\qquad -2m\int\!\mathrm{d}^3\mathbf{y}\int\!\mathrm{d}^3\mathbf{x}\int_{y_0+\epsilon}^{y_0+t}\mathrm{d}x_0\,\epsilon^{abc}\Big\langle P^a(x_0,\mathbf{x})A_0^b(y_0,\mathbf{y})\mathcal{O}_{\mathrm{ext}}\Big\rangle \\
&\qquad -m\int\!\mathrm{d}^3\mathbf{y}\int\mathrm{d}^3\mathbf{x}\int_{y_0-\epsilon}^{y_0+\epsilon}\mathrm{d}x_0\,\epsilon^{abc}\Big\langle P^a(x_0,\mathbf{x})A_0^b(y_0,\mathbf{y})\mathcal{O}_{\mathrm{ext}}\Big\rangle\,. \qquad \text{(C.6)}
\end{aligned}
$$

The contact terms are the same as those appearing in (8.28) and thus integrable under a four–dimensional integration. The limit of $\epsilon \to 0$ can hence be performed and the final result is

$$
\begin{aligned}
&i\int\!\mathrm{d}^3\mathbf{y}\;\Big\langle V_0^c(y_0,\mathbf{y})\mathcal{O}_{\mathrm{ext}}\Big\rangle = \\
&\int\!\mathrm{d}^3\mathbf{y}\int\!\mathrm{d}^3\mathbf{x}\,\epsilon^{abc}\Big\langle A_0^a(y_0{+}t,\mathbf{x})A_0^b(y_0,\mathbf{y})\mathcal{O}_{\mathrm{ext}}\Big\rangle \\
&\qquad -2m\int\!\mathrm{d}^3\mathbf{y}\int\!\mathrm{d}^3\mathbf{x}\int_{y_0}^{y_0+t}\mathrm{d}x_0\,\epsilon^{abc}\Big\langle P^a(x_0,\mathbf{x})A_0^b(y_0,\mathbf{y})\mathcal{O}_{\mathrm{ext}}\Big\rangle\,.
\end{aligned}
$$

Appendix D

List of simulation parameters and results

In Table D.1 the simulation results for Z_{A} and Z_{V} are collected. The algorithm is specified in the same manner as in Table 6.1. The number of measurements N_{meas} is multiplied with the number of replica and as before τ_{meas} is the molecular dynamics time between consecutive measurements. The PCAC mass am is defined through (8.37) and the column Z_{V} refers to the definition (8.36) before taking the chiral limit.

For completeness the results for Z_{A} are also given for the estimate using only connected diagrams in the evaluation of the correlation functions f_{XY}, see Section 8.3.4. This is denoted by $Z_{\mathrm{A}}^{\mathrm{con}}$. An (additional) superscript "old" refers to the estimate from the massless condition from ref. [11], where the $m\tilde{f}_{\mathrm{PA}}^{\mathrm{I}}$ term is neglected.

algo	β	κ	L	T	N_{meas}	τ_{meas}	am	Z_{A}	$Z_{\mathrm{A}}^{\mathrm{con}}$	$Z_{\mathrm{A}}^{\mathrm{old}}$	$Z_{\mathrm{A}}^{\mathrm{con,old}}$	Z_{V}
H_2	5.200	0.13550	8	18	16·200	4	0.01718(90)	0.7301(173)	0.8411(80)	0.5039(159)	1.0124(224)	0.7509(6)
P_{140}	5.200	0.13550	8	18	16·40	10	0.0159(11)	0.7186(295)	0.8455(108)	0.5026(156)	1.0174(227)	0.7497(14)
P_{140}	5.200	0.13560	8	18	16·225	3	0.01310(68)	0.7157(137)	0.8212(96)	0.5546(117)	0.9627(123)	0.7471(7)
P_{140}	5.200	0.13570	8	18	16·230	2	0.0088(11)	0.7134(126)	0.8302(70)	0.6222(149)	0.9114(113)	0.7447(8)
P_{140}	5.200	0.13580	8	18	16·230	2	0.00194(81)	0.7176(114)	0.8588(99)	0.7032(115)	0.8773(104)	0.7424(14)
P_{140}	5.290	0.13625	8	18	16·50	2	0.0031(18)	0.7527(102)	0.8103(167)	0.7391(108)	0.8437(179)	0.7507(19)
P_{140}	5.290	0.13641	8	18	16·120	2	−0.00512(61)	0.7540(124)	0.8378(73)	0.7421(120)	0.8081(62)	0.7490(12)
H_2	5.500	0.13606	12	27	16·25	6	0.02254(26)	0.8417(222)	0.8077(26)	0.3918(137)	1.0732(261)	0.7853(14)
H_2	5.500	0.13650	12	27	16·44	3	0.00758(27)	0.7987(153)	0.8100(45)	0.6063(143)	0.8630(57)	0.7738(8)
H_2	5.500	0.13672	12	27	16·80	3	0.00041(25)	0.7888(32)	0.8048(54)	0.7861(33)	0.8096(56)	0.7650(21)
H_2	5.500	0.13672	8	18	1·318	4	−0.00168(62)	0.8105(64)	0.8168(38)	0.8148(58)	0.8111(42)	0.7750(45)
H_2	5.715	0.13665	16	36	1·106	2	0.00194(57)	0.8142(135)	0.8079(31)	0.7811(60)	0.8199(20)	0.7827(11)
H_2	5.715	0.13670	16	36	1·54	2	−0.00060(69)	0.8004(26)	0.8120(30)	0.8014(23)	0.8098(28)	0.7793(20)
H_2	5.715	0.13670	12	27	4·62	2	−0.00100(34)	0.8021(38)	0.8182(18)	0.8071(34)	0.8138(19)	0.7861(18)
H_2	7.200	0.13420	8	18	1·220	2	0.00029(45)	0.8721(24)	0.8772(18)	0.8699(22)	0.8787(18)	0.8573(9)
H_2	7.200	0.13424	8	18	1·164	2	−0.00028(42)	0.8683(22)	0.8732(18)	0.8707(36)	0.8716(28)	0.8553(6)
H_2	7.200	0.13424	12	27	16·50	2	−0.00049(15)	0.8685(23)	0.8717(8)	0.8717(23)	0.8697(7)	0.8543(18)
H_2	7.200	0.13424	16	36	1·80	2	−0.00023(41)	0.8678(18)	0.8670(17)	0.8694(14)	0.8652(11)	0.8508(18)
H_2	8.400	0.13258	8	18	4·40	2	0.00023(40)	0.8990(28)	0.8956(16)	0.8962(26)	0.8973(19)	0.8839(15)
H_2	8.400	0.13262	8	18	4·45	2	−0.00183(42)	0.8998(25)	0.8953(13)	0.9184(39)	0.8845(15)	0.8826(7)
H_2	9.600	0.13140	8	18	4·100	2	0.00021(15)	0.9137(14)	0.9154(7)	0.9110(18)	0.9166(8)	0.9040(4)
H_2	9.600	0.13142	8	18	4·125	2	−0.00059(15)	0.9118(12)	0.9155(7)	0.9188(18)	0.9121(10)	0.9034(4)

Table D.1: Summary of simulation parameters and results for Z_{A} and Z_{V}.

Acknowledgments

Here is a (most likely incomplete) list of people whose help, knowledge, patience and support were indispensable for a successful completion of this work.

- I would like to thank Ulli Wolff for giving me the opportunity to work in his group and the encouragement throughout my time here.
- Thanks to the ALPHA people for a fruitful and interesting collaboration. In particular to Rainer Sommer for the many interesting discussions about our work.
- Special thanks to all the members of the COM group in the last three years, especially Francesco, Andreas, Michele, Björn, Tom, Magdalena and Oliver. I think we had a great time.
- I am especially indebted to Francesco Knechtli for recruiting me to Berlin and to Andreas Jüttner for sharing the COM-PhD experience!
- Michele not only showed amazing knowledge and patience in the discussion of physical questions, his advice was also essential for bringing my thesis into its final form. Thanks!
- I am grateful to Martin Lüscher and Stefan Sint for illuminating discussions and Hartmut Wittig for communicating details about the simulations and the TAO code from the quenched Z_{A} project.
- I thank Stephan Dürr for his valuable work in the early stages of the c_{A} project and Heiko Molke for contributing the implementation of the spatial wave functions.
- Thanks to the DFG for the scholarship within the Graduiertenkolleg 271 (Strukturuntersuchungen, Präzisionstests und Erweiterungen des Standardmodells der Elem entarteilchenphysik).
- I am also indebted to my family, who provided continuous support and encouragement for my scientific endeavors.

Lebenslauf

Name:	RolandHoffmann
1996	Abitur am Ernst-Mach-Gymnasium Haar
10/1997 - 8/2002	Studium an der Universität Regensburg in der Fachrichtung Physik
8/2000 - 7/2001	Studium der Physik an der University of Colorado
10/2002 - 8/2005	Promotion an der Humboldt-Universität zu Berlin, Lehrstuhl Prof. Dr. U. Wolff, Institut für Physik

Selbständigkeitserklärung

Hiermit erkläre ich, die vorliegende Arbeit selbständig ohne fremde Hilfe verfaßt und nur die angegebene Literatur und Hilfsmittel verwendet zu haben.

Roland Hoffmann
18. Mai 2005